WATER CALORIMETRY FOR PROTON THERAPY

IMPLEMENTING A PRIMARY DOSE MEASUREMENT STANDARD

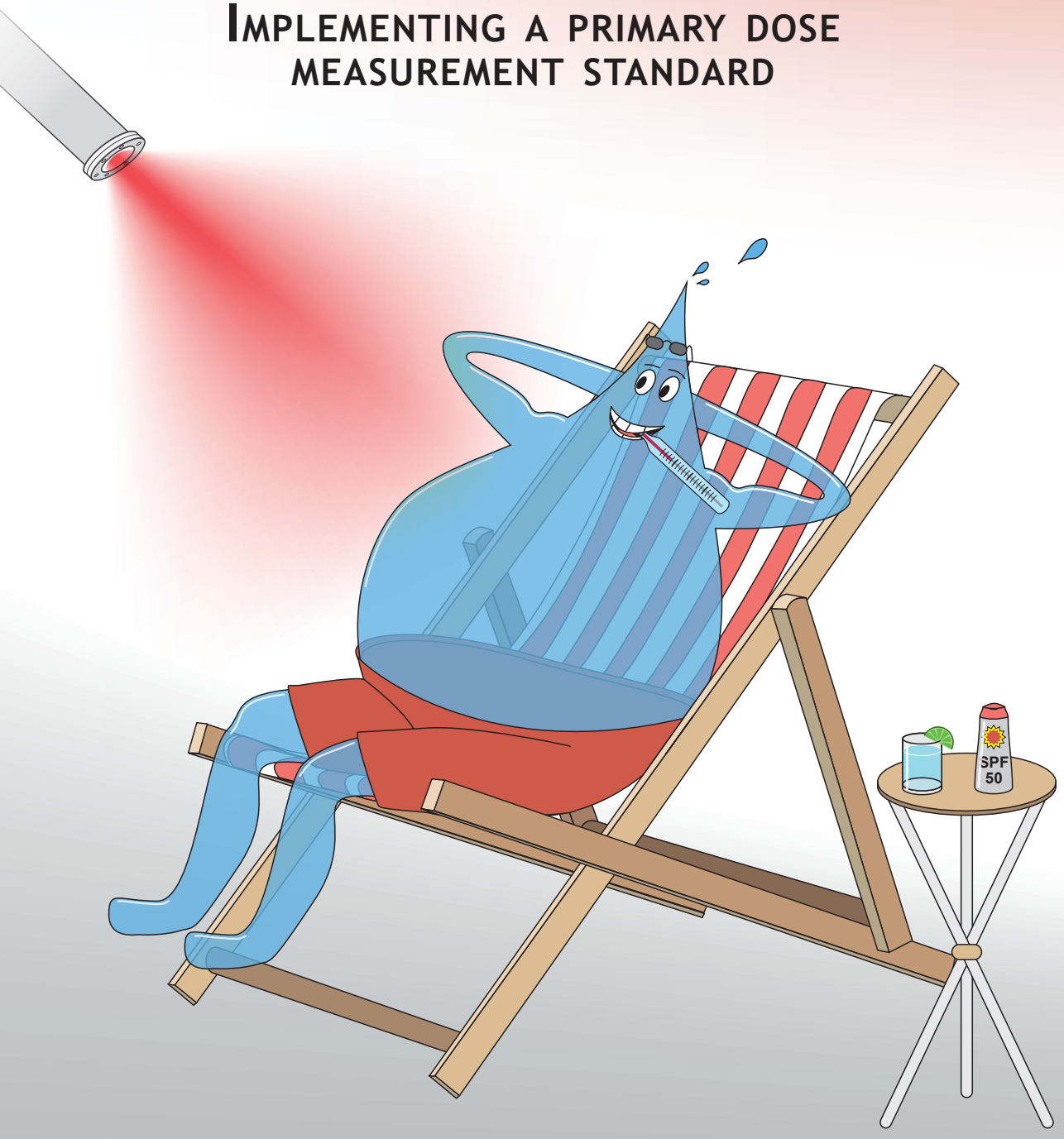

Josbert Mulder

Water calorimetry for proton therapy

Implementing a primary dose measurement standard

PhD thesis

Josbert Mulder

Front cover:
Mr H_2O enjoying a bit of warmth after having been maintained at a frigid 4.0 °C at work.

Back cover:
Computer rendering of the HPC (glass vessel) used for some of the experiments (chapter 5). The vessel includes alignment markers on the front and back-wall and along the top of the cylinder and recess at the bottom. Also shown are the proton beam, a glass coated mixing bead and adjustment screws for temperature probe positioning.

rijksuniversiteit groningen

kvi - center for advanced radiation technology

University Medical Center Groningen

connecting innovators

This research is supported by the Dutch Technology Foundation STW (grant No. 10863), which is part of the Netherlands Organisation for Scientific Research (NWO), and which is partly funded by the Ministry of Economic Affairs.

This work is part of a research program funded in part by the Stichting voor Fundamenteel Onderzoek der Materie (FOM), which is financially supported by the Nederlandse Organisatie voor Wetenschappelijk Onderzoek (NWO).

ISBN: 978-90-367-9853-2 (printed version)
ISBN: 978-90-367-9854-9 (electronic version)

rijksuniversiteit
groningen

Water calorimetry for proton therapy

Implementing a primary dose measurement standard

Proefschrift

ter verkrijging van de graad van doctor aan de
Rijksuniversiteit Groningen
op gezag van de
rector magnificus prof. dr. E. Sterken
en volgens het besluit van het College voor Promoties.

De openbare verdediging zal plaatsvinden op

vrijdag 30 juni 2017 om 11.00 uur

door

Josbert Mulder

geboren op 21 april 1986
te Winschoten

Promotores
Prof. dr. S. Brandenburg
Prof. dr. J.M. Schippers

Beoordelingscommissie
Prof. dr. A.M.J. Paans
Prof. dr. F.J.W. Verhaegen
Prof. dr. A.J. Lomax

Contents

Chapter 1

Introduction

In radiation therapy, the outcome of the treatment is strongly dependent on the administered radiation dose. Therefore, there is a need for calibrated dose delivery. In the case of proton therapy, there is a lack of direct sources of calibration, which results in a relative increase of the uncertainty of the applied physical dose. The subject of this thesis is the use of a water calorimeter as a primary measurement standard for the calibration of therapeutic radiation doses in proton therapy. This chapter discusses the use of water calorimeters within the context of the medical dosimetry that is required in clinical protocols for proton therapy. It then briefly covers the water calorimeter in general and some of the research questions that have been addressed in this thesis.

1.1 Proton therapy

Proton therapy is a technique for medical radiation therapy which uses energetic protons instead of gamma-ray or x-ray photon sources. The technique was suggested in a 1946 article by Wilson[1]. In this remarkably concise article, Wilson makes a point about the potential advantage of protons (and other ions), resulting from their associated characteristic dose distributions. Even in this early paper, he pointed out some of the challenges and possible solutions for practical implementation of the technique.

In the 21st century, the technique of proton therapy is of increasing interest, given the fast increase of the number of facilities in the last decade[2]. As is apparent from statistics of April 2016[3], the combined number of planned proton facilities and those under construction is almost as large as the number of facilities already in operation, indicating nearly exponential growth. The technique of proton therapy is described in a review article by McDonald and Fitzek[4]. Paganetti[5] presents several chapters contributed by various authors on almost any aspect of

proton therapy physics. A rather extensive overview of proton therapy is provided in report 78 by the ICRU[6], which includes a section on dosimetry and calibration standards.

The advantage of proton therapy over conventional photon (x-ray) radiation therapy is the better conformity of the dose distribution to the tumour that can be achieved. Due to the finite range of the protons in the patient, there is essentially no dose deposited behind the targeted tissue. This results in lower doses in healthy tissue and therefore a lower probability for severe complications. The high conformity of the irradiation in some cases allows for treating tumours in locations close to sensitive tissues (organs at risk), which would not otherwise be treatable with radiotherapy due to the expected complications from the unavoidable co-irradiation of the healthy tissue.

1.2 The need for a low uncertainty in applied dose

The promise of proton therapy compared to conventional x-ray therapy is that it increases the width of the therapeutic window. This window is the gap in dose which exists between the dose value where tumour killing becomes effective and the dose value where the side effects (complications) due to irradiation of healthy tissue become prohibitive. The advantage of proton therapy is thus the reduced probability of severe side effects for an equal probability of tumour control.

The clinical benefit is however dependent on reliably reaching a desired tumour-control/complication probability ratio in the therapeutic window. Among other things, good reliability requires that the treatment doses are reproducible and comparable between clinics. In an article considering photon and neutron irradiations, Mijnheer et al.[7] derived a requirement of a standard uncertainty of absolute dose less than 3.5 %, based on the steepness of the dose-response curves for complications due to irradiation of healthy tissue. The authors also note that in some specific cases, one might even desire a somewhat smaller uncertainty. Using similar reasoning, Brahme concludes[8] that the dose uncertainty should preferably be smaller than 3 %.

Thwaites[9] examined both the required and practically achievable dose uncertainties for IMRT treatments. He shows that the total uncertainty is compatible with the commonly required uncertainty of about 3 %. Although the total uncertainty of the dose in the patient is a few times higher than the uncertainty of an ionization chamber calibration (less than 1 %), it consists of several uncertainty components of similar or only slightly larger magnitude. He concludes that individual uncertainties (such as the ionization chamber calibration) are to be on the order of 1 % or less to achieve the combined goal of 3 %.

Given that the objective for proton therapy is high accuracy in the conformity of the dose distribution, the accuracy of the amount of delivered dose should also be of the highest standard. It is reasonable to state that the required uncertainty for a ionization-chamber proton dose calibration should be at least as low as for

x-ray therapy and preferably lower. Keeping in mind that there is some additional uncertainty in transferring the dose measurement of a primary dose standard to an ionization chamber, the primary dose standard for proton dose should achieve a absolute uncertainty well below 1 %.

1.3 Dose traceability and quality assurance

The work presented in this thesis is part of the field of dosimetry standards. It is essential for both clinical practice and clinical scientific studies to have a common internationally implemented definition of what a clinical dose is and how it should be measured. As mentioned in the previous section, the applied amount of dose is always a balance between the direct benefit of tumour killing and adverse complications. This directly brings about the need for a reliable and reproducible dosimetry system.

Equally important is the need for internationally comparable clinical studies. Certainly in the Netherlands, the introduction of proton therapy as a treatment modality is to be accompanied by extensive clinical research programmes[10, 11, 12, 13], in order to assess the effectiveness of various treatments. These scientific efforts require internationally comparable dose delivery.

In order to facilitate both the day-to-day clinical dosimetry requirements as well as to provide an internationally harmonized dosimetry system, protocols like IAEA TRS398[14] (which includes a section specifically for proton therapy) and the Dutch NCS18[15] (photons and electrons only) were created. Invariably, such protocols require dose to be measured in a water volume and the calibration of the measurement equipment to be traceable to a primary measurement standard.

Thus, by taking dosimetry to be a vital part of the quality assurance system, and by making measurements the basis of such quality systems, determining dose becomes (in part) a metrological act. This is no different from common practice in the various branches of industry. Essentially, by requiring that clinical dose measurements are to be traceable to recognised international standards, dose delivery becomes internationally reproducible.

It should be noted that the required confidence of the dose calibrations for the purpose of clinical scientific studies must be at least as good as that which is used for daily clinical practice. In fact, since these scientific studies should be able to distinguish different clinical practices via clinical outcome in terms of dose-response relations, the underlying dose variable should be determined to lower uncertainty than is required for sufficiently reproducible treatment. This means that the calibration chain should be traceable to a primary dose standard with an absolute uncertainty significantly lower than that which is required for routine clinical treatments.

1.4 Dose measurement with ionization chambers

For practical reasons, in the clinic ionization chambers are used to measure dose, rather than primary dose standards (often calorimeters). Ionization chambers measure the electric charge that is released in an air cavity by the effects of the irradiation as a proxy for the dose delivered to the medium into which they are placed. A calibration coefficient is needed to convert the measured charge into a dose in the surrounding medium. Although it is possible to use physics models and Monte Carlo calculations* to obtain a conversion coefficient, the resulting accuracy is limited by the knowledge of the exact geometry of each individual chamber and the accuracy of the physics modelling. Instead, in the interest of accuracy and maintaining traceability to a primary measurement standard, the ionization chambers are calibrated against a primary measurement standard of dose.

TRS398[14] uses the following simple formalism to establish dose using an ionization chamber in ^{60}Co radiation beams:

$$D_{w,Q_0} = M_{Q_0} N_{D,w,Q_0} \tag{1.1}$$

In the above equation D_{w,Q_0} is the dose-to-water in the radiation beam (with the subscript Q_0 denoting ^{60}Co radiation), M_{Q_0} is the reading of the ionization chamber (released charge) and N_{D,w,Q_0} is the calibration coefficient for the chamber in ^{60}Co radiation. The N_{D,w,Q_0} factor is determined for an individual chamber by measuring under identical conditions both the dose D_{w,Q_0} with a primary standard and the released charge in the ionization chamber M_{Q_0}.

^{60}Co beams are used in dose standards because they are extremely stable and very well characterized. However, in the clinic ^{60}Co beams are nowadays no longer frequently used. In the case of photons, multi-MV x-ray beams are used. This means that the N_{D,w,Q_0} calibration factor is not applicable in those clinical beams, since it explicitly refers to ^{60}Co beams. TRS398 therefore defines a second formalism that enables the use of a ^{60}Co-calibrated chamber in a MV photon beam:

$$D_{w,Q} = M_Q N_{D,w,Q_0} k_{Q,Q_0} \tag{1.2}$$

In the above equation $D_{w,Q}$ is the dose-to-water in a radiation beam of a type denoted by the subscript Q, M_Q is the ionization charge measured in the beam Q, N_{D,w,Q_0} is the ^{60}Co calibration coefficient for the chamber as described above and k_{Q,Q_0} is a factor that corrects for the fact that the sensitivity of the chamber is different in the beam of type 'Q' compared to the ^{60}Co beam 'Q_0' in which it was

* A Monte Carlo calculation in the context of radiation physics refers to a numerical method of simulating the microscopic interactions of radiation and secondary radiation in order to derive macroscopically relevant quantities, such as the spatial dose distribution or particle fluence spectra. Through the modelling of physics based on known or estimated interaction coefficients, the Monte Carlo calculation is a simulation of the physical processes in nature. A detailed description of the method and its applications is given in a book by Seco and Verhaegen[16].

calibrated. Effectively, the calibration value of the chamber is corrected for the non-reference conditions:

$$N_{D,w,Q} = N_{D,w,Q_0} k_{Q,Q_0} \tag{1.3}$$

In principle, once the so called 'beam quality conversion factor' k_{Q,Q_0} is known for a specific type of chamber and for the beam type 'Q', that ^{60}Co calibrated ionization chamber can then be used directly to measure the dose for the beam type type 'Q'. It is required that the sensitivity of any individual ionization chamber in beam 'Q' is strongly correlated to its sensitivity in the ^{60}Co calibration beam 'Q_0'. Thus, even though the chamber is not directly calibrated against a primary standard in a clinical type of beam, through its ^{60}Co calibration it is traceable to a primary dose standard. Except for the conversion factor k_{Q,Q_0}, the calibration chain is maintained.

The issue with this methodology is that the k_{Q,Q_0} conversion factors have to be calculated with Monte Carlo simulations. This means that the derived calibration coefficient for a clinical beam $N_{D,w,Q}$ will carry an extra uncertainty that is related to the accuracy of the Monte Carlo simulation of the physics. Another issue is that variations in geometry between individual chambers of a specific chamber type will also cause slight variations in the k_{Q,Q_0} factor that is to be applied for each individual chamber. In principle, it has to be shown that batches of manufactured ionization chambers have a sufficiently reproducible and consistent response in terms of k_{Q,Q_0}. For MV photon beams, TRS398[14] assigns a standard uncertainty of 1.0 % to such type-generic k_{Q,Q_0} factors, which is mostly a Monte Carlo simulation uncertainty and which does not include any uncertainty due to variations in chamber geometry of individual chambers. In constrast, NCS18[15] relies in part on water calorimetery for the MV photon beams and assigns a lower uncertainty of 0.4 % for type-generic k_{Q,Q_0} factors, limited to the chamber types listed in NCS18.

1.4.1 Proton dose measurement with ionization chambers

In the case of clinical proton beams, the dose is also measured with ionization chambers. To determine dose in these beams, the TRS398 protocol prescribes the use of the same formalism that is also used for photon beams:

$$D_{w,Q_p} = M_{Q_p} N_{D,w,Q_0} k_{Q_p,Q_0} \tag{1.4}$$

In the above equation D_{w,Q_p} is the dose-to-water in the proton beam with 'Q_p' indicating that the type of beam is a proton beam, M_{Q_p} is the charge reading of the ionization chamber, N_{D,w,Q_0} is the ^{60}Co calibration coefficient for the chamber and k_{Q_p,Q_0} is the conversion factor that corrects for the fact that the sensitivity of the ionization chamber for proton dose is different from the sensitivity in the ^{60}Co beam in which it is calibrated. Note that the indicator 'Q_p' also refers to properties of the proton beam itself such as the energy of the protons at the point of measurement or the presence of secondary radiation.

The advantage of the above formalism is that it relies on the existing (and reliable) infrastructure for calibrating ionization chambers against a primary standard in ^{60}Co radiation. The main difference with high energy photon calibrations is the fact that the calibration for one type of particle is translated into a calibration that is valid for another type of particle and this is the main source of uncertainty (besides the detriment of using chamber-type specific k_{Q_p,Q_0} factors instead of unique calibrations for each chamber). As a result, the Monte Carlo simulation that is needed to derive k_{Q_p,Q_0} needs to accurately model the chamber response both for photons and for protons. Effectively, uncertainties related to ^{60}Co ionometry that are normally resolved through calibration are re-imported in the conversion factor. This results in a significantly higher uncertainty for the value of k_{Q_p,Q_0}. TRS398[14] assigns an uncertainty of 1.7 % to the value of k_{Q_p,Q_0} for cylindrical ionization chambers. The quoted uncertainty (which is only a part of the total uncertainty) is already much larger than the desired upper limit of 1.0 %.

Fortunately, experiments relying strongly on the accuracy of calculated conversion factors have yielded good results. Measurements of the value of the specific ionization energy of air W_{air}* have shown remarkably consistent results[17]. Keeping in mind that a gradient correction applies, Gomà et al. [18, 19] have found fairly good agreement between various types of ionization chambers in a clinical proton beam, although the authors point out that it is not possible to conclude from the coherence of such data that the k_{Q_p,Q_0} conversion factors are correct in an absolute sense.

1.4.1.1 The introduction of primary standards in the calibration chain

Even if the uncertainty of calculated k_{Q_p,Q_0} factors can be slightly reduced, in the interest of traceability, there still is a need for direct calibrations in terms of proton dose-to-water. At some point, primary standards for proton radiation dose will have to be introduced into the dosimetry system. The calibration of ionization chambers can then be implemented in three slightly distinct ways.

Firstly, one could measure the calibration factors of each chamber individually, in the proton beam qualities at the clinic:

$$N_{D,w,Q_p} = \frac{D_{w,Q_p}}{M_{Q_p}} \tag{1.5}$$

That is, one would measure the proton dose D_{w,Q_p} in the clinic with a primary standard (calorimeter), directly establishing a proton dose calibration N_{D,w,Q_p} which is no longer dependent on a ^{60}Co calibration. From a purely metrological point of view, this by far the best option. However, such practice is very costly in

* W_{air}, sometimes called simply 'W-value', is the mean energy deposited in air to create an ion-pair. This value is an important factor in the calculation of dose using ionization chamber theory. Measurements of W_{air} often rely heavily on application of the theory and Monte Carlo calculations.

terms of clinical beam time. Adding to this all of the complications and logistics of operating a primary measurement standard in a clinic quickly makes this route an unattractive option.

A second option is to continue using the TRS398 formalism of equation 1.4 (which relies on ^{60}Co calibrations), but derive experimental type-specific k_{Q_p,Q_0} conversion factors, rather than purely calculated conversion factors. This implies performing calorimetry in a proton beam only once for each specific type of ionization chamber, rather than for each chamber individually. It would still prove a major burden on clinical beam time initially, but once the calibration chain has been 'bootstrapped' with experimental k_{Q_p,Q_0} values, a QA system using cross-checks could be set up in such a way as to minimize the amount of beam time required for quality control of the standard itself.

A third, more viable, intermediate option is to perform calorimetry in a non-clinical proton beam instead, and correct for the small differences that result from the differences between the clinical and non-clinical beams:

$$D_{w,Q_p} = M_{Q_p} N_{D,w,Q_{p'}} k_{Q_p,Q_{p'}} \tag{1.6}$$

That is, in order to measure the dose D_{w,Q_p} in a clinical proton beam 'Q_p', one performs calorimetry to calibrate an ionization chamber in a non-clinical beam '$Q_{p'}$' to obtain $N_{D,w,Q_{p'}}$. Then subsequently a small correction $k_{Q_p,Q_{p'}}$ is needed to correct for the differences in particle spectrum (such as differences in the proton energy or the neutron dose fraction) between the clinical beam and the non-clinical beam. The non-clinical proton beam '$Q_{p'}$' could be obtained at an accelerator institute. This restores traceability to a primary standard, without the burden of large amounts of beam time in clinical facilities.

It should be pointed out that the situation of the 'intermediate option' is not necessarily different from the current practice in photon dosimetry, since the ^{60}Co beam that is available at primary standards laboratories is not used in the clinics. For the time being, dosimetry can be performed according to equation 1.6. However, there is nothing to preclude also calibrating those ionization chambers in ^{60}Co. Having established experimental values for k_{Q_p,Q_0}, proton dose-to-water in the clinic could be measured using the formalism of equation 1.4, relying once again on ^{60}Co calibrations, but without the added uncertainty of calculated k_{Q_p,Q_0} factors. While it remains to be shown experimentally for ionization chambers that the ^{60}Co dose calibrations are sufficiently correlated to their proton dose calibrations, being able to tie the proton dose dosimetry to the existing infrastructure of ^{60}Co calibrations is surely beneficial.

No matter what route is taken, in order to reach the goal of less than 1 % uncertainty for dose calibrations, absolute dosimetry standards are required that can assign dose at a far lower uncertainty.

1.5 Calorimetry dose calibration standards

Any primary source of dose calibration should provide dose values in terms of the SI unit of absorbed dose, which is the Gray: $1\,\mathrm{Gy} = 1\,\mathrm{J\,kg^{-1}}$. While there are many techniques for measuring dose, protocols like TRS398[14] and ICRU report 78[6] recommend that the primary dose calibration standard should be a calorimeter. In clinical practice, the desired quantity is the dose-to-water. While other materials such as graphite are also used in calorimeter designs[20], the use of water has the benefit of directly measuring the quantity of interest. In this section, the role of a water calorimeter in the proton dose calibration chain will be briefly discussed.

1.5.1 Water calorimetry as a primary calibration standard

As described in section 1.4.1, proton doses are at present measured by using ^{60}Co calibrations of ionization chambers according to the TRS398 formalism for the determination of dose:

$$D_{w,Q_p} = M_{Q_p} N_{D,w,Q_0} k_{Q_p,Q_0} \tag{1.7}$$

The calibration factor N_{D,w,Q_0} is determined for each individual chamber under ^{60}Co reference conditions by comparison to a water calorimeter, which is a primary standard. This does not make the proton dose measurement traceable to a primary standard in a strict sense, because of the conversion factor k_{Q_p,Q_0}.

In order to restore the calibration chain, the proton dose must be measured directly with a primary standard. A water calorimeter measures the dose rather directly by measuring the temperature increase ΔT of the water due to the irradiation:

$$D_{w,Q_p} = C \cdot \Delta T \tag{1.8}$$

In the above equation C is the specific heat capacity of the water and ΔT is the measured temperature increase due to the irradiation. Thus, the calibration factor of an ionization chamber for proton radiation dose N_{D,w,Q_p} can be measured directly with a water calorimeter:

$$N_{D,w,Q_p} = \frac{C \cdot \Delta T}{M_{Q_p}} \tag{1.9}$$

In the above equation, the dose $C \cdot \Delta T$ is measured with a water calorimeter and the ionization charge M_{Q_p} is measured with an electrometer. It should be noted that the above equation contains only terms that have a direct interpretation as measured values with SI-units. An important aspect is that the technique of water calorimetry is, at least in first order, independent of the type of radiation. In fact, equation 1.8 would apply equally well for ^{60}Co irradiations. The practical realisation of the measurement apparatus does cause perturbations that are beam type dependent, meaning that small corrections should be applied to equation 1.8

and 1.9. This causes small contributions in the uncertainty estimate. However, the gross-scale response in temperature is directly related to the dose and the heat capacity of water.

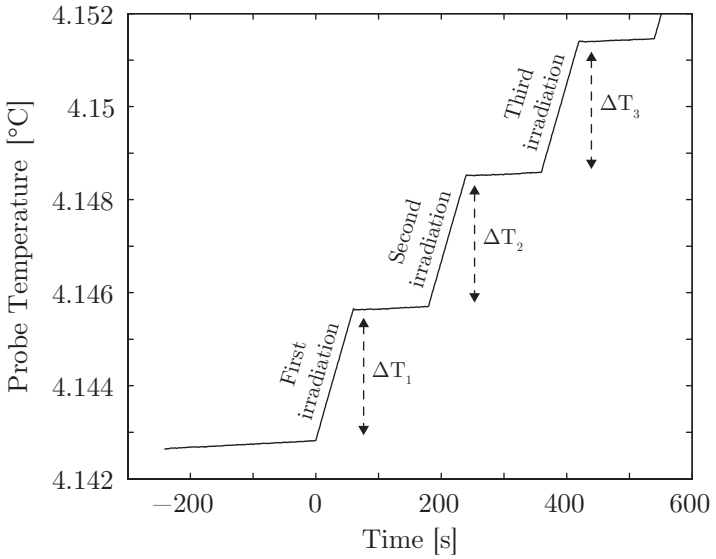

Figure 1.1 – Example of the temperature signal measured in the water calorimeter during an irradiation. Displayed is a series of multiple irradiations of about 11.6 Gy per irradiation. The temperature increase during each irradiation is 2.76 mK.

Figure 1.1 shows experimental data as measured by a water calorimeter in a proton beam. Calorimetry experiments typically consist of sequences containing about 10 irradiations. The temperature increases $\Delta T_1, \Delta T_2 \ldots \Delta T_n$ are measured with sensitive thermometers. Multiplication with the value of the heat capacity of water yields the delivered dose in each irradiation.

Compared to ionometry, the method of calorimetry is very different physically. It is very unlikely that there are strong correlations between the ionometry response and the calorimetry response other than the dose itself. Therefore, water calorimetry is a suitable source of proton-dose calibration for ionization chambers. Proper implementation of the standard for protons can retain the benefit of the simplicity of the $N_{D,w}$ formalism while further reducing the uncertainty on patient dose. By setting up water calorimetry for protons, one obtains the required QA and traceability for internationally comparable delivery of dose.

1.6 Thesis outline

Although a water calorimeter is particularly suitable for measuring the dose-to-water, the underlying assumptions to the calorimetry equation are generally not fulfilled at the desired level of confidence. In the case of photon-dose calorimetry, extensive modelling and validation experiments have resulted in very low uncertainties, while experiments with proton calorimetry were limited by the lack of available beam time in clinics.

For the work described in this thesis, a dedicated water calorimeter was operated in the 190 MeV proton beam of the AGORFIRM irradiation facility at KVI-CART. Performing calorimetry at a physics research facility has the benefit of a slightly less scarce beam time availability and a quick turn-around time for successive experiments. Although KVI-CART is not a medical facility, the beam qualities are not necessarily very different from clinical beams. With the exception of pencil beam scanning, the scattered beam of the AGORFIRM facility can be configured to resemble clinical proton beams to great extent. This thesis explores some of the issues of performing calorimetry in a scattered beam as well as extensions to scanning beams by modelling.

Chapter 2 details the water calorimeter apparatus, as well as the irradiation facility. It introduces calorimetry and shows the general procedures for performing a calorimetric experiment at KVI-CART. It also shows some of the data processing techniques.

Chapter 3 describes the effect of radiation induced chemical reactions in water on the measurement of the radiation-induced temperature increase. Appendix A shows a model for the radiochemistry effects, which is used in chapter 3 to predict the response of the calorimeter in the scattered proton beam at KVI-CART. The model extrapolates to higher dose rates to reveal issues with performing calorimetry in clinical scanning proton beams. An experiment to test the radiochemistry model in a scattered beam is described.

Chapter 4 explores the effect of neutron production in the beam line elements of the scattered beam, which is largely absent in clinical scanning beams and in addition, the neutron dose that is due to neutrons that are generated in the water volume itself is examined. Via Monte Carlo calculations, the fraction of the dose that is due to neutrons as well as the spectrum of the neutrons and the proton recoils is calculated. The calculated dose is verified experimentally by comparison with water calorimetry and ionization chamber dosimetry.

Chapter 5 explores time dependent heat transfer effects that result from the thermal conductivity of the water and the direct heating of the temperature sensors due to the proton irradiation. Models are presented for the heat transfer that results from heat conduction near dose gradients in the scattered beam as well as a model for the heating of the temperature probe. Experiments testing these models are discussed.

Chapter 6 summarizes the above chapters and it discusses appropriate ways for implementing the proton dose calibration chain, given the constraints that are apparent from the challenges identified in the preceding chapters.

Chapter 2

Experimental Methods

The outcome of a medical treatment with proton irradiation is strongly dependent on the delivered radiation dose. In order to guarantee reliable treatments in every clinical facility the administered doses should be calibrated against a common (primary) standard through measurements. As with any measurement system, the reliability of the measurements (or rather, the amount of uncertainty) depends on the details of how it is implemented and on how it is used. The following chapters in this thesis will discuss some of those details and their related measurement uncertainties. First, a general overview is in order.

In this chapter, the method of calorimetry as a way to measure absorbed dose is introduced. A short summary of the development of the primary measurement standards is given after which the equipment is described that was used in the experiments at KVI-CART, including a description of the experimental facility at KVI-CART. Also listed are some of the procedures which are used in a typical calorimetric experiment.

2.1 Absorbed dose

The clinical quantity of interest in radiotherapy is the dose-to-tissue, although clinical equipment is usually calibrated by measuring the dose-to-water. What exactly constitutes dose is subject to definition. The most commonly used definition refers to the directly imparted energy by ionizing radiation[21, 22]:

$$\epsilon = (E_{\text{in}} - E_{\text{out}})_{\text{uncharged}} + (E_{\text{in}} - E_{\text{out}})_{\text{charged}} + \sum Q \tag{2.1}$$

Here ϵ is the net energy deposited in a small volume V, calculated as the difference of the kinetic energies carried into and out of the volume V by uncharged and charged particles. This equation includes interactions of uncharged particles that result in newly liberated charged particles, such as the photo-electric effect, pair creation and Compton scattering for gammas or nuclear scattering of neutrons

on hydrogen atoms. Nuclear reactions and annihilations are accounted for by the last term, which is the sum over all of the conversions in the volume V (mass to energy conversions are considered positive). Note that this equation describes energy carried by ionizing particles only, meaning that the energy associated with radiation induced chemical reactions only contributes in ϵ for as much as the chemical species are created directly by the interaction of a single ionizing particle.

The quantity of dose is then defined as:

$$D = \frac{\mathrm{d}\epsilon}{\mathrm{d}m} = \frac{1}{\rho} \cdot \frac{\mathrm{d}\epsilon}{\mathrm{d}V} \tag{2.2}$$

This is by definition an average over a volume $\mathrm{d}V$ (with a mass $\mathrm{d}m$ and density ρ), although it is often thought of as a point value. The unit of dose is the Gray (Gy) and the SI base-unit is $\mathrm{J\,kg^{-1}}$. Any measurement device which has a fairly direct correspondence between dose and signal could act as primary standard. In practice most primary standards are based on chemical methods (Fricke dosimetry), or calorimetry (either directly in water or in graphite)[14]. The methods other than water calorimetry have in common that they depend on detailed knowledge of the interaction of the radiation and subsequent effects (e.g. chemical yields and reaction modelling for Fricke dosimetry, and knowledge of absolute stopping powers through the stopping power ratio graphite/water for graphite calorimetery).

2.1.1 The principle of calorimetry

Calorimetry relies on measuring the local increase in temperature of a medium resulting from the dose deposited by an irradiation. Once the temperature increase ΔT has been determined, the absorbed dose is calculated by multiplying this increase with the heat capacity C of the material in the medium:

$$D = C \cdot \Delta T \tag{2.3}$$

Calorimetry is particularly attractive for use as a measurement technique in a primary standard because of the simplicity* of the measurement principle. The above equation contains only factors which also have physical meaning outside the realm of radiation dosimetry. Furthermore, the heat capacity of the material and the temperature difference can be determined by making use of primary calibrations against temperature standards. The above equation does not contain *any* reference to the nature of the radiation. This means that calorimetry provides a way to make a dose calibration standard that is first-order insensitive to variations in the nature of the radiation and that also ties the measured value to the SI base units by referencing primary standards of mass and temperature. As such it is a suitable primary calibration standard for absorbed dose.

* Ofcourse, to measure anything with a low uncertainty is usually not simple, but this by itself can not be held as an argument against the practice of calorimetry.

It should be pointed out that the definition of dose in equation 2.2 does not unequivocally coincide with the definition of dose in equation 2.3 because the former refers only to ionizing radiation while the latter also includes the effects of non ionizing radiation, to the extent that it causes a temperature increase. Likewise, chemical reactions are not specifically mentioned in equation 2.2, because the chemical species involved are presumed to be non-ionizing (meaning that any energy that goes into the formation of chemical species is considered to be part of the total dose), while any measurement according to equation 2.3 would include the chemical reaction heat. Another difference is that nuclear reactions and decays are explicitly included in equation 2.2 while the calorimeter only includes decays on the time scale of the irradiation.

2.1.2 Water calorimetry

Water is used as a reference medium for clinical dose because of the similarities between water and tissue regarding radiation interaction properties[23, 24]. The quantity of interest is thus the dose-to-water D_w. Domen claims[25] that calorimetrically measured doses in materials other than water would require extensive knowledge (spectra) about the radiation and the dose that would have been deposited into water could only be calculated based on theoretical models. He also shows that the dose can be measured calorimetrically directly in water. Water calorimeters are suggested as primary dose calibrations standards in IAEA TRS398 [14] because of the close relation between the physical principle of the experimental method and the unit of dose.

The value of the specific heat capacity of water C is about $4.2\,\mathrm{kJ\,kg^{-1}\,K^{-1}}$[26, 27] which determines the sensitivity of the measurement standard. There is a temperature dependence in the heat capacity and values of higher precision can be found in the cited sources.

A standard uncertainty in the range of 0.03 % to 0.05 % is usually assigned to the heat capacity data[28, 29], although in some cases fits of tabulated data are used which increases the uncertainty to 0.08 %[30]. Departure from the idealized situation of equation 2.3 results in additional uncertainties, the largest of which are discussed in this thesis. However, the uncertainty of the heat capacity of water itself puts a limit on the magnitude of the type of effects which warrant detailed investigation. Effects that result in uncertainties much lower than 0.03 % to 0.05 % would bring about the need to tighten the error bounds on the heat capacity as well. Therefore uncertainties lower than 0.01 % are essentially negligible in the context of water calorimetry.

A water calorimetry standard involves a carefully designed thermal shield in order to be able to resolve the small temperature signal of $1/C = 0.24\,\mathrm{mK\,Gy^{-1}}$ with sufficient precision. The components of a typical calorimetry setup are shown schematically in figure 2.1. In order to reduce the effects of heat diffusion on the temperature measurement, the beam radius is chosen to be a few centimetres and the temperature is measured roughly in the centre of the irradiated volume. For

visual reference, figure 2.4 shows a drawing of the internal components in relation to the size and shape of the proton beam. The effects of heat transfer are discussed in chapter 5.

2.1.3 Graphite calorimetry

It is possible to take materials other than water for the measurement medium. One interesting material is graphite. The use of graphite calorimeters for proton beams is being explored by Palmans et al. [31, 20]. The PhD-thesis by Lauren Petrie[32] considers the heat transfer effects of both scattered and scanned proton beams as well as calorimeter-core gap corrections and volume averaging effects.

The thermal properties of graphite[20] as compared to water[33] give rise to both advantages and disadvantages. One obvious advantage is that the heat capacity of graphite is much lower than that of water. This results in about 5.8 times more signal in graphite for the same dose. From a statistics point of view this is highly desirable given that access to proton beam time is often very limited. A disadvantage is that the thermal conductivity of graphite is about 236 times larger than that of water. Its effect is somewhat reduced by the relative density of graphite of 1.8. The resulting thermal diffusivity of graphite is 774 times higher than that of water. This creates interesting challenges as significant heat conduction occurs during the irradiation, which means that the field shape and the manner in which the dose is delivered become an important factor in the performance of a graphite calorimeter. The graphite calorimeters usually consist of a graphite 'core' which is surrounded by graphite thermal shields and which is separated from those shields by air-gaps or vacuum gaps.

Graphite calorimetry is however a less direct calibration reference than water calorimetry if the desired quantity is the dose-to-water and an ionization chamber is the target of the calibration. In such cases one must consider the differences between stopping power ratios of water/air and graphite/air or fluence correction factors to convert the measured dose in graphite to a dose in water. Such corrections are usually derived from Monte Carlo calculations which slightly weakens the calibration chain.

Graphite calorimetry does have advantages over water calorimetry in terms of ease of transport and robustness. Water calorimetry requires maintaining a large volume of ultra pure water at 4 °C and needs relatively long preparation time and thermal stabilization time. Because of the high thermal diffusivity, a graphite calorimeter could be set up in a fairly small amount of time and, in addition, running a graphite calorimeter in the so-called 'isothermal mode' could greatly increase the time-efficiency of the calorimetry, which is highly beneficial in clinical scanned beams[32].

2.1.4 Perturbation corrections and uncertainty

The measurement principle of calorimetry is very powerful in that it directly senses the effect of dose in the actual medium where it is deposited. The applicability of equation 2.3 however is limited by any observed temperature increase or decrease that is not directly due to the deposited dose. In addition, the mere presence of the calorimeter in the radiation field will change the properties of the radiation field itself.

In practice correction factors k_i are applied to account for such effects:

$$D_w = C \cdot \Delta T \prod_i k_i \tag{2.4}$$

The corrections are almost always multiplicative because deviations from equation 2.3 are mostly due to systematic effects that are physically related to the applied dose. Additive effects, such as temperature fluctuations in the water volume, do exist. However, because such effects are usually not correlated in time to the repetition cycle of the irradiations the additive effects tend to show up in the measured data as random fluctuations*. Therefore, most of the additive effects are simply absorbed into the estimates of the statistical uncertainty.

Each systematic effect brings about the need for a correction factor and the uncertainties in the values of the correction factors are determined by the uncertainty in the estimates of the magnitudes of the various effects. As a result, the total uncertainty of a measurement according to equation 2.4 is determined mostly by the correction factors and measurement noise. Note that equation 2.4 is somewhat compact. Most of the k_i apply to the ratio of the actual dose D_w and the actual temperature difference ΔT, while the measurement of ΔT itself also brings about systematic effects. In addition there are positioning and volume averaging effects. The temperature increase is measured at a slightly different position compared to the location at which the nominal dose D_w is desired to be determined, which means that the precision of the positioning of the temperature sensors also introduces a systematic uncertainty, due to local dose gradients. For the purpose of an ionization chamber calibration, the average dose over the full area of the chamber is required, which requires a-priori knowledge of the spatial dose distribution.

2.1.5 Uncertainty budget

Lists of the most important uncertainties encountered in water calorimetery for ^{60}Co were published in a paper by Karger[34] and in ICRU report 78[6]. More detailed lists can be found in commissioning reports by Domen[35], Medin[36], Krauss[28] and De Prez[30]. There are slight differences in the quoted uncertainties between these sources, but the largest sources of uncertainty are:

* An exception is the modulation (due to water flow) of the sensing-current-related thermistor temperature offset, which is discussed in section 5.5.2. This effect is correlated to the measurement cycle, because of the mixing that occurs at the end of each cycle.

- Thermistor calibration: 0.07 % to 0.2 %
- Statistical uncertainty: 0.2 % (typical values averaging over multiple irradiations in a standards laboratory)
- Radiolysis (reaction enthalpy): 0.2 % to 0.5 %
- Heat Transfer: 0.1 % to 0.2 %

Radiolysis can induce chemical reactions whose heat of reaction is added to the heat caused directly by the dose deposition. This extra heat can have a positive or negative sign. The name 'heat defect' is commonly used to mean the relative amount of missing thermal heat. The chemical heat defect due to radiolysis is discussed in more detail in chapter 3. Heat transfer is an important aspect of water calorimetry, because significant diffusion of heat can occur during the time of the measurement. This effect is related to heat conduction on temperature (dose) gradients in the water or the difference in heat capacity between non-water materials and water. A more elaborate description of these effects is given in chapter 5.

The resulting combined uncertainty is usually well below 0.6 %. Most of the k_i correction factors are within about five per mille of unity. Heat transfer effects and radiolysis often dominate the systematic error budget.

Uncertainty budgets for proton irradiations are mostly similar to those of ^{60}Co irradiations, with the exception that the contributions of radiolysis and heat transfer are often much higher. Estimations of such uncertainties can be found in papers by Palmans[37], Sarfehnia[38] and Medin[39]. The uncertainty due to radiolysis is in the range of 0.3 % to 0.5 %. Uncertainties due to heat transfer differ depending on the irradiation technique and chosen location of the measurement point. Estimates range from 0.1 % in the case of an unmodulated scattered proton beam to 0.4 % in the case of Pencil Beam Scanning.

2.2 Water calorimetry equipment for protons

Equipment for water calorimetry in proton beams is not essentially different from already existing water calorimeters, which are routinely in use for photon calorimetry. Water calorimetry equipment for photons has evolved into a common design which is used by most metrology laboratories. All designs feature a thermally insulated tank of water inside of which is placed a glass vessel with ultra pure water containing two temperature sensors. The following sections give a short survey of existing water calorimeters, followed by a description of the calorimetry hardware as used in the experiments at KVI-CART.

2.2.1 Existing water calorimeters

Water calorimetry has been a calibration standard for ^{60}Co radiation for many years while calorimetry standards for proton and heavy ion beam radiation are still under development. It is interesting to briefly summarize the development of the primary standards.

Most of the history described here has been published in a paper by Ross and Klassen in considerably more detail[24]. A similar review describing the use of calorimetry and other dosimetry systems for ion beams has been published by Karger et al.[34].

An early version of a water calorimeter is described in a paper by Domen[25]. It was an open-water design with a thermistor sandwiched in-between thin plastic sheets. The system was operated at room temperature. Though the experiments showed that the temperature signal was sufficiently large, the system suffered from problems with convection and a chemical heat defect due to radiolysis induced chemical reactions within the air saturated water.

Another design, also by Domen[35, 40], has electrodes mounted in the water to compensate a cooling drift by Joule heating. The chemical heat defect however was still not under control.

Schulz et al. [41] mentioned that the main problems with the second Domen calorimeter were due to the water purity not being preserved and due to convection. In their paper they describe the use of thermistors encapsulated in a glass probe attached to the wall of a glass container, the whole of which was a single piece.

Improving on his first designs, Domen arrived at a more mature calorimeter[23], resembling the current primary standards. It contained a glass High Purity Cell (also called 'vessel') with glass thermistor probes and it could be operated at 4 °C to prevent convection. The High Purity Cell (HPC) is a glass vessel primarily intended to maintain a chemically clean environment around the probes to combat the effects of impurities on radiolysis. Because the size of the glass vessel was small the walls acted as a convection barrier such that it could also operate at room temperature. Nowadays, calorimeters use significantly larger vessels, which prohibits operation at room temperature.

Modern calorimeters are essentially the same except for the design of the High Purity Cell. In order to reduce the effects of heat transfer by irradiation of non-water components and the effects of beam disturbance by the glass, the size of the cells was increased. Some calorimeters use accurately dimensioned cells [33, 28] to simplify heat transfer calculations.

The water calorimeter that was used for the research presented in this thesis is very similar to the calorimeters that are currently used to provide primary calibrations in ^{60}Co radiation. The following sections show a description of the hardware and its usage.

2.3 Thermostat and phantom

The calorimeter used in this research was on loan from METAS* and was used previously by METAS in a pencil beam scanning experiment at PSI[42, 43, 44]. It consists of a thermostat and a water phantom. The calorimeter is of the type that is intended to be used at a water temperature of 4 °C which eliminates convection because the volume expansion coefficient is zero at that temperature[24]. Figure 2.1 shows a schematic overview of the calorimeter.

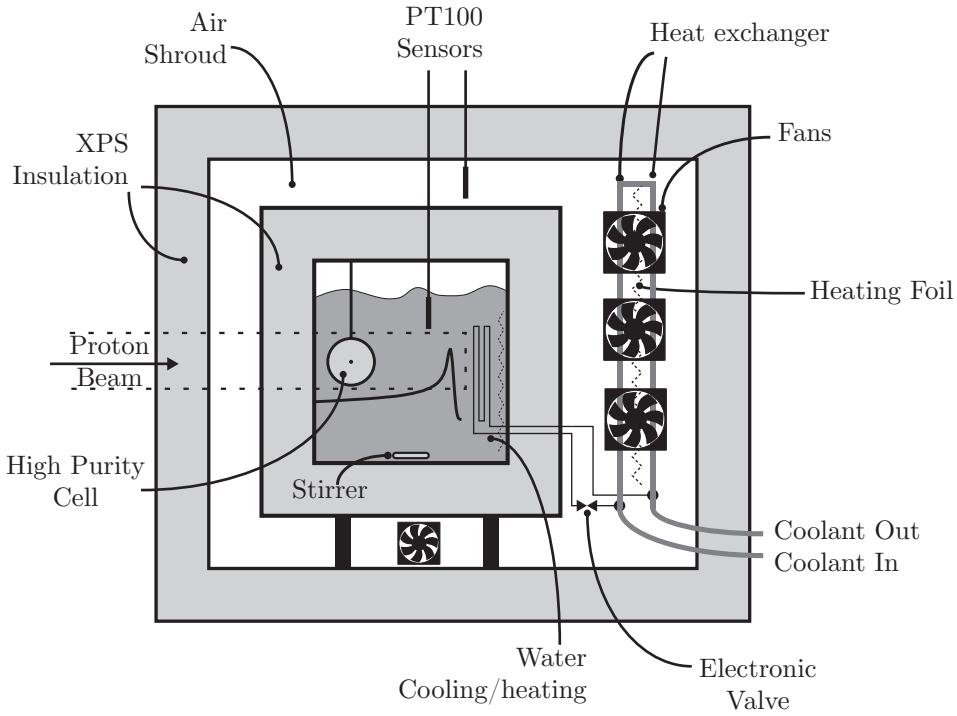

Figure 2.1 – METAS water calorimeter: thermostat and water phantom[44]. The PT100 sensors are used for coarse regulation of the temperature inside the water phantom and air shroud. The dose-related temperature increase is measured with thermistors installed in the High Purity Cell. Two different types of HPC were used (figure 2.2 and 2.3).

The thermostat consists of three layers. The outer layer is a wooden box clad with 5 cm thick expanded polystyrene (XPS) insulation (the type which is also used in roof insulation). Its purpose is to reduce the heat flux from the outside to the inside but it does not have to be perfectly insulating. Large gaps in the insulation must be avoided though to prevent excessive condensation, because the interior is cooled down to about 4 °C.

* Federal Institute of Metrology METAS, Switzerland

Inside the outer layer of insulation is an air shroud in which air is circulated. By providing a large air flow any hot spots due to imperfections in the outer layer of insulation are washed out. The temperature of the inside air is controlled by a heater/cooler combination. Coolant (water with added glycol) is continuously provided by a Neslab RTE 10 temperature controlled flow bath. The coolant is fed through a heat exchanger inside the air shroud. Mounted close to the heat exchanger is a heating foil. The heating power of the foil is set by a Lakeshore 331 Temperature Controller. It uses a PID loop fed with a 4-wire temperature signal from a calibrated PT100 thermistor mounted in the air flow. The temperature of the air is regulated to within 0.01 K of 3.95 °C, which is slightly below the phantom* temperature. The Neslab flow bath (not shown in the figure) is PID-regulated to a temperature much below the air gap temperature. Typical values are in the range of 0.5 °C to 1.8 °C. The exact value depends on the ambient air temperature and the quality of the sealing of the outer layer of insulation. Without active regulation, the inside air temperature is roughly determined by the balance between cooling power from the Neslab flowbath, heat leakage through the outer layer of insulation and the power dissipated in the fans. The active regulation only provides fine polishing to compensate small changes in ambient conditions. The power dissipated in the fans is 16 W while the maximum power that the Lakeshore controller can source into the heating foil is 41 W. Before the start of an experiment the temperature of the flow bath is adjusted such that the air temperature controller operates at about half of the maximum heater power. Typically more heat enters the air shroud by other means than by the action of the air temperature controller. The advantage of having an air shroud is that it washes out small heat leakages and that temperature regulation can be quite fast due to the low thermal capacity of the air and the low circulation time. Because of the strong mixing of the air this strongly reduces the effects of hot spots in the outer layer. There are other systems that use a 'water shroud' instead of an air shroud by directly controlling the temperature of water circulating around the inner layer of insulation[45]. Such systems require careful control of the water temperature at all positions around the inner insulation, but have the advantage that they are much more compact which is of great value when used in clinical environments.

Within the air shroud, another layer of 5 cm XPS is used to shield the inner parts of the calorimeter. The water phantom is a 30x30x30 cm PMMA tank. In the side wall facing the proton beam an 0.4 mm thick polystyrene entrance window is placed. The phantom is filled with deionized water having a resistivity of a few MΩ cm. There is no active temperature regulation during experiments. At the bottom of the phantom is a mixing bead, which can be used to stir the water. The cooling down of the water is sped up by the forced convection caused by the motion

* A 'phantom' is a piece of material that causes a certain amount of attenuation, scatter and electronic and nuclear build up of the radiation field, allowing an ionization chamber (or a calorimeter) to correctly sample the effect of the radiation at the depth of interest in the medium. For standard dosimetry, the material is almost always water. In the case of a water calorimeter, the sensitive medium is the water itself.

of the stirring bead. Before starting an experiment the mixer is turned on and the water is brought to 3.95 °C by actuating a valve which feeds some of the coolant through a heat exchanger inside the water phantom. The temperature of the water is measured with a calibrated 4-wire PT100 which is read out with a Keithley 2001 multimeter. Also installed inside the water phantom is a small heating coil which can be used should the water temperature end up being lower than desired. Before starting a series of measurements, the stirrer is activated again in order to even out temperature differences in the water. During measurements, the water is at a standstill.

Protons enter the water calorimeter from the left in figure 2.1. With a primary energy of 190 MeV, the protons stop inside the water phantom without hitting the heat exchangers in the back. The High Purity Cell (filled with high purity water) containing two thermistors is aligned with the centre of the beam. Beam diameters of nominally 70 mm and 50 mm were used. The two thermistors were positioned symmetrically relative to the centre of the beam, such that the tip of each thermistor is at a distance of 5.5 mm from the beam axis. The dose is measured at the location of the thermistor tips by sensing the radiation induced temperature rise.

2.4 High Purity Cell

The heart of the calorimeter is the High Purity Cell containing two thermistors probes. In principle, the beam should be disturbed as little as possible and the probes could be positioned directly into the bulk of the water in the phantom. However, it is difficult to control the purity of the water because it is exposed to the surrounding air. That means it is saturated with oxygen from the air and it probably also contains other contaminants resulting from handling the equipment. This causes problems with radiolysis-related heat generation during irradiations. To provide a chemically stable environment close to the temperature probes, they are fitted inside a thin-walled glass vessel[41]. This configuration allows for controlled and reproducible determination of dose. For the experiments described in this thesis two different vessels were used.

2.4.1 Cylindrical vessel

Figure 2.2 shows a design of a cylindrical High Purity Cell. Most water calorimeters use a very similar design. The vessel is made out of borosilicate glass and has a diameter of 68 mm and a wall thickness of 1 mm. Two threaded ports allow the insertion of the thermistor probes. The port holes are sealed with a Teflon coated rubber washer. Threaded nuts provide compression of the washer and allow positioning of the thermistors by adjusting screws which clamp the tube of the probe. Additionally, the cell contains two ports which are used to fill the vessel with water. They also act as gas inlets and outlets for removal of oxygen from the

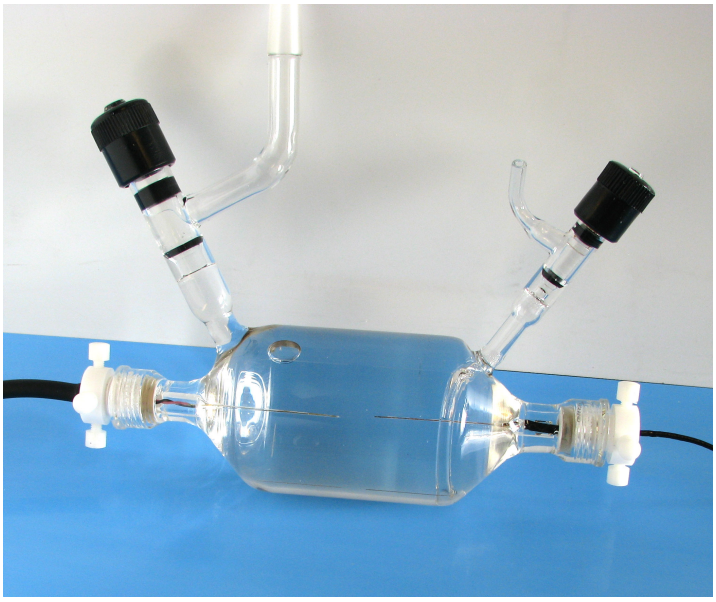

Figure 2.2 – A cylindrical High Purity Cell containing two thermistor probes. Its main function is to keep contaminants away from the point of measurement. The vessel is made out of borosilicate glass and filled with purified water. Each temperature probe contains a small NTC thermistor at the very tip (figure 2.6). Before use, the entire assembly must be cleaned thoroughly and the water must be deaerated.

water. Glass valves with Viton O-rings seal the vessel from the outside. Once the vessel has been cleaned and the valves have been closed the vessel remains sealed. It is essentially air-tight even against a small pressure difference. A small bubble of gas is visible inside the cell. Before an experiment the vessel is tilted to trap the bubble inside the filling port in order to move it away from the irradiation field. A cell like this provides a small cocoon of ultra-pure water surrounding the thermistor probes.

2.4.2 Flat-windowed vessel

In addition to the cell described in the previous section a new type of cell was designed. The cell shown in figure 2.3 is similar to the cells used by PTB[33, 28] in that it has flat beam entrance and exit windows. It still is a cylindrical vessel, however the cylinder is rotated 90 degrees relative to the beam direction such that the two flat glass windows face the beam perpendicularly. With the typical beam geometries used at KVI-CART, the beam only hits the front and back windows and not the cylindrical glass parts of the glass vessel. In comparison with the PTB cell the cylinder is three times longer in order to reduce the effects of glass heating on the measured temperature differences. Another difference is that it

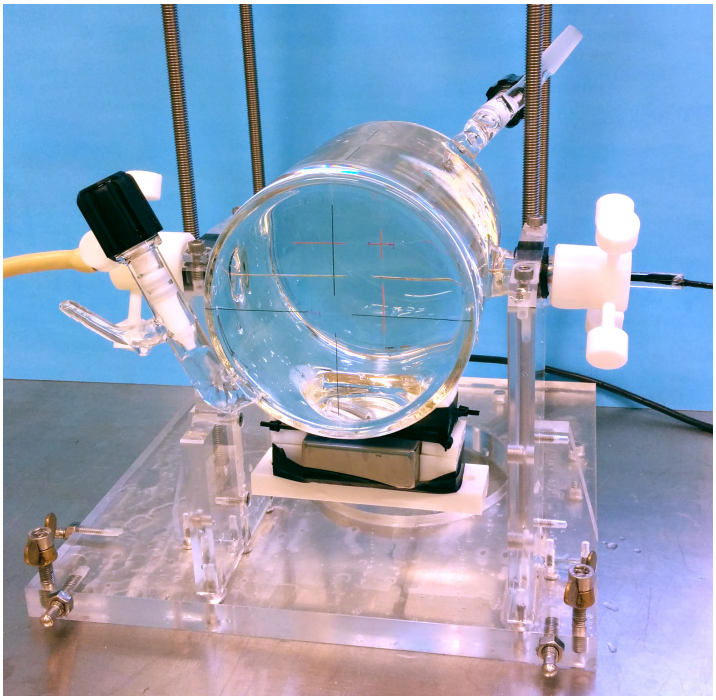

Figure 2.3 – A new type of elongated flat-windowed cell, featuring a stirring mechanism. Like the cylindrical vessel (figure 2.2) its main function is to keep contaminants away from the point of measurement. Due to its size and shape (section 5.3), it does not cause any significant thermal perturbations. The included mixer is used to remove temperature gradients in the water, which allows for beam-time efficient experiments.

has a built-in stirring mechanism, which can be used to homogenize the water temperature distribution on the inside of the glassware. This type of cell was used in experiments validating heat transfer modelling, where irradiation of glass components is important. More details are provided in chapter 5.

For visual reference, figure 2.4 shows a computer-rendered image of the vessel and the field collimator as they are positioned in the beam line. The aperture of the collimator is a circular hole with a diameter of 70 mm and the diameter of the glass vessel is 100 mm. Also shown are the two thermistor probes at the centre of the vessel, which sample the temperature at a distance of about 5.5 mm from the central beam axis.

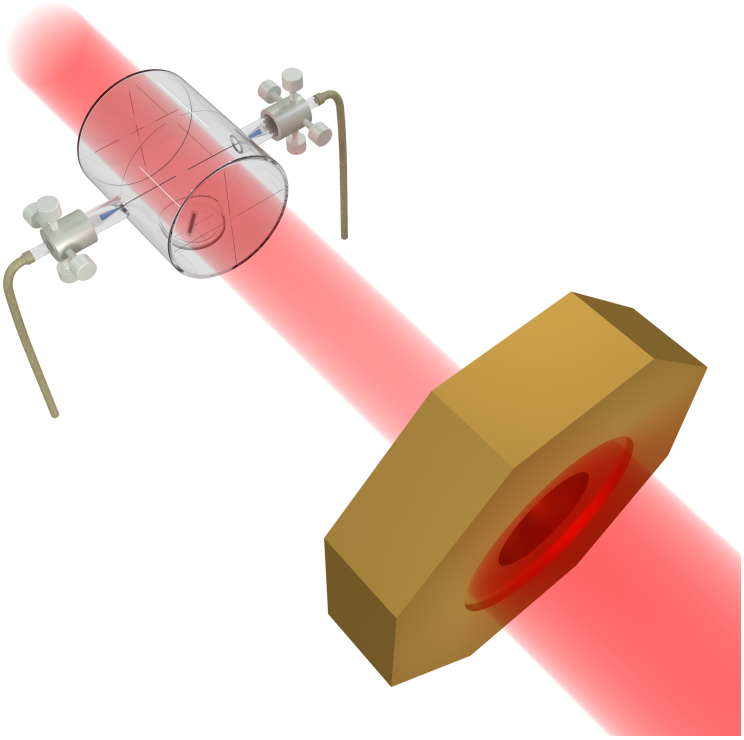

Figure 2.4 – Computer rendering looking down at the field collimator, proton beam and glass vessel (figure 2.3) with thermistor probes installed. The diameter of the beam is well within the diameter of the vessel and the thermistors sense the temperature near the centre of the field. A magnetic stirring bar coated with borosilicate glass is placed inside the vessel.

2.5 Glass preparation and cleaning

The apparent temperature increase resulting from the application of dose can be influenced significantly by the presence of impurities which participate in reactions with radiolysis products. Domen found a difference of 3.5 % between calorimetry using air saturated water and graphite calorimetry. Ross et al. describe[46] a persistent exothermal response below an accumulated dose of 100 Gy and an endothermal response above 100 Gy for N_2 saturated water. They attribute this to the presence of organic impurities. Because the chemical heat defect depends on the presence of impurities, the glass parts of the calorimeter must be cleaned thoroughly each time before an experiment. The standards laboratories use protocols for the cleaning procedure to ensure that the cleaning is reliable and the results are reproducible. While the protocols differ in the types of cleaning agents and the handling methods of the glassware, there are some similarities. The principle is

always the same in that contamination is first removed from the surface after which it is purged by rinsing the glassware many times with ultra pure water, effectively diluting the contaminant by orders of magnitude with each rinsing. Most protocols use an aggressive acid, sometimes combined with a strong reducing agent to etch the surface of the glassware. A second step which is sometimes performed is to use organic solvents or alkali detergents to remove any remaining organic residues from the glass. Gaskets and other non-glass materials are cleaned with alkali detergents. Throughout the procedures the glassware is rinsed frequently with ultra pure water.

2.5.1 Summary of the cleaning procedure

For the experiments at KVI-CART a cleaning procedure is used which was developed by METAS for ^{60}Co calorimetry[47]. The procedure relies on cleaning the glassware with chromo-sulfuric acid. All tools need to be cleaned as well and the gloves are washed thoroughly with ultra pure water before handling glassware. Touching already cleaned glassware, even with gloves, should be avoided as much as possible. The procedure is somewhat involved and takes about one day. A brief summary of the procedure is listed below. It should be noted that the METAS procedure was not followed exactly, because there are differences in the equipment which require slightly different handling techniques.

- Soak the glass vessel in a chromo-sulfuric acid solution ($H_2SO_4 > 92\%$ + $CrO_3 > 1.3\%$) for at least four hours.
- Soak non glass components in a 5 % Hellmanex-III* solution.
- Soak any other glass parts in chromo-sulfuric acid solution for at least ten seconds and then rinse with ultra pure water† (18.2 MΩ cm, TOC $\leq$ 4 PPB). Repeat five times.
- Rinse the outside and inside of the vessel with ultra pure water for a few minutes.
- Rinse the vessel three times with ultra pure water, filling and emptying the vessel completely each time.
- Rinse the non glass components for a few minutes.
- Install the thermistor probes into the vessel and align them.
- Rinse the inside of the vessel, with the probes installed. Repeat six times.

* An alkali cleaning agent produced by Hellma GmbH & Co. KG, Germany.

† The ultra pure water is produced from deionized water by a Milli-Q Advantage A10, manufactured by Merck Millipore, Merck KGaA, Germany. TOC is the amount of Total Oxidizable Carbon expressed in Parts Per Billion (µg L^{-1}) and it is measured by the Milli-Q Advantage A10. Its value varies and typically reads 2 PPB to 5 PPB .

- Fill the vessel with ultra pure water one last time and seal the vessel by closing the valves.

According to the procedure, the cleaning with chromo-sulfuric acid is optional if the vessel has been sealed and stored at 4 °C continuously. In that case the inside of the vessel is rinsed thoroughly, but the vessel is not disassembled. In many cases this was not an option. The choice for adopting the METAS procedure, using rather aggressive cleaning agents, was motivated by the need for a tried and tested cleaning method. Although less aggressive cleaning methods are used nowadays[48], the aggressive methods provide a degree of robustness which is desirable because in a physics laboratory the environment is generally less well conditioned compared to a national standards laboratory. Moreover, since experiments are confined to limited amounts of strictly scheduled beam time, a failure due to inappropriate cleaning is a rather costly waste of time and money.

2.5.2 Gas saturation and saturation mixtures

As a final step in preparing the High Purity Cell, all oxygen must be removed from the water, since the dissolved oxygen in air-saturated water leads to a chemical heat defect of a few percent[33, 49]. For the experiments at KVI-CART a procedure similar to the one currently in use at METAS[50] was set up. Figure 2.5 shows gas bubbling through the high purity cell. Depending on the type of experiment either pure argon, pure hydrogen or a mixture of hydrogen and oxygen was used. Standards laboratories commonly use either nitrogen or argon because they are inert gases. In such cases the only role of the bubbling gas is to purge the water from oxygen and gaseous organic contaminants. However, to stabilize the heat defect, especially in high dose rate beams the water can also be saturated with hydrogen[51]. The flow rate was set to 200 mL min^{-1} using Vögtlin red-y compact mass flow meters which have a specified accuracy of of better than 2 %.

After performing the bubbling procedure the valves are closed. A small bubble of gas has to remain inside the cell, to prevent glass fracture due to the change in volume of the water as it is cooled down.

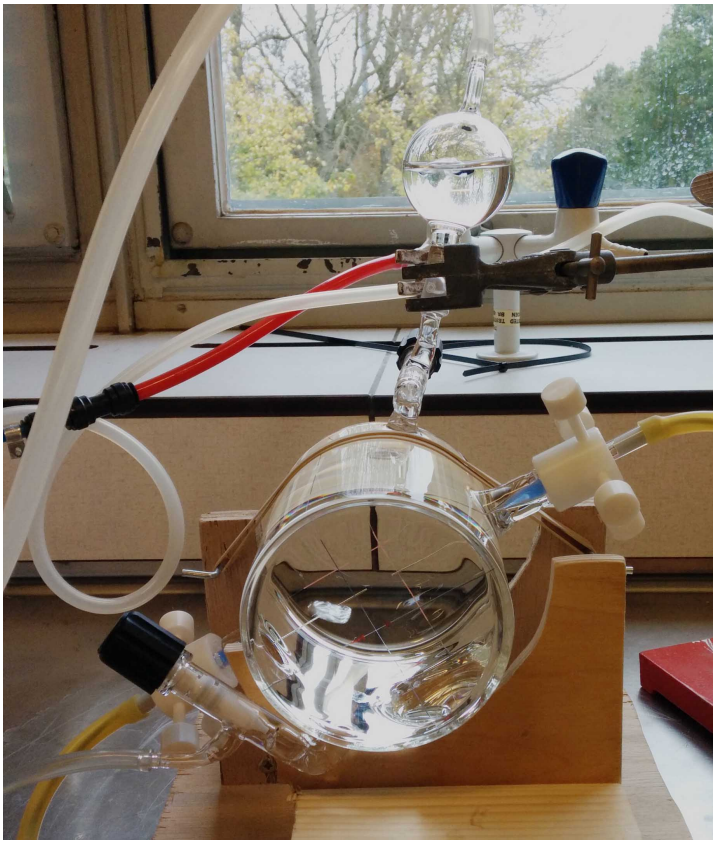

Figure 2.5 – Gas is bubbling through a high purity cell in order to deaerate the water. A bubble originating from the input valve on the lower left is seen just in front of the left thermistor. The gas exits through an expansion tube mounted on top of the high purity cell.

2.6 Temperature probes

The sensing elements of the water calorimeter are temperature probes containing NTC-thermistors. As shown in figure 2.4 they are positioned near the centre of the dose field. The requirement of water purity demands the thermistors to be encapsulated in borosilicate glass. However, because the heat capacity of glass is about five times lower than that of water, during irradiation, it shows a very strong heating effect relative to the water which perturbs the measurements of the water temperature (see section 5.4.2 for more details). This differential heating also exists for the NTC-thermistor bead itself, but this can not be avoided. In order to reduce the magnitude of the effect the irradiated amount of glass should be minimized. Therefore the optimal geometry is that of a narrow glass tube with the thermistor located at the very tip. These probes are typically manufactured by

elongating borosilicate pipettes[23]. However, this requires careful manual handling of the glass and the resulting pipette shape (which is important due to its related heat transfer effects) is not very well controlled.

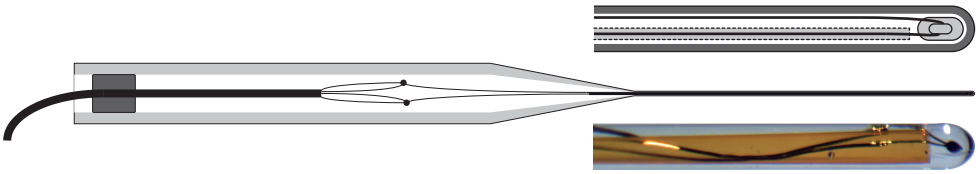

Figure 2.6 – Drawing of a thermistor probe manufactured by Metroglas based on a design by METAS. Located at the tip of the probe is the NTC thermistor (visible as a black dot in the lower in-set). The outer envelope is made entirely out of borosilicate glass. The probe illustration is approximately true size.

Another option is to weld thin glass tubes onto a larger tube. An illustration of such a probe and a macro photo of the probe-tip is shown in figure 2.6. The thin tube then becomes the probe tip and can be made with high precision since it does not have to be drawn from an existing pipette. The wall thickness of the tube is very well controlled. The diameter of the tip is 0.6 mm and the wall thickness is 100 µm. Located at the tip is a General Electric BR11KAS432J thermistor bead. The bead has platinum-iridium wires. A plastic microtube is put over one of the wires to provide electric insulation. Additionally, to provide electric insulation and stabilisation, the tip is filled with a UV-curable epoxy. The larger tube contains the soldering joints of the platinum-iridium wires with the attached cable. At this point a transition is made to a four-wire cable. For the experiments described in this thesis both types of probes were used.

2.6.1 Probe calibration

Because the measured temperature differences are directly translated into dose the probes need to be calibrated in the operating region of the calorimeter against temperature standards. The thermistor beads inside the probes have a nominal resistance of 9 kΩ at a temperature of 4 °C. The sensitivity is about $4\,\%\,\mathrm{K}^{-1}$, which translates into $86\,\mathrm{m\Omega\,Gy}^{-1}$. The probes have been calibrated at VSL* to the ITS-90 scale† by measuring the resistance against a temperature standard in an alcohol flow bath[30]. The resistance of the probes is measured in the interval of 2 °C to 6 °C at steps of 0.2 °C.

* Dutch Metrology Institute VSL

† The International Temperature Scale of 1990[52] is a set of calibration points which can be used to calibrate absolute thermodynamic temperatures over wide temperature range.

The thermistors are of the Negative Temperature Coefficient type. Their resistance varies exponentially with temperature[53]. In the context of water calorimetry the following fitting equation[23] is often used:

$$R(T) = R_0 \cdot \exp\left(\beta\left(\frac{1}{T} - \frac{1}{T_0}\right)\right) \tag{2.5}$$

The temperatures are absolute temperatures. The temperature T_0 is some convenient reference temperature (4 °C for water calorimetry) and R_0 is the resistance at that temperature. The sensitivity is related to the β constant:

$$S(T) \equiv \frac{dR/dT}{R(T)} = \frac{-\beta}{T^2} \tag{2.6}$$

For the purpose of calorimetry the inverse of equation 2.5 is often used:

$$T(R) = \frac{1}{\frac{\ln(R/R_0)}{\beta} + \frac{1}{T_0}} \tag{2.7}$$

This does however require accurate determination of the β and R_0 constants and assumes that equation 2.5 is valid. To account for deviation from this relation additional terms can be included[53]. In that case $\beta = \beta(T)$. Following the procedures used for calorimetry at VSL, the probes were characterized by fitting a second order polynomial in $\ln(R)$:

$$1/T = a + b \cdot \ln(R) + c \cdot (\ln(R))^2 \tag{2.8}$$

In the above equation the constants R_0 and T_0 from equation 2.7 are wrapped in the offset a. In many cases, the inclusion of an additional c term in the fit was found to be unnecessary and the standards laboratory supplied calibrations without a c term.

The uncertainty in the measured temperature differences is essentially the uncertainty of the β constant. In case of frequent calibrations the uncertainty of the β constant is assumed to be 0.1 %[30]. For the experiments in this thesis only relative effects within the time frame of one experiment are examined, which means that small drifts of β are not important.

2.7 Resistance measurement

As described in section 2.6.1 the temperature is derived from thermistor resistance measurements. For the experiments described in this thesis two different systems have been used simultaneously. The first technique uses an AC-wheatstone bridge while the second technique relies on a calibrated multimeter to perform a four-wire resistance measurement. Noise generated in the thermistor causes statistical fluctuations in the measured dose of about 2.1 % for a 1 Gy irradiation in the

case of the AC measurement system, while the 4-wire multimeter system shows a slightly higher noise level of 2.4 % for a 1 Gy irradiation. These noise levels are roughly comparable to the measurement noise in the standards laboratories if one considers that usually the results of two probes are averaged. Higher doses yield a proportionally lower relative statistical uncertainty.

2.7.1 AC Lock-in detection

In water calorimetry an AC-Wheatstone bridge is often used because the sensitivity of the probe is only $86\,\mathrm{m\Omega\,Gy^{-1}}$. Any direct measurement requires sensitivities on the order of 1 mΩ or less which means a relative resolution of 10^{-7}. The Wheatstone bridge configuration is typically used in such cases.

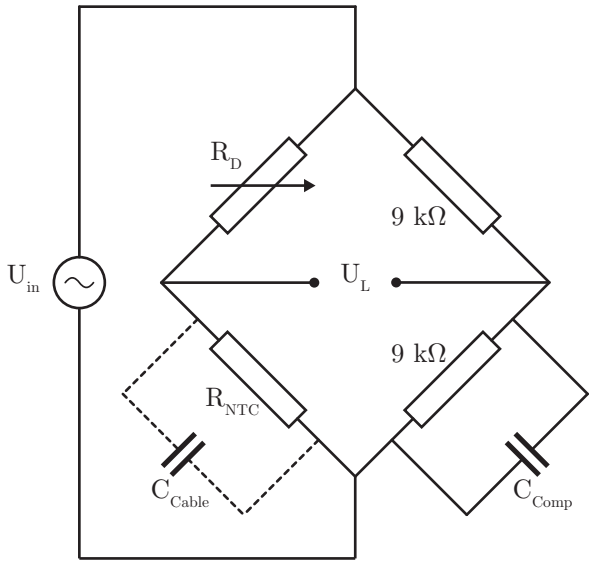

Figure 2.7 – Wheatstone bridge configuration of the AC measurement chain. A resistor decade R_D is used to balance the bridge by matching the resistance of the thermistor R_{NTC}. The parasitic capacitance C_{Cable} associated with the thermistor and its connecting cables is compensated by setting a capacitance decade C_{Comp} in the opposing arm of the bridge.

Figure 2.7 shows the Wheatstone bridge used in the AC measurement chain. The drive voltage U_{IN} is 1 V at a frequency of 21 Hz and it is supplied by a Signal Recovery 7265 lock-in amplifier. One arm of the bridge contains two Vishay VHP102 high precision resistors of 9 kΩ, which matches the resistance of the probes under operating conditions. The other arm contains a Burster 1422-IEC high precision resistance decade, R_D, and the NTC thermistor probe, R_{NTC}. The thermistor probe is connected through two times 7 m of RG 71 B/U coaxial cable, which has a capacitance of $41\,\mathrm{pF\,m^{-1}}$. In the AC configuration each pair of the four-wire connector is shorted to a single conductor. The output voltage U_L of the bridge is

measured by the lock-in amplifier at an input impedance of 1 MΩ. The nominal sensitivity of this configuration is $28\,\mu V\,\Omega^{-1}$ and the overall sensitivity of the measurement chain is $2.4\,\mu V\,Gy^{-1}$. The resistance decade is used to balance the bridge before a measurement series and is also used to calibrate the sensitivity of the bridge by measuring the output voltage as a function of the decade resistance.

The Wheatstone bridge also includes a capacitance C_{Cable} parallel with the NTC thermistor. The origin of this stray capacitance is largely the combined capacitance of the coaxial cable and the wires in the probe itself. This capacitance will slightly tilt the bridge, adding a constant out-of-phase signal. In principle this is of no concern because the sensitivity of the bridge does not change. However, the added out-of-phase signal increases the overal signal level at the input of the lock-in amplifier and limits the dynamic reserve which reduces the maximum clip-free-gain of the lock-in input amplifier. This causes a decrease in digitization resolution. The issue is solved by adding a compensating variable capacitance C_{Comp} in the range of 400 pF to 700 pF in the opposite arm of the bridge. Before each experiment, the capacitance is tuned manually, eliminating the out-of-phase signal such that optimum measurement resolution is obtained.

2.7.2 DC multimeter

The DC-measurement chain uses a calibrated Agilent 3458A-opt2 multimeter, set to measure in the 10 kΩ scale. It provides a little over 9 digits of output over the GPIB bus. This translates into 4 digits per Gy with about 2 noise-free digits. The multimeter uses the four-wire technique with separate sensing lines to counter the effects of cable resistance.

2.8 Read out

The temperature signal of the probes is read out by the lock-in amplifier and by the multimeter. No implicit conversion is performed on the measurement values. The values returned from the lock-in amplfier are in units of µV and the values returned by the multimeter are read directly in Ohms.

2.8.1 Conversion to temperature

Before further processing, the measured values are converted to temperature. It should be noted that this yields the temperature of the probes, not the temperature of the water. There is an offset because of the heating effects of the sensing current on the NTC resistor. In the case of the probe which is attached to the Agilent multimeter, the measured value in Ohms is plugged into equation 2.8 resulting in a temperature in the unit of Kelvin. In the case of the probe which is attached to the lock-in amplifier, the measured value is the in-phase bridge voltage in µV (the out-of-phase bridge voltage carries no useful information). To deduce the resistance

value from the Wheatstone bridge voltage, the bridge sensitivity S_B in units of $\mu V\,\Omega^{-1}$ first has to be determined before each experiment. To do this the change in measured output voltage per unit change of resistance is measured by applying small changes in the resistance of the resistor decade. An algorithm similar to the one that is described in section 2.8.2 is used to subtract background drifts from the bridge voltage signal. Using the bridge voltage U_L, the bridge sensitivity S_B and the value of the resistor decade R_D the resistance of the temperature probe is calculated as:

$$R_{NTC} = R_D + \frac{U_L}{S_B} \tag{2.9}$$

The value resulting from the above equation is plugged into equation 2.8 to yield the temperature of the probe.

2.8.2 Linear fitting procedure

Because of the ever present background temperature drifts and because of the noise in the temperature signal a linear fitting procedure is used to cancel the effects of such slow temperature variations while at the same time reducing the effects of noise.

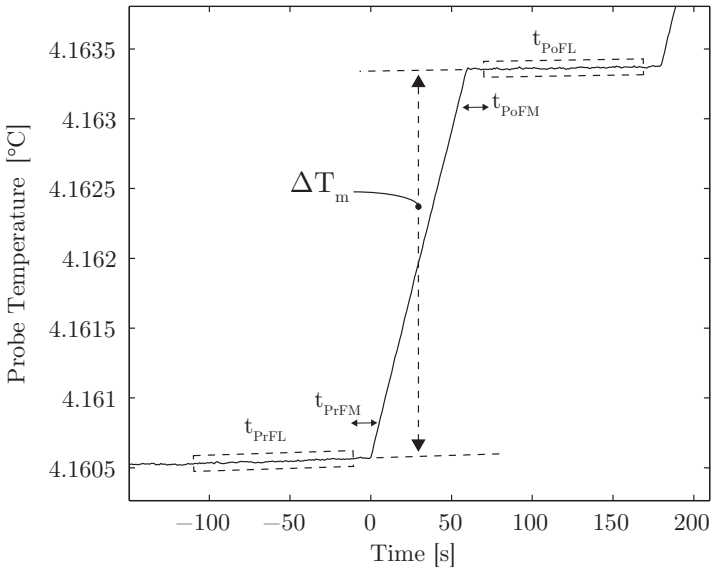

Figure 2.8 – Linear fitting procedure used to derive the beam induced temperature increase. The shown data is from an actual measurement and was measured by the DC multimeter during a proton irradiation. The temperature drift on both sides of the irradiation is extrapolated to the mid-point of the irradiation in order to separate the temperature increase ΔT_m from the background signal. The deposited dose is about 11.7 Gy.

ΔT_m	Temperature difference at mid-point
t_{PrFL}	Pre-irradiation Fit Length
t_{PrFM}	Pre-irradiation Fit Margin
t_{PoFL}	Post-irradiation Fit Length
t_{PoFM}	Post-irradiation Fit Margin

Table 2.1 – Linear fitting interval constraints.

The procedure is depicted in figure 2.8, showing actual measurement data recorded during one of the experiments. At time $t = 0$ the beam is turned on causing a temperature increase. Two linear fits are performed: one fit uses data taken before the irradiation in a time interval with a length t_{PrFL} while another fit uses data taken after the irradiation during the time interval t_{PoFL}. Both linear fits are then extrapolated to the point in time which lies halfway between the start and the end of the irradiation. The beam-induced temperature increase ΔT_m is calculated as the vertical distance between the two line fits at that point in time. The advantage of this method is that it is, in first order, insensitive to back ground temperature drifts. It is however in second order sensitive to differences in the slope between the time regions of t_{PrFL} and t_{PoFL} due to the extrapolation and it is also sensitive to any apparent temperature offset that occurs between these time intervals.

The time indices used to delineate the fitting intervals are derived from the time stamps of the irradiation control system. To avoid problems with timing accuracies and to avoid a large contribution from probe excess heat a set of margins is used around the time period of the irradiation. In figure 2.8, t_{PrFM} shows the margin used before the irradiation and t_{PoFM} shows the margin used after the irradiation. The choice of the values of each of the four fitting interval constraints (t_{PrFL},t_{PrFM},t_{PoFL} and t_{PoFM}) determines the sensitivity of the temperature measurement to beam-induced heat transfer. For the experiments in this thesis, the two fitting intervals both have a length of 100 s while both fit margins have a length of 10 s. With an irradiation time length of 60 s and a time between the irradiations of 120 s, the fitting interval constraints provide a symmetric arrangement for each irradiation. In this case, experimental estimates of the statistical standard uncertainty need to account for correlations between two subsequent irradiations, because the temperature data for any post-irradiation fit is exactly the same as the data for the pre-irradiation fit of the following irradiation (see section 2.13 for further details). Thermal transients are present in the first few seconds after the beam is turned off because of the differential temperature increase of the probe relative to the water. This is due to the large difference in heat capacity between the two materials. The length of the post-iradiation fit margin t_{PoFM} has an effect on the magnitude of measurement error due to these transients. As a whole, the fitting procedure is also sensitive to

background temperature drifts caused by heat transfer in the water volume due to thermal gradients that are in turn caused by dose gradients. These issues are addressed in more detail in chapter 5.

2.8.3 Conversion to dose units

Conversion of the measured temperature difference requires multiplication by the heat capacity of water:

$$D = C_p \Delta T_m \tag{2.10}$$

The value of the heat capacity at 4.0 °C is 4207.5(34) $\mathrm{J\,kg^{-1}\,K^{-1}}$[30]. It should be pointed out that any absolute dose measurement is only as good as the absolute determination of the heat capacity against a common temperature scale. The thermodynamic properties of water are published by the IAPWS[27] as thermodynamic equations fitted to experimental data. Current practice at VSL is to interpolate tables of the heat capacity as a function of temperature[30] leading to a overall uncertainty of 0.08 %. Another option is to use experimental data published in 1939[26]. They quote a value of 4204.8 $\mathrm{J\,kg^{-1}\,K^{-1}}$ which differs from the value mentioned above by only 0.06 %. In this thesis, the value of the heat capacity is derived from the interpolation tables used by VSL.

2.9 Calorimetry experiments

The water calorimetry experiments described in this thesis have been performed at the AGORFIRM irradiation facility at KVI-CART. A functional overview of the measurement system is shown in figure 2.9. The red arrows in the figure indicate the path of the protons through the setup.

Most of the time the experiments use an existing infrastructure, AGORFIRM[54], which is also used for radiation hardness testing and radio-biology experiments. Typically a user requests a certain beam (particle type, energy and beam current) which is then developed by the AGOR cyclotron operator. The beam is directed towards a dedicated irradiation room where the user can place hardware targeted by the beam. Finally, the user is given control over the beam. The beam can be turned on and off at will or it can be automatically controlled by an irradiation control system.

The irradiation control system is not directly connected to the computer that is controlling the calorimeter. This results in two separate log files. By synchronising the clocks of the control computers via the Network Time Protocol (NTP) to a common source, the two logfiles can later be combined into one data structure.

Details about each of the components of the measurement system are described in the following sections.

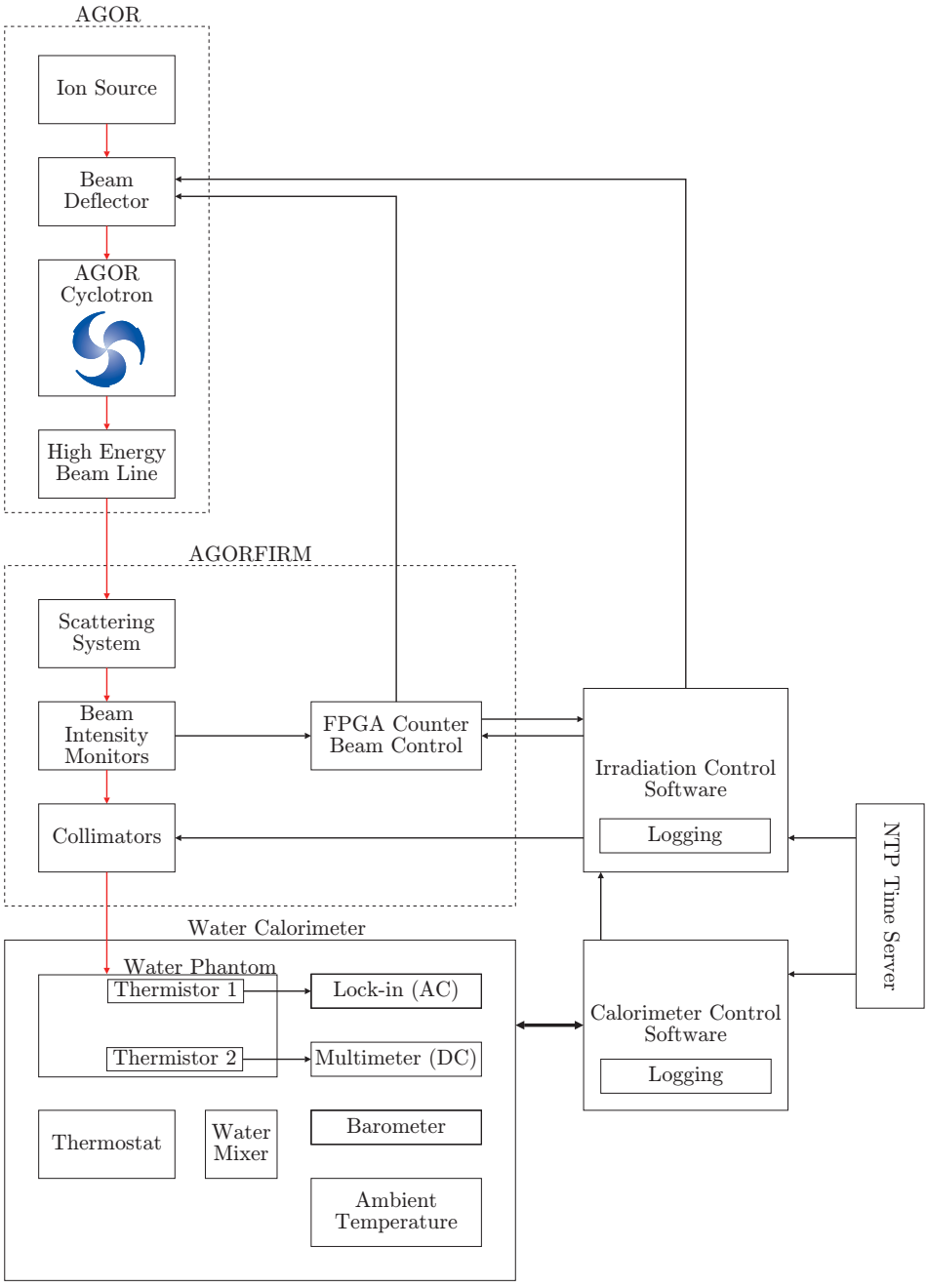

Figure 2.9 – An overview of the measurement system showing the accelerator, irradiation facility and the water calorimeter as separate units. The red arrows indicate the path of the protons through the system.

2.10 Beam line

The calorimetry experiments are done using the AGORFIRM facility [54, 55]. A simplified schematic of the beam line is shown in figure 2.10.

Beam intensity is controlled by the cyclotron operator who changes settings of the ion source to yield a certain beam current at the end of the high energy beam line. In practice, the beam current is regulated to a little more than the requested beam current after which it is further reduced by moving slits into the beam line between the ion source and the cyclotron. These instruments are not part of a feed-back loop and the beam intensity can fluctuate in the range of 3 % to 6 % during a time span of a few seconds. Variations as much as 10 % peak-peak are not uncommon over a time span of a few minutes. Slow intensity drifts on the time scale of many hours are also present, caused by drifts in the magnetic field inside the cyclotron. If the beam is controlled to deliver a constant dose, any such variations change the duration of an irradiation which has an effect on the relative timing of the linear fitting procedure described in section 2.8.2. It also prevents direct application of pre-calculated time dependent heat transfer correction factors since the time structure changes with each irradiation.

The beam deflector switches the beam off by applying a transverse electric field. The action of the deflector is controlled by an Field Programmable Gate Array (FPGA) receiving signals from the Beam Intensity Monitors.

After passing the deflectors the beam is injected into the AGOR cyclotron. AGOR is capable of accelerating many types of ion beams, including heavy ions. Proton beams can be accelerated to energies up to 190 MeV with extracted beam intensities routinely reaching a few hundred nA[55]. Beam currents can be adjusted over many orders of magnitudes, ranging from as low as a few protons per second to a little below 1 µA.

The beam is guided to the irradiation vault and is initially positioned by examining the signal of a wire grid, inserted into the beam line between the two scatter foils but with these foils removed. Alignment of the beam is done with a second wire grid up-stream. Using the steering and focussing magnets, the beam is centred on the position of the scatter foils while the focal point is usually placed somewhere on the centre line between the two scatter foils, creating a beam spot of minimum width ('waist'). A typical size for this beamspot is 4 mm FWHM[56]. Finally, scatter foils are placed in the beam line and the alignment is tuned by examining scintillation images of the field shape (see section 2.10.1).

The scattering system transforms a narrow pencil beam of protons into a much broader distribution. This is shown schematically in figure 2.10. The scattering system of the AGORFIRM facility has previously been described in the PhD-thesis of Peter van Luijk[57]. It consists of both a homogeneous (flat) scatter foil and an inhomogeneously shaped foil.

Configurations with only a single uniform scatter foil generate approximately Gaussian proton fluence distributions. This configuration may be used if the desired field radius is much smaller than the 1σ width of the scattered proton beam. The

collimator selects only a small central part of the spatial distribution of the protons. The radiation field that is due to the portion of the beam that is passed through will be reasonably uniform ('flat'). Such a single-scatterer configuration is rather inefficient since only a very small portion of the incoming proton current ends up in the irradiation field. Large fields require a thicker scattering foil to maintain the same uniform flatness of field, which results in a large amount of neutron and gamma contamination. In a circular field, the useful fraction of the protons (those that are not stopped in a collimator) is approximately equal to the fractional decrease of the proton fluence at the edge of the field compared to the fluence at the centre. This means that a one percent variation of proton fluence comes at the expense of an efficiency of only one percent.

To increase this efficiency a double scatter configuration is used. Downstream of the first uniform scatter foil a second scatterer is placed which has a non uniform thickness as a function of distance to the beam axis. The raised-cosine shape[58] will scatter protons in the centre of the field more than protons near the edges. Effectively the protons in the centre of the field are redistributed. Instead of a nearly Gaussian spatial distribution, the result is an approximately flat top-hat dose distribution, with Gaussian tails. This increases the beam efficiency resulting in a beam with fewer neutrons. For the experiments described in this work, using a 1.16 mm lead primary scatterer and a 1.03 mm tungsten second scatterer results in about 6% of the 190 MeV protons impinging on the first scatter foil to end up in a collimated field of 70 mm diameter. The field is flat within about 0.5 % out to a radius of 30 mm, however there are also local variations on the order of 3 % due to collimator scatter and imperfections in the scatter foil. Collimator diameters smaller than about 50 mm should be avoided because the heat-loss due to thermal conduction becomes very noticeable. In practice, the field flatness is never good enough to allow for assumption-free calorimetry. This means that the field shape at the position of the temperature sensors must be fully mapped by measurements in order to facilitate calculations for heat transfer corrections (chapter 5). The transverse field shape is measured with a scintillation screen and the depth-dose curve is measured with an ionization chamber. At a depth of 65 mm in the calorimeter phantom the required primary beam current per unit dose rate is about 2.1 nA Gy^{-1} min.

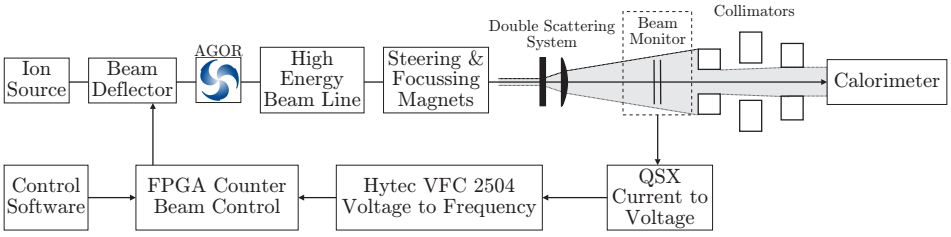

Figure 2.10 – Schematic drawing of the AGORFIRM beam line, showing the scattering system and the locations of the beam monitor, collimators and the calorimeter.

The scattered beam then passes through a Beam Intensity Monitor (BIM) which is a set of two ionisation chambers, mounted back-to-back, sharing a common cathode. A beam monitor is needed to provide a measure of the proton fluence, because the beam intensity fluctuates. The electrodes are thin aluminized mylar foils. Each foil is aluminium-coated on both sides to prevent local charging effects. Positive high voltage is applied to the outer foils while the signal is collected on the inner electrode which is near ground potential (the ionization current flowing into the amplifier input impedance causes a negligible voltage to appear on the input terminal). The plate separation is 5 mm with a polarisation voltage of 2.00 kV. The resulting electric field of 400 V/mm is more than a factor of two higher than the electric field typically used in most clinical parallel plate ionization chambers. Because of this the beam monitors behave linearly over a wide dose-rate range. Van Luijk[57] analysed the recombination in this arrangement at a fairly high dose rate of 70 Gy/minute at the target position and found that even at a plate voltage of 800 V the chamber is driven well into saturation. While there may still be recombination on the 0.1% level or so it is clear that the BIM can be used as measure of dose output. The BIM chambers do not have a guard ring* however and since they are placed upstream before the collimators, the relation between monitor units and dose is not perfectly reproducible between experiments due to variations in beam alignment.

The positive charge collected from the BIM is then routed via a 50 Ω coaxial cable to a QSX current-to-voltage converter (Triumf, Canada). These QSX amplifiers are truly differential current to voltage converters. As long as the instantaneous ionization current is within the measurement range the response is linear and the time integral of the output is proportional to the charge, regardless of the time structure of the beam. The output voltage of the QSX amplifier is fed into a Hytec VFC 2504 synchronous voltage-to-frequency converter. The number of output pulses is proportional to the time integral of the input voltage. When used with the QSX converters each output pulse represents a certain amount of charge. Since negative offsets can not be corrected for, the offset of the pre-amplifier inside the VFC is deliberately detuned slightly to have a low count rate at the output even if the beam is off. In that case the background count rate can be measured and subtracted from the data. The response of the entire system was checked with a Keithley K263 current source and the linearity was found to be excellent.

The output pulses from the VFC are routed to a National Instruments Compact Rio micro controller, which includes an FPGA. The FPGA is programmed to accept count signals from the VFC into a set of programmable counting registers, each of which can be read out at any time. By timed interrogation of the counting registers the dose rate may be determined. A single counting register acts as a beam control register, preloaded with a certain number of counts and set to count down upon receiving pulses from the VFC. The FPGA can then be commanded to

* A guard ring is a separate set of electrodes that is used to shape the fringes of the electric field inside the active volume of the ionization chamber.

turn on the beam by signalling a TTL output. Reaching a count value of zero in the preloaded register causes the FPGA to turn off the beam immediately. Mainly because of the limited bandwidth of the QSX the beam will always be turned off slightly late. The VFCs will continue to count for a few milliseconds after beam off because the QSX signal is lagging slightly. These 'overshoot' effects represent real dose. By keeping the counting registers active for an additional second even these last counts will be included in the total tally.

The counting registers of the FPGA can be accessed by software via Ethernet. The controlling computer, running Labview software, keeps track of the exact time the beam is turned on and off as well as the counts in the various counting registers of the FPGA. Background measurements are typically done before each irradiation or before the experiment. The FPGA code includes online background subtraction for the register controlling the irradiation. The beam output during an irradiation is expressed as the background-corrected counts of the beam control register.

Apart from the scatter foils, the field shape is determined by collimators. The collimators at KVI-CART are made of MS58 Brass alloys. At a thickness of 45 mm they completely stop a proton of 190 MeV. While in principle only one collimator is needed right in front of the target it can be beneficial to reduce the field size much further upstream as well. Because the beam efficiency is on the order of a few percent, most of the beam current eventually ends up in a collimator. Without additional collimators the resulting beam contamination (gammas, neutrons and electrons) would be produced close to the target in the last collimator. With additional collimators upstream the production of that contamination occurs at a larger distance from the target. It also reduces the activation of the last collimator (the field collimator) which is chosen according to the desired field size. Prior to an experiment two field collimators can be selected each of which can then be placed into the beam line remotely via pneumatic actuators. This way the experiment does not have to be interrupted if another field size is required. The field collimators used in the calorimetry experiments have circular openings with diameters of 120, 70 or 50 mm.

2.10.1 Field shape imaging

Before each experiment the proton beam was aligned with the beam line by examining scintillation images taken at the position of the temperature probes of the calorimeter. While an initial guess using wire grids as described in section 2.10 can produce an reasonable alignment, careful adjustment of the magnets is needed to produce a flat dose distribution.

The setup for field imaging is shown in figure 2.11. The proton beam direction is from left to right. Visible on the left is the field collimator. A Lanex scintillation screen is placed downstream, at the location of the thermistor probes in the calorimeter, but also at the correct water equivalent depth. As the scintillation screen can not be submerged into water, a stack of polystyrene material is placed upstream of the scintillation screen, which reduces the beam energy to the required

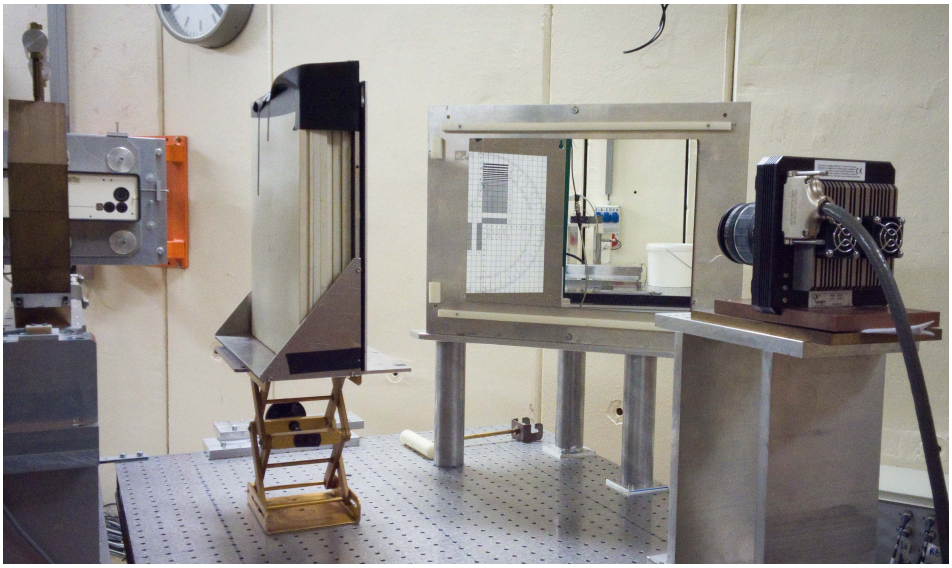

Figure 2.11 – Setup for field imaging with a CCD camera. Showing field collimators on the left and a stack of polystyrene degrading material. A test-chart for camera focussing and image-alignment is visible via the mirror. The grid on the chart is used for perspective correction and size calibration.

value and causes an almost similar amount of scattering as in water. The CCD camera that observes the Lanex screen via a mirror is visible on the right. A test chart is used to focus the camera and to provide dimensional calibration. A typical field shape image as delivered by the camera is shown in figure 2.12. The field collimator used in taking this scintillation image has a diameter of 70 mm and the scintillator screen was placed 31 cm downstream behind the collimator. In the image, both hot pixels and other hot spots which are thought to be mostly due to neutron interactions in the camera's CCD are observed. The hot pixels are single pixels or sometimes short rows of pixels which have been permanently damaged as the result of the effects of stray radiation. Hot spots are fairly intense clusters of over-bright pixels, which are due to the interaction of radiation in the CCD as the image was taken. The clusters are often several pixels in width and represent the path of charged particles. Extensive image processing methods are needed if the images are to be used directly in (2D) heat transfer calculations because the presence of a hot spot in the image near the position of the probes can disturb the calculated heat transfer correction. Offsets due to residual light in the room and actual dark current are removed by subtracting a 'dark image' (an image having the same integration time but without any irradiation). It has been suggested[59, 57] that 5 to 7 pixel wide median filtering can be applied to the raw CCD images without causing any systematic effects while preserving sharp gradients. Removal of isolated hot pixels and dead pixels surely benefits from a

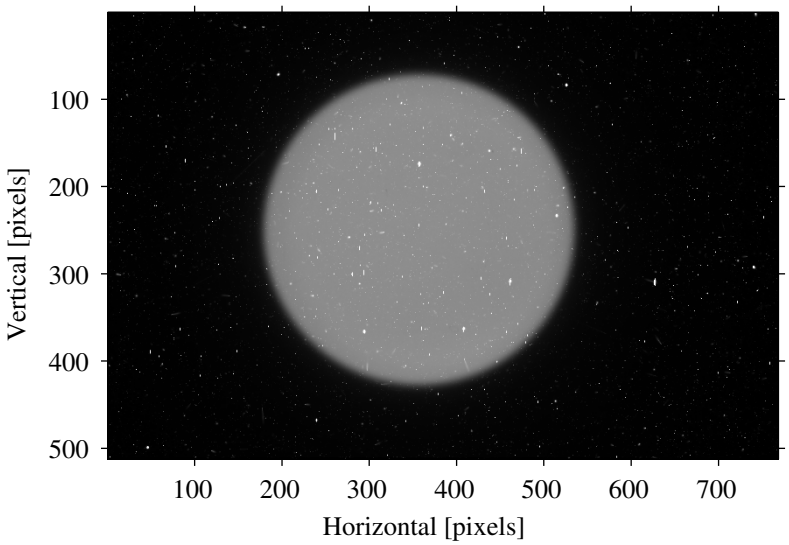

Figure 2.12 – Lanex scintillation image of a 70 mm field at a water equivalent depth of 65 mm, captured with a CCD camera. The white spots are due to neutron interactions in the CCD sensor.

median filtering approach, however the removal of random hot spots due to neutron interactions is another matter since those features are often much wider than just a single pixel. In fact, these image features cause a local increase in signal amplitude unless the filtering width is much larger than the feature. If the density of these neutron affected pixels is high enough it causes a systematic increase in signal amplitude.

A better approach is to remove the hot pixels and hot spots completely. An algorithm was developed that detects regions of the image suffering from neutron spikes or 'bad' pixels (hot pixels or dark pixels). The algorithm searches for bad pixels by thresholding the dark image over three standard deviations of the dark signal. This finds non functional pixels which are either true hot pixels, dead pixels or at least partly damaged. In addition, for the sole purpose of finding neutron spikes, the field image itself is median filtered with a 5x5 pixel filter and then blurred with a 50 pixel wide Gaussian filter to arrive at a good estimate for the peak amplitude in the centre of the field. The image is then thresholded over 110 % of the maximum amplitude, flagging the pixels for removal with a added margin of 1 pixel. The image is also thresholded over the local amplitude, flagging additional pixels for removal with added margin. This results in a bad pixel map for each particular scintillation image. Figure 2.13 shows the pixels that have been selected for removal. Those pixels contain essentially no useful information and may as well be removed.

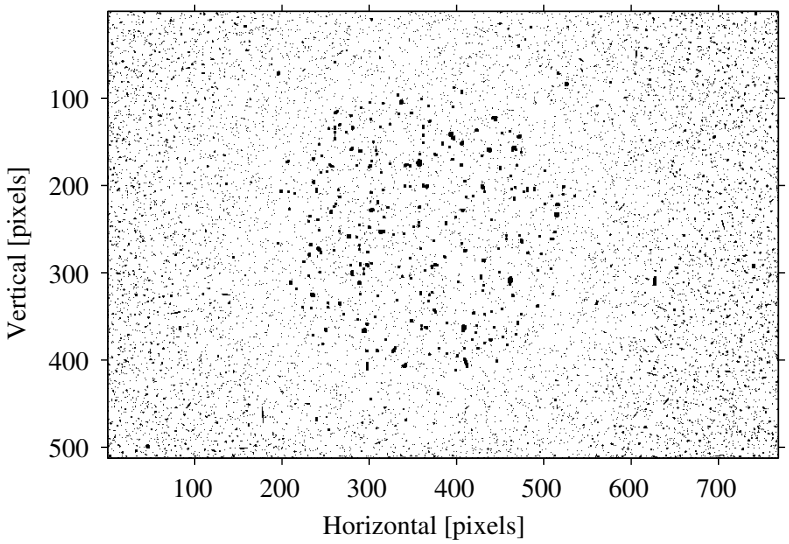

Figure 2.13 – Processed scintillation image showing in black which pixels have been flagged for removal.

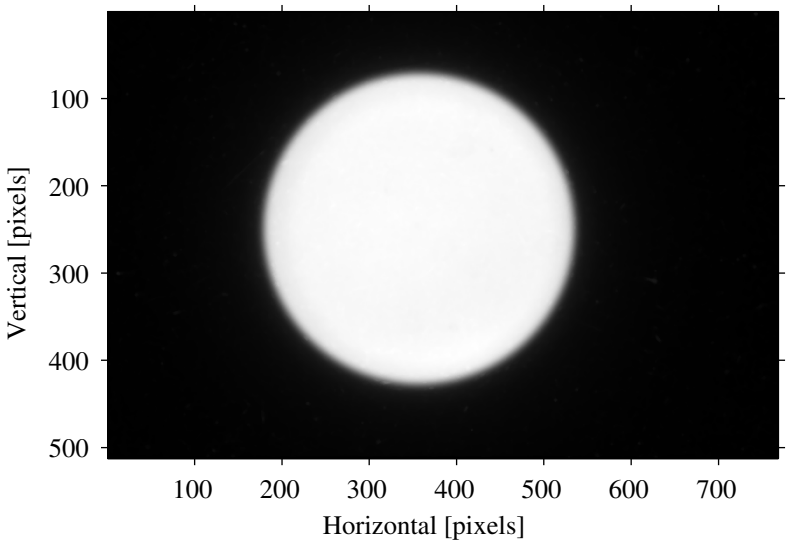

Figure 2.14 – Scintillation image after performing the clean up procedure.

Figure 2.14 shows the result of the image after the bad pixels have been removed. The method first substracts the dark image from the untreated field image and then uses the bad pixel map to clean it up. The procedure is to remove a patch

of bad pixels by diffusion of information from the edges of the bad patch. In this algorithm, in each iteration the local neighbourhood of each bad pixel is convoluted with a Gaussian filtering matrix of $\sigma = 0.5$, thus steadily allowing good pixels to bleed into their faulty neighbours. That is, at each iteration, the pixel value of each faulty pixel at location i, j is set by a local convolution of the following matrix centered on the faulty pixel:

$$G = \begin{bmatrix} 0.011 & 0.084 & 0.011 \\ 0.084 & 0.619 & 0.084 \\ 0.011 & 0.084 & 0.011 \end{bmatrix} \tag{2.11}$$

The values mentioned above represent a standard Gaussian filtering kernel as generated by Matlab. Since only the faulty pixels are altered, over time with each iteration, the faulty pixels will be filled in with values from close neighbours. In doing so any slope in the data is preserved. The stopping condition for the iteration is that the absolute difference summed over all pixels in the iteration is lower than 1.0 ADU*:

$$\sum_{i,j} \left(P_{ij} - P'_{ij} \right) < 1 \tag{2.12}$$

Using such algorithms it is possible to remove large sections of the image while still preserving gradients. There is no effect on further processing as long as the second derivative of the field in any direction is small.

Figure 2.15 shows a line profile in both the original and cleaned image. The algorithm removes large features due to neutron interactions as well as bad pixels in a consistent way.

As a last step, the algorithm uses the cleaned image and the image from the test chart to perform perspective correction. The image is up-sampled to a constant 10 pixels/ mm. An additional algorithm finds the centre and size of the field by maximizing a convolution of a thin circle with the gradient of the image. That is, the algorithm computes the following image:

$$M_{ij} = (\nabla I)_{ij} \cdot \exp\left(-0.5 \frac{\left(\sqrt{(i-i_0)^2 + (j-j_0)^2} - r_0 \right)^2}{4^2} \right) \tag{2.13}$$

The algorithm maximizes $\sum_{i,j} M_{ij}$ and in doing so finds the coordinates i_0, j_0 of the centre of the field as well as the radius r_0. The right hand side of the above equation represents an image of a ring with an edge that looks like a four pixel wide Gaussian profile. The algorithm consistently finds the same coordinates and radii with sub-pixel resolution, independent of the initial values of i_0, j_0 and r_0.

Integration over 2π yields a amplitude version radius plot, shown in figure 2.16 for a 70 mm field. The top panel shows a fitting function that agrees with the measured profile to within 1 % and the bottom panel shows the residuals of the fit.

* ADU: Arbitrary Dose Unit, the change in light intensity corresponding to a change of the Least Significant Bit of a CCD-pixel value.

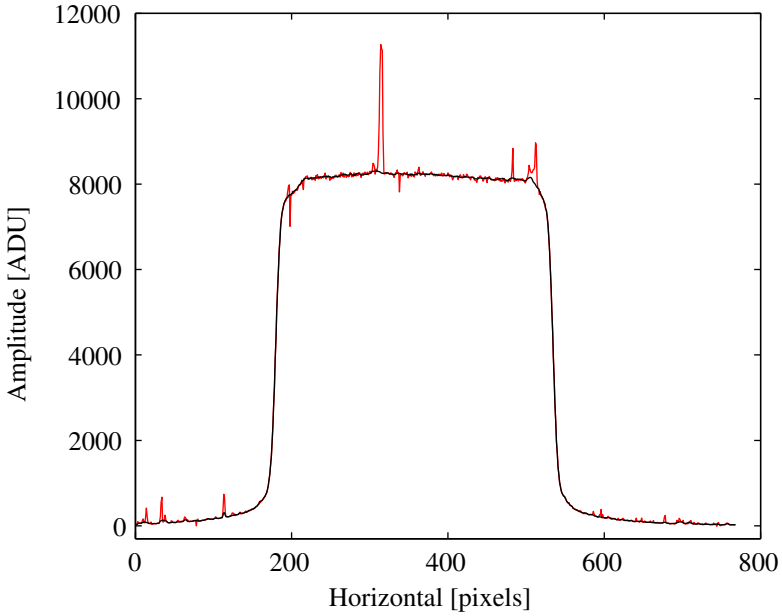

Figure 2.15 – A line profile over one row of pixels taken from the scintillation image, before (red line) and after (black line) image clean-up.

A model function containing a sum of two error functions was used:

$$A(r) = \frac{1}{2}\left(a \cdot \mathrm{erfc}\left(\frac{r-b}{c}\right) + d \cdot \mathrm{erfc}\left(\frac{r-e}{f}\right)\right) \tag{2.14}$$

In the above equation, r is the radial distance from the centre of the field in the image plane, and a and d are the intensities of two different contributions, each of which has an associated field-width (b or e) and scattering width (c or f). Table 2.2 lists the results of a fit for two different field sizes. As can be seen in figure 2.16 it takes more than just one error function to map the field shape. The edge is quite sharp but on top of that there is an additional contribution with a much more diffuse edge. Fit parameter c describes the scattering of protons which have passed through the opening of the collimator without interaction in the collimator itself. The scattering width of 1.6 mm is roughly consistent with multiple scattering in 65 mm of water according to the Highland approximation[60], but it only accounts for 85 % of the dose. For both field sizes there is a 15 % dose contribution which is characterized by a much larger scattering width f of about 10.5 mm. This second contribution is related to entrance face collimator scattering[57].

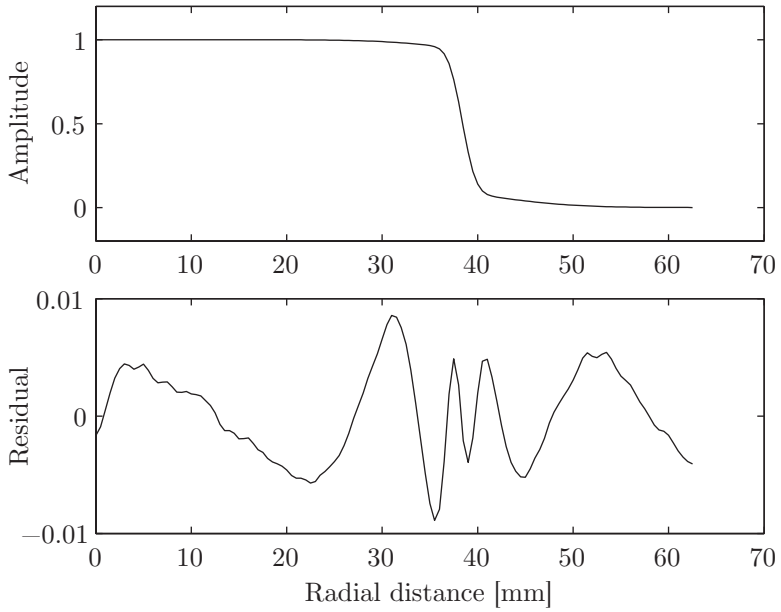

Figure 2.16 – Top: A fit of equation 2.14 to the dose profile of figure 2.14, showing the relative dose as a function of radial distance from the centre of the field. Bottom: residuals to the fit.

	Field Diameter			
	50 mm		70 mm	
a	0.854(6)		0.852(5)	
b	27.390(8)	mm	38.374(8)	mm
c	1.619(19)	mm	1.586(18)	mm
d	0.146(5)		0.149(5)	
e	28.10(14)	mm	40.44(15)	mm
f	10.7(4)	mm	10.3(3)	mm
$1 - R^2$	7×10^{-5}		7×10^{-5}	

Table 2.2 – Fit parameters for equation 2.14 for two different field sizes. The water equivalent depth is 65 mm.

2.11 Initial beam line calibration

Before each calorimetry experiment the beam current and the signal from the beam monitors is calibrated against a measurement of dose with an ionisation chamber. This relates the Monitor Units (MU) from the Beam Intensity Monitors (BIM) and the beam current measured by the operator at the extraction of the cyclotron to a measured dose and dose-rate at the position of the calorimeter probes. To

measure the dose, a PTW 30001 Farmer ionization chamber is used in a 5x5x5 cm polystyrene phantom. The ionization chamber has been calibrated against a water calorimeter in a ^{60}Co beam. A water proofing sleeve is available, however, setting up an additional water phantom takes a lot of time with little benefit since absolute dosimetry is not required at this point because the absolute measurements will be done by the calorimeter. Instead, polystyrene plates are used to degrade the energy to achieve the required water equivalent depth. The ionization chamber itself is positioned at the location of the water calorimeter probes. The ionization charge is readout with an PTW Unidos 10001 electrometer set to current-integration mode, medium range. Based on this calibration the dose rate can be adjusted during the experiment without actually measuring the dose with the calorimeter. As long as experiments do not rely on absolute dose calibration this simple technique will suffice. The only corrections which are applied are a stopping power correction according to TRS-398[14] and corrections for temperature and pressure.

2.12 Environmental monitoring

The Beam Intensity Monitors are used to measure the delivered proton fluence in each irradiation. They can also be used to control the delivered proton fluence for specific experiments in which the duration of the irradiation is not important. Because the output of the cyclotron is never ultimately stable, even relative measurements need to be normalized to the delivered proton fluence. The signal of these ionization chambers is proportional to the density of the air inside the BIMs and the measured values should be corrected for air pressure and temperature variations which occur during the experiment[14]. These effects are corrected by applying a correction factor:

$$k_{TP} = \frac{273.15 + T}{273.15 + T_0} \frac{P_0}{P} \tag{2.15}$$

Usually the temperature is specified in °C. In the case of a reference ionization chamber, T_0 and P_0 are the pressure and temperature at which the original calibration factor is valid. In the case of the BIMs it is the temperature and pressure at the time of the initial beam line calibration before each experiment. Taking the value of k_{TP} into account yields a normalized value of the dose:

$$D^* = D \cdot \frac{1}{MU \cdot k_{TP}} \tag{2.16}$$

The reported dose has units of $\mathrm{Gy\,bar\,MU^{-1}\,K^{-1}}$. It is a property of the beam line but its value can change depending on how the beam is aligned on the scatter foil. The effect of air humidity is small[6] and changes in humidity are assumed to have negligible effects.

2.12.1 Air pressure and temperature measurement

Air pressure is measured continuously throughout the experiment with a Druck DPI 140 pressure sensor. The pressure sensor contains active electronics which means it cannot be mounted in the irradiation room itself. Instead the pressure sensor is located in the basement with the other control electronics of the calorimeter. It is assumed that a constant pressure equilibrium exists between the basement and the irradiation room as there are open air passages directly between the two rooms. The pressure variation with altitude (the pressure sensor is mounted about 4 m lower than the BIM) is neglected in this thesis, although it should be pointed out that an absolute calibration should include a correction for barometer altitude. Ambient air temperature is measured with a PT100 sensor mounted close to the Beam Intensity Monitor. This sensor is similar to the sensors used in the calorimeter thermostat.

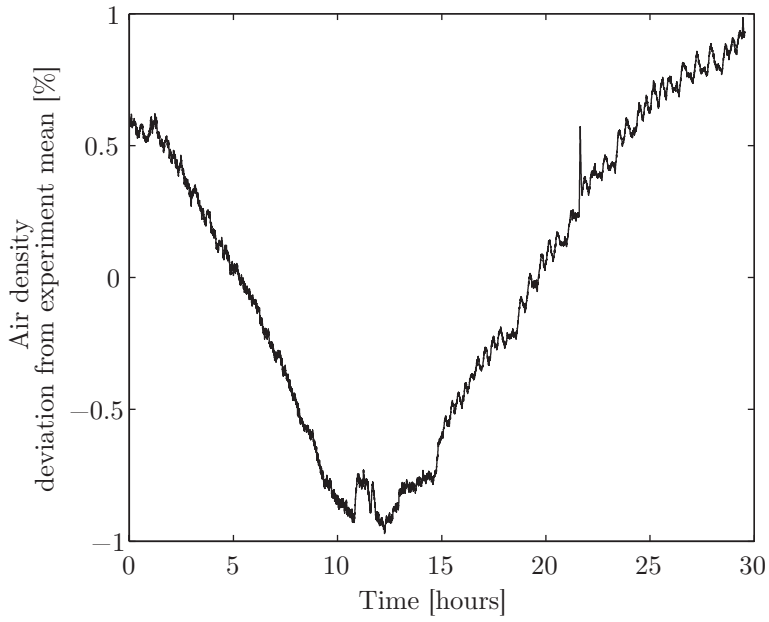

Figure 2.17 – Variation of the air density (derived from barometer and temperature data) as a function of time relative to the mean air density during an experiment. The large 2 % swing during this experiment was due to a storm passing by.

Figure 2.17 shows the magnitude of the air density variation during an experiment when a storm passing by caused a sharp dive in air pressure, which accounts for most of the variation seen in the plot. Evidently, one cannot do without temperature and pressure measurements, since the air density may vary by several percent during an experiment. Even on the time scale of an hour there can be per-mille level variations.

2.13 Evaluation of statistical uncertainty

The statistical uncertainty in the determination of ΔT_m is inevitably one of the largest contributions to the total uncertainty budget. After all, in most cases there is little benefit in trying to improve the statistical uncertainty by increasing the number of measurements if the statistical uncertainty is on the same level as the systematic uncertainties. Therefore, correct evaluation of the statistical uncertainty of the measurements deserves explicit attention.

The statistical uncertainty is determined by first converting the measured temperature increases ΔT_m (shown in figure 2.8) into values of dose per monitor unit, then applying various corrections (environmental, heat transfer) after which the standard deviation is calculated. The corrections need to be applied if they have temporal variations, in order to ensure that the estimate of the standard deviation reflects the true repeatability of the experiments. Finally, confidence intervals are obtained by using the Student's-t distribution and a standard uncertainty is obtained from the standard deviation by applying a Student's-t factor.

The calculation starts with a standard deviation, which is calculated from the unbiased estimator of the variance:

$$\sigma^* = \sqrt{s^2} = \sqrt{\frac{\sum_{i=1}^{N} (D_i - \langle D \rangle)^2}{N^* - 1}} \tag{2.17}$$

In the above equation, N is the actual number of irradiations while N^* is the effective number of irradiations. N^* is less than N because the determinations of the ΔT_m are not statistically independent. Figure 2.8 shows how ΔT_m is determined from temperature data in the drift period before the irradiation (t_{PrFL}) and after the irradiation (t_{PoFL}). With the fitting interval constraints and beam cycle described in section 2.8.2, the post-irradiation fit of the i'th irradiation is exactly the same as the pre-irradiation fit of the $(i+1)$'th irradiation because they are derived from the same data. Thus, in the case of a long sequence of irradiations, each linear fit is used approximately twice. For very short irradiation sequences of multiple successive irradiations the exact effective number of samples is slightly larger, because the results from the first and last curve fit in the sequence are used only once, such that the effective number of irradiations is:

$$N^* = N/2 + \frac{1}{2} \tag{2.18}$$

A calculation which takes into account the typical time needed for temperature stabilization and a sequence length of 10 irradiations shows that the beam time required for a give effective effective number of samples could be about 30 % lower if the time between irradiations is extended such that the linear fits no longer overlap. However, because the irradiation sequences are longer, the heat transfer calculations would need to be accurate over a longer time period as well. Additionally, the longer

irradiation sequence would provide a larger window of opportunity for thermal disturbances to reach the thermistors and it requires that the stability of the beam is to be maintained for a longer period. Although the chosen symmetric arrangement of the fitting interval is not optimal, it is more robust against various disturbances and interruptions.

Since the effective number of degrees of freedom is less than the number of irradiations, the estimation of the standard uncertainty should be based on an effective standard deviation:

$$\sigma^* = \sqrt{\frac{N-1}{N^*-1}}\hat{\sigma} = \sqrt{2}\hat{\sigma} \tag{2.19}$$

In the above equation, $\hat{\sigma}$ is the usual standard deviation. The above equation is exact and the correction to $\hat{\sigma}$ is independent of the number of irradiations in a series. However, this does not mean that it is also valid for any combination of multiple series if $\hat{\sigma}$ is simply computed over the entire data set since it does not account for the slightly less correlated data in that case. The experimental standard deviation of the mean $\langle D \rangle$ is computed from σ^*:

$$\hat{\sigma}_{\langle D \rangle} = \frac{\sigma^*}{\sqrt{N}} = \frac{\sqrt{2}\hat{\sigma}}{\sqrt{N}} \tag{2.20}$$

In the above equation $\sqrt{N}$ must be used rather than $\sqrt{N^*}$ because the correlations are already accounted for in an effective standard deviation σ^*. The above estimate, based on the variance in the data itself, yields the Type-A standard uncertainty compatible with the Guide to the expression of Uncertainty in Measurement 'GUM'[61], but it should be noted that the unbiased quantity referred to in the GUM is the experimental variance. The GUM does make reference to the requirement of a sufficient sample size for σ, but only addresses its biasedness in the evaluation of confidence intervals using Student's t distribution. As discussed in the following section, the estimate of the standard deviation of the experimental mean is biased towards lower values.

2.13.1 Unbiased estimate of the experimental standard deviation of the mean

Although the variance estimator is unbiased, the derived standard deviation estimator $\hat{\sigma}$ is significantly biased for low N^*. This issue is not the same as the bias that can be corrected by applying the well known Bessel correction (the subtraction of one degree of freedom in the estimate of the population standard deviation), since here it is not the variance which is biased, but rather the standard deviation which is based upon a estimate of the variance. The unbiased, correlation corrected estimate of the standard deviation of the experimental mean is:

$$\hat{\sigma}^u_{\langle D \rangle} = \frac{\sigma^*}{T(N^*)\sqrt{N}} = \frac{\sqrt{2}\hat{\sigma}}{T(N^*)\sqrt{N}} \tag{2.21}$$

Note that the above equation includes a factor of $\sqrt{2}$ to account for the correlation in the calorimetry data. The divisor $T(N^*)$ is a correction for the bias in the estimator $\hat{\sigma}$. James[62] and Holtzman[63] list a $T(N^*)$ which is defined relative to a standard deviation based on the biased estimator of the variance. For the unbiased estimator (containing the Bessel correction) used here $T(N^*)$ is[62]:

$$T(N^*) = \sqrt{\frac{N^* - 1}{2}} \frac{\Gamma(N^*/2)}{\Gamma((N^* + 1)/2)} \tag{2.22}$$

The unbiased estimate for the standard deviation of the mean becomes:

$$\hat{\sigma}^u_{\langle D \rangle} = \frac{2}{\sqrt{N/2 - 1/2}} \frac{\Gamma((N/2 + 1/2 + 1)/2)}{\Gamma((N/2 + 1/2)/2)} \frac{\hat{\sigma}}{\sqrt{N}} = c(N) \frac{\hat{\sigma}}{\sqrt{N}} \tag{2.23}$$

The magnitude of the combined correction $c(N)$ is:

$$c(N) : \begin{cases} N = 3 & c(N) = 1.8 \\ N = 5 & c(N) = 1.6 \\ N = 10 & c(N) = 1.5 \end{cases} \tag{2.24}$$

As the number of irradiations in a series increases, $c(N)$ approaches $c(N) \approx \sqrt{2}$. Generally, the number of irradiations in a series N will be larger than $N = 5$ and the simplification that $c(N \geq 5) \approx \sqrt{(2)}$ will be in error by less than 13 %.

An important issue is that equation 2.22 refers only to the result of a single series. If multiple series are to be combined their contributions to the mean and their variance estimates are to be added with weights proportional to $1/\hat{\sigma}^2_{\langle D \rangle}$. This can be somewhat tedious because the series' lengths can be reduced due to beam interruptions. However, for series of length $N \geq 5$ it is safe to simply assume that a constant factor of $\sqrt{2}$ applies, because the extra 1/2 degree of freedom per series does not improve the statistics a lot while the large number of samples N removes most of the bias in the $\hat{\sigma}$ estimator. Therefore, in most cases in this thesis the standard deviation of the mean is estimated by:

$$\hat{\sigma}_{\langle D \rangle} = \frac{\sqrt{2}\hat{\sigma}}{\sqrt{N}} \tag{2.25}$$

It must be pointed out that the samples of $\hat{\sigma}$ are not normally distributed (in fact, it is chi-distributed). For situations where there is a relatively low number of samples it is more appropriate to specify uncertainty in terms of confidence limits.

2.13.2 Evaluation of confidence limits

In the previous section the standard uncertainty $\hat{\sigma}_{\langle D \rangle}$ was estimated and it was pointed out that its distribution is not a normal distribution. Likewise, the estimate for the mean $\langle D \rangle$ itself also does not follow a normal distribution when

the deviations from the true mean are specified relative to the estimated standard uncertainty. Since the estimate of $\hat{\sigma}_{\langle D\rangle}$ is not independently established from the estimate of $\langle D\rangle$, the deviations of the experimental mean from the true mean and subsequently divided by the estimated standard uncertainty, will have a Student's-t distribution.

The usage of the Student's-t distribution when applied to evaluation of confidence limits is described in detail in a publication by the BIPM[61] and is briefly summarized here. The t-distribution is given by the following probability density function:

$$p(t,\nu) = \frac{1}{\sqrt{\pi\nu}} \frac{\Gamma\left(\frac{\nu+1}{2}\right)}{\Gamma\left(\frac{\nu}{2}\right)} \left(1 + \frac{t^2}{\nu}\right)^{-(\nu+1)/2} \tag{2.26}$$

where ν is the number of degrees of freedom used in the estimate

The above distribution applies to the statistic t:

$$t = \frac{\langle D\rangle - \mu_D}{\hat{\sigma}_{\langle D\rangle}} \tag{2.27}$$

where μ_D is the (unknown) true value of the dose. With the t-distribution, the Student's-t factor is defined as:

$$t_{P,\nu} = t \leftrightarrow \int_{-t}^{t} p(t,\nu)\,\mathrm{d}t = P \tag{2.28}$$

That is, $t_{P,\nu}$ is the symmetric confidence interval of the t-distribution for ν degrees of freedom having a full width of $2t$ such that the probability for values occurring within this interval is P. The t-distribution converges towards a normal distribution, meaning that $t_{68.27\%,\infty} = 1$ and $t_{95.45\%,\infty} = 2$.

The Student's-t factor $t_{P,\nu}$ is used to calculate confidence limits, expressed in units of the estimate of the standard deviation $\hat{\sigma}_{\langle D\rangle}$:

$$D = \langle D\rangle \pm t_{P,\nu} \cdot \hat{\sigma}_{\langle D\rangle} \tag{2.29}$$

Effectively, applying the $t_{P,\nu}$ factor allows one to correct for the fact that the estimate $\langle D\rangle$ in terms of the estimate of the standard deviation is not normally distributed, taking into account the value of ν which is the effective number of degrees of freedom: $N^* - 1$. The t-distribution is tail-heavy, for example $t_{68.27\%,2} = 1.32$ and $t_{95.45\%,2} = 4.53$, that is, the 95.45% confidence limits correspond to an interval which is a factor of $t_{95.45\%,2}/t_{95.45\%,\infty} = 2.27$ wider than is expected from a normal distribution. It is important to use the right estimator for the standard deviation when calculating the confidence intervals. Equation 2.29 explicitly refers to the experimental standard deviation of the mean according to equation 2.20, which is a standard deviation with only a Bessel correction. It does *not* refer to $\hat{\sigma}^u_{\langle D\rangle}$ in equation 2.21 because the definition of the Student's-t distribution itself is given in terms of $\hat{\sigma}_{\langle D\rangle}$ relative to equation 2.20. In fact the correction shown in equation 2.22 is already included in the probability density function of equation 2.26.

Chapter 3

Chemical effects in calorimetry

The dose to water is used as a reference in clinical dosimetry, because of its similarities to human tissue[23, 24]. Clinical dosimetry protocols such as TRS398[14] suggest the use of calorimeters as primary measurement standards for the dose to water. Water calorimetry in particular is appealing because the temperature increase directly yields the dose-to-water which is the quantity of interest.

The general assumption in water calorimetry is that all of the dose deposited by ionizing radiation is converted locally into heat. It is well known, however, that irradiation of pure water results in the production of chemical species other than water[64, 65]. It was recognised early on that the heat of chemical reactions from the radiolysis of water (perhaps involving impurities) could contribute significantly to the calorimetric result [46, 66]. This fact makes the standard dependent on extensive physics and chemistry models, which is undesirable given its role as a primary absolute standard. Generally, this means that the reactions should be well under control or that the expected effect is known to be very small.

Given the fact that the chemical effects are important in the case of existing calorimeters for photon dosimetry, they should also be examined for proton irradiation beam qualities. In an effort to provide a level of confidence in the results, it is first necessary to discuss water radiolysis in general. In this chapter the heat defect is defined and the theory of water radiolysis will be shortly discussed. It is explained how reverse reactions can reform water from radiolysis products leading to the existence of an equilibrium such that there are no net chemical effects on the time scale of a single calorimetric measurement. The role of molecular hydrogen and oxygen in the various reactions is examined. Then it is explained on the basis of the radiolysis model described in appendix A how the effects of high dose rate and high LET associated with proton beam qualities can lead to a non-negligible chemical heat defect in pure water and how this can be mitigated. The detrimental effects of impurities in the water are also discussed. Thereafter it is shown that

by dissolving hydrogen in the water the effects of high dose rate, high LET and high impurity levels can effectively be prevented, leading to a zero chemical heat defect. Finally, an experiment is described which shows that using this mechanism the water decomposition reactions are in fact halted in the beam quality of the KVI-CART irradiation facility, which (for this beam quality) allows to assign the same uncertainty to the effects of radiolysis as is already in use in ^{60}Co water calorimetry.

3.1 The chemical heat defect

The chemical heat defect (often referred to simply as 'the heat defect') is defined as the difference between the amount of measured heat (E_h) and the amount of heat that is expected based on the dose actually applied (E_a), when all other systematic effects have been accounted for[46]:

$$hd = (E_a - E_h)/E_a \tag{3.1}$$

The heat defect requires a correction factor to be included in the determination of the absorbed dose:

$$D = c_p \Delta T \cdot k_{hd} = c_p \Delta T \cdot \frac{1}{1 - hd} \tag{3.2}$$

A 'positive' heat defect is an endothermal response, meaning that net energy is lost in chemical reactions. Negative heat defects (exothermal, i.e. 'extra heat') are the result of impurities because formation of chemical species other than water from pure water requires a net energy input. The sign and magnitude of the chemical heat defect depend on the presence of dissolved gases and impurities[46, 49] as well as the charged particle spectrum[67, 68, 69] and dose rate[70, 71, 72, 73]. In principle, the value of the chemical heat defect averaged over the entire charged particle spectrum can be directly measured using various forms of total absorption calorimetry. Such experiments, which rely on total absorption of an electron beam with known energy and beam current, were performed by Roos et al. [66, 74]. Also, Brede[67] performed total absorbed dose measurements for irradiations with various ions (including low energy protons) which relied on the ratio of the temperature response due to dose absorbed in gilded copper and water.

3.2 Radiation induced chemistry in water

The origin of the chemical heat defect is a net change in chemical composition of the water, caused by the break up of water molecules (and possibly other dissolved species) by ionizing radiation and the subsequent reactions. It is the heat of reaction (the difference in enthalpy of the chemical species before and after the reaction) which causes a certain change in temperature. A description of the

various mechanisms of radiolysis can be found in the book by Choppin[65] and in a review paper by Jonah[64]. A more detailed treatment of the physics is given in the book by Mozumder[75]. This section provides a short summary of radiolysis theory.

3.2.1 Water break up

Passage of a charged particle through a water volume creates tracks of ionization. The track itself consists of a number of discrete spurs. There is no common definition of what is a spur and what is a track, however Mozumder[75] and McCracken[76] define spurs as isolated ionizations caused by a secondary electron with an energy below 100 eV*. Inside these spurs chemical reactions are initiated. For aqueous solutions which contain only low amounts of solutes it is reasonable to assume that the radiation has a direct effect on water molecules only and not on the solutes. The chemical reactions are initiated by splitting of water molecules in ions, radicals and electrons. Stripping an electron initially results in ionized water:

$$H_2O \xrightarrow{\text{Rad}} H_2O^+ + e^- \tag{3.3}$$

On a time scale of 1×10^{-14} s the ionized water reacts with the large surplus of water molecules:

$$H_2O^+ + H_2O \longrightarrow OH + H_3O^+ \tag{3.4}$$

Another pathway for radiolysis is the initial excitation of water:

$$H_2O \xrightarrow{\text{Rad}} H_2O^* \tag{3.5}$$

Within 1×10^{-13} s the excited water then dissociates into radicals and hydrogen molecules:

$$H_2O^* \longrightarrow H + OH \tag{3.6}$$
$$H_2O^* \longrightarrow H_2 + O \tag{3.7}$$

3.2.2 Microsecond radiolysis yields

Directly after the passage of the charged particle the liberated electrons are thermalized and solvated within 1×10^{-12} s, meaning that they become trapped in a cage of oriented water dipoles. The chemical species in the spur begin to diffuse

* At higher secondary electron energies, the resulting ionizations are called 'blobs' (e.g. a large elongated spur) and 'short tracks' until above 5 keV they are called tracks of their own. This nomenclature does not fully apply to heavy charged particles such as protons, because at the end of the proton track the spur density is very high such that the track forms a cylindrical distribution of ionization, rather than isolated spurs. While the track structure for protons at low energies is markedly different from electrons, at high energies the spurs are still isolated and in this thesis the nomenclature of 'spurs' is retained, even though it does not always fully apply.

outwards and participate in reactions with other chemical species produced in the same spur. For dilute aqueous solutions, at this stage, it is assumed that there are no reactions between the radiolysis products diffusing from the track and solutes from the bulk volume.

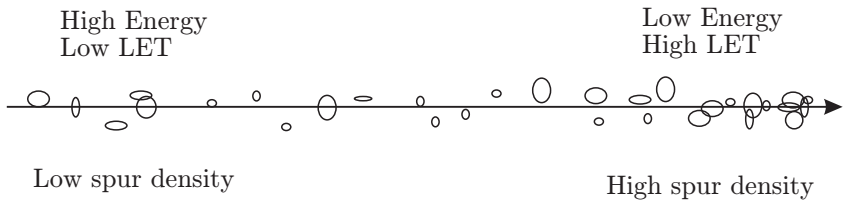

Figure 3.1 – A proton creates a track of spurs in the water as it slows down. Near the end of the track the LET increases and the spur density becomes higher, creating overlapping spurs[77].

After about 1 µs the spur is considered to be fully chemically developed. Due to the diffusion of the species the local chemical concentrations have become very low and the reaction dynamics after 1 µs can best be described by assuming a homogeneous distribution of chemical species, since the probability for interactions between species created in the same track becomes extremely low*.

The number of molecules of a certain radiolysis product present in the bulk water volume after 1 µs is called the 'radiolysis yield' or 'escape yield' or simply 'g-value'†. The escape yields are typically measured by introducing a moderate amount of a scavenger molecule which attacks only one specific spur product. Spectroscopy or titration is often used to measure the value of the yield. Wishart[78], McCracken[76] and Elliot[77] describe various techniques and their associated challenges. By definition, the escape yield is the amount of substance formed per amount of deposited dose. The units are usually specified as a number of molecules produced per 100 eV ([#/100eV]). Appendix A.4 lists the escape yields for proton radiation of varying LET, which were obtained from publications by Elliot[77] and Anderson[79].

Radiolysis is thought to be adequately described in two steps. First, the physical interaction of the charged particle and the chemical reactions at short time intervals are seen as a instantaneous conversion of pure water into radiolysis products:

$$H_2O \xrightarrow{\text{Rad}} e^- + H + OH + H_2 + H_2O_2 + H_3O^+ + OH^- + HO_2 \qquad (3.8)$$

* For isolated spherical distributions this works quite well, however for cylindrical distributions the reactions inside the spur continue for much longer because of the long tailed cylindrical geometry[75]. However, by the time of 1 µs, most recombinations have already taken place and if the water contains scavengers the remaining recombinations would have to compete with the scavengers.

† In this thesis, the lower case $g(E)$ is a notation for the localized (differential) yield at a specific point along the charged particle track, while the capitalized $G(E)$ is a notation for the average yield, integrated along the entire track. The integral is defined in equation A.13 in appendix A.4.5.

Secondly, after 1 µs the spur-products from equation 3.8 are assumed to be homogeneously distributed and to be participating in radiolysis reactions with substances from the bulk medium. The set of reactions occurring in the bulk medium and their reaction rates is listed in table A.1 in the appendix. This reaction set was obtained from a publication by Klassen and Ross[73].

There is a certain arbitrariness in the sharp divide between interactions at times of less than 1 µs and more than 1 µs. Certainly, at high scavenger concentrations the spurs have not fully developed chemically before being attacked by the scavenger. This sometimes leads to experimentally determined g-values which are somewhat higher than could be expected from radiolysis of pure water[77, 76]. Then again, choosing a lower scavenger concentration could cause it to be (locally) depleted or will allow enough time for bulk reactions to occur or could allow impurities to compete with the scavenger, resulting in g-values which are lower than expected and which also depend on the other solutes present in the water. The radiolysis yields are a source of uncertainty in the case of a non zero chemical heat defect. Even more so, being operationally defined the way they are and considering the difficulties of obtaining accurate experimental yield values, if the value of the heat defect would depend directly on the yields then the uncertainties of the yields would factor into the uncertainty of the calorimetrically measured dose, creating major difficulties in implementing a primary calibration standard.

3.2.3 Radiolysis yield dependence on proton LET

The radiolysis yields for high energy electron radiation are operationally defined as the escaping chemical species originating from individual isolated spurs, which survive spur expansion at 1 µs after passage of the charged particle. In the case of proton or ion irradiation, the spurs are not that well separated and in particular at low energies the track resembles a column of ionization rather than isolated spurs. Because of this, the amount of radical species actually escaping to the bulk is considerably lower and measurements of the radiolysis yields are complicated because the scavenger is at risk of being depleted, while using increased scavenger concentrations results in an overestimate of the escape yields because the scavenger starts to attack the radiolysis products even before track spur expansion is completed[77].

Apart from changing the absolute combined yield of all chemical species other than water, irradiation at higher LET as compared to lower LET will also change the ratio between the amounts of radical and molecular products escaping from the spurs. Figure 3.1 schematically shows spurs drawn as ellipsoids along the proton track. The spur density increases towards the end of the proton track such that the spurs tend to overlap. Due to the increased concentration, this overlapping favours recombination of radicals into H_2O, H_2 and H_2O_2. As depicted in figure 3.2, the increased radical concentration in the overlap between the spurs results in

increased production of these chemical species. As a result, the radiolysis yields change due to proximity of one spur to another, making the yield dependent on particle LET.

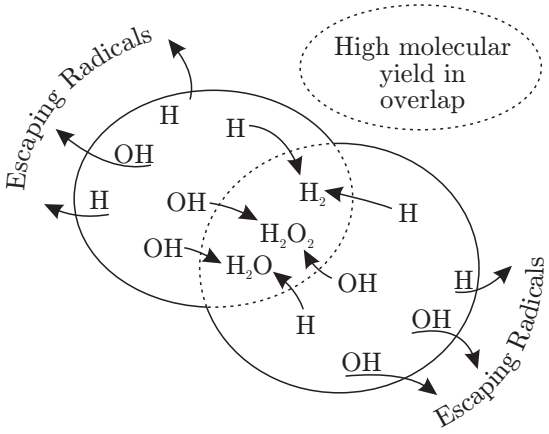

Figure 3.2 – Overlapping spurs at high LET cause a relative increase in molecular radiolysis products, while fewer radicals escape the spur cluster.

Because the generation rate of species of a certain type depends on the LET, the resulting reactions in the bulk proceed differently as a function of the LET and can change the calorimetric response, resulting in a LET dependent heat defect.

For the purpose of radiolysis modelling the radiolysis yields are calculated based on experimental data. A model derived from characterisations of radiolysis yields compiled by Elliot[77] is described in appendix A.4.5.

3.3 Equilibrium concentrations under radiolysis

The reason why calorimetry in ^{60}Co beams works is that calculations and calorimetric experiments show that pure, deaerated water does not exhibit net radiolysis[46, 80, 73, 28], at least at low dose rates and low LET. Radiolysis models indicate that after a small preirradiation dose of a few tens of Gray there is no net change in concentration of the chemical species for subsequent applications of dose. Stable concentrations of chemical species necessarily lead to a zero* chemical heat defect, because there is no energy lost or gained due to enthalpy changes.

In principle a heat defect cannot remain constant because the associated change in chemical concentrations would also cause a change of the reaction speeds. At some point the increasing concentrations give rise to new phenomena such as

* An exception is the case where the time dependence of the chemical reactions is such that significant changes in concentration occur some time after the irradiation has ended. The resulting thermal transients can influence the measurement result, even though the average concentrations during the measurement cycle do not change.

outgassing. If ultra-pure deaerated water is used, a stable calorimetric response is an indicator that the heat defect is zero. However, if the concentrations are changing very slowly the accompanying change in response might not be detected, which could lead to a false claim of attaining zero heat defect. Fortunately, in such cases the value of the heat defect will also be small. One possibility to get a quasi constant non zero heat defect is a continuous inflow of oxygen or other impurities into the water inside the glass vessel. Various experiments over a large time span have not revealed any evidence of such effects[81], although it might depend on the vessel geometry and cleaning techniques.

The uncertainty on the mentioned 'zero' heat defect cannot be deduced from radiolysis models, precisely because the models predict a zero heat defect[81]. Therefore the uncertainty on the chemical heat defect is fully determined by the applicability of the model itself, possible deviations from initial conditions and the presence of impurities for which mostly there are no reactions included in the model. The issue is that changes in the assumed radiolysis yields will not cause any change in the final value of the heat defect (zero), although it will be shown in this chapter that it changes the speed at which the chemical system approaches a zero heat defect through radiation induced chemical reactions and that, fortunately, this process can be dramatically accelerated by dissolved hydrogen.

In the grand scheme of things, the calorimetric uncertainty is as good as the degree to which the practical situation (water purity) corresponds to the model rather than the other way around. For this reason the uncertainty is usually taken to be the difference between experiments in which the purified water is saturated with various gases, for all of which the calculated heat defect is zero. [28, 73]. The obtained deviations probably reflect the quality of the water preparation rather than the applicability of the model.

3.3.1 Reverse reactions

In pure water, at low LET and low dose rate, radiolysis is stable because there are reverse reactions which convert as much molecular products back into water as are produced. That is, there are reactions which convert the stable radiolysis products H_2, O_2 and H_2O_2 back into water. The full set of reactions is listed in table A.1. The set of equations which convert stable radiolysis products back into water is[65, 82]:

$$\text{R15: } OH + H_2 \longrightarrow H + H_2O \tag{3.9}$$

$$\text{R10: } H + H_2O_2 \longrightarrow OH + H_2O \tag{3.10}$$

$$\text{R9: } H + OH \longrightarrow H_2O \tag{3.11}$$

This is the primary reaction mechanism in the case that there is little or no O_2 dissolved in the water. The reaction is initiated by H and OH radicals and is then propagated by the H radical. It is a chain reaction in that both R15 and R10 yield radicals which can participate in further reactions. The stoichiometry of the above

reaction-set is that two H radicals are consumed in the back conversion of a single H_2O_2 molecule. If it were not for reaction R15, the reaction speed would be limited by the supply of H radicals produced as primary yields in the track of the ionizing particles. With reaction R15 however, the reaction speed is essentially determined by the amount of H_2, because the combined result of reaction R15 and R10 is that the radicals are not consumed (the supply of H radicals is produced from H_2 present in the bulk). In principle, in the presence of a little H_2, the concentration of H radicals could continue to grow but ultimately it is limited by reactions R10 and R9 which act a sink for radicals.

Starting from pure water, the concentrations of the stable radiolysis products H_2 and H_2O_2 will increase when the radiation beam is turned on. They are produced directly as primary radiolysis products in the tracks of the ionizing particles, but also from recombination reactions in the bulk. In principle, small amounts of oxygen can also be accommodated if the radiolysis yield of H_2 is high enough:

$$\text{R11:} \quad H + O_2 \longrightarrow HO_2 \tag{3.12}$$

$$\text{R12:} \quad H + HO_2 \longrightarrow H_2O_2 \tag{3.13}$$

$$\text{R19:} \quad HO_2 + HO_2 \longrightarrow H_2O_2 + O_2 \tag{3.14}$$

The back-conversion rate of oxygen is however limited because unlike the back-conversion of H_2O_2 it is a two-step reaction, the second of which terminates the reaction chain. Thus, the reaction feeds on beam-generated primary H radicals and on whatever amount of H radicals happen to become available through reaction R15 if there is sufficient H_2, but ultimately the reaction speed is determined by the direct production of radicals by the beam. Because there is no recovery of an OH radical, as was the case for reaction R10, the reverse reaction R11 and R12 is self limiting. Very small amounts of oxygen (on the order of a few $\mathrm{nmol\,L^{-1}}$) have a minimal impact on the pre-irradiation dose required to achieve a zero heat defect. However, it will be shown in sections 3.3.3 and 3.4.2.2 that only slightly higher amounts of oxygen cause the chemical system to enter a state of higher equilibrium concentrations, significantly increasing the required pre-irradiation dose.

3.3.2 Radiolysis equilibrium

Ultimately, for low LET radiation at low dose rates, the end result is that under irradiation there is an equilibrium between water and the stable radiolysis products:

$$H_2O \underset{\uparrow g(E)}{\overset{\text{Radicals}}{\rightleftharpoons}} \begin{cases} H_2 \\ O_2 \\ H_2O_2 \end{cases} \tag{3.15}$$

The presence of radiolysis radicals activates this equilibrium, since there are no reverse reactions without the mediation of radicals. While some reactions are still active even after the beam has turned off, most of the important reactions feed

on beam generated radicals. Since the molecular products do not react without the presence of radicals, the concentration of these stable radiolysis products is essentially frozen after the beam is turned off. Net conversion of one molecular species into another happens essentially only during the time that the radiation beam is on.

Starting from pure water, when the beam is turned on, initially the concentrations of H_2 and H_2O_2 will increase until the reverse reaction becomes fast enough to compensate the primary production in the spurs. The location of the equilibrium in terms of the concentrations of H_2 and H_2O_2 (and in some cases O_2) depends on the dose rate and on the radiolysis yields $g(E)$. The actual behaviour of the radiolysis system can be rather complex as there are many coupled reaction equations. Increasing the concentration of any of the radiolysis products does not always decrease the concentration of the others. As is evident from the elaborate treatments of radiolysis by Allen[82] and Elliot[77], it is sometimes difficult to interpret the outcomes of radiolysis experiments which rely on presumed reaction mechanisms, because simplifications of the models including only some of the reactions are often not good enough.

It is not necessarily true that the equilibrium in equation 3.15 actually exists. As shown by Hart et al.[83] there definitely is a net decomposition of water at high LET. This occurs because the increased production of the molecular species H_2O_2 and H_2 in the proton track is accompanied by a decreased amount of radicals escaping to the bulk. Since the radical species H and OH are subject to recombination back to water in the bulk and since they are required in the reverse reactions with H_2O_2, the concentrations of H_2 and H_2O_2 would need to increase to high levels. The very high level of H_2O_2 then triggers the formation of O_2, which can cause run-away radiolysis. Allen[82] calculated a stability criterion based on reaction constants and the primary yields (g-values) as well as an initial excess of H_2 or O_2/H_2O_2. The same calculation also yielded predictions for the steady state concentrations that agreed well with experimental data. Similarly to the situation at high LET, high dose rates can also trigger O_2 production.

Out-gassing can occur as is the case in nuclear reactors, which has the effect of completely blocking the reverse reaction, because the H_2O_2 concentration can continue to grow while the H_2 concentration is limited by the out-gassing. The equilibrium in this case can not be reached because it lies beyond the out-gassing concentrations. Gas exchange across a water-gas interface also exists in water calorimetry, because the high purity cell usually contains a small bubble of gas. However, calorimeters operate in an entirely different dose rate and LET regime, which does not cause straight out-gassing. Even without straight out-gassing some of the H_2 and O_2 will still diffuse into the gas space, which temporarily can have similar effects. The reverse is also true: small amounts of oxygen present in the bubble may diffuse into the water some time after the dissolved oxygen in the bulk has been 'burned off' by the radiolysis. Even without out-gassing there can be an effective non-zero radiolysis effect, because the equilibrium concentration may be

so high that it simply takes too long to reach it. Radiochemistry effects in water calorimetry are thus not related to *bulk* conversion of water in gas and peroxide, but rather to small changes in the equilibrium concentrations.

3.3.3 The role of peroxide and oxygen

The position of the equilibrium of equation 3.15 shifts towards higher concentrations at higher dose rates and higher LET. In the following sections it will be shown that this equilibrium is only marginally stable. Allen[84, 82] and Fletcher[80] have previously described this mechanism in detail. The explanation presented here is slightly different because the presumed reaction set is not the same (mostly because of expansion of reactions into intermediate steps).

The origin of the marginally stable behaviour is the comparable rate constant of the following reactions:

$$\text{R15:} \quad \mathrm{OH} + \mathrm{H_2} \longrightarrow \mathrm{H} + \mathrm{H_2O} \tag{3.16}$$

$$\text{R16:} \quad \mathrm{OH} + \mathrm{H_2O_2} \longrightarrow \mathrm{HO_2} + \mathrm{H_2O} \tag{3.17}$$

The ratio of the rate constants is $k_{15}/k_{16} = 1.34$. Both H_2 and H_2O_2 compete for the OH radical. If pure water is irradiated at a low dose rate with low LET radiation the concentrations will be nearly equal because of the mass balance:

$$\mathrm{C(H_2)} = \mathrm{C(H_2O_2)} \tag{3.18}$$

As long as reaction R15 is fast enough, it can completely convert all freshly generated H_2O_2 back to water via the chain reaction mechanism of R15 followed by R10. At higher dose rates the concentrations of OH and H_2O_2 increase, resulting in an increased concentration of HO_2 via reaction R16. This enables the production of O_2^- via the following reactions:

$$\text{R35:} \quad \mathrm{HO_2} \longrightarrow \mathrm{H^+} + \mathrm{O_2^-} \tag{3.19}$$

$$\text{R22:} \quad \mathrm{H^+} + \mathrm{OH^-} \longrightarrow \mathrm{H_2O} \tag{3.20}$$

$$\text{R37:} \quad \mathrm{OH^-} + \mathrm{HO_2} \longrightarrow \mathrm{O_2^-} + \mathrm{H_2O} \tag{3.21}$$

Reaction R37 is essentially the combination of reactions R35 and R22. The newly formed O_2^- can then combine with OH radicals to form oxygen:

$$\text{R18:} \quad \mathrm{O_2^-} + \mathrm{OH} \longrightarrow \mathrm{O_2} + \mathrm{OH^-} \tag{3.22}$$

Reaction R18 supplies the needed OH^- ion for reactions R35, R22 and R37. The sum of the reactions R16 with R35, R22, R37 and finally with R18 is:

$$\mathrm{OH} + \mathrm{OH} + \mathrm{H_2O_2} \longrightarrow \mathrm{O_2} + \mathrm{H_2O} + \mathrm{H_2O} \tag{3.23}$$

This combined reaction reduces the efficiency of the reverse chain reaction(R15 and R10), by removing the OH radical from the chain. Thus, the H_2O_2 can partially inhibit its own destruction by producing oxygen. Because the production of O_2 consumes OH radicals, the left over H radicals recombine into H_2 until its concentration becomes large enough to cope with the primary production of H_2O_2 via R15 and R10, establishing the equilibrium at a higher concentration.

The presence of significant quantities of O_2 however prevents the H_2 from achieving equilibrium even at this stage, because once more, additional reaction channels are opened up, one of which is:

$$\text{R11:} \qquad H + O_2 \longrightarrow HO_2 \tag{3.24}$$

This is the first step of the 'oxygen burning' reactions. Once formed, some of the HO_2 will make its way through R35/R22 or R37 and finally through R18. The sum of these reactions is:

$$H + O_2 + OH \longrightarrow H_2O + O_2 \tag{3.25}$$

The above reaction is similar to reactions R15/R10. However, unlike R15/R10 it does not convert molecular products into water without consuming radicals, but rather the other way around: the above mechanism converts primary radicals back into water without consuming any molecular product. The reaction katalyzes the recombination of H with OH, effectively speeding up reaction R9.

Thus, the presence of large quantities of H_2O_2 triggers a situation which results in significant amounts of oxygen being produced. The oxygen (in the form of O_2 and HO_2) in turn reduces the efficiency of the reverse reaction mechanism such that the equilibrium is established only at very high concentrations.

3.3.4 The role of hydrogen

In many ways, H_2 can be seen as the counter part of O_2 and H_2O_2. The stoichiometry dictates that when one starts out with pure water containing only inert deaeration gases the concentration of H_2 is:

$$C(H_2) = C(H_2O_2) + 2\,C(O_2) \tag{3.26}$$

This means that no matter what physico-chemical processes are involved, stable radiolysis in pure water always results in a relative excess of H_2 compared to O_2 and H_2O_2. Normally, the relatively large amounts of H_2 enable the chain reaction pair R15/R10:

$$\text{R15:} \quad OH + H_2 \longrightarrow H + H_2O \tag{3.27}$$

$$\text{R10:} \quad H + H_2O_2 \longrightarrow OH + H_2O \tag{3.28}$$

This chain reaction catalytically decimates the concentration of H_2O_2 by supplying the only consumed component, which is the H-atom. By cutting off its supply of OH, R15 also prevents R16 (which ultimately leads to production of O_2):

$$\text{R16: } OH + H_2O_2 \longrightarrow HO_2 + H_2O \tag{3.29}$$

Reaction R15 also allows for efficient 'oxygen burning', again by producing the needed H-radicals from H_2:

$$\text{R11: } H + O_2 \longrightarrow HO_2 \tag{3.30}$$
$$\text{R12: } H + HO_2 \longrightarrow H_2O_2 \tag{3.31}$$
$$\text{R19: } HO_2 + HO_2 \longrightarrow H_2O_2 + O_2 \tag{3.32}$$
$$\text{R10: } H + H_2O_2 \longrightarrow OH + H_2O \tag{3.33}$$

The last set of reactions can be viewed as the reverse of the oxygen production chain described in section 3.3.3. The set of reactions which starts with H_2 not only allows for the back-conversion of O_2 into water, but it also cuts off the reactions that produce it by competing for the needed OH radicals and additionally prevents the O_2 production chain from competing at all by actively consuming H_2O_2, which is the first step in the production of O_2. This 'triple-action mechanism' is what allows low LET and low dose rate calorimetry to reach a negligible heat defect with a small pre-irradiation dose. It does hinge however on the relative speed of reaction R15 being larger than just about anything else. As such, the 'triple action' mechanism is rather fragile: If for whatever reason R15/R10 is interrupted or inhibited, all of the three benefits disappear and the reactions described in section 3.3.3 ensue.

3.4 The radiolysis challenge

In the following sections, the break down of the 'triple action mechanism' (the break down of the self limiting effect due to H_2) is examined in the case of high LET, high levels of impurities and high dose rates. It will be shown by the use of numerical calculations that each of these three factors can significantly increase the needed pre-irradiation dose to reach a negligible heat defect.

The chemistry model used in the following sections is described in appendix A. It was based mostly on data published by Elliot[85] and Klassen and Ross[73]. Each of the simulations assumes pure deaerated water as the initial condition, in some cases with additional dissolved hydrogen and oxygen. An irradiation cycle is implemented where the 'beam' is turned on and off with a repetition time of 180 s. Each irradiation consists of a single rectangular pulse, which is then followed by an idle-time to complete the full 180 s period. Micro-structure caused by the cyclotron RF-frequency is not modelled. The dose rate, dose per irradiation and duration of the irradiation are varied depending on the situation studied. One restriction of

the model is that it is a '1-D' model since the time is the only coordinate. This means that the effects of the spatial distributions of the radiolysis products and their diffusion processes are not taken into account. Effectively, the entire water volume is assumed to be uniformly irradiated with particles of the same LET. In reality, diffusion of radiolysis products from the Bragg-peak or pencil beam could interfere with the radiochemistry at any other point in the water volume.

3.4.1 Dose rate

Radiolysis for ^{60}Co radiation is thought to be stable and relatively insensitive to dose rate[46], but it should be pointed out that the dose rates used in a typical ^{60}Co calorimetry experiment are rather low (less than 1 Gy min^{-1}). For higher dose rates, net decomposition of water results up to a certain amount of accumulated dose because an additional reaction channel is opened which generates oxygen.

The higher dose rates necessarily lead to higher concentrations of radicals and H_2O_2. As shown in equation 3.23, a high concentration of H_2O_2 and OH radicals lead to the production of O_2, partially inhibiting the reverse chain reaction R15/R10. The newly formed oxygen further reduces the efficiency of R15/R10 by catalytically reforming radicals back to water via the mechanism of equation 3.25. The equilibrium concentration of H_2O_2 then becomes proportional to the square root of the dose rate[70, 82].

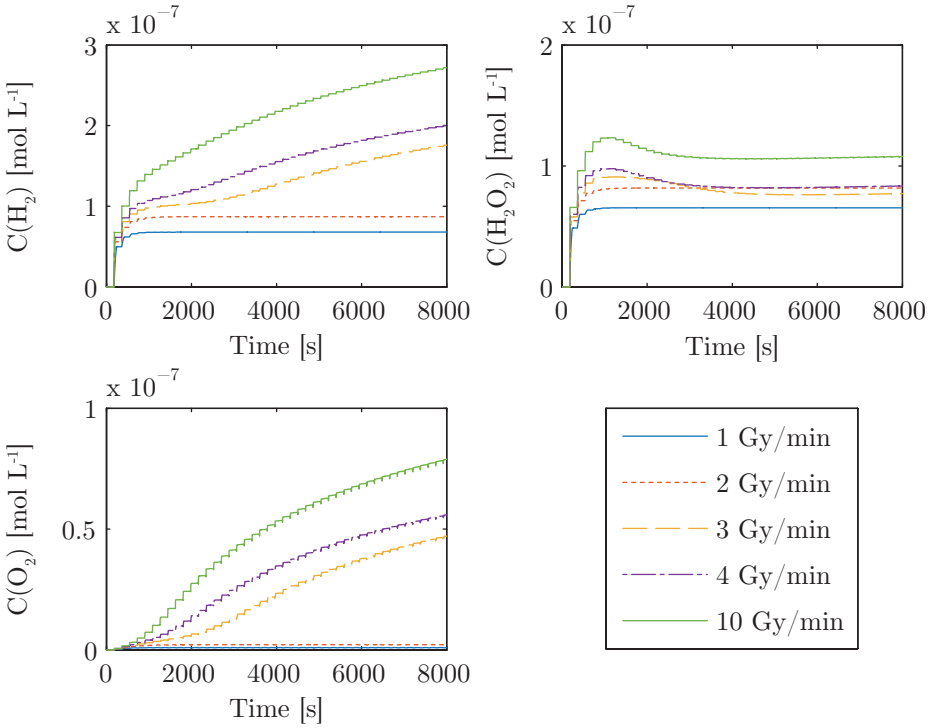

Figure 3.3 – Calculation of radiolysis at a LET of $0.2\,\mathrm{eV\,nm^{-1}}$ (corresponding to the average electron LET caused by ^{60}Co radiation), with a repetition time of 180 s. The dose per irradiation is 1 Gy and the duration of each irradiation is inversely proportional to the dose rate. The calculation starts with only pure water present at the time $t = 0$ and the chemical species shown are produced from the water. There is little or no production of O_2 for the lowest dose rate.

Figure 3.3 shows a calculation of the radiolysis for ^{60}Co radiation at different dose rates. The water is assumed to be pure and deaerated. Modelled is an irradiation cycle consisting of irradiations of 1 Gy which are repeated every 180 s. The duration of the irradiations is determined by the prescribed dose of 1 Gy and varies with the dose rate. Each irradiation is followed by a pause to complete the 180 s repetition time. Stable radiolysis is achieved at 1 Gy min^{-1} and 2 Gy min^{-1} but not at higher dose rates. The dose rate of 3 Gy min^{-1} is marginally stable. It appears to achieve balance, but after a short time net radiolysis still occurs. The higher dose rates do approach an equilibrium, however it takes quite a lot of accumulated dose. Of particular interest is the curve for a dose rate of 3 Gy min^{-1} because it shows the onset of the effects of the catalytic radical recombination caused by the presence of high concentrations of H_2O_2 and O_2. For this dose rate, the concentration of oxygen is such that the system cannot remain in the regime of a low concentration equilibrium and eventually it results in the production of even more oxygen, switching the system to a high concentration equilibrium.

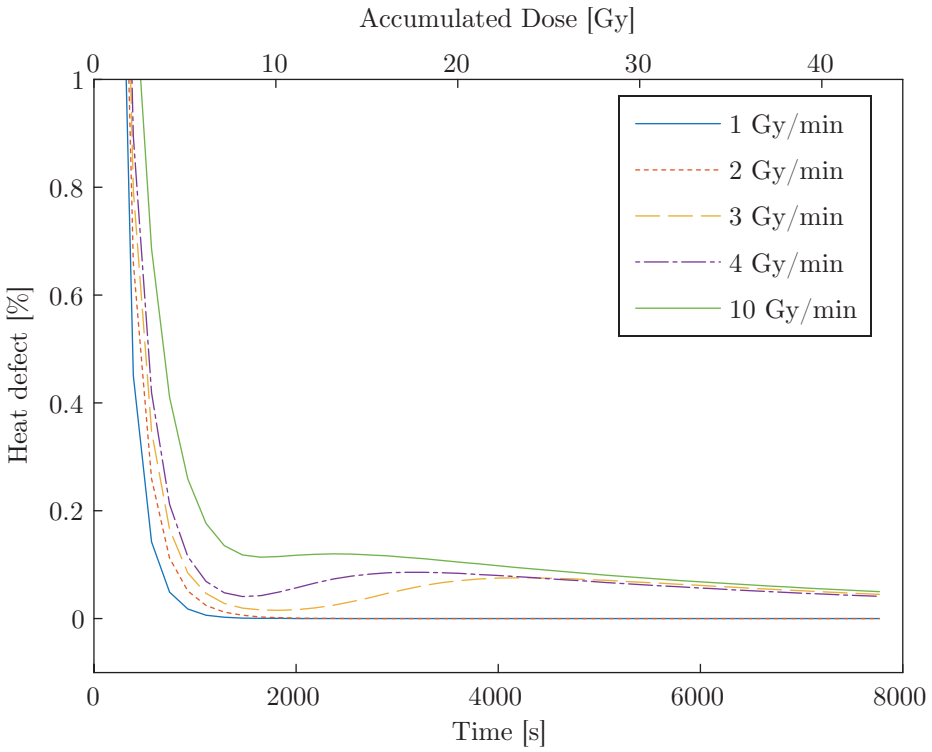

Figure 3.4 – Calculated chemical heat defect for a LET of 0.2 eV nm^{-1} (^{60}Co) at different dose rates. The concentrations of the chemical species are shown in figure 3.3. The heat defect of the first irradiation is in the range of 1.9 % to 2.5 % and quickly reduces with accumulated dose for the lowest dose rates.

Figure 3.4 shows the calculated chemical heat defect that is caused by the changes in concentration of the chemical species shown in figure 3.3. In pure water the heat defect is positive (endothermic). The radiolysis stabilizes quite quickly such that after only a small pre-irradiation dose the heat defect is zero at low dose rates. However, in the case of the higher dose rates which are marked by the onset of oxygen production, the heat defect is small, but not negligible. An oscillation is visible for the case of $3\,\mathrm{Gy\,min^{-1}}$ and $4\,\mathrm{Gy\,min^{-1}}$ which shows the marginally stable behaviour in this region. At even higher dose rates the 'bump' disappears into the first few irradiations as it shifts forward in time, because the onset of high oxygen levels occurs earlier.

The higher dose rates take longer to reach low values of the heat defect, because they lead to higher equilibrium concentrations of chemical species and therefore also a larger heat defect on the path to achieving equilibrium. Clinical dose rates can vary over orders of magnitude. Although the average dose rate for a field relevant for reference dosimetry is on the order of a few $\mathrm{Gy\,min^{-1}}$, instantaneous dose rates can be much higher. In a pencil beam scanned (PBS) system several $\mathrm{Gy\,s^{-1}}$ is a more reasonable figure[51], however PBS systems can reach instantaneous beam currents up to 10 nA which results in instantaneous dose rates up to $2 \times 10^2\,\mathrm{Gy\,s^{-1}}$, defining the upper end of the scale. The lower dose rates are relevant for photon and scattered proton beams (LET effects are examined in section 3.4.3), while the higher dose rates are relevant for scanning beams. The following calculations at high dose rates are not entirely applicable to scanned beams though, because they still assume broad-beam homogeneous irradiation of the entire water volume and because the scanning introduces additional time structure which is not modelled (because of the computational complexity).

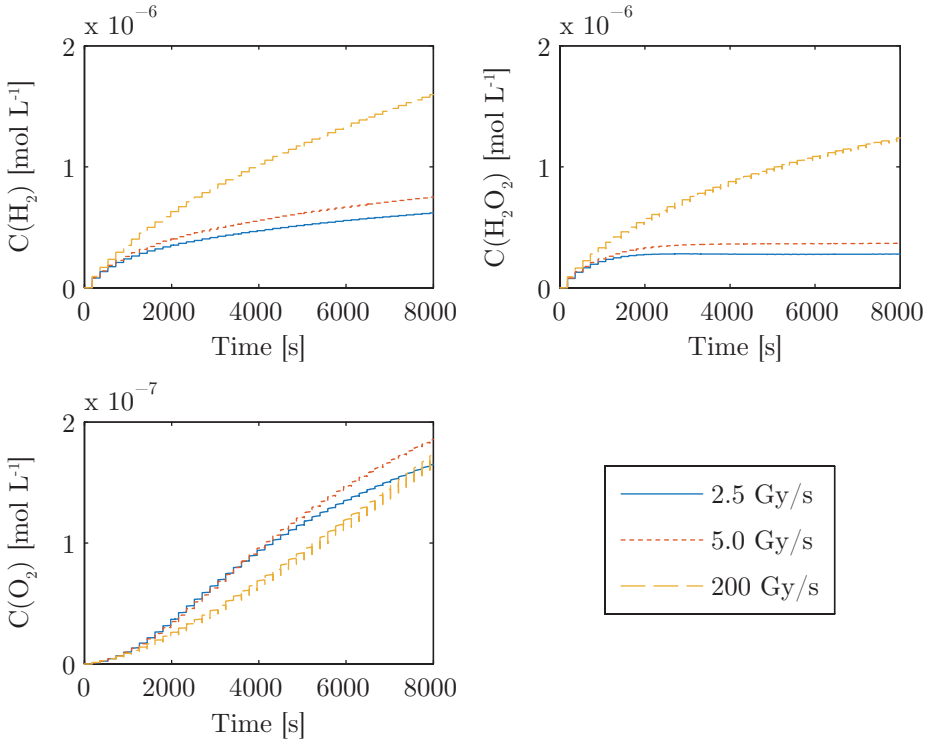

Figure 3.5 – Calculation of radiolysis at a LET of $0.2\,\mathrm{eV\,nm^{-1}}$ (^{60}Co) at very high dose rates. The time structure is the same as in figure 3.4. At a time of 8000 s, the accumulated dose is 44 Gy.

Figure 3.5 shows a calculation of low LET ($0.2\,\mathrm{eV\,nm^{-1}}$) radiolysis at very high dose rates. The time structure is the same as in figures 3.3 and 3.4. Although the equilibrium concentration of H_2O_2 varies as the square root of the dose rate, most of the dynamics over time is determined by the production of O_2. Even at very high dose rates the system approaches an equilibrium, although it takes a very long time. On the time scale of the figure, the concentration of O_2 for the dose rate of $2.5\,\mathrm{Gy\,s^{-1}}$ is just beginning to level off.

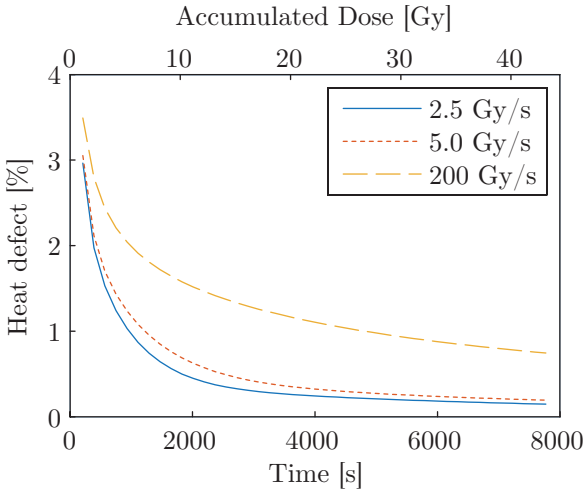

Figure 3.6 – Calculated chemical heat defect at a LET of $0.2\,\mathrm{eV\,nm^{-1}}$ (^{60}Co) at very high dose rates. The concentrations of the chemical species are shown in figure 3.5.

Figure 3.6 shows the calculated heat defects that correspond to the calculated concentrations in figure 3.5. The heat defect does approach zero as the radiolysis approaches equilibrium, however, even after a time of 8000 s the heat defect is not negligible. While the curves for the heat defect definitely level off, they do not quite reach a low value of the heat defect, showing that much larger pre-irradiation doses are required.

Figure 3.7 shows the needed pre-irradiation dose to bring down the chemical heat defect to negligible levels ($< 0.01\,\%$) for ^{60}Co irradiations. The data in the figure span a dose-rate range from $1\,\mathrm{Gy\,min^{-1}}$ to $200\,\mathrm{Gy\,s^{-1}}$. The plot shows the result for pure deaerated water and also shows results for two levels of oxygen contamination, which are described in the next section. For pure water there is a low dose rate region up to about $1.4\,\mathrm{Gy\,min^{-1}}$ where the required pre-irradiation dose is less than 7 Gy. Above this dose rate the required pre-irradiation dose jumps to 93 Gy and then continues to climb to 589 Gy at a dose rate of $200\,\mathrm{Gy\,s^{-1}}$.

It is clear that assuming the heat defect to be zero for high dose rate beams requires fairly large pre-irradiation doses. For pencil beam scanning in pure deaerated water, the highest instantaneous dose rates could require up to 0.6 kGy of pre-dose, and some margin should be applied to the doses calculated here mainly because the water purity which is actually obtained inside the high purity cell is generally not known. The effects of contamination are explored in the next section.

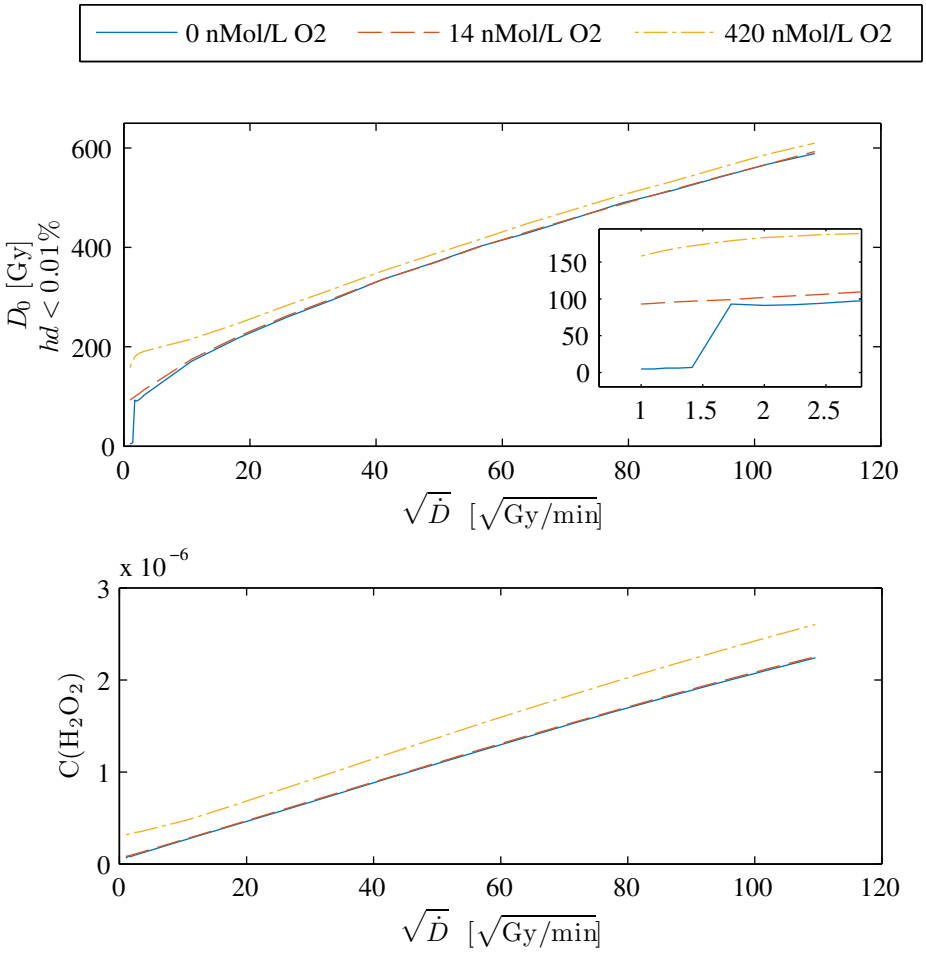

Figure 3.7 – Calculation of the chemical heat defect at a LET of $0.2\,\text{eV}\,\text{nm}^{-1}$ (^{60}Co) for irradiations over a range of dose rates. Top pane: Required pre-irradiation dose D_0 needed to achieve a heat defect lower than 0.01 %. Bottom pane: concentration of H_2O_2 at the time a heat defect lower than 0.01 % is reached. The time structure of the irradiation is the same as in figure 3.4. The graphs show calculations for initially pure water which yields the lowest concentrations of H_2O_2 and D_0 as well as calculations for pure water containing initial contaminations of $14\,\text{nmol}\,\text{L}^{-1}$ and $420\,\text{nmol}\,\text{L}^{-1}$ of O_2.

3.4.2 Oxygen and organic impurities

One of the issues with the predictions of radiolysis of 'pure' water is that impurities can have very large effects, since the small amount of radicals created by the beam can be effectively scavenged by a very small amount of impurities in the bulk. Water purity for radiolysis experiments and indeed also water calorimetry is

always a challenge. Traditionally, water purity is measured in terms of its ionic conductivity, however generally it is mostly the organic impurities that scavenge the radicals. In the context of radiolysis studies with pure water, Allen describes the — seemingly — overly careful preparation of pure water[82]:

> "Pure water is obtained at Brookhaven by redistilling ordinary distilled water first from an acid dichromate solution, then from alkaline permanganate, and finally with no added reagent into a fused silica container. Each distillation is done through a column packed with glass helices; at the top of the column, a short section is heated externally to break the film of water on the inside of the column and prevent impurities from creeping over by capillarity. The distilled water feed is brought in through tubes that contain only metal and glass ; the water must not come in contact with rubber or plastic. The stills are protected from dust or vapors in the outside air by tubes of activated charcoal. Each of these precautions was found by experience to be necessary."

The sensitivity of radiolysis to scavenging by impurities raises the question whether purified water is suitable at all for water calorimetry. In practice though, at the low dose rates used with ^{60}Co irradiations, a preirradiation dose of 20 Gy to 200 Gy on moderately carefully prepared water is enough to render the measured calorimetric result stable[49, 46] and predictable in terms of the effects of dissolved gases. Effectively, the radiation itself is used to 'burn' the (organic) impurities and traces of oxygen, which is quite desirable since it also establishes the correct limiting values of radiolysis products in the water. It has not been shown that this produces satisfactory results when impurities are combined with high LET and high dose rates. Any one of these three factors can lead to net radiolysis and it is not at all evident that the results obtained for ^{60}Co (stable calorimetry after less than 200 Gy) carry over to irradiations with protons or other ions. The calculations presented hereafter show that this is in fact not the case.

3.4.2.1 Estimation of impurity levels

The calculations for pure water are not very relevant in practice, because of impurities which are always present. Therefore, reasonable estimates of the impurity level (i.e. order of magnitude) are needed.

Generally, it is assumed that the flushing gas is either inert (Ar or N_2) or beneficial in controlling the radiolysis (H_2), however, impurities present in those gases can be a source of a non zero heat defect. A lower bound for the effect of impurities may be determined by assuming that the impurities in the gas used to deaerate the water consist entirely of oxygen. The mole fraction solubility of oxygen in water is 2.5×10^{-5}[86]. The typical purity of laboratory grade gas is 10 PPM. If oxygen is the only impurity, the final concentration of oxygen in the water will be about 14 nmol L^{-1}, based on the solubility. This may not seem much, but it

amounts to about 10 times more than is expected from radiolysis of pure deaerated water after reaching equilibrium. In reality, a large fraction of the impurities in pressurized gas cylinders consists of water, which is of no concern. However for the sake of being conservative it is assumed here that it consists of oxygen.

A further source of impurities are the organic substances already dissolved in the water. The ultra pure water used for our experiments is produced by a Millipore water purification appliance*. It continuously measures the concentration of organic impurities of the dispensed water. The reading is typically 3 PPB to 5 PPB which corresponds to $3\,\mu g\,L^{-1}$ to $5\,\mu g\,L^{-1}$ of carbon. The concentration of carbon in the solution is $250\,nmol\,L^{-1}$ to $420\,nmol\,L^{-1}$. Assuming that organic impurities have similar effects as oxygen (they scavenge OH radicals, while reactions with oxygen feed on H/OH via R15), the reverse-reaction chain of R15/R10 would be slowed down, mimicking the effects of high LET or high dose rate. For the sake of simplicity, in the following calculations it is assumed that organic impurities can be replaced with equal amounts of oxygen.

3.4.2.2 Impurities in high dose rate beams

Figure 3.7 shows the pre-irradiation dose needed to reach a chemical heat defect below 0.01 % (which could be considered negligible) as a function of dose rate for various levels of oxygen contamination. Conventional ^{60}Co calorimetry supposedly operates in the low dose rate region, where in the case of zero contamination only a few Gy of dose is necessary to achieve a negligible heat defect. The inevitable slightest impurity will raise the required pre-irradiation dose to somewhere in the range of 100–200 Gy. This is also seen in practice where in the case of a significant endothermicity resulting from the use of 'pure' water, the required dose to establish equilibrium is about 100 Gy[46, 49]. A calculation for a more realistic impurity level assuming a concentration of $420\,nmol\,L^{-1}$ shows that the needed pre irradiation dose for dose rates less than $1\,Gy\,min^{-1}$ may be on the order of a few hundred Gy. This is likely largely covered by calorimetry protocols which already assume that some extra dose margin is needed to take care of the impurities and is also covered by the uncertainty assigned to the chemical heat defect. The effect of impurities does appear to diminish at extremely low dose rates, however dose rates much lower than $1\,Gy\,min^{-1}$ are not very relevant for primary standards. At low to medium dose rates oxygen impurities have very similar effect as the dose rate itself in that it causes a high concentration equilibrium. Higher concentrations of impurities further extend the required pre-irradiation dose by as much as a factor of two. At high dose rates the chemical effects are dominated by the effect of the dose rate and impurities have a comparably smaller effect. At low dose rates the impurity level is dominant, which means that in practice about 400 Gy of pre-irradiation dose would be necessary to be on the safe side. At high dose rates a minimum of 610 Gy is predicted by the model.

* Milli-Q Advantage A10, manufactured by Merck Millipore, Merck KGaA, Germany.

3.4.2.3 Time dependence

One issue with the previous description of the dose rate and impurity effects is that it does not reveal the effects related to the duration of the irradiation itself, which was varied together with the dose rate. The chemical effects are mostly related to the amount of dose, however some of the reaction channels which are opened up by the larger amount of oxygen (due to impurities or generated due to radiolysis) have longer time constants. The time dependence exists because during the time that the beam is on a large amount of O_2^- is generated from the molecular O_2 in the solution. The O_2^- is generated by interaction with radicals, for example:

$$\text{R5:} \qquad e^-(aq) + O_2 \longrightarrow O_2^- \tag{3.34}$$

The formation of O_2^- is triggered by high levels of O_2 (which occur at high dose rates, high LET or with impurities) and because it feeds on the radicals this process is also dependent on dose rate. While the beam is on the concentration of O_2^- is limited by reactions with radicals:

$$\text{R6:} \quad e^-(aq) + O_2^- + (H_2O) \longrightarrow OH^- + HO_2^- \tag{3.35}$$

$$\text{R13:} \quad H + O_2^- \longrightarrow HO_2^- \tag{3.36}$$

$$\text{R13:} \quad OH + O_2^- \longrightarrow O_2 + OH^- \tag{3.37}$$

The radical reactions are typically very fast and the equilibrium sets in very quickly. When the beam is turned off however, these reactions are cut off and a significant amount of O_2^- is stuck in a set of very stiffly coupled equilibrium reactions:

$$\text{R35:} \quad HO_2 \longrightarrow H^+ + O_2^- \tag{3.38}$$

$$\text{R36:} \quad H^+ + O_2^- \longrightarrow HO_2 \tag{3.39}$$

$$\text{R37:} \quad OH^- + HO_2 \longrightarrow O_2^- + H_2O \tag{3.40}$$

$$\text{R38:} \quad O_2^- + H_2O \longrightarrow OH^- + HO_2 \tag{3.41}$$

The sink for this set of reactions is a reaction involving both O_2^- and HO_2:

$$\text{R20:} \quad O_2^- + HO_2 + (H_2O) \longrightarrow H_2O_2 + O_2 + OH^- \tag{3.42}$$

This reaction is not driven by radicals and instead can only feed on the products that become available from the equilibrium reactions above. After the beam is turned off there is a quasi-exponential decay of the O_2^- concentration, with a time constant of about 190 s according to the simulations. Because the time constant is comparable to the repetition time of the irradiations, the exact timing of the irradiations becomes important.

Figure 3.8 shows differences between irradiation schemes where the duration of the irradiations is fixed and schemes where the dose per irradiation is fixed. The constant duration schemes are shown only for dose rates above $1\,\mathrm{Gy\,s^{-1}}$. Of course,

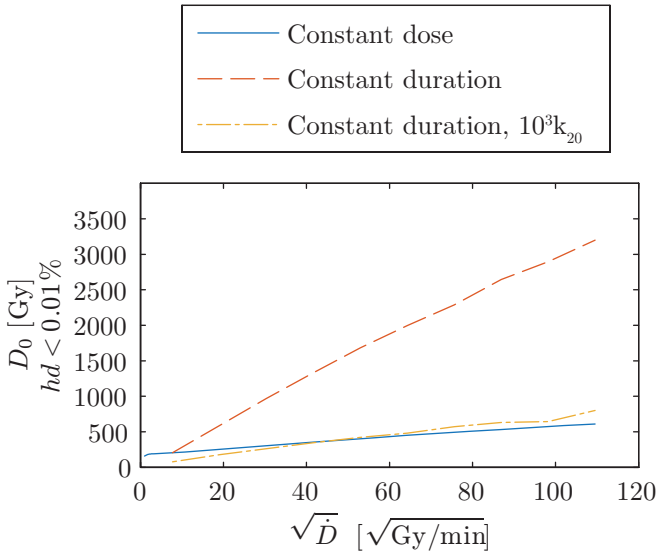

Figure 3.8 – Calculation of the chemical heat defect for ^{60}Co irradiations over a range of dose rates, for an oxygen impurity concentration of 420 nmol L^{-1}. Shown are curves for two different time structures. One is an irradiation scheme where the time per irradiation is fixed at 1 s and for comparison another curve shows the results when the dose per irradiation is fixed at 1 Gy, which is the same curve as shown in figure 3.7. Additionally, the graph shows the constant-duration simulation with a modified value of the reaction constant k_{20}, which was increased by a factor of thousand.

at the highest dose rate of 200 Gy s^{-1} the dose per irradiation is not clinically relevant. Nevertheless, the graph does show that there is a huge effect if the high dose rates are sustained for a relatively long time of 1 s. If, on the other hand, the reaction speed of reaction R20 is increased in the calculation by a factor of thousand, the result becomes similar to the constant dose irradiation scheme, and the required minimum pre-irradiation dose is much reduced. The plot does show some signs of numerical instability and effects due to the granularity of the very large single dose deposits at the highest dose rates.

It should be pointed out that figures such as figure 3.7 and 3.8 were calculated based on the assumption that there are little or no chemistry effects a few seconds after the beam is turned off, and the line fitting procedure described in section 2.8.2 was not used. Realistic simulations would have to include this time dependence as well by calculating the chemically induced temperature deviation at each point in time and performing the line fits. One might wonder whether confidence in such procedures is warranted given the complexity of the chemical dynamics.

3.4.2.4 Feasibility of very high dose rate calorimetry

Although the average dose rate for clinically relevant beams is much lower than the peak instantaneous dose rates, it appears on the basis of the simulations described in the previous sections to be sensible to perform a pre-irradiation of at least 600 Gy, which according to the model should render the heat defect negligible. Whether this is realistic from a practical point of view is another matter.

In order to achieve equilibrium, the pre-irradiations should have the same (or very similar) time structure and spatial structure as the actual calorimeter runs. While it is possible to perform a continuous irradiation in order to arrive at the required pre-irradiation dose more quickly, one issue is that it is still required to calculate the heat defect associated with the change in time structure such that to some extent one still relies on the accuracy of the radiochemistry model. In addition, there is a clear benefit in monitoring the results of the first few irradiations because the initial variation in thermal response is an indicator of water purity. Continuous irradiation will not provide orders of magnitude of speed-up and given the additional complexities of such a procedure this approach is to be avoided.

Since a typical clinical irradiation involves dose fractions of a few Gy which may take a few minutes, the time needed to perform a pre-irradiation could be half a day. In addition, even if the radiochemistry is stable in the sense that there is no variation in concentration at equivalent points during the irradiation cycle, there might still be an effect related to chemical reactions which occurs even after the beam is turned off. Those reactions result in a transient heat signal, which changes the shapes of the temperature curves which are used in the fitting procedure described in section 2.8.2. Since the slope of those linear fits directly alter the determined dose, chemistry effects can give rise to a systematic error even though the chemical concentrations have not changed after one complete irradiation cycle. Although the chemistry model does compute the transient heat signal, the linear fitting procedure is not actually applied in the subsequent analysis, but only equivalent points in the irradiation cycle are compared. If large chemical transients are present they may cause a significant 'chemical' contribution to the systematic measurement error and more detailed modelling is called for. It should be noted however that this puts tighter requirements on the model, since reactions whose speeds were not critical at first suddenly enter into the measurement error.

3.4.3 High LET

The effect of LET on radiolysis in the context of water calorimetry has been examined experimentally[69, 87, 68, 67], by comparison of water calorimetry to ionometry and total absorption calorimetry. Sassowsky and Pedroni[51] explicitly raised the issue of the effect of high LET at the end of the proton range on the chemical heat defect. The effect of high LET is also studied extensively in the realm of nuclear reactor radiochemistry. Pastina et al. [88] show experiments on water decomposition in high LET radiation due to the ^{10}B(n,α) reaction, which generates

^{7}Li and ^{4}He ions at a very high LET of 203 keV µm^{-1}. Already in 1965 Hart et al. [83] described similar experiments using the same nuclear reaction and regarding net water decompositon they clearly showed the existence of LET threshold effects. In another paper by Pastina[89] experiments examining the effects of high LET radiation on the radiolysis of water with added H_2O_2 are described.

Net radiolysis comes about because of the relative increase of molecular radiolysis products produced in the track and the relative decrease of radicals escaping the track. Because the radical yield is significantly reduced, the reverse chain reaction becomes slower:

$$\text{R15:} \quad \mathrm{OH} + \mathrm{H_2} \longrightarrow \mathrm{H} + \mathrm{H_2O} \tag{3.43}$$

$$\text{R10:} \quad \mathrm{H} + \mathrm{H_2O_2} \longrightarrow \mathrm{OH} + \mathrm{H_2O} \tag{3.44}$$

The chain is slowed down at high LET because the yield of OH decreases significantly, while the yield of H_2 increases only slightly. At the same time the primary yield of H_2O_2 also increases slightly and the chain reaction is unable to keep up with the production of H_2O_2, which enables reaction R16:

$$\text{R16:} \ \mathrm{OH} + \mathrm{H_2O_2} \longrightarrow \mathrm{HO_2} + \mathrm{H_2O} \tag{3.45}$$

The effects of high LET radiolysis are similar to the effects of high dose rates because the chain reaction efficiency is greatly reduced, leading to the production of oxygen which further complicates the situation. In contrast with the situation at high dose rates however, for very high LET there is no stable radiolysis equilibrium[82], because the primary yield of the radicals is reduced to such a level that it can never catch up with the molecular radiolysis yields. The LET of a proton beam however is such that for clinically relevant dose rates a stable chemical equilibrium can be achieved, although as shown in this section, it takes a very large pre-irradiation dose.

Figure 3.9 shows calculations using the radiolysis yields $g(E)$ as calculated using equation A.26, at a dose rate of 1 Gy min^{-1}. At lower energies the higher LET causes a steady decomposition of the water and a significant heat defect of the order of half a percent. The heat defect does not become zero within any reasonable time, except for the higher energy. The last 1 cm to 2 cm of the proton track is characterised by a significant heat defect due to radiolysis, which can not be 'cured' by providing a sufficient pre-irradiation dose. The simulated dose rate of 1 Gy min^{-1} is quite optimistic as well, since pencil beam scanning systems can reach instantaneous dose rates of several Gy s^{-1}. While LET-induced radiolysis is not necessarily an issue for most of the proton range, it does become an issue if the distal edge is in any way close to the measurement point, or if the position of the distal edge is within the high purity cell (glass vessel) of the calorimeter.

Figure 3.10 shows the required pre-irradiation dose to reach a heat defect lower than 0.01 % as a function of dose rate for a number of proton energies in deaerated water with a residual oxygen impurity level of 420 nmol L^{-1}. At lower energies

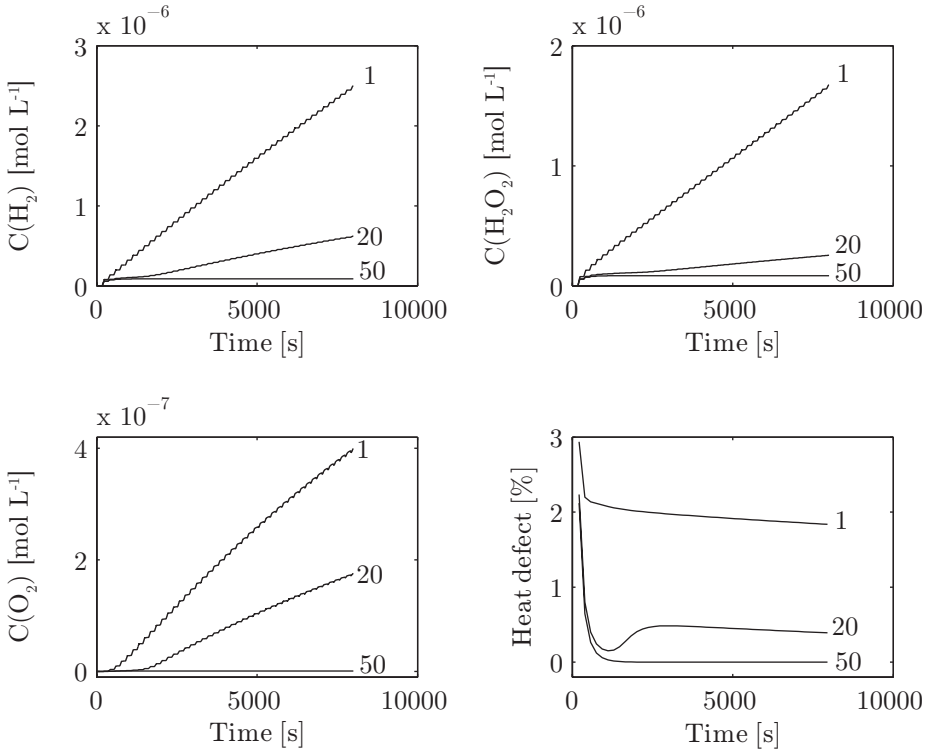

Figure 3.9 – Calculation of radiolysis at proton energies of 1 MeV, 20 MeV and 50 MeV in pure deaerated water, with a dose rate of 1 Gy min^{-1}. The numerals next to the graphs represent the proton energy in MeV. These graphs are similar to those obtained by Sassowsky and Pedroni[51], except that primary radiolysis yields according to equation A.26 were used instead of yields depending on the track-averaged LET. Also shown is the heat defect in these situations.

the threshold below which only small pre-irradiation doses are required sinks to lower dose rates and the required pre-irradiation dose above this dose rate increases dramatically. Impurities have a comparatively small effect in these cases because the concentrations of radiolysis species produced by the high LET radiation become much larger than the concentration of the impurities. Pre-irradiation doses should be a couple of kGy even at low dose rates, because the low dose rate window is shut for all practical purposes. Figure 3.10 suggests a minimum pre-irradiation dose of about 1 kGy, however one has to keep some margin due to uncertainties related to the chemistry model. It might appear that water calorimetry could be stable even at high dose rates and at high LET because the heat defect does go down to 0.01 %, however the required pre-irradiation dose is very prohibitive, because in principle it would have to be supplied by the same clinical beam quality or at least by a beam with very similar LET and dose rate. In theory it is possible to

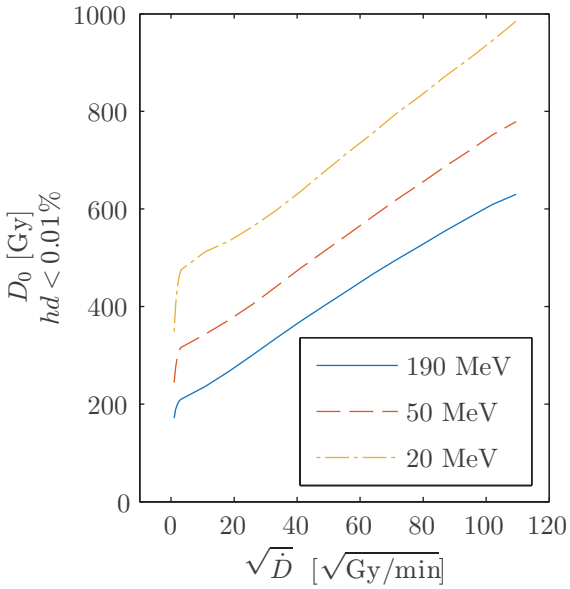

Figure 3.10 – Calculation of radiolysis at various proton energies in deaerated water containing an oxygen impurity level of 420 nmol L^{-1}, with varying dose rates. Displayed is the pre-irradiation dose needed to achieve a chemical heat defect lower than 0.01 %. The irradiation sequence is the same as the sequence which was used to create figure 3.7.

expedite the radiolysis stabilization at high LET by doing a pre-irradiation at low LET, however, this would require an enormous dose rate. Apart from all sorts of practical issues one might wonder if the radiochemistry models apply at all at these high dose rates.

3.4.4 Implications for water calorimetry regarding robustness

Considering radiolysis in calorimeters, the curves for the dose rate dependence suggest that in the case of pure deaerated water one operates in the realm of non negligible systematics. The only exception is perhaps the very low dose rates (1 Gy min^{-1} or less) such as commonly in use in primary standards labs. Robustness is typically provided in such cases by the careful cleaning procedures and analysis of the relative heat in the first few Gy of dose. Higher dose rates require a few hundred Gy to reach a negligible heat defect of 0.01 %. Before the chemistry stabilizes, the uncertainties of the radiolysis yields and the chemistry calculation would determine the uncertainty of the heat defect correction. Given the complexity of the calculation, it is hard to assign an uncertainty to the calorimetric result in this case. In practice the quality of the water preparation may also have an effect on the heat defect. After the chemistry has stabilized there is still an uncertainty

related to both the calculation and the quality of the water preparation because the onset of the negligible uncertainty might not be predicted correctly or it might not be reproducible. Because the return of the thermal response back towards a zero heat defect is quite slow, small errors could translate into large changes in the required pre-irradiation dose. These doses are quite significant even in the best possible scenario (pure deaerated water at low LET). Impurities also greatly increase the required dose and high LET irradiations can increase that dose by an order of magnitude. Considering all this, the usage of dose rates above about $1\,\mathrm{Gy\,min^{-1}}$ is not recommended for deaerated water.

3.5 Hydrogen stabilization

It might appear from the previous sections that calorimetry in clinical proton beams is a hopeless endeavour because of the radiolysis issues. However, as pointed out by Sassowsky and Pedroni[51], the situation can be resolved by deliberately adding H_2 to the water, which their calculations show could stabilize the radiochemistry at high LET. The stabilizing effect of hydrogen is well known from nuclear reactor research[77, 89]. Hart et al.[83] showed that LET threshold effects exist for the net decomposition of water and also showed that addition of hydrogen shifted the threshold towards much higher LET. There is a LET and dose rate dependent 'critical hydrogen concentration'[90, 91], above which net radiolysis is prevented [92, 88]. The critical hydrogen concentration is also being researched for supercritical water (regarding the phase of the fluid) reactors[93], although the reaction constants are radically different due to the supercritical conditions.

If the hydrogen concentration in the high purity cell is increased beyond the critical concentration, the concentrations of the radiolysis products should stabilize and the final concentrations will become smaller, reducing dependencies on changes in dose rate and LET.

$$\mathrm{H_2O} \xleftarrow[\uparrow g(E)]{\substack{\text{Radicals,}\\ \text{Excess } \mathrm{H_2}}} \begin{cases} \mathrm{H_2} \\ \mathrm{O_2} \\ \mathrm{H_2O_2} \end{cases} \tag{3.46}$$

As shown schematically in equation 3.46 the effect of adding excess H_2 is to shift the dynamic equilibrium towards reformation of radiolysis products into water. In section 3.3.3 it was shown that the presence of O_2 and H_2O_2 promotes net radiolysis rather than inhibiting it, but via the catalytic mechanism described in section 3.3.4 an excess amount of H_2 can effectively suppress radiolysis. It should be pointed out that although H_2 is consumed in the reverse reactions, stoichiometry dictates that the same amount is produced in the direct action of the charged particle.

When a significant quantity of H_2 is added, the dynamic equilibrium still exists, however the increased levels of H_2 greatly speeds up the reverse reactions, thus lowering the final concentrations of the radiolysis species. Because the reaction is much faster, it is more robust against effects of impurities, dose rate and LET. The final concentrations of the radiolysis species are reduced by orders of magnitude which means that the variation of the concentration with LET and dose rate (which, as discussed above, is expected to cause problems for clinical proton beams on deaerated water) is reduced as well.

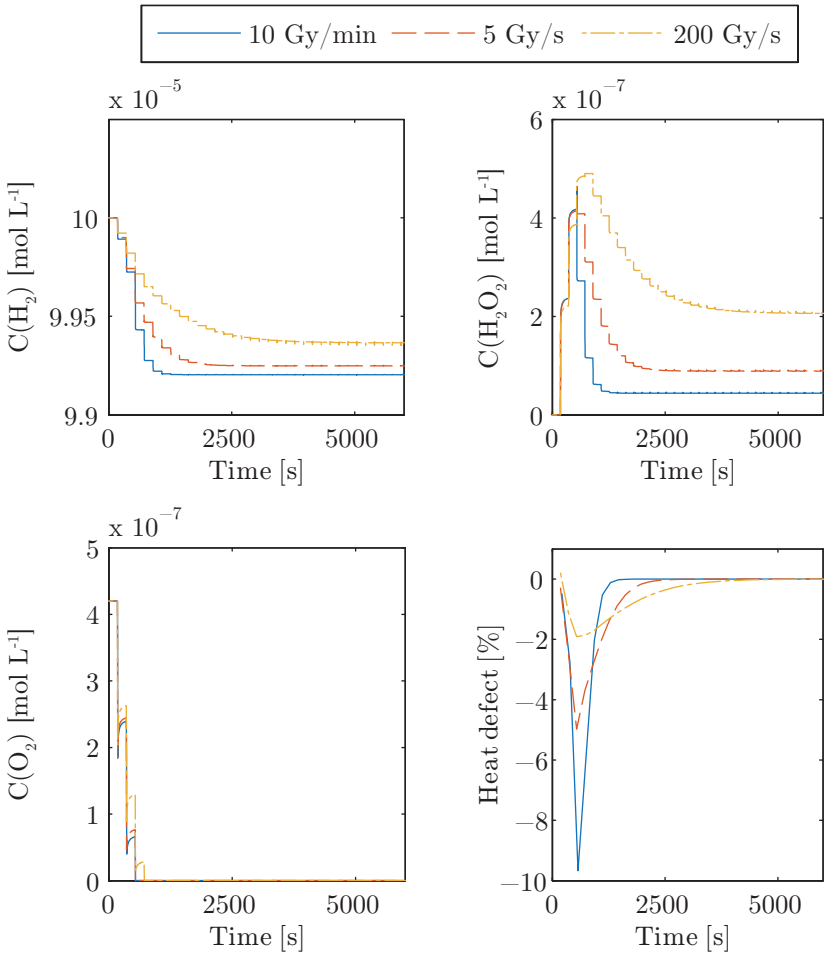

Figure 3.11 – Calculation of high LET radiolysis at a proton energy of 20 MeV in pure water containing 420 nmol L^{-1} of O_2 (assuming the role of impurity), at three dose rates. The water also contains H_2 at a concentration of 100 µmol L^{-1}. Calculated are series of discrete irradiations with each irradiation delivering a dose of 1 Gy. The irradiations are repeated every 180 s.

Figure 3.11 shows a calculation of radiolysis which could be considered a 'worst case scenario'. Calculated is irradiation at a proton energy of 20 MeV with water containing 420 nmol L^{-1} of O_2. The dose rates used are 10 Gy min^{-1}, 5 Gy s^{-1} and 200 Gy s^{-1}. Additionally an initial concentration of 100 µmol L^{-1} was set for H_2. From the previous sections it is clear that, normally, the high level of O_2 impurities combined with high LET and high dose rate should cause large endothermic heat defects which fade away only after many hundreds of Grays of dose. Figure 3.11 however shows that the small amount of H_2 added to the water quickly stabilizes the radiochemistry by removing the oxygen from the system. Sassowsky and Pedroni calculated that 1 µmol L^{-1} of added H_2 was sufficient[51] to counter the effects of high LET radiation. For the calculations presented here a little extra H_2 was needed because these calculations additionally include the effects of impurities and dose rate, and include very short irradiations at very high dose rates. To effectively speed up the reverse reactions about 7 µmol L^{-1} of added H_2 is needed for a dose rate of 5 Gy s^{-1}, while at 200 Gy s^{-1} an initial concentration of 10 µmol L^{-1} of H_2 is needed to prevent the H_2O_2 concentration from growing even after all O_2 has been removed. The graphs shows calculations for a concentration of 100 µmol L^{-1} of H_2 which causes the H_2O_2 concentration to drop significantly after the O_2 destruction phase. The pre-irradiation dose to reach a negligible heat defect in this case is 28 Gy, which is close to the value that is obtained with full H_2 saturation. At room temperature the mole fraction solubility of H_2 in water is 1.455×10^{-5}[86]. This corresponds to a H_2 saturation concentration of 808 µmol L^{-1}, which means that in practice the scavenging capacity for OH radicals can be made an order of magnitude larger than the minimum required to achieve a negligible heat defect.

It should be pointed out that although adding H_2 will speed up the reaction forming the start of the chain reaction which destroys H_2O_2, it only speeds up that reaction relative to other reactions competing for the OH radical. Ultimately, if there is an excess amount of H_2, the rate at which O_2 is destroyed is determined by the product of the dose rate and the radical yields.

3.5.1 Organic impurities

A remaining question is what happens in the radiolysis of aqueous solutions of organic contaminants in the presence of excess H_2. In the previous sections it was assumed that the organic contaminants would behave similarly to oxygen because similarly to oxygen these organic impurities would react with the radicals such that the reverse reaction chain is inhibited, which leads to the production of comparable amounts of H_2O_2 and O_2. It is clear that an excess of H_2 can cure the imbalance in the pure water chemistry caused by scavenging of radicals by the organic impurities. However, the reactions with the organic impurities themselves also contribute to the chemical heat defect directly. It appears reasonable to assume that the bulk of the organic impurities which are left in the water after purification and cleaning of the high purity cell consist of organics with hydroxy groups (alcohols) due to their high solubility in water. Various reactions involving alcohols are listed in the book

by Allen[82]. Without an excess of H_2, alcohols are converted into organic radicals by abstraction of an H-atom by the OH radicals. Further reactions with OH, O_2 or H_2O_2 then yield aldehydes and ultimately CO_2. All of these steps are dependent on oxygen atoms, supplied via OH, O_2 and H_2O_2. An excess of H_2 however will remove these species from the water. The rate constants for reactions of alcohols with H and OH are listed in a compilation by Buxton[94], in the case of methanol the rate constant with the OH radical is $9.7 \times 10^8\,\mathrm{L\,mol^{-1}\,s^{-1}}$ while the rate constant for H is $2.6 \times 10^6\,\mathrm{L\,mol^{-1}\,s^{-1}}$. At a dose rate of $1\,\mathrm{Gy\,min^{-1}}$ with excess H_2, the radiolysis model predicts a steady state concentration of $1.2\,\mathrm{nmol\,L^{-1}}$ for H during irradiation, which implies a time constant for the destruction of methanol of $3.2 \times 10^2\,\mathrm{s}$. Given the long time constant, caution is in order.

Whether this results in an appreciable heat defect can not be concluded from the calculations presented here. However, Klassen and Ross[49] noted that the spurious excess heat often observed at the beginning of a calorimetry session is likely due to reactions with the OH radical and that such spurious heat was not observed in systems having a scavenger for OH radicals (such as H_2, although perhaps the initial spurious heat in their system may have been too low to be detected). They also note that the largest discrepancies between calculations and experiments exist for aqueous systems which did not contain a OH scavenger. It appears then that an excess amount of H_2 may prevent such impurities from reacting at all, or at least it causes them to react very slowly. Krauss and Kramer report on the routine use of H_2 saturation at PTB for ^{60}Co beams and show that no detectable change in response is detected up till very high accumulated doses[81]. Krauss did find a small (but barely statistically relevant) difference between saturation with H_2 and N_2[28]. Calculations which assume that N_2 is inert predict that both chemical systems should yield a zero heat defect. The observed discrepancy was used by Krauss as a basis for assigning the uncertainty due to radiolysis of H_2 saturated calorimetry at 0.14 %. It is tempting to attribute such observed differences to the effect of organic impurities, which react in the N_2 system due to the lack of an OH scavenger. Anyway, until the effect of organic impurities is experimentally resolved, the uncertainty due to radiolysis in proton beams should have at least the same value as the uncertainty in ^{60}Co beams. Unlike the situation for ^{60}Co however, the uncertainty for proton beams can not be derived from experimental differences between saturation gasses, because modelling predicts that in high dose rate and high LET proton beams without H_2 situation very large pre-irradiation doses are needed. It is not likely that there is a confounding effect of organic impurities on the behaviour of high LET H_2 systems, because the impurities would have to compete for the OH radical with the very large amount of H_2. The hydrogen largely inhibits the reaction of OH with the organic contaminants, which is also the cause of the relatively large time constants of the organic reactions.

3.5.2 Minimum pre-irradiation doses

The results presented in the previous sections force a choice. Either one deliberately admits the reactive species H_2 into the water while having confidence in the prediction that the heat defect will become zero very quickly, or one uses an inert gas and also has confidence (in an absolute quantitative sense) in the model and the water quality. The previous sections clearly advocate the use of H_2 saturation. In the remainder of this section, the detriment of using an inert saturation gas as opposed to H_2 will be explored, as well as the question whether accepting a somewhat larger residual heat defect can be beneficial given a limited amount of beam time.

Figure 3.12 shows calculations for three different situations. The $200\,\mathrm{Gy\,s^{-1}}$ irradiation at an energy of 20 MeV with $420\,\mathrm{nmol\,L^{-1}}$ of O_2 could be considered a 'worst case' situation. Additionally a somewhat milder situation is shown for a 150 MeV near-plateau irradiation at $5\,\mathrm{Gy\,s^{-1}}$ and $14\,\mathrm{nmol\,L^{-1}}$ O_2. Clearly, at very high dose rates and high impurity levels the situation does not improve significantly, since about 490 Gy is still required to reach a heat defect below 0.1 %. The medium dose rate shows a significant improvement, because a residual heat defect of 0.1 % now only requires 90 Gy of pre-irradiation dose. However, more importantly, if one uses H_2 stabilisation, the needed pre-irradiation dose is quite within reach. The figure shows the response of the high dose rate case, with added H_2.

The response in the case of H_2 stabilisation shows a marked exothermal peak, which could be used as a measure of the impurity level at the very beginning of calorimetry session. Quickly thereafter, the residual heat defect reaches a value of 0.01 % at a dose of only 24 Gy. Since the H-atoms needed for the impurity reactions is supplied by the added H_2, it is also possible to 'burn off' the impurities with gamma irradiation. However, in this case one still has to bridge the gap between the low dose rate equilibrium resulting from the gamma irradiation and the high dose rate equilibrium resulting from the proton beam. To reach a negligible heat defect of 0.01 %, the gamma pre-irradiation does not change the needed pre-irradiation dose, although higher residual heat defects are reached more quickly.

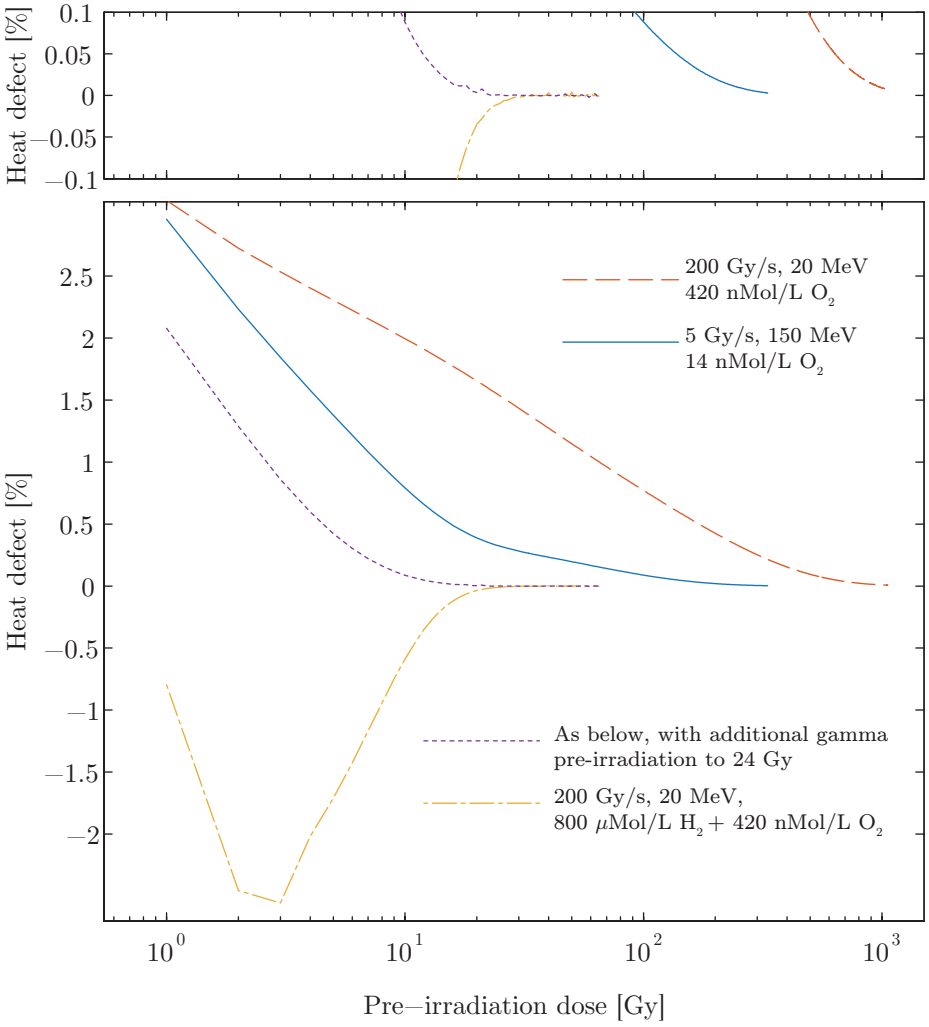

Figure 3.12 – Calculation showing the heat defect as a function of the accumulated pre-irradiation dose for a high dose rate, high impurity, high LET case, as well as a medium dose rate, medium impurity level and medium LET case. Additionally, the plot shows the effects of H_2 saturation, which is characterized by an exothermal response. Another calculation shows the situation with H_2 saturation where impurities have been previously 'burned off' in a $1\,\mathrm{Gy\,min^{-1}}$ ^{60}Co beam quality.

The curve for $150\,\mathrm{MeV}/5\,\mathrm{Gy\,s^{-1}}$ suggests that it would be possible to use deaereated water without H_2 saturation in a scanned beam, if the irradiation is in the plateau and one accepts a heat defect of 0.1 %. However, the required pre-irradiation dose in that case is significant compared to the total amount of dose that is needed to gather sufficient statistics for a calibration (200–400 Gy). In addition, the statistics prevent feedback from the measurement itself and since direct dependence on the radiochemistry model or the assumed impurity level is to be avoided, one would have to multiply the pre-irradiation dose with a coverage margin to achieve robustness.

The idea of H_2 saturation is that one not only reaches a negligible heat defect very quickly, one also races past this point at great speed such that the result of every additional irradiation thereafter becomes essentially independent from modelling details. Clinically, using H_2 is the only option.

3.6 Experiment

The radiolysis model described in the previous sections advocates the use of H_2 saturated water in calorimetry of any beam quality because of the stabilisation effect. While the radiolysis model suggests that for this system the chemical heat defect is zero it remains to be shown that the stabilisation effect can be observed experimentally in a proton beam, under conditions as similar as possible to an actual calibration experiment.

There is a whole set of reasons to perform an experiment to specifically validate the chemical heat defect modelling. The main reason is that uncertainties for the chemical heat defect for ^{60}Co are quite large and are derived from discrepancies in the observed calorimetric response [28, 30, 95] for various saturation gasses. Furthermore, there is no data on the chemical heat defect in proton beams except from total absorption experiments by Brede and Giesen[67, 69, 68]. Experimental data on the stabilisation of the radiochemistry in H_2 saturated water that confirms that the chemical heat defect is zero for proton beams in a beam quality which is also used to perform calorimetry are not available. Although it appears from nuclear reactor research that the radiochemistry can be stable even at very high LET and very high dose rate, no experiments have been performed which show that the hydrogen stabilisation effect actually occurs in practice inside a water calorimeter. It is essential to obtain experimental confirmation of the model predictions, because if the hydrogen stabilisation is not activated the system becomes more sensitive to impurities, high LET and high dose rate, which will strongly contribute to the overall uncertainty budget of the calibration standard. Finally, to rule out any systematic effects related to the practical implementation of the water calorimetry in the laboratory, tests should be done which can reveal effects of imperfect cleaning or handling of the glassware. Because in water calorimetry achieving cleanliness is notoriously difficult, it should be shown that under the actual experimental conditions stable radiolysis can be achieved.

3.6.1 Experimental technique

Because the radiolysis modelling predicts that the heat defect for H_2 saturated water is zero and because a primary standard is, after all, the only source of calibration*, the only option is to resort to internal consistency checks. The most obvious form of such a check is the stability of the measured response as a function of accumulated dose. Because non-zero heat defects are caused by changing chemical concentrations, observing a stable response would indicate that no such changes in concentrations are occurring. Nevertheless, because the models correlate non zero heat defects with changing chemical concentrations, any test that can show stability over a large range of accumulated dose would be sufficient. In an experimental irradiation facility, such experiments are difficult to perform frequently because of the rather large amount of beam time that is required to obtain a sufficiently large data set, while it is quite prohibitive in the case of a clinical facility.

The underlying mechanism of H_2 stabilisation is what causes stable radiolysis in both pure water and hydrogen saturated pure water. It is exactly this mechanism that one would like to test. Showing that the mechanism is active also proves that any inadvertently present impurities do not disturb† this mechanism with the water quality which is obtained in practice in the laboratory. It also shows that the LET of the protons and the dose rate (at least at the beam quality used in the experiment) do not adversely affect the back-conversion mechanism to the extent that it is no longer dominating.

H_2/O_2 peak system A direct test of the back conversion mechanism has been performed before for ^{60}Co by Ross, Klassen and Smith[46]. Krauss and Roos performed similar measurements, obtaining very good results[96]. In both of these tests, a small amount ($< 10\,\%$) of O_2 gas was mixed into the H_2 flow which is used to deaerate the water. The amounts were measured with flow meters. Using Henry's law and tabulated solubilities of O_2 and H_2 and assuming saturation, the concentrations in the water could be calculated. The gas mixture causes a very characteristic heat-defect signal which is of great value in validation experiments.

This type of test is very useful because it activates all of the important reactions. The mechanism is described in detail in section 3.3. Because H_2 is in excess, the production of O_2, which depends on the presence of OH, is cut off entirely. Instead, the excess H_2 causes a high concentration of H radicals which are consumed entirely by the oxygen burning reactions. This constitutes a conversion of O_2 into H_2O_2:

$$H_2 + O_2 \longrightarrow H_2O_2 \tag{3.47}$$

* A notable exception is perhaps a graphite calorimeter which could be used to measure the chemical heat defect in a direct comparison, assuming that the graphite-to-water dose conversion is known independently.

† As explained in section 3.5.1, direct reactions with impurities can still cause a heat defect.

The O_2 also efficiently scavenges the H radicals in this conversion, such that the newly formed H_2O_2 survives attack by the H radicals. The concentration of H_2O_2 will increase because of direct production by water radiolysis and because of the above mechanism. When the O_2 is almost entirely depleted, the back-conversion mechanism converts the H_2O_2 into water:

$$H_2 + H_2O_2 \longrightarrow H_2O + H_2O \tag{3.48}$$

The mechanism is important, because it is a two-step operation. The speed of the first step is limited by the production rate of radicals by the beam, which are consumed in the conversion of O_2 into H_2O_2. However, when the second phase kicks in, the H_2O_2 is catalytically converted into water because the radical intermediates are not consumed. Both steps are exothermal and show an appreciable exothermal heat defect compared to pure-water or purely-H_2-saturated radiochemistry. The last step which is catalytic in nature can show exothermal effects on the order of 100 %[96], depending on the amount of O_2 initially present in the water. After the two steps have occurred and all O_2 and H_2O_2 have been consumed, the chemical system is believed to be calorimetrically equivalent to pure deaerated water, or H_2 saturated water, because the system has entered the equilibrium phase. The appeal of using this kind of test is that the two steps needed for stability as well as the stable region itself are easily observed because of the large differences in exothermicity. The fact that the reverse reactions are dominating need not be inferred from the lack of drift in the calorimetric response. Instead, with this system, its response as a function of accumulated dose constitutes the proof that the reverse reactions are dominating.

3.6.1.1 Implementation

The measurement apparatus and related techniques have been described in chapter 2 and the high purity cell is shown in figure 2.2. After the cell was cleaned and filled with purified water, the content of the cell was bubbled with a mixture of H_2 and O_2. Solubilities for H_2 and O_2 were obtained from the book by Lide et al. [86]. The target concentration of O_2 was 76 µmol L^{-1} which is the same as used by Krauss and Roos[96], while the concentration of H_2 (about 800 µmol L^{-1}) is determined by the magnitude of the gas flow which is needed to achieve the proper partial pressure of O_2 in the mix. The flow ratio H_2/O_2 required to obtain the target concentration of O_2 was calculated by applying Henry's law while using measured values for the ambient air pressure and temperature of the water. Using Vögtlin red-y compact mass flow meters the flow rates of the gases were set to yield the required mixture such that the combined flow rate was about 200 mL min^{-1}. The flow rate was maintained for three hours, which is assumed to result in saturation. The exit valve of the high purity cell was connected to a wash bottle such that a similar concentration of O_2 would accumulate because it samples the same gas flow. The amount of H_2 in the water is not directly measured since it is not critical at all. After sealing the valves of the high purity cell, the O_2 concentration inside

the wash bottle was measured with a Hach LDO HQ10 dissolved oxygen probe, yielding a value of $2.7\,\mathrm{mg\,L^{-1}}$ ($84.3\,\mu\mathrm{mol\,L^{-1}}$). The mass flow meters are used only to roughly set the oxygen concentration in the gas mix. Finally, the cell was cooled down from room temperature to the operating temperature of the calorimeter. A small gas bubble preventing glass fracture upon cool-down was trapped in the outlet tube, which is located far from the NTC temperature probes.

A circular field with a diameter of 13 cm was used such that almost all of the cell volume was irradiated. The cell was positioned such that the probes were located at a water depth of 5 cm. The proton beam energy was 190 MeV, which results in a near-plateau irradiation at an energy of 160 MeV at the location of the thermistors. The LET of the primary protons is about $0.52\,\mathrm{eV\,nm^{-1}}$. As described in section 2.11 the beam line is first roughly calibrated in terms of dose with a Farmer ionization chamber in a polystyrene phantom. The duration of the irradiations was 60 s at a dose rate which was a little under $10\,\mathrm{Gy\,min^{-1}}$. Data from both NTC probes was averaged on a point-by-point basis and normalized to the response of the beam intensity monitors, corrected for air density.

3.6.1.2 Results

Figure 3.13 shows the result of both the radiochemistry calculation and the experiment. Three distinct regions are observed in both the experiment and in theory. The first phase of O_2 conversion is visible as a slow incline in the heat defect, while the phase of H_2O_2 destruction is visible as a large exothermal peak. Following the peak is a long region where the heat defect is stable (and according to the model, zero).

The experimental data have been normalized to the region following the large peak. That is, the experimental data is normalized to a mean value of unity in the zoomed-in region, after which the percent-difference from unity is plotted:

$$hd_i = \left(\frac{D_i}{\left\langle D_i \right\rangle_{474\,\mathrm{Gy}}^{1338\,\mathrm{Gy}}} - 1 \right) \cdot 100\,\% \tag{3.49}$$

In the above equation, the heat defect hd_i for each irradiation is derived from the measured data by assuming that the heat defect after the exothermal peak is zero.

The time at which the onset of the exothermal peak occurs depends on the shape of the depth-dose curve. Effectively, a wave of heat will sweep across the thermistors from the distal side of the high purity cell to the proximal side, because the dose accumulates faster on the distal side such that the chain reaction back conversion is activated earlier at the distal side than at the proximal side of the vessel. Krauss found that such effects were present[96] in ^{60}Co calorimetry due to the photon depth-dose curve. These additional temperature gradients and the resulting heat transfer effects are not corrected for. Having subtracted out the stable region of the experimental data and neglecting the effects of heat transfer, it

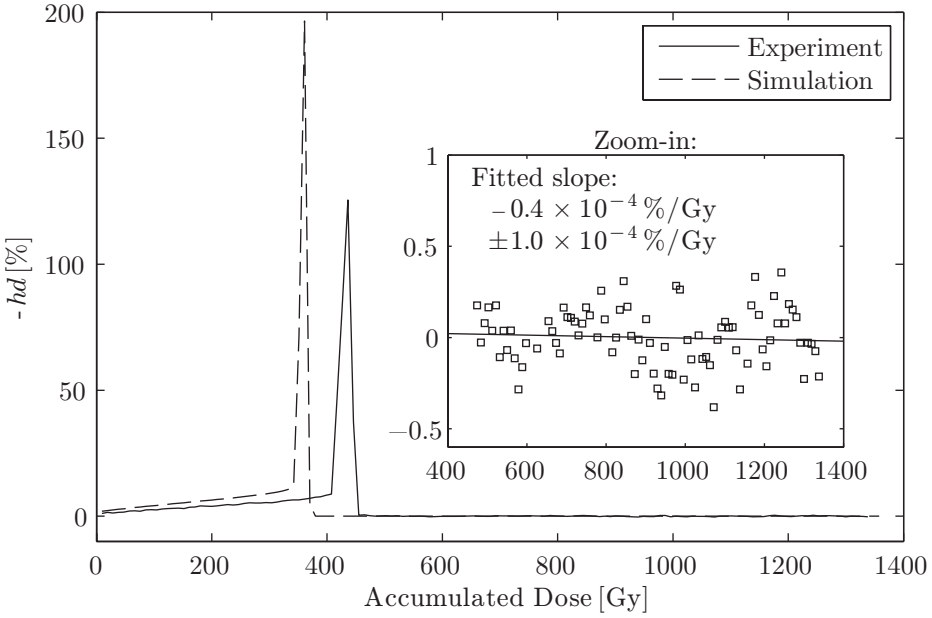

Figure 3.13 – Calculation of the heat defect and experimental results of the H_2/O_2 peak system with proton irradiation. Plotted is the measured negative heat defect $-hd$ (i.e. exothermicity) as a function of accumulated dose. The experimental data has been normalized to the data visible in the inset. The initial O_2 concentration at the beginning of the calculation is 84.3 µmol L^{-1}.

is possible to determine the amount of O_2 that was in the water from the graph in figure 3.13:

$$C(O_2) = \frac{\langle D \rangle}{\Delta H_r} \sum hd \tag{3.50}$$

where $\langle D \rangle$ is the mean dose delivered per irradiation, $\Delta H_r = -551.56\,\mathrm{kJ\,mol^{-1}}$ is the reaction enthalpy for the reaction $2\,H_2 + O_2 \longrightarrow 2\,H_2O$ and $\sum hd$ is the total chemical excess heat in the entire experiment expressed as a fraction of the energy of a single dose deposit. This calorimetrically determined amount of oxygen is $C(O_2) = 83\,\mu\mathrm{mol\,L^{-1}}$, which is within the read-out resolution error (1.9 %) of the value measured with the LDO probe (84.3 µmol L^{-1}).

A linear fit in the region after the peak indicates that the slope is $(-0.4 \pm 1.0) \times 10^{-4}\,\%\,\mathrm{Gy^{-1}}$, with statistical confidence limits of 68.27 %, meaning that the observed slope is statistically compatible with zero. The estimate for the statistical uncertainty takes into account the correlations between the samples by including a multiplicative factor of $\sqrt{2}$ as described in section 2.13. These bounds are comparable to those obtained for ^{60}Co by Krauss and Kramer[81], who quote a slope of $8 \times 10^{-5}\,\%\,\mathrm{Gy^{-1}}$ with a relative standard uncertainty of 90 %.

There is an obvious mismatch between the calculation and the experiment in that the exothermal peak occurs at a higher accumulated dose than predicted. The radiochemistry calculation when supplied with the radiolysis yields for ^{60}Co produces a peak at the same location and of similar shape as reported by Krauss[96]. One explanation might be that the concentration of O_2 is higher than assumed. However, the measurements with the LDO oxygen probe and those derived from calorimetry agree very well. Since two different measurement techniques have been used that work on the basis of different physical principles it is not likely that there is a large error in the assumed O_2 concentration. The more likely cause of the shift in peak position is an error in the assumed radiolytic radical yields (section A.4.5). An overestimate of the radical yields would overestimate the rate of conversion of O_2 into H_2O_2, such that the exothermal peak appears early in the simulation.

The experiment clearly shows that the reverse reaction chain is activated and that there is no appreciable slope following the peak. The absence of any appreciable slope indicates the absence of net chemical reactions. There is at this point no experimental data which hints at a chemical heat defect other than zero.

3.6.2 Discussion

The remaining question is what uncertainty to apply to the zero heat defect that is emergent from calculations and data. As was shown in this chapter, without H_2 saturation, the calorimeter would most likely operate in the regime of non negligible systematic errors due to a chemical heat defect, while with H_2 saturation those errors are negligible. This matter has already been discussed for ^{60}Co by Krauss and Kramer[81, 28]. The main issue was that no significant change in the model parameters could generate a heat defect any other than zero. The solution was to assign the uncertainty of the heat defect based on observed differences between H_2 and N_2 saturated water, each of which is calculated to yield a heat defect of zero. Although this might make the estimation of uncertainty of the H_2 system dependent on the practical characteristics of the N_2 system it is a sensible thing to do, since characteristics of the system which are not included in the model (such as oxygen leaking in through the vessel seals) can produce a non-zero heat defect, even with the H_2 system.

On the other hand, the effects of H_2 on radiochemistry are well known outside of the realm of the standards laboratories and it is possible to prevent water decomposition even at very high LET and very high dose rates. The models used in water calorimetry are based on the same reaction sets as those in use for nuclear reactors and it would appear reasonable to state that if it works in those situations, it should certainly work for water calorimetry. Whatever information is available suggests that water radiolysis for proton beam qualities is stable if pure water is saturated with H_2.

The only real issue appears to be the effect of impurities. Impurities (notably oxygen) might diffuse into the glass vessel through the seals, or they might leach out of the glass over time. This issue exists independently of the understanding of the

radiochemistry and might also be different for the various existing implementations of the calorimeter standards. One can say however that H_2 saturation has a huge capacity to deal with oxygen leakage as is demonstrated in our experiments as well as in the experiments by Krauss and Kramer. There is a case to perform experiments specifically to examine the effect of organic impurities. Until data becomes available which suggests that it is sensible to do otherwise, it is prudent to assign to proton calorimetry the same systematic uncertainty which was apparent from experiments with H_2 and N_2 saturated water in ^{60}Co, at a value of 0.14 %[28].

3.7 Conclusion

In this chapter the effects of radiochemistry have been examined in theory, through calculation and in experiment. It was shown how the dynamics of the radiolysis products can produce time dependent changes in chemical concentrations through various interlocking equilibrium reactions. The resulting equilibria were shown to be fragile.

By numerically solving the reactions equations it was shown that for various combinations of LET, impurities and dose rate the chemical system could be in a state where the chemical heat defect is non negligible up to high accumulated doses. In order to render the heat defect in pure deaerated water to be negligible even at the highest relevant dose rates, pre-irradiation doses of 0.6 kGy to 1.0 kGy are required, depending on the the impurity level and local LET. These dose levels are quite significant. Additionally, time dependent effects would have to be modelled as well, which increases the complexity of the model. Given the effects of high LET and high dose rate, any application of proton dose calorimetry requires the use of water that is deaereated by saturating it with hydrogen.

It was shown that by adding an excess amount of dissolved H_2 the system quickly regains a stable state in which, theoretically, the heat defect is zero. The required pre-irradiation dose depends on LET, dose rate and the impurity level, however in the worst case examined the pre-irradiation dose was reduced from 1 kGy to only 24 Gy. The general statement that the heat defect is negligible is supported by an experiment with the beam quality used for calorimetry experiments at KVI-CART, which clearly highlights the mechanism by which the steady state is achieved. Following a small pre-irradiation dose, the chemical heat defect in a H_2 system would be zero and there are no experimental results which indicate that this does not occur at the tested conditions. Uncertainties in the radiolysis yields $g(E)$ do lead to an uncertainty in the needed pre-irradiation dose to attain a negligible heat defect, but since that dose is very low it does not lead to an appreciable uncertainty. This means that the chemical heat defect in a proton beam is controlled to a level which is as good as is common for ^{60}Co calorimetry.

Chapter 4

Neutron dose

For clinical radiation therapy, the administered dose needs to be well under control because it directly determines the result of the treatment. For this reason, primary measurement standards (such as water calorimeters) are used to calibrate the dose delivery. One should be aware that any measurement is a type of comparison and that two unique measurements ('comparisons') are only absolutely compatible if they are performed under the exact same conditions. Indeed, the mere fact that a measurement device is present usually changes the value of the desired measurement. A well characterized calorimeter may give a very accurate value of the dose as it occurs in the core of the calorimeter, but this dose value may not fully apply for routine dose measurements in clinics, because those measurements depend on the use of ionization chambers without the calorimeter being present. This doesn't mean that the calorimeter gives false readings, but simply that the obtained values are not perfectly applicable for their intended use. Generally, this is always the case. But fortunately, often small numerical corrections can be applied, imparting only small uncertainties to the total uncertainty budget. Unless the ionization chambers are only used in the exact same conditions as in which they were calibrated with a calorimeter (i.e. in-the-clinic calorimetry), one should be aware that those differing conditions could have non negligible effects on the applicable calibration value of the chambers. One of the aspects of the measurement conditions that needs to be characterized is the unintended neutron dose that occurs in proton irradiations.

In this chapter the contribution of neutrons to the measured dose value in a proton beam is investigated. Water calorimeters are thought to be as sensitive to neutron dose as to proton dose. However, this is not the case for ionization chambers, which creates an issue if a chamber that has a calibration based on water calorimetry is to be used in irradiation fields with a different relative neutron contribution. Scattered beams (used in our experiments) necessarily result in an increased neutron dose due to neutrons produced in the collimators. This dose contribution due to collimator-generated neutrons is absent in pencil beam scanning

systems. For this reason, it has to be shown that ionization chambers that have been calibrated in a scattered beam can be used in scanning beams without a large increase in dose-uncertainty.

The metrological issue is first identified as being a challenge of variations in beam quality*. Experiments are presented where the neutron dose in water was measured directly with a water calorimeter as well as with an ionization chamber. Geant4 Monte Carlo models matching the experimental conditions have been made and the calculated doses are compared to the experimentally determined values. The Monte Carlo model is then used to make quantitative statements on the neutron contribution to the dose during a water calorimetry measurement with a proton beam. The effect of the neutron dose on ionization chamber calibrations is estimated using the particle spectra as calculated with the model. In addition, the neutron dose calibration for a Farmer type chamber was determined by comparison with the water calorimeter. Finally, the uncertainty contribution to the calibration of an ionization chamber due to neutron dose is estimated.

4.1 Beam qualities: scattered vs. scanned beams

From a beam quality point of view, the fundamental difference between the various proton scanned-beam techniques and scattered-beam irradiations is that scanned beams result in much lower doses due to secondary radiation generated in the beam line elements. In a scattered beam, collimators define the shape of the irradiation field. Most of the dose in the irradiated volume is caused by protons passing through the collimator opening. However, because of the secondary radiation that is generated in the beam line elements, there is an additional contribution to the dose that extends out to well beyond the edges of the dose distribution of the primary protons. This unintended extra dose is mostly due to neutrons and gammas.

Water calorimetry generally requires extensive amounts of beam time. The availability of clinical scanned beams is quite limited while obtaining beam time for scattered beams in physics institutes is more feasible. Therefore it would be very beneficial if calibrations of ionization chambers obtained through calorimetry in a scattered beam could also be used in scanned beams. The issue is that the dose-sensitivity of ionization chambers depends on the type of the radiation (particle type and energy spectrum) while the sensitivity of a calorimeter is largely independent of such aspects of the beam quality. Specifically, in the case of neutrons, the dose in water is caused mostly by proton recoils. Since the energy spectrum of those recoils is vastly different from the spectrum of the primary protons and since the

* 'Beam Quality' is often not narrowly defined, but it can be loosely understood to mean the full phase space of all ionizing radiation in the measurement geometry. It describes the properties of the beam but it does not necessarily mean an appraisal of the degree of desirability. Within specific contexts it can also refer directly to certain properties of the ionizing radiation at a specific location (for example, the residual range of protons is often used to characterise the proton energy at the point of measurement).

sensitivities of ionization chambers are energy dependent, the chamber calibration coefficient in turn is dependent on the amount of neutron contamination. Thus, regarding the secondary radiation, calorimeters may be used in both scattered and scanned beams, while in principle ionization chambers require a separate calibration in both types of beams. If an ionization chamber is only calibrated in a scattered beam against a water calorimeter, the use of that chamber in a scanned beam (or in another scattered beam with a different beam line geometry) will result in a measurement error if the original calibration value is assumed to be valid. The beam quality conversion factor which is to be used to convert a ^{60}Co calibration into a scanned proton beam calibration $k_{Q_{p\mathrm{PBS}},Q_0}$ will be different from the factor $k_{Q_{p\mathrm{SB}},Q_0}$ that is valid for a specific scattered beam. The difference will depend on the relative magnitude of the secondary radiation dose in the scattered beam. It should be noted that beam qualities such as Q_p or Q_0 generally refer to the measurement conditions and particle spectra at a specific location inside the volume of a water phantom, which is needed for build-up.

The relative intensity of the secondary radiation in scattered beams is related to the beam efficiency. The final collimator that was used for most of the experiments described in this thesis has an opening diameter of 70 mm and the beam line uses a double scatterer configuration with a homogeneous and an inhomogeneous scatter foil. In this configuration, about 9 % of all the protons that enter the beam line will make it through the opening of the collimator, while the remainder is stopped in the various collimators along the beam path. Due to nuclear interactions, neutrons and gamma rays are produced in these collimators, which cause unintended dose in any object close to the beam line. In the case of scanned proton beams the field shape is defined by the scanning action and the field collimators are absent, which means that the 'efficiency' is 100 %. In scattered beams, most of the protons never contribute to useful dose while they do produce secondary neutrons and gammas. The actual dose at the measurement position in a water phantom also depends on the distance between the collimators and the phantom and the amount of protons being stopped in each individual collimator. As such, the neutron fraction of the total dose in the phantom depends on the geometry of the beam line. Given the efficiency of a delivery system based on scattering, the total amount of neutrons produced is an order of magnitude higher compared to that of a system based on scanning. For this reason, the effect of the neutron contribution to the dose as measured in a calorimeter should be examined.

As a final remark it should be pointed out that both scanning beams and scattered beams cause neutron production in the water phantom (or in the patient in the clinic) and that this causes an (unavoidable) neutron-induced dose both inside and outside of the region of the proton dose distribution. Thus, even in scanning beams the neutron dose fraction may vary, mostly because of differences in initial energy of the beam and the field size. Although the neutron dose due to the collimators can be significant, it is not the only effect due to secondary radiation that is relevant to dosimetry. The effect of gamma rays is not examined in this thesis, because the associated ionization chamber sensitivities only differ

by a few percent from the proton dose sensitivities while the gamma ray dose is relatively small due to self-shielding effects in the collimators and the isotropic nature of their production.

4.1.1 Patient neutron dose

The order of magnitude of the metrological issue can be estimated by referring to calculations made for patient neutron doses. Published calculations[97] typically show values in units of Sv, which includes biological weighting factors which makes it difficult to deduce the local neutron dose in absolute units. A publication by Brenner and Hall[98] lists values of neutron dose in units of Gy, for various positions in a patient receiving a lung-irradiation. The highest value listed occurs in the lung, close to the irradiated part of the patient. Relative to the planned dose it amounts to 0.05 % due to neutrons originating from outside the patient. Incidentally, at that location the neutron-induced dose due to neutrons being generated inside the patient is slightly higher than the dose due to externally generated neutrons. Morávek and Bogner[99] use Monte Carlo calculations to analyse the secondary particle spectra as a function of depth for a proton pencil beam incident on water. Graphs in their paper show that the neutron-induced dose can amount to a few per mille. Moyers et al. [100] show Monte Carlo calculations of the neutron dose in a clinical scattered proton beam and comparisons with various detectors, including ionization chambers. They reported neutron physical dose values (Gy's) on the beam axis of about 0.4 % of the direct proton dose.

The relative dose sensitivity for neutron-induced dose as compared to the primary proton dose of ionization chambers that are mounted in a water phantom can be lower by a significant factor. This means that the dose error due to neglecting such effects could be on the level of about one per mille, which is not completely negligible given the uncertainty objectives for absolute dosimetry. Because the neutron-induced doses also depend on the exact beam line geometry, the neutron contributions to the dose should be evaluated in both calculations and experiments.

4.2 Neutron production and interactions

Neutrons are produced in all clinical proton therapy facilities, although the amount of neutrons produced in proximity to the patient depends on the proton kinetic energy for the treatment, as well as on the technique that is used to vary the proton energies. Tesch[101] tabulated total neutron yields of stopping protons as function of the initial energy of the protons. For a 200 MeV proton beam that is stopped in copper, the total yield is about 0.8 neutrons per incident proton.

A short description of the production processes is published in the book by Cossairt[102]. The neutron production cross-sections for proton energies below 10 MeV are characterized by the effect of the binding energies of the nucleons. However, the majority of the neutrons is produced by protons with energies much

higher than 10 MeV. Cossairt defines an energy range of 10 MeV to 200 MeV (roughly the energy range of clinical proton beams), which is characterized by evaporative neutrons for the lower energies and cascade neutrons for the higher energies. Evaporative neutrons are the result of excitation of the nucleus by a passing proton and the neutrons are emitted isotropically. Cascade neutrons are the result of direct interactions between the incident proton and the nucleons, which results in a forward-peaked emission distribution. Higher energy neutrons have a more forward-peaked angular emission distribution than the lower energy neutrons. The total neutron yield is proportional to E^2, meaning that the actual yield depends on the properties of the beam. A rule of thumb is that in a clinical proton beam at full initial energy, the number of neutrons produced in stopping the protons is of the same order of magnitude as the number of protons entering the beam line.

4.3 Neutron-induced dose measurement

Neutrons cause dose in water mainly through elastic scattering on hydrogen nuclei. The proton recoils of the p(n,n)p scattering can have any energy below the energy of the incident neutron. Since the neutrons produced by the proton beam have relatively high energies, a small fraction of the recoil protons can have energies as high as the primary proton energy, although the spectrum is dominated by recoils due to low energy neutrons. These recoil protons are charged particles which can be detected by an ionization chamber if they have sufficient energy to penetrate the chamber wall.

When placed in a water phantom, ionization chambers will have roughly equal sensitivity to the neutron-induced dose and the direct proton dose, because of the relatively high energy of the recoils. The materials used in constructing the ionization chamber need not necessarily have a high cross-section for neutron interactions if the chambers' walls are thin, because the surrounding water can provide sufficient buildup. However, in the case of low primary beam energies or in the case of thick-walled ionization chambers a wall material should be used that contains a hydrogen fraction that is comparable to water, in order to achieve equilibrium. The relative neutron dose contributions can reach several per milles and the sensitivity is expected to depend on the spectrum of the recoil protons for each individual geometry. Therefore there may be variations on the per mille level in the sensitivity of the ionization chamber to the total dose (neutron-induced dose and direct proton dose combined).

The neutron induced dose in the experimental calorimetry setup is due to neutrons originating from the collimators as well as due to neutrons created in the water phantom itself. Because of the issues mentioned in the previous sections, having an experimental estimate of the neutron-induced dose is desirable. In the context of absolute standard dosimetery, using the same measurement principle consistently in most aspects of the characterization experiments is valuable. The

water calorimeter, which in principle directly measures dose in the water volume, is particularly suitable for the measurement of neutron dose because it is first-order insensitive to variations in the neutron spectrum. The major drawback of using a water calorimeter is that the sensitivity itself is fairly low.

It is not possible to directly measure the neutron-induced dose fraction in the standard irradiation geometry with the water calorimeter because the primary proton dose is roughly three orders of magnitude larger. However, because the primary protons can be stopped, it is possible to create very similar geometries wherein the primary proton dose is absent in the calorimeter phantom, but the neutron dose still contributes to the signal. This chapter describes experiments in which the neutron-induced dose due to neutrons generated in the collimators and the water phantom is measured separately. Earlier measurements of the neutron dose in scattered beams by Moyers et al. [100] did not include calorimetry and water phantoms were not used for the ionometry. Calorimetry has been performed in low energy neutron fields with considerable less resemblance to a clinical scattered beam. Galloway et al.[103] used a 15 MeV deuterium beam on beryllium with a water calorimeter design that is much like one of the earlier designs by Domen. Brede et al. [69] used a 13.2 MeV deuterium beam on beryllium with a much more complicated calorimeter design[87]. The experiments presented in this section involve neutron fields generated by stopping a 190 MeV proton beam in brass or water. The neutrons have a mean energy of 19.2 MeV at the position of the thermistors while the majority of the energy is carried by neutrons with energies that are much higher. In comparison with the other neutron calorimetry experiments, the neutron and proton-recoil spectra are considerably harder, which means that ionization chambers will be much more sensitive to charged particles generated in the water. The close resemblance of the experimental geometries presented here to a normal water calorimetry experiment allows to obtain meaningful estimates of the effects of neutron irradiation on the calibration of the ionization chambers.

Figure 4.1 schematically shows the beam line geometries that were used in both experiments and Geant4 Monte Carlo calculations. Geometry A is the geometry for a regular calibration experiment, where the dose in the phantom is due to both primary protons and neutrons. For the other geometries, there is no dose contribution from the primary protons. The neutron-induced dose for geometry A is due to neutrons generated in the collimators as well as in water, for geometries B and C the dose will be due to the collimator neutrons only, while in geometries D and E the dose is entirely due to neutrons generated in water. An overview of the upstream section of the beam line is presented in figure 4.2.

The rationale for the described method is twofold. Firstly, although the beam line geometries in situations B, C, D and E are not exactly the same as in a regular calorimetry experiment A, one can still use the measured neutron doses as an estimate (or in some cases as an upperbound) for the neutron-induced dose. Such doses can serve as input to uncertainty estimates. Secondly, the described set of experiments can serve as a validation for a Monte Carlo calculation. The measured dose values will be sensitive to the neutron production yields in both water and

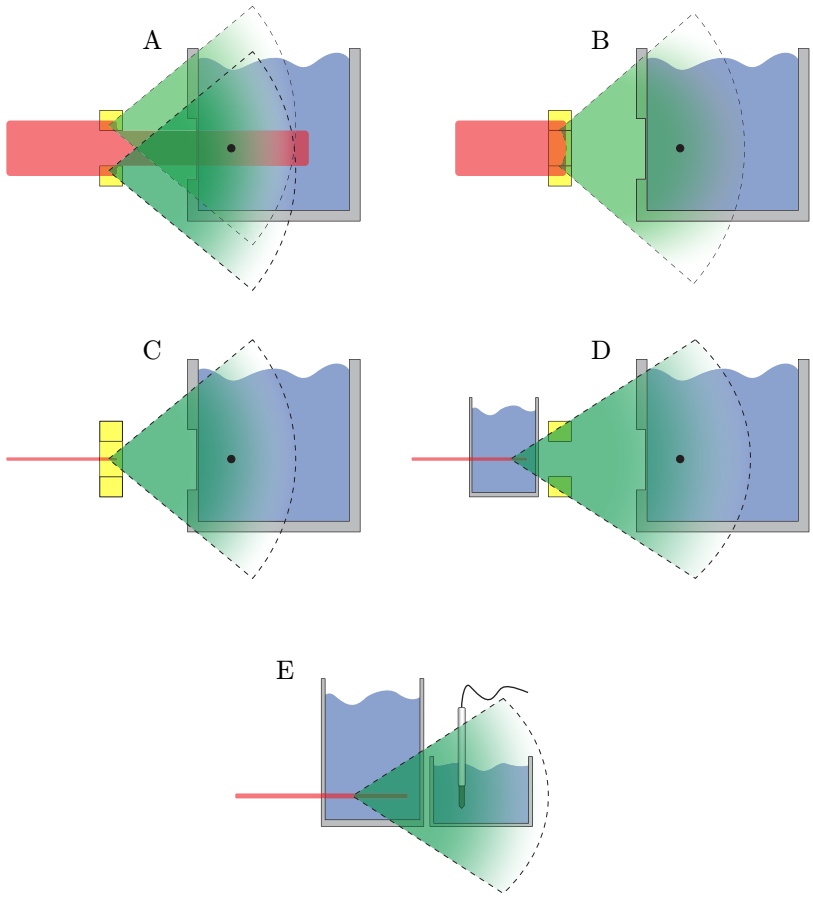

Figure 4.1 – Schematic overview of the experimental geometries. Various combinations of open and closed collimators are shown as well as pencil beam and scattered beam configurations. The beam is shown in red coming from the left. Geometry A is a normal calibration configuration, where the beam is stopped in the calorimeter phantom, while in geometry B the beam is fully stopped in the collimator material because the central hole is closed. In all configurations other than A the beam is fully stopped in the collimator or in a separate water volume. Neutrons are produced along almost the entire length of the beam path in the collimators or in the water phantoms. Only the downstream part of the beam line is included in the drawing. Geant4 Monte Carlo simulations (including the beam line setup shown in figure 4.2) were made for all shown geometries. The ionization chamber shown in geometry E is for visual reference and was not included in the simulation.

collimator-material and the interaction cross-section of neutrons in water. The Monte Carlo calculation, combined with the data set from experiments B, C, D and E allows quantitative estimates of the neutron-induced dose fraction in the regular calorimetry geometry A. Additionally, the experiments are also sensitive to the efficiency of the beam line as a whole, meaning that it also serves as a validation of the modelling of the beam line elements other than the field collimator.

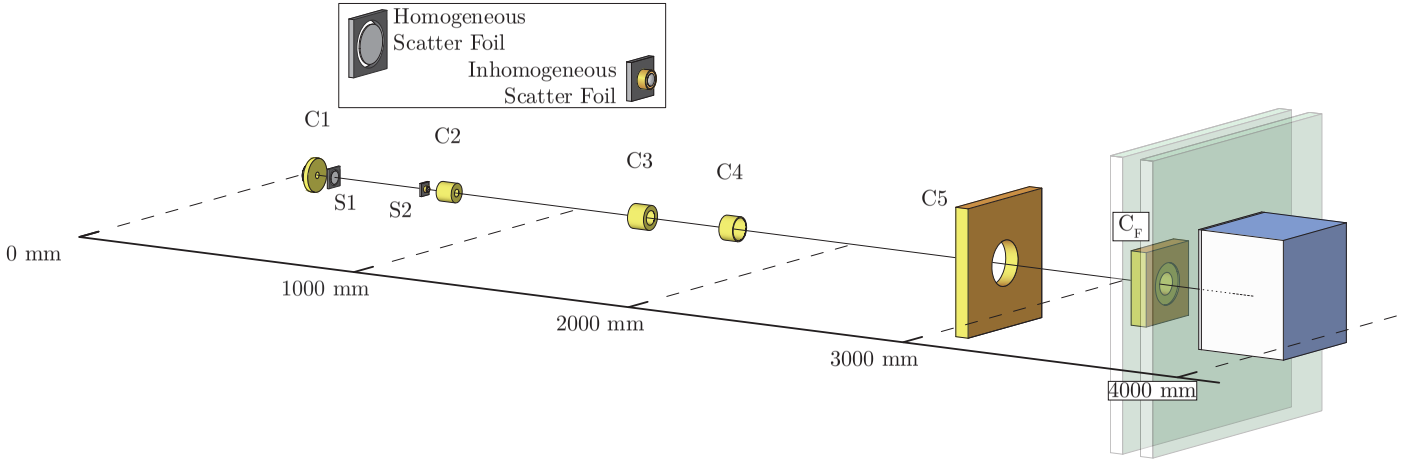

Figure 4.2 – Drawing of the simulation geometry in Geant4, showing the scatter foils, collimators and the calorimeter phantom with thermal insulation material upstream. The protons enter the beam line from the left as a pencil beam. A number of variations of this geometry were used for the simulations presented in this chapter. The displayed configuration is that which is used during a normal calorimetry experiment.

4.3.1 Implementation

The geometries A through D were used in actual water calorimetry measurements. In these cases the high purity cell is positioned such that the temperature probes are at a depth of 65 mm in the phantom. Many of the procedures and techniques described in section 2 were used such that the measurements resemble a normal calibration measurement. However, the primary goal of the experiment was to establish an experimental upper bound for the collimator-neutron and phantom-neutron dose contributions and a secondary goal was to arrive at more quantitative results. Because accuracies better than 10 % to 20 % were not deemed to be required nor feasible given the time constraints, and because of safety issues and beam time requirements, the full cleaning procedure was not used and only a quick cleaning with Hellmanex cleaning solution was used followed by the usual thorough rinsing with ultra pure water. Hydrogen flushing was used as usual to remove the oxygen from the water. The H_2 saturation also has the benefit that the heat defect which is associated with the high LET of the proton recoils is effectively mitigated. With the exception of the usual calibration geometry A there is very little field shape related heat transfer, because the neutron-induced dose distributions have half-widths that are mostly wider than the phantom itself. Because percent level accuracy was not the goal of the experiment and because it would additionally require extensive modelling and validation no attempt was made to correct the obtained data for heat transfer effects. The proton beam current was measured slightly upstream of the AGORFIRM beam line with a Faraday cup and this value serves as a primary calibration of experimentally delivered proton charge in the beam line. Contrary to the other experiments in this thesis, the beam ionization monitors were not used to compare the delivered doses, mainly because of the risk of damage due to the high proton fluxes and other related issues. During the experiment, beam currents up to 600 nA were used in order to obtain sufficient temperature signal to do calorimetry.

For geometry A, the duration of each irradiation was 60 s followed by an idle time of 120 s. Because the neutron-induced doses in geometries B through D are around three orders of magnitude lower than the direct proton doses it was anticipated that the calorimetrically determined neutron-induced doses could be comparable to the noise floor and that they could possibly be affected by temperature gradients in the water, which can cause systematic errors due to the fitting procedure that is used to derive the temperature change. For this reason the experiments for geometries B through D used a timing scheme where the duration of the irradiation was 20 s followed by a fairly long idle time of 180 s. The long idle time can be used to squeeze in an additional ‘dry run’ where one performs the fitting procedure as usual, but without actually turning the beam on. This allows one to sample the noise floor as it appears during the experiment and it can be used as a correction for inadvertent temperature fluctuations in the phantom.

Geometry E was tested with a PTW30001 Farmer ionization chamber. It was positioned in an additional* water phantom which is directly behind a water phantom in which the proton beam is fully stopped. This version of the Farmer chamber has a graphite coated PMMA wall and it is fitted with a PMMA water proofing sleeve. Because PMMA contains a relatively large fraction of hydrogen, the chamber is expected to have a sensitivity for neutron dose-to-water that is of the same order of magnitude as its sensitivity for proton dose-to-water.

4.3.2 Results

By increasing the beam current by a factor of about 40 relative to a regular calorimetry experiment, the neutron signal contribution becomes visible even in the scattered beam configuration. Figure 4.3 shows a trace of the bridge voltage of the lockin detector, which was attached to one of the NTC resistive temperature probes in the phantom. Each irradiation has a duration of 20 s and the repetition time of the irradiations is 200 s. The steps in temperature are clearly visible above the noise floor which means that the neutron-induced dose can be measured directly.

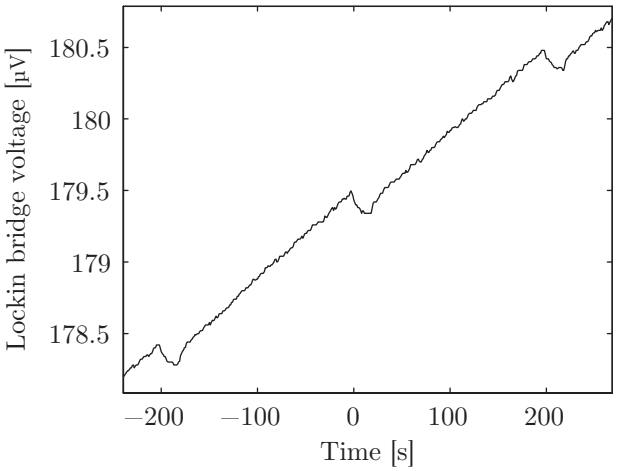

Figure 4.3 – The figure shows the bridge voltage of the lock-in detector, for an experiment where a scattered proton beam is fully stopped in the collimator (geometry B in figure 4.1). Three separate irradiations are visible in the graph. Due to the high beam current, the neutron-induced dose causes a quite measurable temperature rise in the phantom behind the collimator.

Figure 4.4 shows the dose values obtained for the experiments using the geometries that are listed in figure 4.1. The first geometry that was tested was geometry A, which is a regular direct proton dose experiment. There is a fairly large exothermal

* For reasons of radiation safety it makes sense to keep the activated water in the stopping tank separate from the water that is used as build-up material for the ionization chamber measurement

peak in the first few irradiations, which is attributed to chemistry effects similar to the intentionally created effects described in section 3.6, although here it is not desirable. The cause of the peak is most likely the presence of impurities, due to the less rigorous cleaning method used here. All of the other experiments were done after the direct proton dose experiment, which means that in those experiments the effects of impurities will have been largely reduced. However, the data does show slight slopes. Because in this experiment the data is not normalized to the signal of a beam monitor, the slopes can be attributed to beam current variations as well as to the effects of radiochemistry. The total dose that is deposited at the location of the thermistors during the experiments in geometries B, C, and D is only 8.8 Gy which contributes about the same as one single direct proton irradiation. Observing any significant slope due to radio-chemistry on those tiny contributions of accumulated dose is therefore unlikely*.

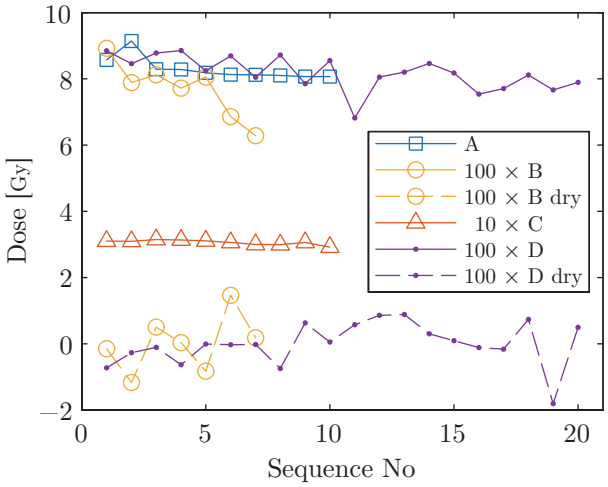

Figure 4.4 – Shown are calorimetrically measured doses for the geometries listed as 'A','B','C' and 'D' in figure 4.1. For two of the experiments the plot also shows data from dry runs where the beam was not turned on. The raw data used to compute the dry-values was taken from the idle period in between the irradiations.

Table 4.1 lists the fitted dose values derived from the data shown in figure 4.4. The third column lists the result of Monte Carlo calculations presented in section 4.4.5. The listed uncertainties for the first and third column are statistical estimates at the 68 % confidence level which include corrections for correlations between the samples and Student's-t statistics. No systematic uncertainties are included in these estimates nor are any corrections applied for systematic effects. The second column shows the measured dose normalized to the estimated integrated proton beam charge of the irradiations. The value for the integrated beam charge is derived from the fixed duration of the irradiations and the beam current as measured on a Faraday

* Further details are provided in chapter 3

cup down stream of the extraction of the cyclotron. Because the beam current is not measured separately for each irradiation and because it is known to fluctuate, an uncertainty of $\sigma = 10\,\%/\sqrt{3} = 5.8\,\%$ is estimated by assuming a rectangular probability distribution. The statistical variance estimates of the calorimetry data and the Faraday cup are added and the effective number of degrees of freedom is estimated using the Welch-Satterthwaite equation[61], assuming infinite confidence in the estimate of the beam current uncertainty. Finally the 68 % confidence limits are calculated from the Student's-t distribution as described in section 2.13.2.

Experiment	Experimental Dose [Gy]	Experimental Dose [Gy µC^{-1}]	Simulated Dose [Gy µC^{-1}]
A	8.14±0.05	9.0±0.5	11.095±0.004
B	(77±5)×10^{-3}	(6.6±0.6)×10^{-3}	(6.71±0.25)×10^{-3}
C	(306±4)×10^{-3}	(26.3±1.5)×10^{-3}	(22.5±0.4)×10^{-3}
D	(81.9±1.7)×10^{-3}	(6.8±0.4)×10^{-3}	(7.53±0.25)×10^{-3}
E	(216±4)×10^{-4}	(36.9±2.3)×10^{-3}	(50.4±2.0)×10^{-3}

Table 4.1 – Displayed are simulated and experimental doses at a depth of 65 mm for experiments A through D. In the last two columns, the dose is normalized to the proton charge entering the beam line. The data for experiment E is for a depth of 50 mm and the experimental dose is estimated by applying the conversion factor of equation 4.10. The experiment labels correspond to the list in figure 4.1. The listed uncertainties are based on statistical and systematic uncertainties and correspond to a 68 % confidence level (see text).

The only difference between experiment B and A is that in experiment B the field collimator does not have an opening. This allows estimating the collimator neutron dose without referring to a Monte Carlo calculation. Since there are no changes in the beam line geometry upstream of the field collimator, the data from experiment B is a good indicator of the neutron-induced dose due to the collimators. However, since in experiment B the field collimator intercepts a larger fraction of the direct proton beam, the data should be interpreted as an upper bound for the amount of neutron-induced dose that is due to neutrons originating from the field collimator. From the middle column of table 4.1 it is clear that the collimator-neutron dose will be lower than 0.07 %. For the 70 mm field, the field collimator intercepts 70 % of the protons that arrive at this last collimator, such that the actual dose due to collimator neutrons in a regular calorimetric experiment (geometry A) will be about 0.05 %. The other components to the dose cannot be estimated in the same fashion because the geometry of the experiments is very different from a regular calorimetry experiment. For those cases a Monte Carlo calculation has to be used. The experiments presented here validate the Monte Carlo calculations in terms of neutron dose, which also allows quantitative estimates of the neutron dose fraction in the geometry of experiment A.

4.3.2.1 Probe excess temperature

The temperature trace in figure 4.3 show distinct 'bumps' at the end of each irradiation. This overshoot is principally well understood and it occurs for both proton and neutron irradiations. For direct proton irradiations it is mainly due to the difference between the heat capacity of water and that of the materials of the temperature probe (see chapter 5 for more details). During the irradiation, the material of the temperature probe (mostly glass) heats up faster than the surrounding water. This 'excess temperature' diffuses out of the probe when the beam is turned off, causing an quasi-exponential decay of the temperature signal.

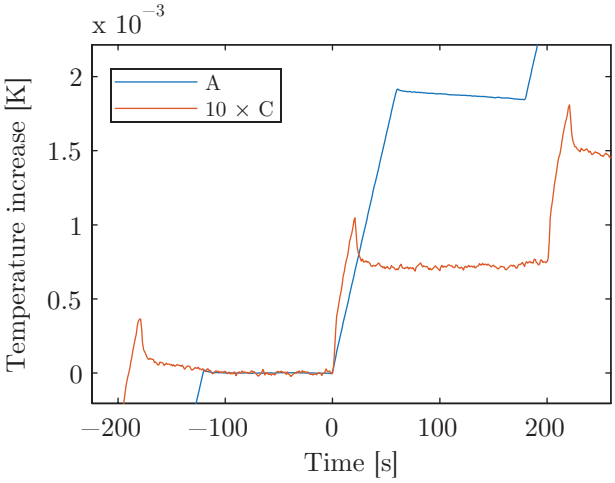

Figure 4.5 – Shown are two temperature traces obtained with the lock-in detector for experiments A and C, listed in figure 4.1. The time $t = 0$ corresponds to the start of the irradiation and the background temperature drifts were subtracted from each trace before plotting. Evidently, the same temperature probe shows a quite different time dependent response for neutron irradiations (C) as compared to proton irradiations (A).

While the size and shape of the overshoot is well understood for proton irradiations, in the case of neutron irradiations the transient shows a different behaviour, as is illustrated in figure 4.5. Centered in the figure are two temperature traces corresponding to data from experiments A and C. For proton irradiations (curve A), the excess temperature of the probe amounts to not more than a few percent of the nominally expected temperature increase. The resulting bump is barely visible on the scale of the graph. Clearly, the neutron irradiations show a much larger excess heat signal, amounting to about 40 % of the nominally expected temperature increase due to the irradiation of the water.

Figure 4.6 shows similar data, except that the temperature traces are aligned at the time that the beam is turned off and that the displayed traces are averages over all of the irradiations in any of the experiment sets A, B, C and D, respectively. The duration of the irradiations for experiment A was 60 s while the duration of

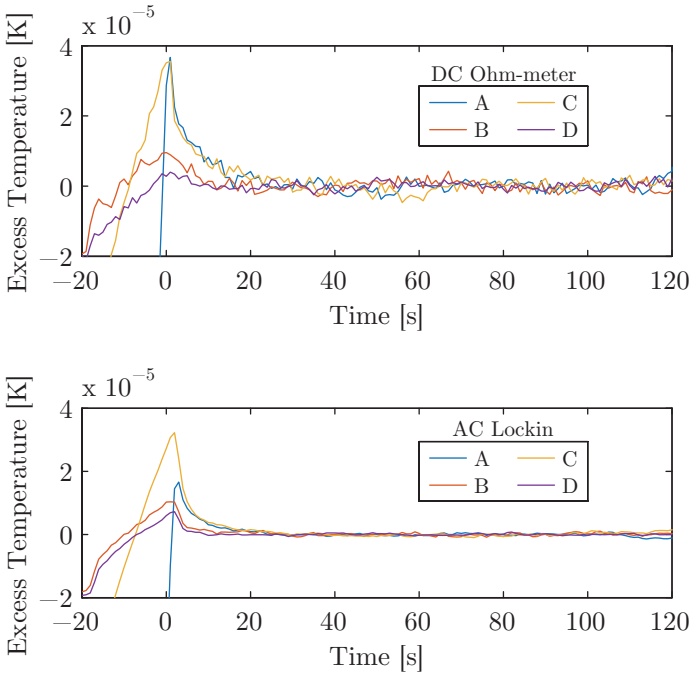

Figure 4.6 – Displayed are averaged traces of the temperature signal for both measurement chains for the experiments A, B, C and D (see figure 4.1). The time of $t = 0$ corresponds to the time that the beam is turned off. The temperature signals of each irradiation were aligned by subtracting the background drift using a linear fit in the idle time for $t > 20\,\mathrm{s}$. The displayed signals are averaged over the set of irradiations for each experiment.

the neutron irradiations of experiments B, C and D was 20 s. All neutron traces (visible for B and D only) show a sharp increase in temperature at the start of the irradiation ($t = -20$) which quickly transitions into a much lower slope, signalling that the probe reaches an equilibrium temperature difference with respect to the water even before the beam is turned off. The probes thus reach their maximum excess temperature during the irradiation in all of the experiments. Therefore the different values of the excess temperature at the end of the irradiation for the neutron irradiations as compared to the proton irradiations cannot be caused by the difference in the length of the irradiations. By comparing the relative magnitudes of the excess heat peak at the end of the irradiation ($t = 0$ in the figure) to the deposited doses listed in table 4.1 it is quite clear that the magnitude of the excess heat peak cannot be explained solely by the dose rate. A purely dose rate dependent effect would predict a peak height for experiment C that is almost nine times lower than the peak height of experiment A. Yet from figure 4.6 it is clear that the peak has approximately the same size for experiment A and C. Experiment D had a slightly higher dose rate (although almost statistically insignificant) compared to experiment B, yet the excess heat magnitudes show the

reverse. The graphs from the two measurement chains look almost identical except for the increased noise level in the DC chain and an even lower peak magnitude for experiment A in the AC chain compared to the DC-chain. The time scale of the observed transients hints at heat conduction. Because most of the temperature traces appear quite similar between the two measurement chains and because both the electronic read-out chain design and the probe design are different, the simplest explanation is that the dose deposited in the probes relative to the surrounding water is different for neutron irradiations as compared to proton irradiations.

Differences in stopping power for the probe materials compared to water are fairly small and would cause under dosage rather than over dosage. Low energy recoil protons may stop within the glass walls of the probe, since the density of glass is higher than that of water. However this involves only protons with energies between 0 MeV to 3 MeV, which is only a small fraction of the proton recoil spectrum. Temperature signals at these time scales are characteristic for heat diffusion in the geometry of the thermistor probe. It is therefore likely that the observed behaviour is a differential heating effect, which would have to be caused by neutron interactions in the materials out of which the temperature probe is constructed.

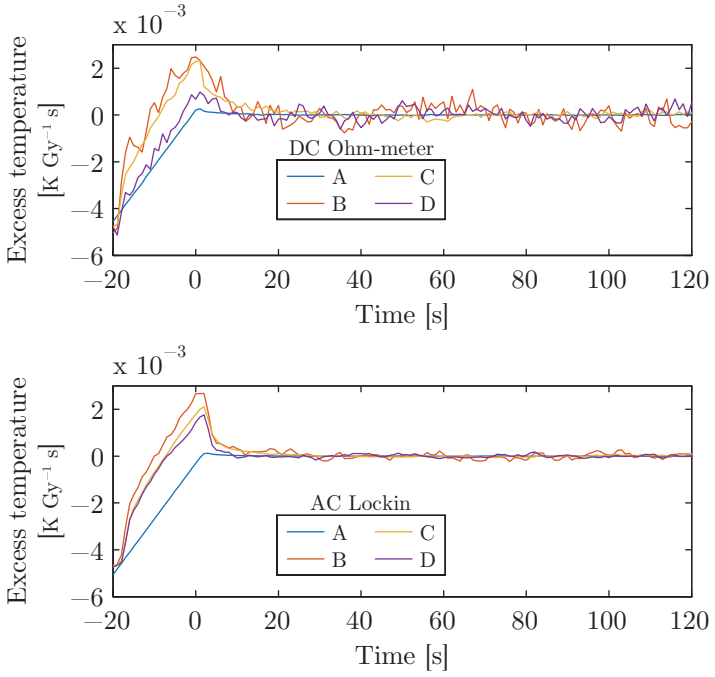

Figure 4.7 – The figure shows the same data from figure 4.6. However, here the displayed data is normalized to the mean dose rate of each experiment.

Figure 4.7 shows the same data as in figure 4.6, except that the data is normalized to the mean experimental dose rate of each experiment series. Due to the normalization, the scatter in the graphs is appreciably lower. However, differences among the neutron-dose experiments B through D still remain. The plots show that the probes reach a quasi-stationary excess temperature while the beam is still turned on. Although there are differences between the various experiments, figure 4.7 shows that the observed very large excess heat is not directly dose rate dependent.

4.4 Geant4 Monte Carlo simulations

Issues related to the details of the beam quality can only be addressed by obtaining detailed knowledge about the radiation field. In practice, the experimentally obtainable information about the beam quality in the KVI-CART AGORFIRM beam line is limited to fluence measurements, local dose measurements or depth-dose curves and two dimensional slices of the dose distribution. These techniques do not reveal the nature of the ionizing radiation.

In order to understand how the beam line at KVI-CART might affect the measurements, a Geant4[104, 105] Monte Carlo simulation was done. It was designed to simulate the experiments described in section 4.3. The Geant4 simulation toolkit* provides various components that allow an end user to construct a unique simulation code based on the users' requirements. Geant4 delivers classes that take care of geometry and particle tracking and it comes with a vast library of physics processes. The toolkit allows an end-user to hook into all parts of the simulation process by providing classes which are called by the Geant4 kernel at appropriate times, thus allowing to extract any desired physics quantity.

4.4.1 Simulation geometry

The simulation geometry was implemented in Geant4 by directly constructing it in a user supplied class derived from the Geant4 'G4VUserDetectorConstruction' base class. Except for the inhomogeneous scatter foil, the entire geometry was constructed using cylinder and box shapes, as well as intersections between those shapes. The geometry has previously been described in detail[56] and was directly implemented in Geant4, with a few minor corrections.

Figure 4.2 shows a render of the Geant4 implementation of the beam line at KVI-CART as configured during a calorimetry session. Depending on the experiment, slightly different geometries were used. The beam enters from the left exiting a beam pipe through a 70 µm aramid exit foil (not visible) and then continues through air. The beam is modelled as a Gaussian-shaped pencil beam having a width of $1\sigma = 1.7$ mm and an angular dispersion of 0.85 mrad. It then passes through the opening of the first collimator C1. Its primary function is

* Geant4-10-00-patch-02

to remove stray particles from the field. Generally, these stray particles are not present with proton beams, however as a primary beam line element, it is modelled anyway.

The protons then reach the scattering system consisting of the scatter foils S1 and S2. The first scatter foil is a homogeneous lead sheet with a thickness of 1.16 mm. The second scatter foil is constructed out of Densimet alloy, which consists mostly of tungsten. The shape of the second foil as described in the PhD-thesis of van Luijk[57] was implemented in Geant4 using an 11-point linear piecewise approximation based on the 'G4Polycone' class. The maximum thickness of the foil is 1.03 mm and it has a FWHM width of 8.3 mm. Shown in the image is also that the inhomogeneous scatter foil is mounted on top of a brass alloy tube which itself is fitted into a aluminium holder. Both the brass tube as well as the aluminium holder see a significant portion of the primary proton beam. Some of the protons that pass through those parts of the second scatterer unfortunately do make it back into the main irradiation field, which leads to several small peaks in the proton energy spectrum at the point of measurement in addition to the full energy peak.

Following the scatter foils is another collimator C2, whose primary function is to remove most of the protons that are scattered over large angles. A little downstream is another collimator C3 which has a similar function. Collimator C4 is actually a holder in which an additional collimator can be placed. Although this extra collimator is not used in the measurements, the holder is still in the beam line and sees a very small fraction of the protons. Collimator C5 is an anti-scatter collimator which prevents protons that are scattered over large-angles from ending up in the walls of the building or in equipment close to the irradiation field. The combined effect of all these collimators is that a lot of the protons that have scattered out-of-field are removed relatively upstream in the beam line, far away from the point of measurement. This also means that a large fraction of the neutrons is produced far upstream in the beam line, resulting in a fairly low neutron dose at the measurement position.

The last collimator on the right is the field collimator C_F. It is contained in a brass holder. The size and shape of the field collimator defines the size and shape of the irradiation field at the measurement position - although the exact width of the field and the width of the penumbra varies with the distance between the collimator and the measurement position downstream. For the experiments in this thesis mostly field collimators with openings of 70 mm and 50 mm diameter were used. Larger diameters are possible but this results in rather large inhomogeneities in the dose distribution near the edges of the field.

Finally, the calorimeter water phantom is behind the field collimator. Upstream of the phantom are two polystyrene insulation sheets (shown in transparent colour). The phantom is modelled simply as a box consisting of pure water with a density of $\rho = 1.000\,\mathrm{g\,cm^{-3}}$ and except for the front wall of the water phantom, the PMMA parts of the phantom are not modelled. The front wall of the phantom is modelled accurately, including a thin-walled section with a polystyrene window. However, it

is only the dose to water that is calculated as the glass parts of the calorimeter are not modelled and the related excess temperature effects (section 4.3.2.1) are not taken into account.

4.4.2 Physics settings

Geant4 employs so-called 'physics lists' to specify the physics processes* that it uses during the simulation. In principle it is possible to manually specify individual physics processes or specific models for those processes, however getting this right is not an easy task and it is generally advisable to use a well-verified set of physics models. Geant4 includes a so called 'physics list factory' which allows a user to combine different pre-defined physics lists for hadronic and electromagnetic physics.

In order to retain consistency with the large amount of existing research regarding physics implementations for particle therapy, a commonly used physics list was activated, even though little verification of the calculated neutron doses is reported in the literature. For dosimetry the particle therapy oriented physics selections should provide good performance since absolute dose estimation is also the goal for particle therapy calculations. Some caution is advisable though, because modelling of electrons and neutrons is less important in therapy, however it can be important for radio-biology and dosimetry depending on the application.

Implemented physics list For the simulation presented here the 'QGSP_BIC_HP_PEN' physics list was used through the physics list factory feature of Geant4. The list includes a data driven binary cascade model. The same model is used for both GATE[107] and TOPAS[108, 109].

The High Precision nuclear physics list 'HP' includes data driven models for neutron energies below 20 MeV[110], using cross-sections from the evaluated neutron data file ENDF/B-VI. This model is also used by both GATE and TOPAS.

The physics list used here is essentially the same as that of GATE and TOPAS, with the omission of isotope decay and ion cascades and with the inclusion of improved models for low energy electron interactions.

4.4.3 Particle spectrum

The response of any ionization chamber (or even the excess temperature effect of the probe) is dependent on the beam quality. The beam quality at a certain position in the phantom is essentially defined by the local energy spectra of all ionizing particles. While the sensitivity of an ionization chamber also depends on the direction of the particles, the particle spectrum is the simplest indicator of beam quality. For this reason the Geant4 Monte Carlo code is used to compute the particle spectrum at the measurement position.

* A short general overview of various physics models is given by Apostolakis[106].

4.4.3.1 Direct proton spectrum

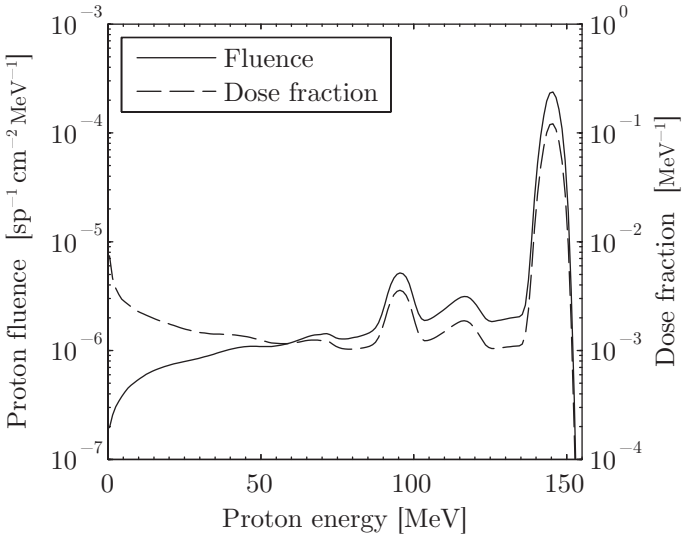

Figure 4.8 – Proton fluence as a function of proton energy at the measurement position in the phantom (at a depth of 65 mm, geometry A in figure 4.1), simulated with Geant4. The axis on the left shows the proton fluence per starting proton (SP^{-1}) impinging on the scatter foils. Also shown is the same curve, but weighted per bin with the stopping power according to PSTAR[111] and divided by the total dose which was scored separately, emphasizing the relative contribution of the proton fluence to the dose.

Figure 4.8 shows the proton particle spectrum at the measurement position in the phantom as simulated using Geant4. The simulated proton fluence was calculated 'online' during the simulation, while the dose fractions were calculated 'offline' after the simulation had ended, by multiplying the proton fluence by the stopping power according to PSTAR and dividing by the total proton-dose.

The largest peak in figure 4.8 corresponds to the energy of the primary protons at the measurement position, after having been slowed down from 190 MeV by passing through 65 mm of water in the phantom. The integral of the graph, starting at an energy of 130 MeV and ending well beyond the primary beam energy shows that it accounts for 81 % of the dose associated with protons. In the range of 80 MeV to 130 MeV there are peaks caused by scraping on the scatter foil assembly and collimator scatter which contribute 8 % of the dose. The long tail at low energies contributes 13 % of the dose. It contains some collimator scatter but it mainly consists of proton recoils due to the direct action of beam-protons on hydrogen nuclei from the water.

The various contributions due to beam line elements do not give rise to large errors in ionization chamber calibrations. If the assumption of a unity chamber perturbation factor (as is the case in TRS398[14]) is true, then the depth variation

of the beam quality correction factor is to be entirely attributed to stopping power ratio variations. Needless to say, this situation does not occur in practice because there is at least always a displacement correction factor*. Neglecting this fact, the relative effect of the lower energy contributions on ionometry can be calculated using fitted water/air stopping power ratios. The following fit is obtained from ICRU-78[6] and TRS-398[14]:

$$s_{w,\mathrm{air}} = a + bR_{\mathrm{res}} + \frac{c}{R_{\mathrm{res}}} \tag{4.1}$$

where R_{res} is the residual range in units of $\mathrm{g\,cm^{-2}}$, $a = 1.137$, $b = -4.265 \times 10^{-5}$ $\mathrm{cm^2\,g^{-1}}$ and $c = 1.84 \times 10^{-3}\,\mathrm{g\,cm^{-2}}$. Converting the energies of the main peak (146 MeV) and the strongest secondary peak (96 MeV) into ranges using PSTAR yields:

$$\frac{s_{w,\mathrm{air},96}}{s_{w,\mathrm{air},146}} = 1.0004 \tag{4.2}$$

Considering that the actual dose contribution for the two secondary peaks together is only 8 %, the effect on any ionization chamber calibration is negligible.

4.4.3.2 Neutron spectra

In order to gauge the effect of neutrons in the KVI-CART beam line it is of interest to see what their energy spectrum is and from which position they originate, since that defines how well the KVI-CART beam line matches a clinical beam. By implementing custom scorer classes, filtering classes and user stepping classes in Geant4, individual particles can be tracked and the production and interaction of neutrons can be studied 'online'.

Figure 4.9 shows the neutron spectrum at the measurement position in the phantom. Integrated over energy, the neutron fluence per starting proton is $4.2 \times 10^{-6}\,\mathrm{sp^{-1}\,cm^{-2}}$, while the proton fluence based on figure 4.8 is 1.8×10^{-3} $\mathrm{sp^{-1}\,cm^{-2}}$. Above an energy of about 10 MeV, 57 % of the neutrons have originated in the water phantom, while 35 % either originate from the field collimator or were generated in the phantom as a result of interactions by neutrons generated in the field collimator. The remaining 8 % of the neutrons were generated somewhere else upstream in the beam line. Because of the dependence of the angular distribution on neutron energy these upstream neutrons have a somewhat lower contribution at low energies. The energy spectrum shown in figure 4.9 includes the effects of scattering and attenuation of neutrons in the water phantom and as such reflects the actual spectrum at the water depth of the measurement. However, since neutrons are not directly ionizing, the graphs are of limited use and the recoil spectra need to be examined.

* Contrary to common perception, a zero dose gradient is not a sufficient condition for a gradient correction equal to unity[112]. As a result, in a proton field the individual contributions to the dose by all spots/energy planes need to be considered.

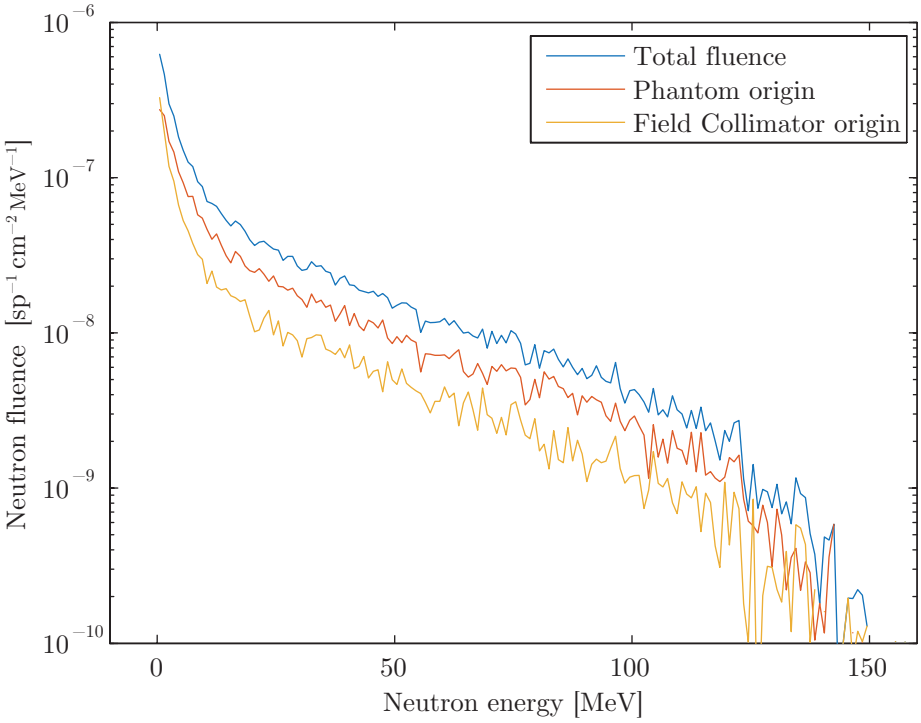

Figure 4.9 – Neutron fluence as a function of neutron energy at the measurement position in the phantom (geometry A in figure 4.1), simulated with Geant4. The axis on the left shows the neutron fluence per starting proton (sp^{-1}) impinging on the scatter foils. In addition to the total neutron fluence, two curves are shown for neutrons originating from the water phantom and from the field collimator. The fluence-weighted mean energy of the neutrons is 19.2 MeV and half of the kinetic energy associated with the neutrons is due to the fraction above 51 MeV.

4.4.3.3 Proton recoil spectra

Using similar techniques for the scoring of dose and fluence as described in the previous section, the recoil spectra of the protons generated by neutron interactions were calculated. The recoil spectra can then be used to derive a 'dose weighted' spectrum, which shows the relative importance of the different LET components. Contrary to the technique used in section 4.4.3.1, for the calculation presented in this section the dose weighted contribution to the spectrum was calculated 'online' for each individual particle and for each step of the simulation. In doing so, possible issues related to the bin-size at low energies are avoided and the value of the dose deposit naturally includes every detail of the physics modelling which is used in the tracking of the protons. The total dose was scored by applying a filter to only

tally proton energy deposits. The dose fraction is calculated as the fraction of the total dose that is caused by recoil protons originating from neutron interactions. Other components to the dose are not included in this tally.

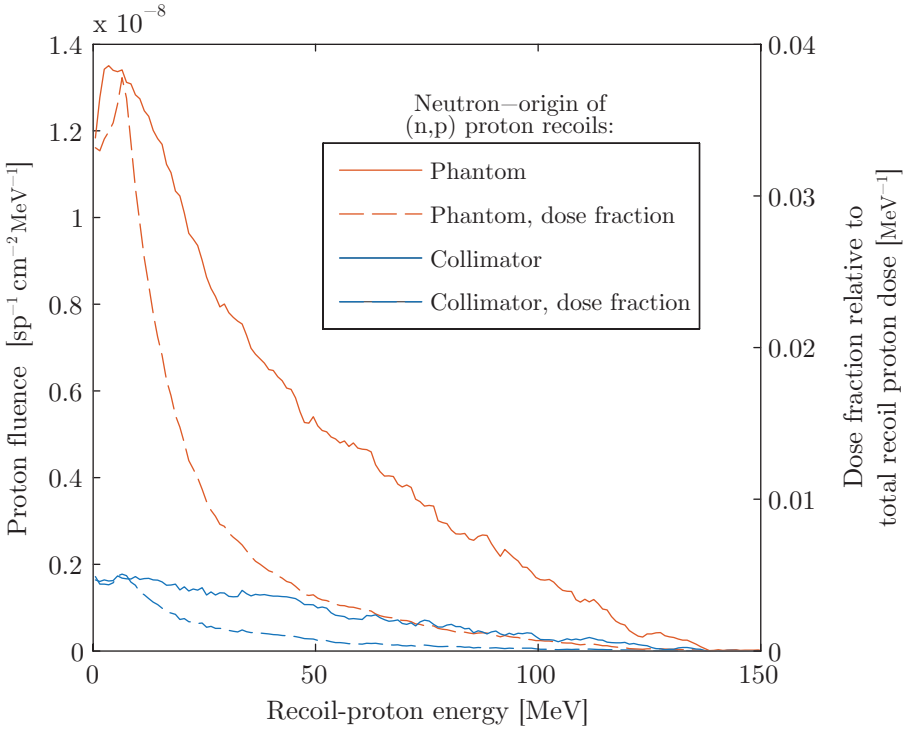

Figure 4.10 – Recoil-proton fluence as a function of proton energy at the measurement position in the phantom, simulated with Geant4. The axis on the left shows the proton fluence per starting proton (SP^{-1}) impinging on the scatter foils. The curve with the highest amplitude shows the proton recoil spectrum due to neutrons that are generated inside the water phantom, while the lower amplitude curve shows only the part of the recoil spectrum which is due to neutrons that are generated in the field collimator. Shown on the axis on the right is the relative contribution of the recoils to the total recoil-dose, which was calculated 'online' during the simulation.

Figure 4.10 shows the simulated proton-recoil fluence at the measurement point as a function of proton energy, separated into graphs for the origin of the neutrons causing the proton recoils. Also shown in the same graph is the total dose associated with these recoil-protons. Like the neutron spectrum, the proton recoil spectrum is heavily peaked at low energies. Being charged particles, the recoil protons have a finite range which reduces the fluence at the lowest energies in the recoil spectrum.

From this figure it is immediately clear that the collimator only has a minor contribution to the neutron-induced dose. Except for a gamma ray contribution, which according to the simulation equals 17 % of the dose due to recoil protons, there are also recoil nuclei and an occasional deuteron or alpha particle, but these

cause very little dose. Almost all of the neutron-induced dose is due to recoil protons and only 14 % of that dose is due to collimator-neutrons. Since most of the neutron-induced dose is due to neutrons which are generated inside the water phantom itself, the use of a scattered beam for calibrations as opposed to a scanning beam will only cause a small error.

4.4.4 Correction factors for neutron beam qualities

It will be shown in section 4.4.5 through simulation that the neutron-induced dose fraction in the proton beam at KVI-CART is 0.34 %. While this number is small it is immediately clear that beam-specific variation of this number could lead to per-mille level uncertainties if the neutron-dose-to-water sensitivity of an ionization chamber is substantially different from its proton-dose-to-water sensitivity. For the purpose of absolute dosimetry it is therefore important to have some idea of the relative response of an ionization chamber to a neutron field as compared to a pure proton field.

A proton dose as measured with an ionization chamber is often expressed through the $N_{D,w}$ formalism described in TRS-398[14]. It assumes that ionization chambers have been calibrated in ^{60}Co which results in an N_{D,w,Q_0} calibration factor. This calibration factor is then converted into a calibration factor for a proton SOBP by applying a beam quality correction factor k_{Q_p,Q_0}:

$$N_{D,w,Q_p} = k_{Q_p,Q_0} \cdot N_{D,w,Q_0} \tag{4.3}$$

In principle, the calibration value N_{D,w,Q_p} should include any effects from neutron contamination as well, however this is not mentioned in TRS-398. In order to assess the effects of a difference in neutron contamination between institutions one would like to have a similar beam quality conversion factor for neutrons. That is, the quantity of interest is a k_{Q_n,Q_0} factor.

Unfortunately, neutron dosimetry is not part of any $N_{D,w}$ formalism and values for the sensitivities of ionization chambers are particularly hard to find. The little information that is available is often based on ^{60}Co kerma calibrations for tissue-equivalent wall materials and tends to focus on neutron energies ranging from thermal energies up to a few MeV. Neutron energies in proton therapy beams can reach up to the primary energy of the beam. Calibration of ionization chambers for higher energy neutrons is notoriously difficult for a number of reasons.

Generally, the calibration factor is valid for a certain spectrum of neutrons. The spectra for which calibration factors exist are usually not comparable to the neutron spectra of a clinical proton irradiation. A complicating factor is that very often, the ionization chambers that are intended for proton dosimetry do not fulfil Bragg-Gray conditions considering their exposure to the high energy proton recoil field. The chamber walls often have thicknesses of several 100 µm. The range in water of a 5 MeV proton is only 360 µm, which means that a lot of the proton

recoils would not make it through the walls. Furthermore there is considerable variation in the design of ionization chambers and the usage of different materials results in large differences of the sensitivity in neutron fields.

There are protocols[113] that are specifically intended for neutron dosimetry. However, it is often not clear how the listed values translate into neutron dose-to-water sensitivities. Becker and Brunckhorst[114, 115] show how they disentangle the dose components of a mixed field using three different ionization chambers having different sensitivities to the three components of the dose. One separates the sensitivity of the ionization chamber into a factor h for gamma beam qualities, k^* for the fast neutron fraction of the dose and i for the thermal neutron fraction of the dose:

$$M \cdot N_{Dw} = h \cdot D_\gamma + k \cdot D_n + i \cdot D_t \tag{4.4}$$

In the above equation, M is the ionization chamber reading (charge) and N_{Dw} is its ^{60}Co calibration coefficient. For the gamma fraction of the dose deposit the same authors suggest to assume that tissue equivalent material is sufficiently equivalent to water to make the approximation:

$$k_{Q,Q_0} = 1/h \tag{4.5}$$

meaning that once the gamma-field in the mix has been characterized in terms of a beam quality Q according to TRS398, one can also use the listed k_{Q,Q_0} values to obtain the relative sensitivity h. It is tempting to invert the argument and to apply the same reasoning to the neutron sensitivity in an effort to obtain k_{Q_n,Q_0}, however due to the lack of charged particle equilibrium this is of limited value.

4.4.4.1 Estimating the fast neutron correction

The lowest value of the factor k in equation 4.4 for a tissue-equivalent-walled chamber with tissue-equivalent gas is listed in the paper by Becker[115]: at a neutron energy of 10 MeV $k = 0.951$, meaning that the response is low by about 5 % relative to ^{60}Co. Data shown in a report by the AAPM[113] suggests that the stopping power ratio wall/gas in low energy neutron fields is about 11 % higher for an air-filled tissue-equivalent-walled chamber than for an tissue-equivalent-gas-filled tissue-equivalent-walled chamber. The same report lists the specific ionization W for neutron beam qualities of both tissue-equivalent (TE) gas and air and the ratio $W_{\text{air}}/W_{\text{TE}}$ is 1.16. Combining these three numbers yields an estimate of $k_{Q_n,Q_0} = 1.36$ for the low energy part of the proton recoil spectrum that can not reach into the ionization chamber.

At higher energies Bragg-Gray conditions begin to be valid and one can assume that a large part of the neutron-induced dose in the cavity of the ionization chamber is due to recoil protons originating from the water outside of the chamber. This means one can apply proton beam quality conversion factors as listed in

* Note the distiction between this 'k' (which describes the sensitivity) and a 'k_Q' which describes the calibration conversion factor.

TRS398[14], although in this case a dose-weighted proton-fluence spectrum is required. In TRS398 beam quality corrections are listed down to a residual range of 5 mm of water, which corresponds to a proton energy of 20 MeV. Currently, the listed values in TRS398 do not contain any proton-perturbation factors other than unity, but one should be aware that these perturbation factors are not applicable to the signal component that is due to recoil-protons originating from neutrons (for one thing, the displacement correction factor is different, because the depth-dose curves are not the same, which applies to proton-proton recoils as well).

Element	Material		
	Water	A-150 plastic[113]	PMMA $(C_5O_2H_8)_n$
H	0.11	0.10	0.08
O	0.89	0.06	0.32
C	0.00	0.77	0.60
	Composition in weight fractions		

Table 4.2 – The elemental composition of water, tissue equivalent plastic and PMMA, showing the major components only.

As for the transition between a thick-wall geometry (low recoil energy) and a thin-wall geometry (high recoil energy) it should be mentioned that most of the neutron-induced dose is due to recoil protons. Ionization chambers with a hydrogen content similar to water are preferable while pure graphite chambers will show a rather low sensitivity to low energy neutrons. Table 4.2 shows the elemental composition of two common materials used in ionization chambers in comparison to water. Because the hydrogen content of each of the three materials is similar they can be expected to have similar low energy neutron sensitivities. The high energy part of the recoil spectrum that was shown in the previous sections needs to be factored in the beam quality conversion factor separately.

4.4.4.2 Estimating k_{Q_n,Q_p} conversion factors

To estimate a beam quality conversion factor from the simulation data presented in the previous sections is not entirely straightforward. One would preferably have simulated the actual geometry for each individual ionization chamber directly in the Monte Carlo calculation to derive a k_{Q_n,Q_0} conversion factor, however this requires much more extensive validation of the simulation and it requires a large amount of CPU time. Fortunately the calibration value for neutrons is not the primary interest here as only the estimate of the uncertainty that is caused by the neutron contamination is required.

For easy comparison, the figure estimated here is a $k_{Q_n,Q_p} = \frac{k_{Q_n,Q_0}}{k_{Q_p,Q_0}}$ factor, which describes the response of the chamber to the neutron field relative to the value listed in TRS398 for protons at the residual range of the measurement. In principle,

one would like to divide the proton recoil spectrum into two parts, specifically a high energy part which includes the protons coming from the water that can penetrate the ionization chamber wall and a low energy part which includes the protons liberated by neutron collisions in the chamber wall. However, since TRS398 does not include tables down to such low energies and since it is not clear whether or not extrapolations down to low energies would yield relevant data, the divisor is chosen at 20 MeV, which corresponds with the lowest proton range listed in TRS398 of 5 mm.

In general, whenever a mixed signal is supplied to a measuring device, any correction factors need to be added by taking the reciprocal. If there are N dose components D_i such that the total dose is $D = \sum D_i$ and if each of the D_i contributes an M_i of measured signal to a total measured signal of $M = \sum M_i$ and if the correction factors $k_i = \frac{D_i}{M_i}$ are known, then the total effective correction factor k for the entire signal is:

$$k \equiv \frac{D}{M} = \frac{1}{\frac{1}{D}\sum_{i=1}^{N}\frac{D_i}{k_i}} = \frac{1}{\sum_{i=1}^{N}\frac{\mathrm{DF}_i}{k_i}} \tag{4.6}$$

where DF_i is the fractional contribution of component D_i to the total dose.

For the high energy part, considering the ratio k_{Q_n,Q_p}, only the variation of the stopping power ratio is relevant. The k_i in equation 4.6 are:

$$k_i = k_{Q_n,Q_p}(E_i) = \frac{s_{w,\mathrm{air},R(E_i)}}{s_{w,\mathrm{air},R=14.4\,\mathrm{cm}}} \tag{4.7}$$

The range $R = 14.4\,\mathrm{cm}$ is the residual range of the protons with an energy corresponding to the main peak in figure 4.8. The part of the recoil spectrum above 20 MeV causes 39 % of the recoil-dose while the spectrum below 20 MeV causes the remaining 61 % of the dose in water. Taking the summation in equation 4.6 only for $E > 20\,\mathrm{MeV}$ and renormalizing to the dose fraction associated with that part of the spectrum yields:

$$E > 20\,\mathrm{MeV}: \qquad k_{Q_n,Q_p} = 1.0019 \tag{4.8}$$

If the neutron dose fraction of 0.34 % in the KVI-CART proton beam is taken to be typical for a clinical beam, this means that when transferring a chamber calibration in a scattered beam to a scanned beam, one does not need to worry about the high energy part of the proton recoil spectrum due to neutrons.

For the low energy recoils ($E < 20\,\mathrm{MeV}$) TRS398 does not list any beam quality conversion factors. The value estimated in section 4.4.4.1 is $k_{Q_n} = 1.36$, which is relative to a ^{60}Co calibration. Taking the value from TRS398 for a PTW 30001 Farmer chamber, the value relative to a proton calibration is:

$$E < 20\,\mathrm{MeV}: \qquad k_{Q_n,Q_p} = \frac{1.36}{1.029} = 1.32 \tag{4.9}$$

Using the values for k_{Q_n,Q_p} estimated above, the total conversion factor for both parts of the spectrum is:

$$k_{Q_n,Q_p} = \frac{1}{0.61/1.32 + 0.39/1.0019} = 1.17 \tag{4.10}$$

This means that the relative perturbation of a measured proton calibration factor k_{Q_p,Q_0} by the presence of a neutron field due to beam line elements is about one sixth of the dose fraction due to that neutron field. For typical neutron doses on the order of a per mille, the effect on a k_{Q_p,Q_0} calibration is close to negligible. The above equation is likely to be an overestimate, because recoil protons in the energy range of 5 MeV to 20 MeV do reach the chamber cavity.

4.4.5 Simulated neutron depth dose curves

To estimate the total neutron-induced dose fraction, the Monte Carlo simulation described in section 4.4 was used, with modified scoring classes and filters. The various classes track each particle and associate flags regarding the particles ancestry which are carried over to all descendant particles. Separate flags are raised whenever a neutron or a gamma photon is created and these flags are tagged with an identifier for the geometric volume in which the event occurred. Once raised, a flag and its volume identifier are retained unmodified in all of the descendant particles, logging only the first occurrence in the event chain. Thus, it is possible to attribute a certain fraction of the dose due to event chains starting with the creation of neutrons or gammas. By applying appropriate combinations of filters for the type of ancestor and geometric volume of origin, the dose can be differentiated into contributions from beam line components as well.

Figure 4.1 shows schematically the various beam line geometries that were simulated. All of the geometries were also used in experiments. The first geometry A is the usual calibration experiment with the water calorimeter phantom. Geometries B, C and D also include the calorimeter phantom, however in these cases the beam is stopped outside of the phantom to create neutrons and gammas without causing dose in the phantom due to the direct action of primary protons. Geometry E shows a separate phantom with an ionization chamber (the chamber was included in the drawing but not in the actual simulation geometry since the estimation of the sensitivity of the chamber relies on estimates based on the recoil spectrum). The neutron fluence (depicted with green colouring) causes dose at the measurement point for all geometries. Figure 4.1 shows for illustrative purposes a forward-peaked angular distribution, corresponding to neutrons with energies which are large fractions of the primary proton energy. In reality, as shown in section 4.4.3.2, the distribution is markedly peaked at energies of a few MeV which is more omnidirectional in nature.

Figure 4.11 shows depth-dose curves corresponding to geometry A in figure 4.1, which is the geometry of a calibration experiment. Displayed are the contributing components to the dose at the measurement point. There is a significant

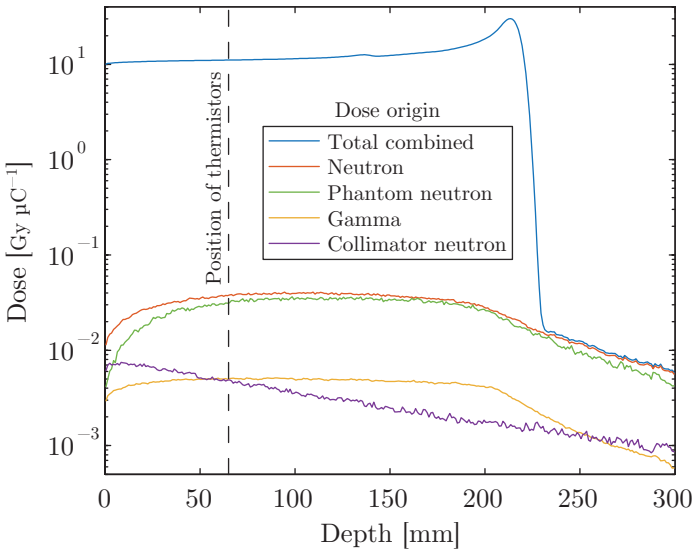

Figure 4.11 – Simulated dose at the measurement position in the calorimeter phantom per amount of proton charge entering the beam line, during a calibration experiment. The simulated geometry is geometry A in figure 4.1. In addition to the total dose the graphs display the dose due to neutrons and gammas. The neutron dose is differentiated according to the origin of the neutrons.

neutron contribution, however most of the neutron-induced dose is due to neutrons that were generated in the phantom. The neutron-induced dose fraction is $(0.341 \pm 0.003)\,\%$ of the total dose whereas the collimator neutron contribution amounts to $(0.043 \pm 0.001)\,\%$. At a depth of 65 mm the neutron-induced build up is nearly complete. The phantom-generated neutrons will appear in any clinical proton beam quality anyway (with possibly the exception of very low energy beams). Since the contribution due to collimator-neutrons is very small it will not lead to a very large error when ionization chambers that are calibrated in the KVI-CART scatter beam are used in a scanned beam.

Figure 4.12 shows the depth-dose curves corresponding to the the other simulation geometries shown in figure 4.1. In each case the beam is fully stopped outside of the calorimeter phantom and in the case of geometries D and E (the latter of which was used with the ionization chamber) the beam stops in a separate water phantom. Geometries B and D score comparatively low amounts of dose, the reasons being a low efficiency in the scattered beam configuration for the former and a large distance between the measurement point and the production location of the neutrons for the latter configuration. Because of the proximity between the stopping medium and the measurement position the pencil beam geometries C and E show a much larger dose contribution (all of the protons in the beam are stopped close to the phantom). Comparison of curve B (closed collimator) in figure 4.12 with the collimator neutron dose (opened collimator) in figure 4.11 shows that

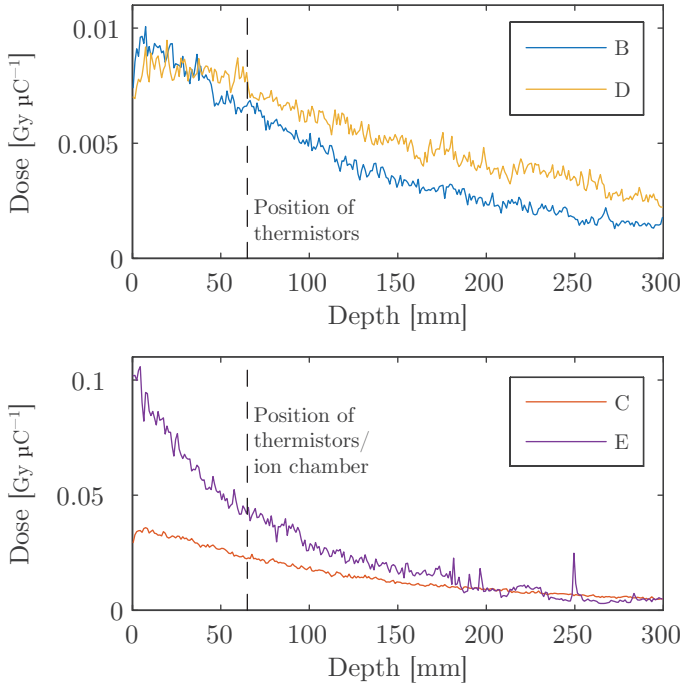

Figure 4.12 – Simulated depth-dose curves for the geometries listed in figure 4.1. The depth of zero corresponds with the front edge of the calorimeter phantom, or in case of geometry E with the front edge of the most distal phantom. Almost all of the dose is due to proton recoils resulting from neutron interactions. The dose is normalized to the total proton charge entering the beam line.

about 72 % of the collimator dose for the fully closed collimator can be explained as being due to the neutrons that are produced in the part of the collimator that also intercepts protons during a normal irradiation with a opened collimator. Thus, geometries A and B are very similar in terms of collimator-neutron dose. The shape of the curves for the graphs are mostly determined by the inverse square law.

4.5 Discussion

The simulations described in section 4.4 implement the geometry of the experiments described in section 4.3, allowing a comparison between the experiment and the simulation. Table 4.1 shows both the experimental and simulated dose values. Clearly, the experimental proton dose in experiment A is 19 % lower than the simulated dose. The remaining calorimetric experiments B, C and D show differences between experiment and simulation of −1.5 %, 17 % and −9 % respectively. The variance in these numbers suggest an accuracy of the simulations of 20 %. Keeping

in mind that the listed uncertainties in table 4.1 are essentially statistical and that various systematic uncertainties have not been accounted for (cross-sections, positioning errors, geometry errors, beam alignment), there is a fair consistency between the experiment and the simulation.

The ionization chamber data from experiment E in table 4.1 is calculated by using the chambers' ^{60}Co calibration factor and by applying the formalism of equation 4.3 to obtain the TRS398 calibration factor for the proton field at a depth of 65 mm in geometry A. This calibration factor is then multiplied by the value of $k_{Q_n,Q_p} = 1.17$ from equation 4.10 to obtain the estimated calibration factor in the neutron field. The listed uncertainty values in table 4.1 correspond to the 68 % confidence level and includes only estimates of the short term reproducibility, beam stability and timing errors. The chamber was fitted with a PMMA water proofing sleeve, which has a slightly lower but still similar hydrogen content per unit weight compared to water.

There is a 27 % difference between the simulated and experimental value for experiment E. In view of the level of consistency of the calorimetric experiments and because there is no well known calibration of the ion chamber for neutron fields (it is instead estimated in equation 4.10) the magnitude of the difference is not very surprising. If the simulated value of $50.4(20) \times 10^{-3}$ Gy µC^{-1} is taken for granted it would suggest a value of $k_{Q_n,Q_p} = 1.60$. The uncertainty of this number is determined mostly by the uncertainty of the simulated neutron dose, since the result from the Monte Carlo simulation appears in this calculation. The accuracy of the simulation is estimated by using an uncertainty of 20 % as indicated by the consistency of the calculations. If in addition the uncertainty of k_{Q_p,Q_0}, the beam current uncertainty, the statistical uncertainty of the Monte Carlo calculation and the uncertainty of the ionometry are factored in, this leads to an relative overall uncertainty on k_{Q_n,Q_p} of 21 %. Thus, even though the dose in experiment E is not measured directly with calorimetry, the neutron dose in experiment E is determined by a simulation that is linked to calorimetry. Therefore the value of $k_{Q_n,Q_p} = 1.60(34)$ is assigned to the PTW30001 when used in the AGORFIRM beam line. The significance of this measurement is not the calibration value itself, but rather the fact that an ionization chamber with hydrogenous wall material will show a appreciable response to the neutron field in a phantom that is irradiated by protons.

4.5.1 Effect on uncertainty of k_{Q_p,Q_0}

The primary goal of this experiment is to evaluate the effect of neutron dose on ionization chamber calibration values obtained by calorimetry in a scattered beam and their applicability in clinical scanning beams. Because there is a large range of different types of ionization chambers and because the actual correction value depends on the relative neutron contribution to the dose which varies due to

differences in beam energy and field size, it is more convenient to cover some of the smaller systematics by an overall neutron uncertainty, without attempting to apply a correction factor.

As shown in section 4.4.5, in an absolute sense, the collimator neutrons contribute 0.043 % of the dose in the beam line at KVI-CART. The most extreme situation that springs to mind is that the ionization chamber to be calibrated shows no sensitivity to the neutron fraction at all. This results in a 0.043 % error due to collimator neutrons. The reverse assumption (where the ion chamber is believed to be unresponsive to the neutron dose contribution while in reality the sensitivity is the same as that for protons) could lead to errors of equal magnitude in the opposite direction. Thus, when using k_{Q_p,Q_0} values that are measured in the KVI-CART beam to determine dose in a scanning beam un uncertainty of $\sigma = 0.043\,\%/\sqrt{3} = 0.025\,\%$ is assigned due to effects of collimator neutrons.

When the wall material is similar to water or tissue in terms of neutron cross-sections, the ionization chamber calibration coefficient can be corrected for the presence of the collimator neutron dose fraction by making use of calculated neutron dose fractions and calculated or measured k_{Q_n,Q_p} values, in which case a lower uncertainty can be assigned. The required correction factor for collimator neutrons is:

$$k_{cn} = 1 - \left(1 - \frac{1}{k_{Q_n,Q_p}}\right) \mathrm{DF}_{cn} \tag{4.11}$$

In the KVI-CART beam line the collimator neutron-induced dose fraction is $\mathrm{DF}_{cn} = 0.043 \times 10^{-2}$ and for the PMMA-walled Farmer chamber the neutron quality correction factor was measured to be $k_{Q_n,Q_p} = 1.60$, which results in a value of $k_{cn} = 1 - 1.6 \times 10^{-4}$. Using the previously mentioned uncertainties of 20 % on the neutron-induced dose due to the collimator neutrons and an uncertainty of 0.34 for the value of k_{Q_n,Q_p}, the uncertainty of the correction is $\sigma_{k_{cn}} = 0.007\,\%$. Thus, in the case of ionization chambers that are both relatively thin-walled and of hydrogenous composition a 'collimator-neutron-free' calibration in the KVI-CART beam line can be obtained without needing to assign any significant uncertainty.

Similarly, the neutron dose due to neutrons generated in the water also has an effect on the uncertainty, since the KVI-CART 70 mm circular field is different from a standard 100 × 100 mm scanned field. In principle the neutron dose fraction of the scanned field should be estimated via Monte Carlo simulation, before using it in an uncertainty estimate. However, if it is assumed that the neutrons have a mean free path that is somewhat longer than the width of the field, one may assume that the neutron dose fraction is proportional to the irradiated area of the field. Thus, a 100 × 100 mm clinical field would have a neutron dose fraction that is about $100^2/0.25\pi 70^2 = 2.6$ times higher than in the 70 mm circular field. As shown in section 4.4.5, the 70 mm circular field is characterized by a neutron dose fraction of 0.30 % due to neutrons generated in the water, meaning that in the square clinical beam a neutron contribution of $(2.6 - 1) \times 0.30\,\% = 0.48\,\%$ is unaccounted for, relative to the KVI-CART calibration. Calculating the correction factors for the

KVI-CART beam and the clinical beam according to equation 4.6 with an assumed value of $k_{Q_n,Q_p} = 1.60$ results in neutron corrections for both fields, $k_{70\varnothing}$ and k_{100^2} respectively. The required conversion factor is $k_n = k_{100^2}/k_{70\varnothing} = 1.0018$. The uncertainty of this correction is mostly determined by the uncertainty of the value of k_{Q_n,Q_p}:

$$\sigma_{k_n} \approx \frac{\sigma_{k_{Q_n,Q_p}}}{k_{Q_n,Q_p}} \left(\frac{100^2}{\frac{1}{4}\pi 70^2} - 1 \right) \cdot 0.30\,\% = 0.10\,\% \tag{4.12}$$

This means that if the neutron dose fraction in the clinic is known and if the k_{Q_n,Q_p} factor of the ionization chamber is also known it is possible to translate the calibrations obtained at KVI-CART into calibrations valid in the clinic, considering the neutron aspect only. While the above calculation shows the typical uncertainty-cost of such conversions, the actual neutron dose fraction for the calibration fields in the clinic should be calculated in order to assess the final uncertainty.

In the case of clinical scattered beam, the situation should be examined with even more caution as the neutron dose could vary considerably depending on the exact geometry of the measurement. In the experiments presented here, the collimators are at an atypically far distance from the phantom, which results in a very low collimator neutron dose. In clinical scattered beams the collimator may be positioned quite close to the phantom. If such a geometry is combined with an unusually thick-walled non-hydrogenous ionization chamber, the dose error may reach into the per mille levels.

4.6 Conclusions

When using ionization chamber calibrations in dissimilar proton beam lines, care has to be taken about the difference in beam qualities between the various beam lines. One aspect of this is the relative contribution of neutrons to the dose in each case and their effect on the calibration factor of the ionization chambers. Considering the neutron dose, the beam line at KVI-CART is different from most clinical beam lines because the field size is comparatively small. In the experimental conditions specific to our experiments, the majority of the neutron dose is due to neutrons generated in the water volume and because the neutron interaction lengths are rather large the small field size results in a lower neutron dose fraction. It should be pointed out that clinical beam lines for scattered beams can have significantly larger collimator-neutrons dose fractions.

Monte Carlo calculations indicate that in the standard beam geometry that is used for calorimetry at KVI-CART, the neutron contribution to the dose is 0.34 % of the total dose. Only 0.04 % of the dose is due to neutrons that are generated in the field collimator. The major fraction of the neutron dose in the water phantom is almost entirely due to neutrons that are generated in the water phantom.

The Monte Carlo calculations were compared to measured doses with a water calorimeter in a series of experiments. Generally the Monte Carlo results are consistent with the measured results. The experiment shows that both the production

and the interaction of the neutrons are modelled to good accuracy, which allows for quantitatively applying the model in various beam geometries. An overall uncertainty of 20 % is assigned to the calculated neutron doses based on the overall consistency of the data.

In absence of information on the response of ionization chambers to build-up neutron fields, one can only assign the total neutron dose fraction as the uncertainty. However, by analysing the simulated recoil-proton spectrum, it is clear that most ionization chambers detect the neutron fraction of the dose with a sensitivity that is of the same order of magnitude as their direct proton dose sensitivity or slightly lower. This reduces the effect of the neutron dose on the uncertainty budget.

Comparison of the predicted neutron dose (which was verified against a calorimeter) and a measured charge with an PTW30001 ionization chamber in water yields a value of $k_{Q_n,Q_p} = 1.60(34)$ for the factor that converts a TRS398 proton calibration value into a pure-neutron calibration value. This value is specific for the beam geometry as used in these experiments, but most importantly it is specific for the primary beam energy as well.

Based on the above value for k_{Q_n,Q_p} and the calculated very small contribution of the collimator neutrons, the measured calibration values at KVI-CART can be corrected to obtain a collimator-neutron free value, without introducing any significant uncertainty. More imporant however is the contribution of the neutrons generated in the water itself and the difference between the KVI-CART beam and a clinical beam. Based on a rough estimate of the neutron dose fraction in clinical beams and the uncertainty of k_{Q_n,Q_p}, the necessary beam quality conversion factors can be applied introducing an uncertainty of only 0.10 % on the total measured dose.

While the above value for the uncertainty is small, it does not apply to the calorimetry calibration itself. Rather, it applies to the corrected value after translating between different beam qualities. Since neutron dose fractions can be on the level of several per mille, these numbers need to be calculated for each individual beam line. In particular, data on the neutron dose fraction in the calibration fields of a clinical scanning beam line are not available. Regarding the scanning systems it is important to point out that although there is no contribution from collimator neutrons, the neutron dose resulting from neutrons that are generated in the water is substantial, and that it will depend on both the field size and initial energy of the beam.

In connection to the metrological issue there appears to be a related clinical issue as well. Given the fact that neutron doses can be a few per mille of the treatment dose the contribution of neutrons should be included in the treatment planning systems that are used for patient dose calculations. Neglecting the neutron dose in such calculations could easily result in errors that are as large as the uncertainty for water calorimetry. For wide clinical fields where the delivered dose is calibrated with an ionization chamber this issue is partly mitigated because many ionization chambers do sense some of the neutron-induced dose in water. However, for small fields this would not apply as there is no sufficient transverse equilibrium in that

case. Moreover, the neutrons also generate de-localized whole body doses. While the use of scanning beams compared to scattered beams is certainly an improvement in terms of reduced neutron dose, the dose due to neutrons generated in the patient must not be underestimated.

Chapter 5

Heat Transfer

Water calorimeters are used in radiation therapy as primary calibration standards for radiation dose. The technique of water calorimetry measures radiation dose by detecting the very small temperature increases that result from the absorption of energy by the water medium. The measurement of the water temperature itself provides a unique set of challenges.

Because the primary signal is an increase in temperature, fluctuations in temperature directly affect the measured value. More important, however, is the fact that the application of dose inherently gives rise to temperature gradients which result in time dependent temperature variations. Other than temperature gradients that result as a direct consequence of dose gradients, there are temperature gradients which are caused by the presence of non-water materials in the radiation field, such as the many glass parts of the calorimeter. Additionally, the operation of the calorimeter and the thermostat also can cause temperature gradients. These non-random temperature signals disturb the measurement, resulting in systematic errors in the measured dose.

In this chapter, the issue of heat transfer as a source of time dependent temperature fluctuations is introduced. A number of analytical calculations is presented that describe the dominant mode of heat transfer that is related to the dose gradients in the water. Next, a design for a new type of enlarged high purity cell ('vessel') containing a stirring mechanism is presented. This design reduces the amount of irradiated glass and increases the distance between the glass walls and the temperature probes, thereby largely reducing the thermal effects that are due to the irradiation of the vessel material. In addition to the analytical calculations, heat transfer simulations made with the finite element differential equation solver Comsol Multiphysics are discussed. The simulations are compared to the analytical calculations where applicable. An experiment is presented which serves as a test for the various heat transfer calculations. It is shown that the mixing action does not significantly disturb the measurement. The overall agreement between the measurements and calculations for effects that are due to dose gradient related

heat transfer is shown to be excellent. The dose homogeneity is identified as a key issue, which is the dominant source of uncertainty related to heat transfer. It will be shown that the experiments show a good level of control of the calorimetry. The combined uncertainty due to heat transfer and dose inhomogeneity is 0.16 %.

5.1 Heat transfer in water calorimetry

Water calorimetry relies on the direct relation between a measured temperature increase ΔT and the dose D:

$$D = C \cdot \Delta T \tag{5.1}$$

The dose can only be established reliably if the difference of the water temperature before and after the irradiation can be measured reliably. In principle, it has to be assumed that the temperature is time dependent:

$$T = T(t) \tag{5.2}$$

Due to the presence of noise, readings of the temperature need to be averaged over time. In addition, the irradiation procedures do not deposit the entire dose instantaneously. The time signal $T(t)$ includes the effects of the water heating by the irradiation beam, the effects of heat loss or gain due to thermal conduction, the effects of thermal disturbances due to the irradiation of materials other than water as well as thermal drifts due to external heat sources. For the purpose of water calorimetry, the variation of the temperature with time $T(t)$ needs to be well understood. The temperature signal needs to be well under control before, during and after the irradiation. In the case of scanning beam calorimetry, the description of the time signal $T(t)$ is rather complex due to the thermal effects of the many individual beam spots.

One of the issues with water calorimetry is that there are always temperature gradients in the water, even though the water phantom is thermally well insulated from the outside world. Because the radiation induced temperature increase is very small ($0.24\,\mathrm{mK\,Gy^{-1}}$) even small disturbances can lead to temperature drifts of the same order of magnitude as the direct effect due to the irradiation. Fortunately, since the calorimeter phantom is quite large, the resulting temperature drifts dT/dt are nearly constant during the irradiation. Domen[40] describes the use of electrodes to counteract the temperature drift using Joule heating. Another technique, also featured by Domen[35] is to extrapolate the temperature drift before and after the irradiation to obtain the temperature increase due to the irradiation only (see section 2.8.2). In the case that the drift dT/dt is constant throughout the entire procedure, there is no error associated with the drift itself. Generally, a carefully designed calorimeter shows only very small temperature fluctuations. It is usually assumed that the resulting non-constant dT/dt causes only small random contributions with a mean of zero, when averaged over multiple irradiations. An exception to this situation is described in section 5.5.2.

Fortunately, even the thermal gradients due to the irradiation have fairly small (although not negligible) effects on the apparent ΔT. Domen[35] used a simple numerical method to calculate the change in temperature after a time that is equivalent to the duration of the irradiation. He calculated a 0.8 % drop in temperature at the position of the dose maximum in a broad electron beam, but he noted that the presence of sharp dose gradients at larger distances could still have an effect on longer time scales. In addition, he warns that non-water materials in the irradiation field can act as heat sources.

5.2 Analytical heat transfer calculations

In order to better understand the issue of heat transfer, it is valuable to have approximate analytical solutions. Although it is possible to perform numerical calculations using appropriate computer software and although the results of such methods can be very accurate, it is often difficult to assess the validity of the calculation. The analytical methods can also serve as an external validation of the numerical method in specific cases.

5.2.1 Heat transfer equation

In water calorimetry it is generally assumed that the only mode of heat transfer is thermal conduction. Convection is assumed to be entirely absent, which is achieved[24] by maintaining the water temperature near its maximum density point at 4 °C. In these cases the heat transfer in a homogeneous medium is fully described by the heat diffusion equation:

$$\frac{\partial T(\mathbf{x})}{\partial t} = \alpha \nabla^2 T(\mathbf{x}) \tag{5.3}$$

The above equation describes the time evolution of the temperature T at any location vector $(\mathbf{x})$. The factor α is the thermal diffusivity of the medium:

$$\alpha = \frac{\lambda}{\rho C} \tag{5.4}$$

In the above equation, the factor λ ($\mathrm{W\,m^{-1}\,K^{-1}}$) is the thermal conductivity of the medium , ρ ($\mathrm{kg\,cm^{-3}}$) is the mass-density and C ($\mathrm{J\,kg^{-1}\,K^{-1}}$) is the specific heat capacity. The unit of α is $\mathrm{m^2\,s^{-1}}$. The values for water at 4 °C are listed in a paper by Krauss[33]. Using those values, the thermal diffusivity of water is $\alpha = 0.135\,\mathrm{mm^2\,s^{-1}}$.

Equation 5.3 is usually solved numerically in meshed geometries to obtain $T(\mathbf{x}, t)$. However, the generalized solution of the equation is[116]:

$$\xi(\mathbf{x}, t) = \frac{e^{-|\mathbf{x}|^2/4\alpha t}}{\left(\sqrt{4\pi\alpha t}\right)^n} \tag{5.5}$$

The above equation represents a normalized convolution kernel that can be used to derive the temperature profile $T(\mathbf{x}, t)$ from any known initial temperature distribution $T(\mathbf{x}, t_0)$. In this equation, n is the dimension number for the diffusion. For the three dimensional case, the temperature profile $T(\mathbf{x}, t)$ follows from the following integral:

$$T(\mathbf{x}, t) = \int_{\mathbf{R}^3} T(\mathbf{x}', t_0)\xi(\mathbf{x} - \mathbf{x}', t)\, d^3\mathbf{x}' \tag{5.6}$$

In many cases the temperate at the centre of the dose distribution is desired, in which case the integral simplifies to:

$$T(\mathbf{x} = 0, t) = \int_{\mathbf{R}^3} T(\mathbf{x}', t = 0)\xi(\mathbf{x}', t)\, d^3\mathbf{x}' \tag{5.7}$$

The above equation applies to an infinitely large homogeneous medium where the diffusion coefficient α is a constant over the entire volume. It should be noted that the temperature distributions $T(\mathbf{x}, t_0)$ that are encountered in calorimetry are generally not directly integrable according to the above definition. For this reason, equation 5.3 is often solved numerically. In specific cases however, approximations of the field shape that can be integrated analytically suffice. Solving equation 5.7 typically requires the exploitation of the planar, cylindrical or spherical symmetries in the geometry of the system.

5.2.2 Length- and time-scales for diffusion

Equation 5.7 can be solved directly in some cases, or it can be computed numerically. However, in order to better gauge the boundaries of validity of any computation one needs to view the magnitude of the temperature gradients in relation with their distance to the position of the temperature sensor.

Equation 5.5 represents a Gaussian diffusion with a standard deviation of $\sigma = \sqrt{2\alpha t}$. Table 5.1 lists relevant geometry scales and time scales based on this relation. In general, one should be careful to gauge the importance of effects by the 1σ widths of the resulting temperature disturbances, because even tiny temperature deviations are important. Generally, the measurements are set up such that the results are affected only by the tails of the Gaussian distributions for most of the effects. It is not unusual for effects to start to become important at a time that is an order of magnitude less than the time suggested based on the geometric length scale. However, the extrapolation technique that is used to derive the ΔT due to the irradiation also provides some protection from the large-scale effects, because it is only sensitive to changes in the temperature drift velocity and not to the drift velocity itself.

Table 5.1 highlights one of the major practical issues in performing water calorimetry, which is that the temperature must be stable and controlled over a very large time scale. Forced convection can be used to significantly speed up the

Scale	Time [s]	Diffusion radius σ [mm]
Temporal:		
Local dose homogeneity/volume averaging	180	7.0
Calorimeter measurement sequence	1.8×10^3	22
Spatial:		
Thermistor probe radius	0.33	0.3
Radius dose-field/cylindrical HPC	4.5×10^3	35
Radius flat-front HPC	9.3×10^3	50
Half length flat-front HPC	12×10^3	57.5
Half width calorimeter phantom	83×10^3	150

Table 5.1 – Relevant temporal and spatial scales for heat transfer. The columns for the time and the diffusion radius are linked through the width of the time dependent heat diffusion kernel. The first two items in the list are related to the time needed to do a measurement, while the other items describe the geometrical dimensions of the temperature probes, the glass vessel and the phantom.

temperature equilibration, but even then it is common to have waiting times that are on the order of hours. In the case of a High Purity Cell (HPC) lacking an internal stirring mechanism, the size of the vessel should not be much larger than the size of the radiation field. If the size of the vessel is too large, mixing the water in the phantom rather than that inside of the HPC will not be very effective in removing the thermal gradients caused by the dose deposition. Additionally, any thermal disturbance of the water (such as caused by the procedure of setting up the calorimeter in the irradiation room) would take a few hours to dissipate. Choosing a smaller vessel size will reduce the time needed for temperature gradients inside the vessel to fade away, such that the inside of the vessel does not need to be stirred. However, due to the difference in thermal heat capacity between glass and water and due to the proximity of the vessel walls to the temperature probes in the case of a small vessel, the irradiated parts of the glass vessel will cause disturbances of the temperature signal.

5.2.3 2D Gaussian dose distribution

Two dimensional Gaussian dose distributions can occur in the case of pencil beam scanning systems or in uncollimated beams with only a single homogeneous scatter foil. In what follows, it will be used as a tool to gauge the effect of non-flat dose distributions. For a two-dimensional geometry, the heat convolution kernel is:

$$\xi(\mathbf{x}, t) = \frac{e^{-|\mathbf{x}|^2/4\alpha t}}{4\pi\alpha t} \tag{5.8}$$

Since both the dose profile and the diffusion kernel are Gaussians, it is easy to calculate the temperature profile. The characteristic time associated with the 1σ width of the dose distribution is:

$$\tau = \frac{\sigma^2}{2\alpha} \tag{5.9}$$

Assuming that the full dose profile is deposited instantaneously, the temperature in the centre of the dose distribution as a function of time is:

$$\frac{T(t)}{T(t_0)} = \frac{\tau}{\tau + t} \approx 1 - \frac{t}{\tau} \tag{5.10}$$

The latter approximation is valid only for $t << \tau$. Considering the goal of sub-percent total uncertainty on the calorimetry and per mille level uncertainty components, errors lower than about 0.01 % can be considered negligible. A negligible drop in temperature of $t/\tau \leq 0.01\,\%$ corresponds to a width of:

$$\sigma \geq \sqrt{2\alpha \frac{t}{1 \times 10^{-4}}} \tag{5.11}$$

For a measurement time $t = 180\,\mathrm{s}$ the required width is $\sigma = 697\,\mathrm{mm}$. This is one to two orders of magnitude wider than any realistic beam. This shows that calorimetry requires relatively flat dose distributions. It also shows that, generally, any realistic beam requires a heat transfer correction due to the dose distribution. A Gaussian beam with a width of $\sigma = 50\,\mathrm{mm}$ would only allow for a measurement duration of $t = 0.9\,\mathrm{s}$. Fortunately, as will be shown in the following sections, locally flat dose distributions improve on this number significantly.

5.2.4 Spherical dose distribution

The estimation of the heat transfer effects in the previous section is rather pessimistic because dose distributions can be approximately flat, out to distances of many centimetres. A generalisation of a dose distribution that is flat and symmetric in all directions is a uniform sphere. No realistic dose distribution resembles a sphere. However, like a uniform spherical dose distribution, a proton SOBP is locally flat out to a certain distance. A hypothetical spherical dose distribution that fits tightly within the volume of the SOBP should show an amount of heat transfer that is slightly larger than that encountered in the SOBP.

The spherical symmetry is incorporated into equation 5.5 and 5.7 by writing them in terms of the radial coordinate $r = |\mathbf{x}| = \sqrt{x^2 + y^2 + z^2}$. In what follows, the temperature T refers to the temperature increase as a result of the irradiation and the following heat transfer only, rather than to the actual absolute temperature. The initial spherical temperature distribution is described by a 3D top hat function:

$$T(r, t_0) = \begin{cases} T_0 & r \leq R_s \\ 0 & r > R_s \end{cases} \tag{5.12}$$

In the above equation T_0 represents the added heat due to the irradiation and R_s is the radius of the sphere. Assuming that the above dose is deposited instantaneously at $t = 0$ equation 5.7 becomes:

$$T(r=0,t) = \int_0^{R_s} T(r,t=0)\xi(r,t)4\pi r^2\, dr = T_0 \frac{4\pi}{\left(\sqrt{4\pi\alpha t}\right)^3} \int_0^{R_s} r^2 e^{-r^2/4\alpha t}\, dr \quad (5.13)$$

Repeated partial integration results in:

$$T(t) = T_0 \left(\operatorname{erf}\left(\frac{R_s}{\sqrt{4\alpha t}}\right) - \frac{R_s}{\sqrt{\pi\alpha t}} e^{-\frac{R_s^2}{4\alpha t}} \right) \quad (5.14)$$

For a sphere with a radius of $R = 50\,\text{mm}$, at $t = 439\,\text{s}$, the temperature in the centre $T(t)$ has dropped 0.01 % relative to the initial temperature T_0. This means that about 2 irradiations can be performed before the temperature starts dropping by more than a negligible amount. After a time of $t = 816\,\text{s}$, the deviation is 1 %. A calorimeter experiment typically consists of a series of about 10 irradiations with a time span of 1800 s. For a single irradiation after a time of $t = 1800\,\text{s}$, the drop in temperature is 16 %. The effects of subsequent irradiations add, which further increases the effect. During the measurement time span of the last irradiation in a series of 10, the temperature will drop by 16 % of T_0 in 180 s due to the combined effect of all previous irradiations, while the total deviation at this point in time is about 50 % of T_0. The fitting procedure as described in section 2.8.2 would significantly reduce this effect. However, since accuracy on the sub-percent level is required, it is clear that detailed calculations are called for, even in fields that are as large as a 1-litre SOBP.

5.2.5 Cylindrical 2D dose distribution

Cylindrical dose distributions occur in the KVI-CART beam line, because the collimators have cylindrical apertures. The cylindrical shape matches the shape of the glass vessel that was used in the heat transfer experiments (described in the next section, 5.3), and the cylindrical symmetry enables analytical heat transfer calculations.

For plateau* or SOBP irradiations, the local depth-dose gradient is very shallow and the field edges are far away from the position of the thermistor sensors. With a cylindrical field shape, the heat transfer pattern is approximately a one-dimensional diffusion with a cylindrical symmetry. While the field inside the radius of the collimator is not perfectly flat, the sharp transverse fall-off near the field edges is far more important than the inhomogeneities within the field radius (with the exception of volume averaging effects on a time scale of the order of about 180 s,

* The 'plateau' in the context of particle therapy describes the dose profile at high residual ranges. The stopping power shows little variation with depth at high energies, which makes for very small longitudinal dose gradients.

see table 5.1). For this reason, a top hat profile is a good representation of the field shape:

$$T(r, t_0) = \begin{cases} T_0 & r \leq R_c \\ 0 & r > R_c \end{cases} \tag{5.15}$$

In the above equation T_0 represents the nominal temperature increase due to the irradiation and R_c is the radius of the cylinder. Even though the heat transfer is purely radial due to the cylindrical symmetry, a 2D heat convolution kernel should still be used:

$$\xi(r, t) = \frac{e^{-r^2/4\alpha t}}{4\pi\alpha t} \tag{5.16}$$

Assuming that the temperature increase of T_0 is induced instantaneously by the beam at $t = 0$ and rewriting equation 5.7 in 2D cylindrical coordinates yields the temperature at the centre of the field as a function of time:

$$T(r = 0, t) = \int_0^{R_c} T(r, t = 0)\xi(r, t)2\pi r \, dr = T_0 \frac{1}{2\alpha t} \int_0^{R_c} r e^{-r^2/4\alpha t} \, dr \tag{5.17}$$

Integration by substitution yields:

$$T(r = 0, t) = T_0 \left(1 - e^{-R_c^2/4\alpha t}\right) \tag{5.18}$$

Since the temperature increase of T_0 is assumed to have occurred instantaneously at time $t = 0$, the above equation can directly be interpreted as a time dependence convolution kernel:

$$\phi(t) = \begin{cases} \left(1 - e^{-R_c^2/4\alpha t}\right) & t > 0 \\ 0 & t \leq 0 \end{cases} \tag{5.19}$$

With the above equation, the temperature response can be derived for time varying dose rates $\dot{D}(t)$ as well. This removes the assumption of an instantaneous deposit of dose. The heating rate for time varying dose rate is:

$$\dot{\theta}(t) = \frac{\dot{D}(t)}{C_p} \tag{5.20}$$

That is, the rate of temperature increase of a material being irradiated is inversely proportional to its heat capacity C_p. The temperature response at the centre of the cylindrical field can be calculated at any time t_e by integration of the time dependence convolution kernel:

$$T(t_e) = \int_{-\infty}^{t_e} \dot{\theta}(t)\phi(t_e - t) \, dt \tag{5.21}$$

Generally, for arbitrarily time-varying dose rates, the above equation would have to be computed numerically. In practice the irradiation closely resembles a constant dose rate that is sustained for the duration of a single irradiation:

$$\dot{\theta}(t) = \frac{\dot{D}(t)}{C_p} = \begin{cases} 0 & t > t_{\text{irr}} \\ \dot{D}/C_p & 0 < t \leq t_{\text{irr}} \\ 0 & t \leq 0 \end{cases} \tag{5.22}$$

With the above constraints on the dose rate, equation 5.21 simplifies to:

$$T(t_e) = \begin{cases} \frac{\dot{D}}{C_p} \int_0^{t_{\text{irr}}} \phi(t_e - t)\, dt & t_e > t_{\text{irr}} \\ \frac{\dot{D}}{C_p} \int_0^{t_e} \phi(t_e - t)\, dt & 0 < t_e \leq t_{\text{irr}} \end{cases} \tag{5.23}$$

It is shown in the above equation that by modifying the integration limits appropriately, the above equation allows calculating the temperature signal during the irradiation as well. It should be noted that in equation 5.23 t_e represents the time that has passed since the beginning of an irradiation. However, of interest is the temperature signal at any time t_e due to a irradiation that occurred before t_e, which requires rewriting the time coordinates such that they are relative to the time of evaluation t_e:

$$t' = t_e - t \tag{5.24}$$

$$T(t_e) = \frac{\dot{D}}{C_p} \int_{t_e - t_{\text{end}}}^{t_e - t_{\text{start}}} \phi(t')\, dt' \tag{5.25}$$

The above equation describes the temperature effect at a time t_e due to a single irradiation that occurred between the times t_{start} and t_{end}. Evaluation of this equation requires the following integral:

$$\int e^{-R_c^2/4\alpha t}\, dt = t e^{-R_c^2/4\alpha t} - \frac{R_c^2}{4\alpha} \text{Ei}\left(\frac{R_c^2}{4\alpha t}\right) \tag{5.26}$$

The above integral is derived through partial integration. The second term in the equation is the exponential integral[117]:

$$\text{Ei}(x) \equiv -\int_{-x}^{\infty} \frac{e^{-y}}{y}\, dy \tag{5.27}$$

Plugging equation 5.26 in equation 5.25 yields:

$$T(t_e) = \frac{\dot{D}}{C_p} \left[t' \left(1 - e^{-R_c^2/4\alpha t'}\right) + \frac{R_c^2}{4\alpha} \text{Ei}\left(-\frac{R_c^2}{4\alpha t'}\right) \right]_{t' = t_e - t_{\text{end}}}^{t' = t_e - t_{\text{start}}} \tag{5.28}$$

$$T(t_e, t_{\text{start}}, t_{\text{end}}) = \frac{\dot{D}}{C_p}\Bigg[(t_{\text{start}} - t_{\text{end}}) + (t_e - t_{\text{end}})e^{-\frac{R_c^2}{4\alpha(t_e - t_{\text{end}})}} - (t_e - t_{\text{start}})e^{-\frac{R_c^2}{4\alpha(t_e - t_{\text{start}})}} + \frac{R_c^2}{4\alpha}\text{Ei}\left(-\frac{R_c^2}{4\alpha(t_e - t_{\text{start}})}\right) - \frac{R_c^2}{4\alpha}\text{Ei}\left(-\frac{R_c^2}{4\alpha(t_e - t_{\text{end}})}\right)\Bigg] \tag{5.29}$$

In the above equation, all of the terms multiplying the nominal heating rate $\dot{D}/C_p$ have units of time. It is an exact calculation of the temperature at the centre of a uniform cylindrical dose distribution. The error integral $\text{Ei}(x)$ has to be computed numerically and most mathematics software packages provide accurate implementations of this function. While equation 5.29 itself is exact, it is an approximation of the situation with the calorimeter because the dose distributions will not be perfectly uniform nor perfectly cylindrical and the thermistors are not positioned in the centre of the field, but a few millimetres off-centre.

Equation 5.29 describes the temperature drift due to a single irradiation at constant dose rate between the times t_{start} and t_{end}. A typical calorimeter measurement protocol consists of many series of about 10 consecutive irradiations. The temperature effects of each of those irradiations have to be added to calculate the temperature at any time during the irradiation sequence:

$$T(t_e) = \sum_{i=1}^{i=N} T(t_e, t_{\text{start,i}}, t_{\text{end,i}}) \tag{5.30}$$

The above equation is an integration of equation 5.21 assuming a piece-wise constant dose rate. Given the duration of an irradiation (60 s) compared to the field size listed in table 5.1, it is clear that the dose rate can be assumed to be constant during any single irradiation. In fact, the effect of the radial heat transfer on the uncorrected measured dose of any one irradiation can scale at most with the dose rates of the individual irradiations preceding that irradiation. As will be shown in section 5.4.1, the magnitude of the corrections amount to only a few per mille, meaning that dose rate variations on the order of 10 % during an irradiation sequence are readily admissible because the magnitude of the corrections will be modulated by at most 10 %.

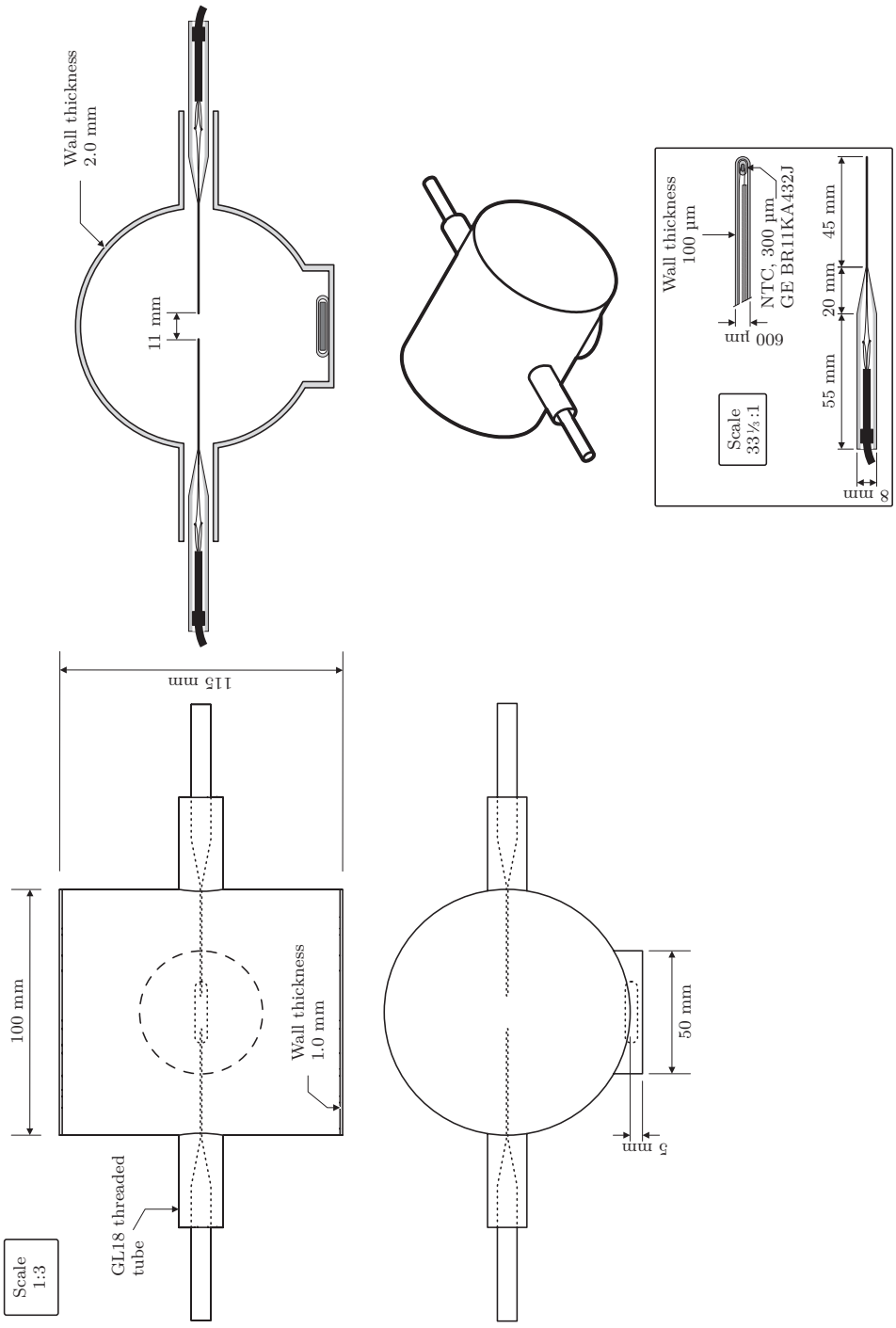

Figure 5.1 – Drawing of the high purity cell ('vessel') that was used for the heat transfer experiments. The drawing is approximately to scale. Not shown are the details of the valves and the mechanism that is used to align the probes. The inset shows a magnification of the tip of the thermistor-probe.

5.3 High purity cell design

The design rationale of the vessel shown in figure 5.1 is that the proton beam does not directly hit the cylinder side walls and that it is long enough to accommodate an entire SOBP such that the Bragg peak never covers the front wall or back wall. If the side wall were to be hit by the protons, it would create complex dose patterns due to scattering of the protons in the glass, as well as complex temperature patterns due to the differential temperature increase of glass relative to water. In the case of a SOBP, the beam could be stopped at a small distance before the back wall, while the front wall would receive a dose that is slightly lower than the dose at the centre of the SOBP. This significantly reduces the effects of the differential temperature increase of the glass in the front and back windows. Additionally, the large dimensions of the vessel also decrease the effect of the chemical heat defect in the air saturated water outside the vessel. While the vessel was designed for SOBP irradiations, the experiments in this thesis involve plateau irradiations such that both the front and back wall are directly irradiated.

In the vessel shown in figure 5.1, the flat front wall and back wall are hit directly by the proton beam. Because of the difference in heat capacity between glass and water, the glass will have a higher heating rate compared to the surrounding water. As described by Krauss[33], the heat generated in the front wall and the back wall of the glass vessel affect the uncorrected measured dose at the centre of the vessel. At a vessel length of 115 mm however, these effects are attenuated significantly, because the vessel shown in figure 5.1 is almost three times longer than the vessel described by Krauss.

This point can be demonstrated by a simple calculation considering the heat conduction in water only. Firstly, it is assumed that the heat transfer is purely one dimensional, meaning that there is only longitudinal heat transfer in the direction perpendicular to the front wall and back wall. Secondly, it is assumed that at the start of a typical series of irradiations, the temperature upstream and outside of the vessel is raised instantaneously by an amount $\theta = \sum D/C_p$ equal to the total nominal temperature increase that is caused by all of the irradiations in the series. Furthermore it is assumed that this temperature increase persists on top of the irradiation signal throughout the entire series of irradiations. The described situation is that of a one dimensional heat penetration in an infinite medium driven by a wall at a constant temperature. The time dependent solution of the heat diffusion equation in this case is[118]:

$$\frac{T(t)}{\theta} = \operatorname{erfc}\left(\frac{L/2}{2\sqrt{\alpha t}}\right) \tag{5.31}$$

In the above equation, L is the length of the vessel and α is the thermal diffusivity of the water. This equation is not a quantitative estimate of any effect, rather it is a huge overestimate of the effects of the differential temperature increase of the glass.

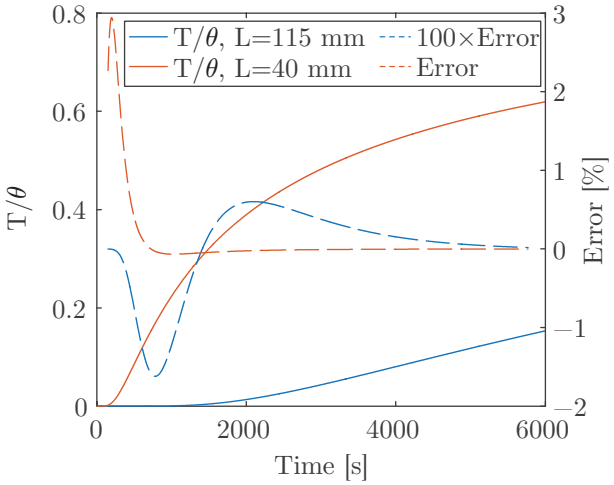

Figure 5.2 – Time dependent temperature drift as calculated with equation 5.31, for two distances out to a constant-temperature boundary condition. The shown error is calculated by calculating the line fits and their extrapolations as if it were a normal calorimeter run. The error is calculated based on the assumption that the nominal temperature increase due to the irradiation of the water is one tenth of the temperature θ of the disturbance, to estimate the effect of a full series of 10 irradiations on the determination of the dose of one of those irradiations.

Figure 5.2 shows the result of equation 5.31 for two sizes of vessels. The longer version with a length of 115 mm was used for the measurements described in this chapter, while a vessel with a length of about 40 mm was used by Krauss in ^{60}Co[33]. Also shown in the figure is the resulting error in the measured dose that is obtained by performing the line fits and extrapolations that are normally used to derive the radiation-induced temperature increase due to the direct irradiation of the water near the thermistors. The calculation assumes that $\theta = \sum D/C_p$ represents the heat of 10 irradiations. Effectively, the calculation assumes that the front wall of the vessel is held at an elevated temperature relative to the centre of the vessel and the magnitude of the temperature difference equals the full temperature increase that can be expected from a complete series of irradiations. This assumed temperature disturbance has a far greater effect than any glass-heating related effect, due to the constant temperature boundary condition. The largest error in the case of the $L = 115$ mm vessel is only 0.015 % and therefore quite negligible. However, for the smaller vessel, the error is significant.

It should be noted that the assumed conditions constitute an overestimate of any wall-related effect. Because of this huge overestimate, the actual error in the measurement system is of no concern. In reality, the diameter of the beam is comparable to the distance between the thermistors and the front and back walls of the vessel. The heat transfer effects are not one dimensional, which further decreases the effect. The temperature increase outside the vessel will be only a

few percent higher compared to the inside due to the chemical heat defect in the oxygen saturated water of the phantom. The assumed temperature disturbance is equivalent to 100 % of the deposited dose, which is a huge overestimate. From this calculation it is clear that the measurements with the large vessel do not suffer from glass-related heating effects or from any chemical heat defect in the water outside the vessel in any significant way.

5.4 Heat transfer simulations

As shown in section 5.2, in some cases meaningful analytic calculations can be performed to obtain the time evolution of the temperature due to the heat transfer effects that are in turn driven by temperature gradients related to the radial dose distribution. However, the dose-depth curve is not conforming to any shape that would make analytic calculations possible. Additionally, the geometry of the temperature probes is too complicated to be able to derive approximate analytical solutions. Even in the case of the radial heat transfer, the analytical solution is only approximate, because the temperature sensors are located a few millimetre off the beam axis and because the field shape is not perfectly uniformly flat within the radius of the radiation field. For these reasons, numerical calculations are essential to obtain accurate results. The analytical calculations serve as a consistency check in the applicable cases.

Calculations of heat transfer effects in water calorimetry have been performed by many research groups. Sassowsky and Pedroni[51] have calculated the thermal effects of spot-scanning in clinical pencil beam scanning systems. Sarfehnia et al. [38] describe heat transfer calculations and glass-heating effects in both scattered and spot-scanned proton beams. Their geometry is similar to the geometry used in this work, except that they used a rather small glass vessel. They also report[119] on heat transfer calculations for brachytherapy dosimetry with a similar system. Krauss[33, 28] discusses the simulation of heat transfer effects for a ^{60}Co water calorimeter, including heating effects due to the direct irradiation of the thermistor probes. De Prez et al. [120] show calculations of heat transfer in MV-photon and ^{60}Co beams.

The calculations and experiments described here are to some extent similar to the work described by Krauss, because of the beam geometry and general methodology of experimental verification of the heat transfer models. The work of Sarfehnia is similar because of the use of a scattered proton beam. In the work of De Prez et al. , the lateral heat transfer effects are similar in character compared to what is shown here due to the limited field size and long duration of their experiments. All of the numerical heat transfer calculations that are described here were performed in Comsol[121], using the time dependent heat transfer module. All materials that were used in the simulation (including water) were assumed to behave as opaque solids, meaning that convection and radiative heat transfer were assumed to be absent.

5.4.1 Transverse field shape

The heat transfer due to the transverse (radial) dose gradients was calculated in Comsol by creating an 1D axisymmetric model. The model fully exploits the symmetry, because only the radial effects need to be modelled. Effectively, the model is a simple 1D diffusion which can easily be solved at sufficient resolution without running into any problems related to numerical stability. The entire volume was modelled to consist only of water and to extend out to a radius of 150 mm. The mesh was modelled as an equidistant grid with a mesh size of 0.2 mm. This mesh density should allow for accurate calculations of heat diffusion near sharp temperature gradients on time scales down to $t = 0.2^2/2\alpha = 0.15\,\mathrm{s}$. Since the dose penumbra is much wider than the mesh density and because it is located far from the measurement point, the chosen mesh density is high enough to accurately model the heat transfer. The time stepping of the simulation between two irradiations was generally confined by a maximum time step of 50 ms. At the start and at the end of an irradiation, the time step drops to as low as 0.2 µs because of enforced relative and absolute tolerances of 1×10^{-10}. The software also integrates the dose rate
completing 11 irradiations over a time span of 2100 s, the error in the integrated dose rate is only 4×10^{-8} of the dose of one single irradiation. The output of the simulation is the temperature at a radial distance of 5.5 mm, which corresponds to the position of the thermistor in the temperature probes.

The spatial dose profile was implemented in Comsol by using error functions to fit experimental transverse dose profiles, as described in section 2.10.1:

$$A(r) = \frac{1}{2}\left(a \cdot \mathrm{erfc}\left(\frac{r-b}{c}\right) + d \cdot \mathrm{erfc}\left(\frac{r-e}{f}\right)\right) \tag{5.32}$$

That is, a time dependant heat source was activated in Comsol according to the specified large scale time structure. The spatial distribution of the heat source was parametrized according to the above equation. The resulting simulation models the large scale heat transfer effects due to the finite field diameter and the small dose gradient within the field, for as much as those gradients are a function of radius.

The parameters of the fit for the collimator opening diameters of 70 mm and 50 mm are listed in table 2.2. Figure 5.3 shows the calculated temperature as a function of time for field collimators with a diameter of 70 mm and 50 mm. The top pane shows Comsol calculations for the temperature with a simulated dose rate of $1\,\mathrm{Gy\,min^{-1}}$. The graphs in the top pane can simply be scaled for higher dose rates, provided that the time structure remains exactly the same. Because heat is diffusing away radially, the curves tend to attain negative slopes during the cycle of irradiations. The bottom pane shows the result of applying the fitting and extrapolation procedure (section 2.8.2) on the simulated temperature data of the top pane and the result is expressed in terms of a deviation of the dose obtained with the fitting procedure from the nominally applied dose. Clearly, both the use of a 70 mm and a 50 mm collimator will result in non negligible heat transfer

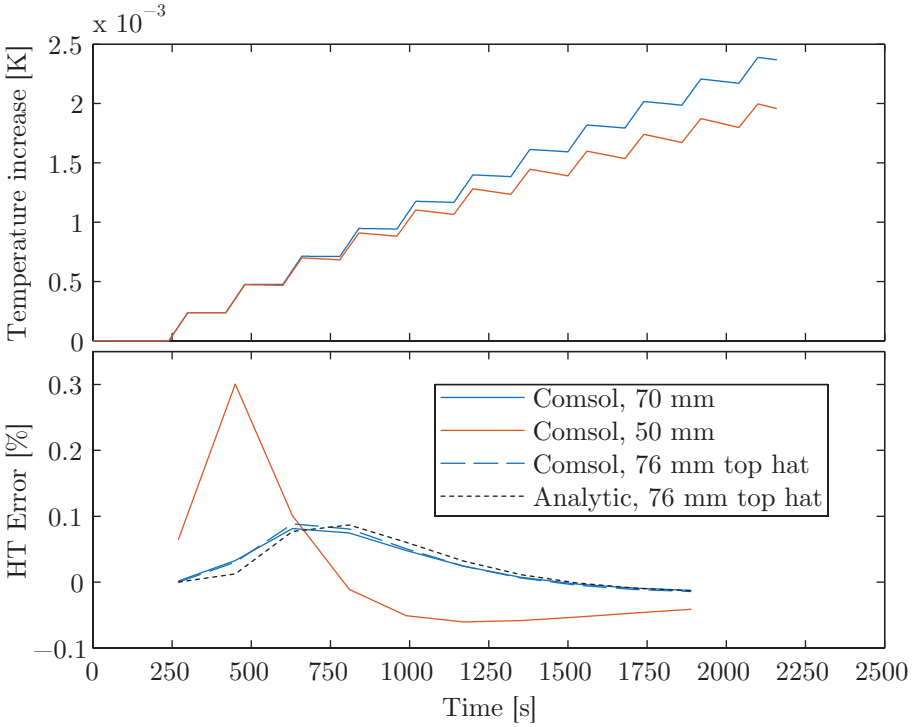

Figure 5.3 – Calculations of the temperature profile due to radial heat transfer for field collimators with a diameter of 70 mm and 50 mm. The top pane shows the simulated temperature due to 11 consecutive irradiations. The bottom pane shows the result of applying the linear fitting procedure and extrapolation (section 2.8.2), expressed as a deviation from the nominal dose value. It also shows the result of simulating a top hat profile with a diameter of 76 mm in Comsol and the analytical calculation according to equation 5.30 of the top hat profile. Note that the simulated heat transfer errors in the bottom pane contain one data point per irradiation.

effects. For comparison, the bottom pane also shows the results when the simulated field is assumed to be a top hat profile with a diameter of 76 mm, matching the measured diameter of the field. The bottom pane also shows the effect of the heat transfer if the temperature as a function of time is calculated analytically with equation 5.30. The results are nearly identical, which validates the simulations in Comsol. The slight difference can be explained by the fact that the analytical calculation computes the temperature at the centre of the dose distribution, rather than at the location of the thermistors. Overall, when using fairly long irradiation sequences of 10 irradiations with the 70 mm collimator, the average error due to heat transfer is very low. The average systematic error due to radial heat transfer over 10 irradiations is 0.0246 % for the calculation based on the experimental dose profiles, 0.0251 % for the top hat profile and 0.0257 % for the analytical calculation. The difference between any of these methods, when averaged over 10 irradiations is

negligible. This shows that, at least for the 70 mm collimator, the radiation field is wide enough for heat transfer effects not to depend on the details of the penumbra of the dose distribution or on the numerical details of the simulation.

5.4.1.1 Field inhomogeneities

One issue with the previous calculations is that it assumes that the radiation field within the radius of the collimator is essentially flat. While the previous calculation shows that the shape of the field in terms of its penumbra is not important for the given collimator dimensions, there is still the possibility that small variations in the field may contribute to heat transfer effects. For this reason, a Comsol heat transfer calculation was also performed using the measured 2D dose profile as input.

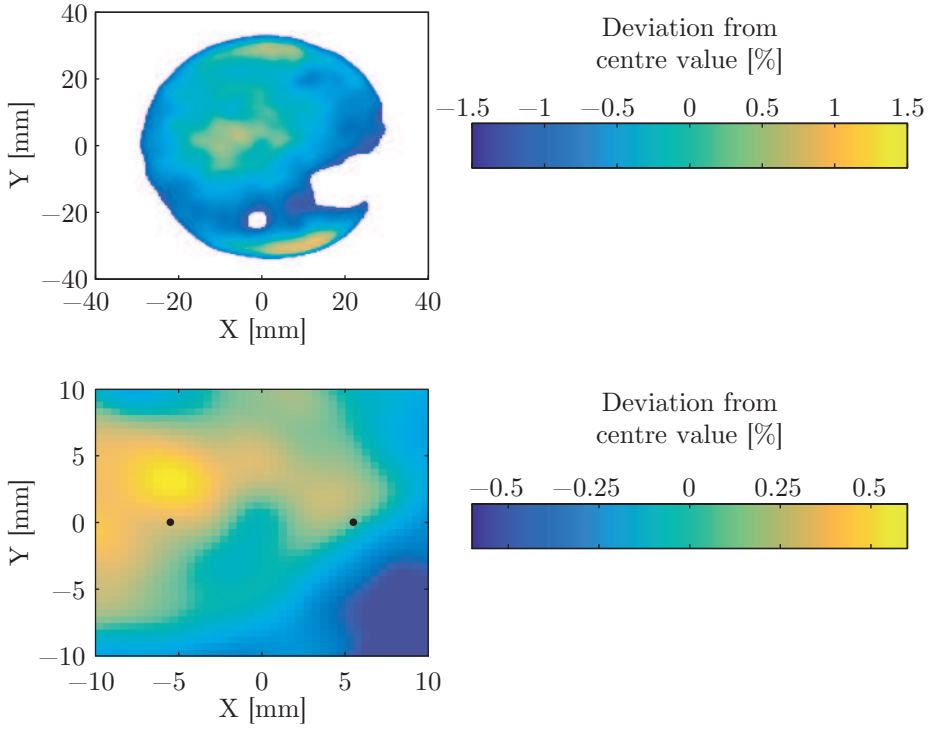

Figure 5.4 – Dose profiles of the 70 mm field obtained with Lanex scintillation imaging. The graphs are the input to the heat transfer calculation in Comsol. Black dots show the position of the thermistor tips in the dose field. The white areas represent pixel values outside of the range of the chosen colour axis. The imaging procedure described in section 2.10.1 was used, with polystyrene degrading material to place the screen at a water equivalent depth of 65 mm. Additionally, a 1σ 1.5 mm Gaussian blur was applied to smooth out some remaining noise. The remaining variations have been determined to be caused by imperfections in the scattering foils and are not of statistical nature.

Figure 5.4 shows the dose distribution that was used as input for 2D Comsol heat transfer calculations. The figure shows an overview of the whole radiation field as well as a zoom-in on the region where the probes are positioned. The field is normalized to the value at the centre position.

Clearly visible is that there are percent level variations in the dose distribution within the radius of the collimator. Near the edges of the field are hot spots due to collimator scraping. More importantly, there are also "strong" variations near the centre of the field. These variations are attributed to imperfections in the inhomogeneous scatter foil that is used to flatten the field. Before an experiment, the thermistor probes are positioned such that their thermistor beads are located on the horizontal axis, at $X = -5.5\,\text{mm}$ and $X = 5.5\,\text{mm}$. Thus, the output of the heat transfer calculation results in a mostly constant multiplicative factor relating the dose at $X = -5.5, 5.5$ to the dose at $X = 0$. The required corrections are $-0.29\,\%$ for the left position and $-0.04\,\%$ for the right position. This is a displacement correction that takes into account that the location of the thermistor is different from the location at which the dose reading is desired.

In addition to the fairly large correction that is described above, there is also the effect due to heat transfer. This includes the effect of the field edges which was described in section 5.4.1, the collimator-scraping hot spots, dose averaging near the thermistor probes and larger scale heat transfer from the hills in the upper left of the distribution to the valleys in the lower right of the distribution. The largest effect in terms of drifting temperature slopes over the duration of a cycle of 10 successive irradiations is the radial heat transfer due to the field edges, the effects of which are shown in figure 5.3. This component of the heat transfer is essentially the same between the radially symmetric calculations in section 5.4.1 and the fully 2D calculations in this section. The other effects become apparent on intermediate time scales, changing the shape of the drift curves after each irradiation.

Figure 5.5 shows the effect of applying the fitting procedure to the data resulting from the Comsol calculation. For comparison, also the calculations from figure 5.3 have been included. Since the 2D Comsol calculation determines the temperature rise at the location of each individual thermistor in the radiation field and since the desired dose is the dose at the centre of the field, the calculated heat transfer errors will include the difference between the doses at these locations. This is a displacement correction, but not a heat transfer correction. In order to emphasize the effects of the heat transfer, the data that was used for the 2D simulation plots have been corrected using the values of the dose rate at the locations $X = -5.5, 5.5$. Clearly, after applying the fitting procedure to obtain dose, the overall shape of the curves is essentially the same. Although there are large differences between the two probes positions, the variations in the curves are almost entirely determined by the effects of the field edges rather than the exact 2D dose distribution closer to the probes. The difference between the left and the right curve reflect the effects of heat transfer due to volume averaging at small distances from the probes and

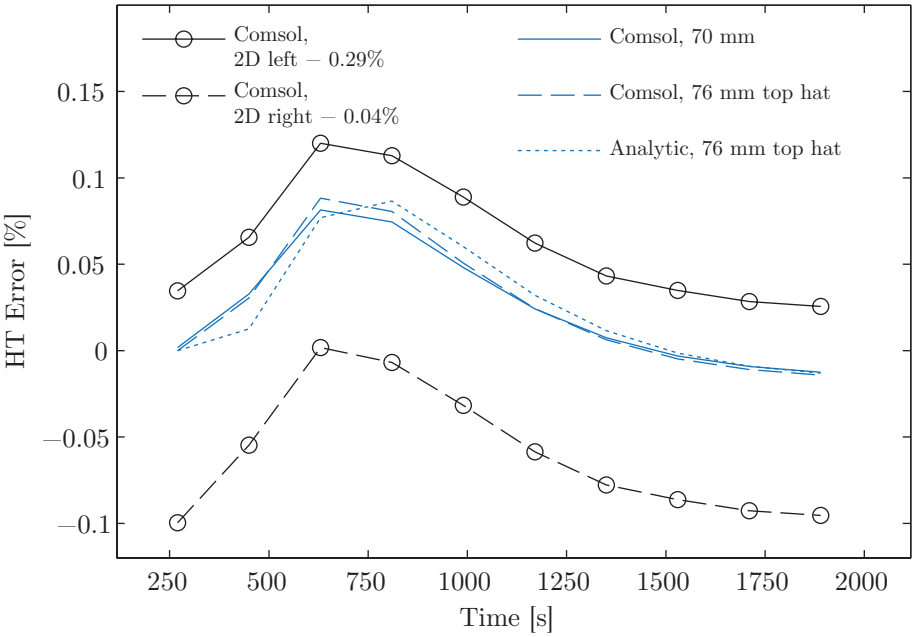

Figure 5.5 – Result of applying the fitting and extrapolation procedure to the simulated temperature transients using the 2D Comsol calculation. For reference, the data from figure 5.3 have also been included and the graphs for the 2D calculation have been shifted with the values that were obtained from figure 5.4. The remaining offset is related to heat transfer.

large scale heat transfer at larger distances. These effects are difficult to observe experimentally as it leads to only little variation in the apparent dose depending on the irradiation-number in a series of irradiations.

Figure 5.6 shows the thermal transients after the first irradiation in a series, as calculated with the 2D Comsol models and the 1D-radial model. Similar to figure 5.5 the curves for the 2D calculations have been corrected based on the values of the 2D dose distribution at the location of each thermistor, thus emphasizing the effects of heat transfer rather than direct differences due to field inhomogeneities. For reference, the result of the 1D-radial model which is sensitive to the field edges is also included. A 1σ diffusion length of 4 mm is associated with the duration of the irradiation of 60 s. Therefore, the difference between the two 2D graphs is attributed to volume averaging near the location of the probe tips. The overall slope of the two 2D calculations is attributed to the heat transfer resulting from the larger scale dose gradient that is visible in the top pane of figure 5.4. Although there is a small difference in the shape of the curves resulting from the 2D models that may be due to difference in volume averaging between the two locations, the main slope is nearly the same which reflects the somewhat larger distances over which heat transfer is occurring. The difference between the two probes is

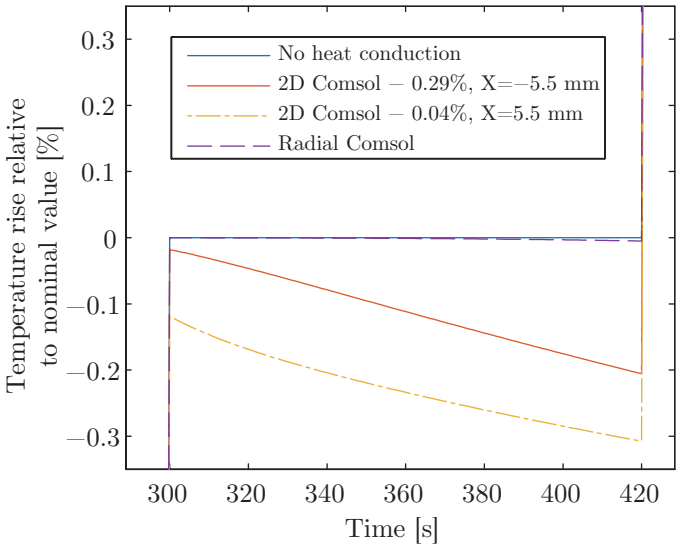

Figure 5.6 – Calculations of the thermal transient due to dose distribution effects. The plot zooms in on the drift curve after the irradiation has stopped. Shown is the difference in temperature relative to the nominal total temperature increase of one single irradiation. The curves for the 2D calculation have been corrected with the values that were obtained from figure 5.4, emphasizing heat transfer effects rather than the direct effect of spatial dose variations.

very hard to resolve experimentally, if one keeps in mind that there is also the issue of each individual probes' calibration and the calibration of its measurement chain. The slope of the thermal transient that is common to both probes can be resolved experimentally if there is low statistical noise. One of the challenges is to resolve this slope against the rather large transients due to the material dependent temperature increase of the probes, which is described in section 5.4.2. Considering scanning beam applications, a recurrent inhomogeneity in spot scanning can cause dose errors of the same magnitude as the inhomogeneity itself. Such effects needs to be corrected, however validation of the corrections below the statistical limit of a routine water calorimetry measurement is more challenging still.

5.4.2 Probe excess temperature

One of the issues in water calorimetry is the differential temperature increase of materials other than water. The temperature probe itself is one of the larger disturbances in the measurement of the radiation induced temperature increase. Materials from which the probe is constructed have different thermal responses to the radiation field as compared to water. Mainly, the effect is due to large

differences in the heat capacity, but there are also variations in stopping power. The effects of temperature probe heating have been described by Krauss[33, 28] using both simulations and experiments.

Neglecting the effects of dose inhomogeneities at the boundaries of the materials due to delta-electrons, the heating rate $\dot{\theta}_m$ of any material relative to the heating rate of water $\dot{\theta}_w$ is:

$$\frac{\dot{\theta}_m}{\dot{\theta}_w} = \frac{S_m/\rho_m}{S_w/\rho_w}\frac{C_{p,w}}{C_{p,m}} \tag{5.33}$$

In the above equation S_m/ρ_m,$C_{p,m}$ and S_w/ρ_w,$C_{p,w}$ are the proton mass-stopping powers and heat capacities for the material and water, respectively. The stopping power ratios for most of the important materials is slightly below unity. Because the heat capacity of water is much larger than the heat capacity of any of the used materials, all of those materials will show a relative heating rate $\dot{\theta}_m/\dot{\theta}_w$ much larger than unity.

It is clear from table 5.1 that this 'excess temperature increase' dissipates to the surrounding water on the time scale of a few seconds. This means that choosing the Post-irradiation Fit Margin t_{PoFM} fairly large would avoid much of the problems of the excess temperature. However, the decay of the excess temperature after the irradiation is not exponential. In fact, the temperature profile resembles the diffusion kernel of equation 5.5. In the middle of the thin shaft of the probe, the temperature response will resemble the $1/t$ behaviour that is associated with two dimensional heat diffusion, because of the cylindrical symmetry. Three dimensional diffusion is characterised by $1/t^{3/2}$ behaviour. Since the NTC sensing resistor is located at the very tip of the thermistor probe, the behaviour will be somewhere between $1/t$ and $1/t^{3/2}$. The issue is that this behaviour is long-tailed. The excess temperature never quite decays entirely before the next irradiation is started, which means that the resulting error of any individual irradiation depends on its position in the sequence of irradiations. While the use of the t_{PoFM} margin makes the measurement less sensitive to the details of the geometry of the probe and the thermal conductivities of the materials, it largely fails to remove the sensitivity to the integrated differential temperature increase according to equation 5.33. Because the fits of the temperature drifts before and after the irradiation are extrapolated to mid-run, the effect of the 'excess temperature increase' is further amplified. Because it is difficult to avoid the effects of the probe excess temperature entirely, it must be studied in detail.

To study the effects of the excess temperature in the probe, a model was created using Comsol. The created model was a 2D axisymmetric model, meaning that the probe is modelled to be fully symmetric in the radial direction, but not in the direction along the length of the probe. The dose distribution in the absence of the probe materials was assumed to be uniform over the entire volume, while the dose in the non-water materials was scaled with the relative stopping powers. A schematic drawing of the probe is shown in figure 5.1. Only the thin 45 mm long tip was considered in this model. Additionally, the model was simplified by not

including the thin wires or the insulating tube that surrounds one of the wires. The cavity of the probe was modelled to contain glue. The NTC thermistor itself was also implemented, including its borosilicate glass coating. The material constants

Material	λ [W m^{-1} K^{-1}]	ρ [kg m^{-3}]	C_p [J kg^{-1} K^{-1}]	α [mm^2 s^{-1}]	$\frac{S_m/\rho_m}{S_w/\rho_w}$	$\dot{\theta}_m/\dot{\theta}_w$
Water	0.568	1000	4206.8	0.135	1	1
Borosilicate Glass	1.1	2230	750	0.658	0.832	5.04
NTC bead	3.5	4000	250	3.5	0.832	15.1
LightWeld Glue	0.1	1040	300	0.321	0.981	13.8
PMMA	0.19	1190	1420	0.112	0.973	2.88

Table 5.2 – Materials used in heat transfer calculations and their properties. The thermal constants for water, glass and the NTC bead have been obtained from a paper by Krauss[33]. No published values were available for the LightWeld glue, which were instead assumed to be the same as for another type of urethane methacrylate [122]. The stopping power ratios were calculated with PSTAR[111]. For the NTC bead, the value of $\frac{S_m/\rho_m}{S_w/\rho_w}$ was taken to be equal to the value for glass. For the LightWeld glue the stopping power ratio was calculated from elemental stopping powers with PSTAR using the elemental composition according to the MSDS[123].

that were used in the simulation are listed in table 5.2. Figure 5.7 shows the geometry of the probe as it was simulated in Comsol. Only the tip is shown in the figure. An insulating boundary condition was enforced at a position of 5.5 mm (on the horizontal axis) from the thermistor tips along the entire radial coordinate to account for the other probe that is installed in the vessel. Error bounds of 1×10^{-8} were enforced, which caused the time steps to be as small as 10 µs near the start and the end of the irradiations.

Figure 5.7 shows the geometry, mesh and the temperature distribution at the end of the first irradiation. Plotted is the excess temperature increase relative to the temperature increase that is expected from water. The thermal gradient near the tip is rather large, due to the breakup of the '1D'-radial symmetry.

Figure 5.8 shows the result of Comsol calculations for two types of probes. In addition to a simulation for the currently used probe where the probe cavity is filled with LightWeld glue, a hypothetical model is included where the probe consists entirely out of glass (except for the thermistor bead). Additionally, the graph also shows the effect of variation of the probe diameter within the manufacturing tolerances. In the latter case, the diameter is decreased by 50 µm. The top pane shows the temperature of the NTC thermistor bead as a function of time during a series of 10 irradiations. The bottom pane shows the result of applying the fitting and mid-point extrapolation procedure to derive the dose, expressed as a deviation from the nominally expected value from the irradiation of water. The graphs show very sharp temperature transients at the start and at the end of the irradiations, which are largely avoided by the fitting margin t_{PoFM}. Because of the rapidly changing slopes of the excess temperature versus time, the slope of the line fits in

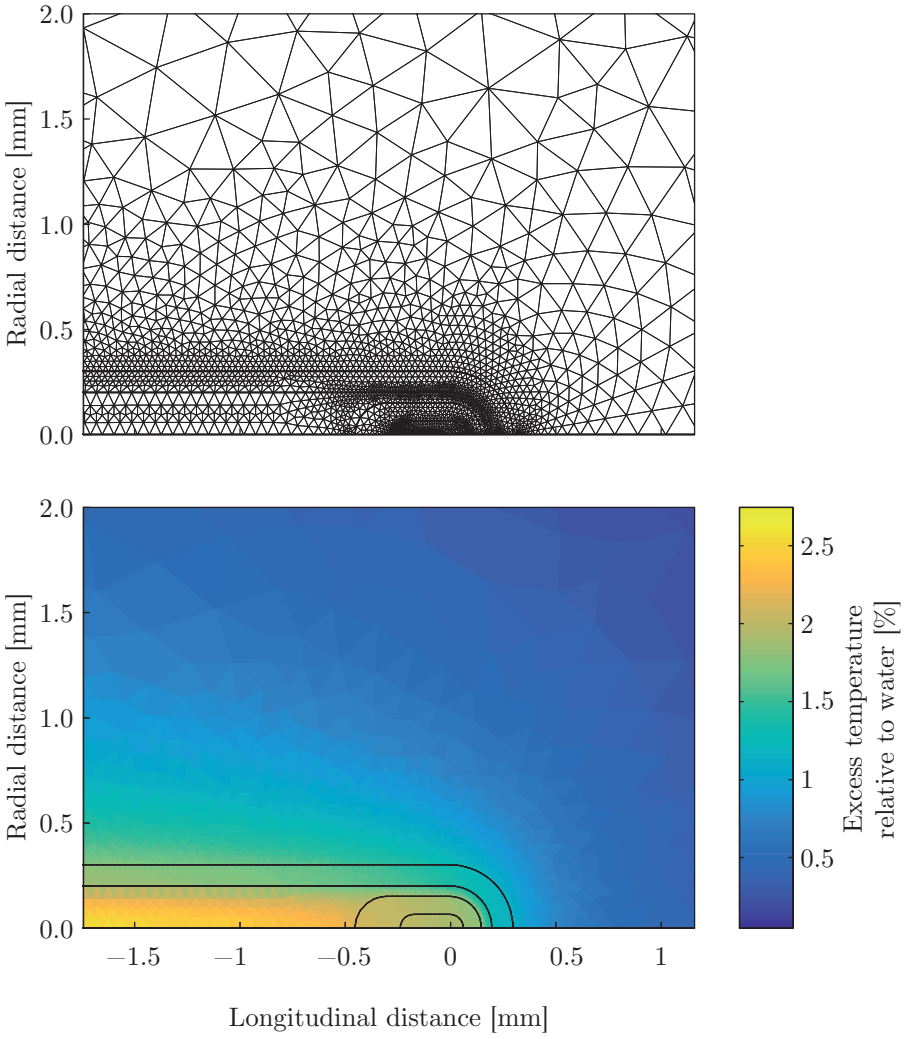

Figure 5.7 – Zoom-in on the probe tip in the Comsol simulation, showing the probes geometry, meshing and the temperature distribution at the end of the first irradiation. The limiting meshing parameter is a number of 5 mesh points in the narrow layers, which results in a mesh size near the inside of the glass tip half-sphere of about 7 µm, occasionally dropping down to 1 µm. In the simulation, the water volume extends to a radius of 30 mm, at which position the mesh size is about 7 mm.

the drift periods between the irradiations will also change. The extrapolation of the line fits to the time of mid-run causes most of the apparent heat transfer error, which is shown in the bottom pane.

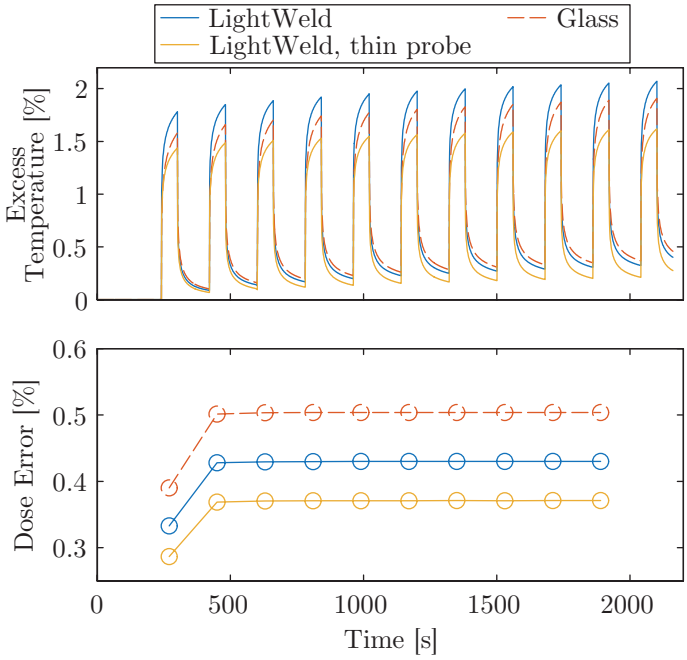

Figure 5.8 – Comsol calculations of the excess temperature of the NTC thermistor relative to the nominally expected temperature increase of the water. The top pane shows the excess temperature as a function of time for a probe of which the cavity is filled with LightWeld glue and a hypothetical probe of which the cavity is filled with glass as well as for a regular probe with a thinner diameter that is within the tolerance of the manufacturer. The bottom pane shows the result of applying the fitting and mid-point extrapolation procedure.

Clearly, the value of the heat transfer error due to differential temperature increase of the probe is very large relative to the uncertainty budget. The required correction of approximately $-0.42\,\%$ is by far the largest correction, but it is also largely unavoidable. Increasing the fitting margin t_{PoFM} by many tens of seconds will not significantly reduce the magnitude of the effect. To further quantify possible modelling uncertainties, the simulation was also performed for a hypothetical probe which consists entirely of glass. The difference in the resulting heat transfer error between these simulations amounts to $0.07\,\%$ of the dose deposited in the water. The relative importance of the heat capacity of the glue in the probe cavity is not quite as significant as might be expected based on its relative heating rate $\dot{\theta}_m/\dot{\theta}_w$. Instead, the thermal conductivity of the filler material determines to which extent the tip (containing the thermistor) is thermally shorted to the long and thin cylinder of the probe. In the case of a glass filler, heat is efficiently transported from the main cylinder to the tip, which causes a increase in the heat transfer error. For a thermally insulating filler material like the LightWeld glue, the probe tip senses a more three-dimensional heat conduction. The sensing bead has a glass

coating that is only slightly smaller in diameter than the diameter of the cavity so that the filler material is less important. With an insulating filler, it is mostly the tip diameter that determines the magnitude of the heat transfer error.

To gauge the possible effect of variations in the tip diameter in the simulation, both the tip diameter and the cavity diameter were decreased by the tolerance of 50 µm specified by the manufacturer. The calculated thermal response curves are very similar to the curves obtained for the probe with nominal dimensions, except that the amplitude is lower. The difference in heat transfer error is −0.06 % of the dose, relative to the error with the nominal probe.

Unfortunately, the calculations shown in figure 5.8 are not easily verified in experiments that are based on the measured dose values, because there is barely any variation in the heat transfer error between successive irradiations. The difference between the first and the second irradiation is correlated with the overall magnitude of the heat transfer error, but the variations are very small. Instead, the time dependent variation of the excess temperature as shown in the top pane may be more easily resolved experimentally. Another option is to decrease the fitting margin, which will amplify the heat transfer error through the fitting and extrapolation procedure. These techniques are used in experimental verifications of the Comsol calculations in section 5.6.3, based on averaged responses over multiple irradiations.

5.4.3 Depth-dose gradient

Another source of heat transfer related errors is the depth-dose gradient. In particular, the large dose gradient of the Bragg-peak creates a large temperature gradient at that location. Fortunately, as shown in section 5.3, such gradients have only minor effects provided that they are located far from the point of measurement. In the case of measurements in the plateau, the dose profile is rather flat. Over the length of the vessel, the dose varies from −7 % to 6 %, relative to the dose at the location of the thermistors. At the front edge of the phantom, there is a region with a length of about 20 mm where there is a very noticeable dose build-up. Beyond the depth of the initial dose build-up, at the location of the thermistors, the dose gradient is almost linear and such gradients do not cause any heat transfer error. This is because the second spatial derivative of the temperature distribution is zero and the diffusion equation 5.3 does not give rise to any change in temperature in this case. To estimate the effects of the depth dose curve, another Comsol simulation was set up. The simulation was very similar to the simulation described in section 5.4.1 in that it was also a one-dimensional simulation. The input to the simulation is the depth-dose profile as determined by the Monte Carlo simulations, described in section 4.4.5 (i.e. the total dose curve in figure 4.11). In principle, the use of measured depth-dose curves is preferred. However, the obtained heat transfer errors would show variations of the same magnitude as the statistical noise in the ionometry data, due to volume averaging effects. The curve from the Monte Carlo simulation was used, because it shows lower statistical variations. To

further reduce the effect of the statistical noise in the depth-dose data, the curve was smoothed with a moving average filter with a span of 10 mm. This removes most of the noise, but will not otherwise affect the calculation, because the dose distribution in vicinity of the plateau is expected to be very smooth.

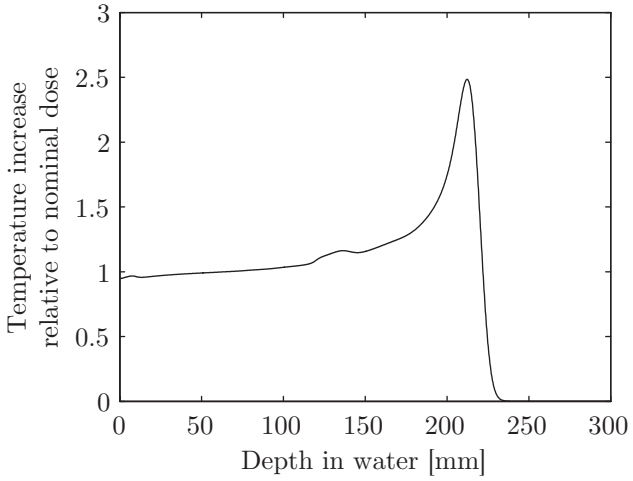

Figure 5.9 – Comsol 1D-simulation of the longitudinal temperature profile at the end of the first irradiation. The temperature is normalized to the expected nominal temperature increase at a depth of 65 mm. The depth dose curve that was used as input for the simulation was based on a curve obtained by a Monte Carlo calculation which is shown in figure 4.11 ('total combined dose') in section 4.4.5. A chemical heat defect of 3.5 %[33] to is assumed to apply outside the confines of the vessel, causing a slight increase in temperature below 7.5 mm and above 122.5 mm. The latter feature is however mostly due to scraping on upstream beam line elements.

Figure 5.9 shows the longitudinal temperature profile at the end of the first irradiation. There is a relative increase in the temperature outside the confines of the vessel (which spans the range of 7.5 mm to 122.5 mm), because the chemical heat defect in the unpure water of the phantom is assumed to be 3.5 %[33] in the simulation. The odd shape at depths greater than 122.5 mm is due to a combination of the heat defect and the secondary Bragg peak due to the scatter foil assembly, described in section 4.4.3.1.

Figure 5.10 shows the simulated error due to longitudinal heat transfer, after applying the fitting and extrapolation procedure to obtain the dose. Shown are 10 successive irradiations. Clearly, the error is negligible. The mean value is $-0.008\,\%$ which is compatible with the remaining noise level after applying the smoothing to the depth-dose curve. This means that for the plateau irradiations, the depth-dose curve is of no concern.

It should be pointed out that the heat transfer effects due to the depth dose gradients depend on the location along the Bragg curve. Clearly, the need for smoothing of the depth-dose curve demonstrates that volume averaging effects are important (the length scales are listed in table 5.1). If accurate calculations

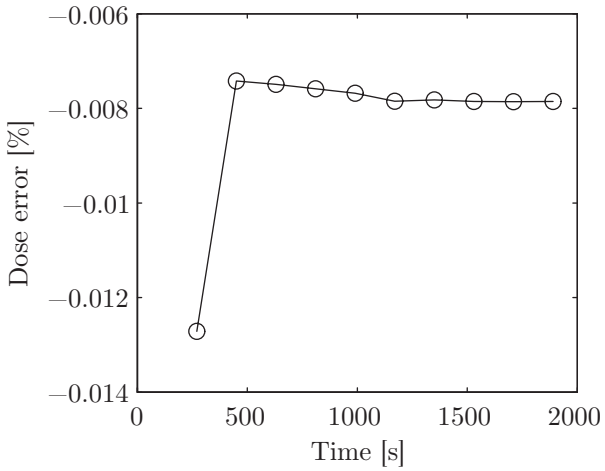

Figure 5.10 – Comsol 1D-simulation of the error induced by longitudinal heat transfer for a series of 10 irradiations, after applying the fitting and extrapolation procedure to derive dose. The data points represents the dose error of each subsequent irradiation.

are desired at locations of high local curvature, better data is required because the smoothing function can not be applied without biassing the results of the calculation. This should also be considered for SOBP irradiations, since most SOBPs have significant residual ripple.

5.5 Experiment

Although heat transfer corrections appear in the uncertainty budget of all calorimetry standards, there have been very few experiments that provide validation of the applied correction factors. The reason for this is most likely that the corrections are small and that the experiments are somewhat difficult to control due to the thermal history of the water, which results in small fluctuating background temperature drifts. Nevertheless, it is important to check the validity of the calculations. Typically, an experiment on the subject of heat transfer also is a good test case for the stability of the system as a whole. If the small effects of heat transfer can be reliably and repeatedly resolved, it shows that there are no significant effects from dose rate instabilities, beam alignment drifts, thermostat performance, water convection, chemical heat defect or the air density correction. As such, if a successful experiment shows that the predicted effects are statistically resolved and that no large discrepancies exist beyond the statistical limit, it provides great confidence in the performance of the standard as a whole.

Since any experiment involves a primary standard, there is no absolute reference to compare measurements to. As such, the only type of experiment that can be performed is one that involves tests that are sensitive to variations in the response.

One type of test is to simply measure the time dependent heat signal $T(t)$, which can then be compared to the calculations. Such experiments have been described by Krauss and Roos[124, 33] for ^{60}Co and by Krauss et al. [125] for low energy x-rays. In another paper, Krauss presents[126] calculations of the effects of small diameter fields, with emphasis on applications for scanning beams. It is difficult to validate heat transfer corrections solely by examining the heat signal $T(t)$, because of the fitting and extrapolation procedure that is used to determine the dose. However, because the heat transfer error for any irradiation is affected by heat transfer effects caused by previous irradiations in the same series, the error will show slight variations depending on the irradiation number in the series. This is exploited extensively by Krauss[33, 28], who describes that the apparent dose resulting from the fitting and extrapolation procedure shows slight variations which could be compared to calculations, thus validating the model.

Data from experiments and calculations for particle beams are scarcely available. This is likely due to the limited beam time that is available, which generally rules out any experimental validation. Simulations on the effects of heat transfer in a scanned proton SOBP were done by Sassowsky and Pedroni[51], who showed that the dominant mode of heat transfer in the scanned SOBP is in the direction of the beam and that the effect of the individual spots can largely be ignored. Sarfehnia and Seuntjens[119] describe extensive Comsol modelling of a calorimeter for brachytherapy. Sarfehnia et al. [38] describe the use of a small flat-front vessel in both scanned and scattered proton SOBPs, but they do not show comparisons between experiment and theory regarding the heat transfer effects. The experiments and analysis shown in this chapter resembles to some extent the work done by Sarfehnia[38] and Krauss[33, 28], because of the use of a flat-front vessel with proton irradiations and because of the general methodology of using heat transfer calculations depending on the irradiation number in a series. In contrast to the work described by Sarfehnia, a scattered proton beam was used to do a plateau irradiation with fixed irradiation durations, rather than a scanned proton SOBP with varying time patterns. Distinct from the ^{60}Co calorimetry performed by Krauss, a large glass vessel is used to eliminate the effect of glass-related heat transfer while the vessel's build-in stirring mechanism allows resetting of the initial conditions which enables studying time dependent effects.

In contrast with the work described by Krauss for ^{60}Co calorimetry, this work describes the use of a large glass vessel to eliminate the effect of glass-related heat transfer, the use of a stirring mechanism to enable resetting of initial conditions and an analysis of the time dependent effects of the excess temperature of the probes.

5.5.1 Experimental technique

The experiment hardware is largely the same as for the other experiments described in this thesis, except for the use of a elongated flat-front vessel. The design rationale was discussed in section 5.3. Figure 5.1 shows the important dimensions

of the vessel, while figure 2.3 in section 2.4.2 shows a photograph. The goal of the experiment is to measure the variation of the heat transfer error as a function of the irradiation number in a series of irradiations.

5.5.1.1 Vessel mixing

While the large vessel design avoids some of the heat transfer errors due to irradiation of glass components, it makes it more difficult to 'erase' the thermal history of the water prior to starting a new series. In water calorimetery, the system is generally reset by mixing the main volume of the phantom using a mixing bead at the bottom of the tank (see figure 2.1 in section 2.3). Krauss used a vessel[33] for which the distance between the thermistor and the walls is about 2 cm. According to table 5.1, mixing the main phantom volume would equilibrate the vessel in about the same time as the time needed to do the irradiations. For the vessel presented here however, the required equilibration time is more than five times longer. This is quite unacceptable in terms of beam time requirements. Therefore, a stirring mechanism was installed in the glass vessel as well. Figure 5.1 shows a cylindrical vessel with a flat protrusion into which a glass-coated stirring bead is placed. Mechanical actuation of the bead with another magnet mounted on a rotor is a too complicated solution. Instead, the photograph of figure 2.3 shows a water proof electro-magnetic driver*. It contains no moving parts or active electronics and it rotates the stirring bead by exciting orthogonal coils with a pulse-width-modulation driver. It was found that the power dissipated in the driver coils was very high, which caused the temperature inside the vessel to increase over time. To decrease the power dissipation, the power supply was modified to decrease the excitation current. The resulting power output during operation of the mixer is about 0.7 W, which is still fairly large. Fortunately, the mixer in the phantom can be turned on at the same time as the mixer in the cell and the forced convection over the water-proof driver unit carries much of the heat away from the vessel.

5.5.1.2 Beam control

One of the issues reported by Sarfehnia et al. [38] is that the beam delivery is not always reliable in time. The dose itself is typically controlled by the beam intensity monitors. However, the time in which this dose is delivered varies from irradiation to irradiation. As a result, the heat transfer correction would have to be calculated based on the actual time structure as measured with the BIMs for each series of irradiations. This makes it very difficult to do heat transfer experiments, because the results can not be averaged. Sarfehnia also reports that if the heat transfer correction is not recomputed for each irradiation it also increases the uncertainty budget because the fitting interval moves relative to highly time dependent effects, such as the decay of the thermistor probe excess temperature.

* MixDrive XS, manufacturerd by 2Mag

One of the attractive aspects of ^{60}Co calorimetery is that the time structure of the irradiation is very well controlled. This enables comparisons between measurement and theory such as described by Krauss[28] by averaging the result of multiple irradiations. Fortunately, a scattered proton beam is somewhat easier to control than a scanning proton beam. In this experiment, rather than controlling the irradiations based on the delivered number of monitor units, the irradiations are controlled by a computer clock. As shown in figure 2.9 in section 2.9, the irradiation control software can also instruct the FPGA beam control system to start and stop the beam regardless of the number of delivered monitor units. The amount of monitor units delivered is still logged and reported for each irradiation. Due to beam instabilities, the amount of dose delivered in each of the irradiations in a series may vary on the order of a few percent. The effect of each irradiation on each subsequent irradiation scales directly with the delivered dose, but since this represents a small perturbation only, a few percent of statistical fluctuations in the magnitude of the error (rather than the magnitude of the full signal) is not an issue. During the experiments, the standard deviation of the delivered monitor units (MU) was 5.2 %, however this number includes long-term drifts over many hours. Over a single series the standard deviation of the MUs is much lower, typically about 1.4 %. With the exception of a single spurious event, the variation in dose rate would not have caused any non-negligible effect on the heat transfer corrections. Therefore, the corrections based on pre-calculated heat transfer errors should still be applicable. In this experiment, the delivery time is fixed, and the delivered dose varies. The determined dose values must still be normalized to the monitor units. The time schedule was a series of 10 irradiations, each of which takes 60 s with a drift time of 120 s in between the irradiations.

5.5.1.3 Measurement sequence

Each irradiation cycle starts with a mixing sequence that is controlled automatically by the computer driving the thermostat. The mixer of the vessel is turned on at the same time as the mixer in the phantom. Mixing continues for 12 min which is equivalent to a little over two times the thermal time constant of the mixed vessel, ensuring proper equilibration. The mixer in the vessel is then turned off for one minute. During this time, the mixer in the phantom continues to stir the water. This removes some of the delayed heat that is emitted from the vessel mixer drive coils after the vessel mixer is turned off. The vessel is then mixed again for one minute, followed by another waiting time of 30 s. The vessel is then mixed again for another 30 s. All the while, the phantom mixer was left on. When the vessel mixer is turned off for the last time, the phantom mixer continues for another minute to disperse some of the remaining heat from the vessel mixer driver. Finally, the phantom mixer is turned off as well.

The purpose of the procedure described above is to ensure that the amount of heat from the mixing driver that enters the vessel is small and that this heat is homogeneously distributed over the entire volume of the vessel and the phantom.

This is necessary because of the close proximity of the drive coils to the vessel combined with the delayed heat from the driver. After turning off the phantom mixer, the water is still in rotation and is left to slow down for another 15 minutes. During this time, some residual heat is still transported away from the drive coils. The thermostat control software then automatically rebalances the resistance decade in the lock-in readout chain. The entire procedure takes about 34 min, which is about the same time as needed to do a series of 10 irradiations. During the mixing procedure, the temperature of the water in the phantom is not actively controlled. Due to the irradiation and the power applied to the mixer driver, the temperature of the water gradually increases during the cause of the experiment. However, if the temperature deviates too much from the normal operating point of the calorimeter (4 °C), the thermostat automatically cools the phantom down while mixing the phantom and the cell simultaneously, followed by the mixing procedure described above.

Following the mixing procedure the experimentalist manually has to start an irradiation sequence, which causes a dispersion of a few minutes between the end of the mixing procedure and the start of the irradiations. The software then automatically performs a series of 10 irradiations with a duration of 60 s with a repetition time of 180 s. The irradiation sequence including the pre-drift time thus takes a total of 1920 s. After completing the irradiations, the cycle can be restarted by beginning the mixing. One entire cycle takes about 66 min. If at any point during the irradiation there is a (partial) loss of beam, the remainder of the irradiation cycle is considered pointless, since the heat profile will be in an unknown and uncontrolled state. The data up to the point of interruption is however considered to be 'good data'. At the moment of a beam loss during an irradiation, the experimentalist aborts the sequence and restarts by performing the mixing procedure.

The advantage of the described measurement sequence is the effective use of beam time (about 50 %), while still achieving stable and reproducible initial conditions. While similar performance could have been achieved by using a smaller vessel, it would not have the benefit of limited glass heating effects.

5.5.2 Correction for mixing effects

The mixing of the water inside the high purity cell is to be considered a rather violent action. Generally, in calorimetry, one tries to avoid any thermal disturbances as much as possible and it is not uncommon for experiments to require several hours for 'things to quiet down'. Therefore one may expect relatively large effects related to the mixing.

One such effect is related to the thermistor temperature offset, due to the power dissipated in the thermistor NTC. The model described in section 5.4.2 was also used to calculate the quasi steady state temperature offset of the probe relative to the surrounding water. The offset amounts to $0.90\,\mathrm{K\,mW^{-1}}$. The highest power dissipation occurs in the DC readout chain. The multimeter uses an excitation

current of 100 µA, which results in an offset of 0.08 K, assuming a 9 kΩ thermistor. This is equivalent to about 440 Gy. The mixing inside the vessel will destroy the quasi steady state of the thermistor probe by convective cooling. The model indicates that 1000 s after the stop of convective flow the error due to the self heat is equivalent to 1 mGy. This small error would present a problem if irradiations were to be performed at dose rates on the order of 1 Gy min^{-1}. The dose rate used in this experiment was slightly under 10 Gy min^{-1}, which reduces the relative dose error to about 0.01 %, which is negligible.

Another effect is the power dissipation of about 0.7 W in the coils of the mixer driver. While the mixing procedure caries most of the heat away from the vessel, some noticeable heat still remains. While the induced temperature deviations are very large, they occur very slowly. Therefore the large distance between the driver and the thermistor sensors should cause relative small effects.

Whatever the magnitude of the effect, it can be measured 'offline' after the main experiment without consuming additional beam time. The effect is correlated in time to the start of the irradiations simply because of the fact that the cell is always mixed prior to any series of irradiations. Therefore it can cause systematic errors in the determined dose which depend on the amount of time that has passed since the last mixing of the vessel. However, the mixing effect is not correlated to the delivered dose or the dose rate. Thus, it is an additive effect which must be subtracted.

In order to be able to correct for any such small effect, the effect of the mixing was examined after the irradiation experiment. The entire calorimetry setup was moved to a separate room in the laboratory, without opening the phantom. This ensures that the thermistors remain in the same position. Over a time period of about two weeks, the mixing procedure was repeatedly applied and each mixing sequence was followed by an idle time that was compatible with the total length of the irradiation sequence.

Figure 5.11 shows the temperature effects due to the mixing. The shown curves were obtained by averaging over data taken for a total of 100 mixing sequences. Clearly visible near time $t = 0$ is the strong increase in temperature due to the restoration of the thermal gradients near the thermistors. The temperature shifts are roughly compatible with the expected temperature offset. For the DC measurement chain the temperature offset is larger because it uses a larger excitation current. The spike in the AC-signal at a time index just under 1000 s is due to the automatic rebalancing of the Wheatstone bridge using the resistance decade. The irradiations would normally start a few minutes later. Around this time, the temperature offset due to the thermistor power dissipation has largely stabilized. However, at about the same time, heat from the mixing coils begins to arrive at the position of the thermistors. In fact, the temperature increase accelerates a small amount just after $t = 2000$ s. Thus, the temperature continues to increase.

Figure 5.12 shows the result of applying the fitting and extrapolation procedure that is used to derive dose to the data shown in figure 5.11. Since figure 5.11 characterizes the temperature effect of the mixing, figure 5.12 is an experimental

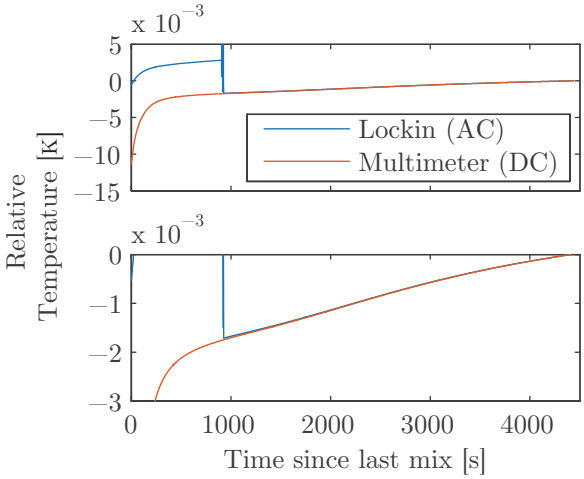

Figure 5.11 – Temperature deviations due the mixing effect. The curves are normalized to zero at time $t = 4400\,\mathrm{s}$ and they represent an average over 100 mixing sequences. The time index is the time that has passed since turning off the mixer in the phantom. The mixer in the vessel is turned off a minute earlier. The sharp transient visible in the Lockin signal is due to the automatic rebalancing of the Wheatstone bridge, which is also performed during the calorimetry experiments.

estimate of the resulting dose error due to the mixing effects. After about 1000 s the measurement error becomes negligibly small. The standard deviation of the signal after this time is 1.5 mGy for the AC-chain and 2.3 mGy for the DC-chain. Relative to the doses used in this experiment the noise level is negligible. The measured data shown in the figure can be simply subtracted from the data obtained with the proton irradiations. In principle, this could lead to a small systematic error on the order of the noise level in the mixing data. However, the time between the end of the mixing procedure and the start of the irradiations is slightly randomized because the irradiation procedure has to be started manually. This prevents selecting the same part of the mixing curves for each new irradiation cycle, thus averaging out some of the noise.

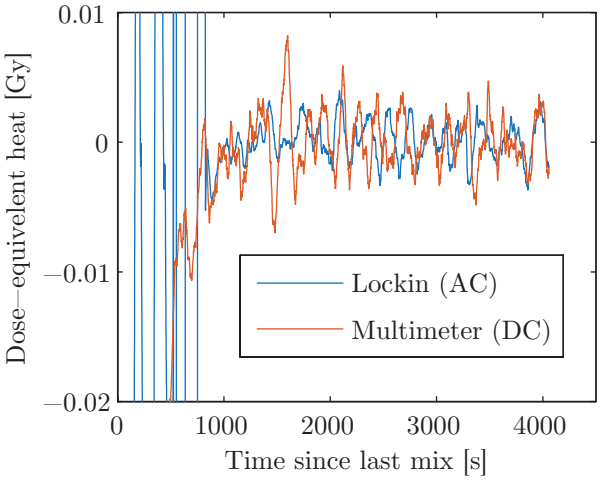

Figure 5.12 – Result of applying the fitting and extrapolation procedure to the data shown in figure 5.11. The graph was computed by sliding the fitting intervals along the graphs of figure 5.11, computing the dose equivalent heat at every second. The oscillatory behaviour is the result of the correlations between the samples, since for each data point the location of the fitting interval changes only by one second. The apparent temperature differences resulting from the fitting procedure are expressed in units of an equivalent amount of deposited dose. The strong variations on the left side of the curve for the Lockin signal are due to the automatic balancing of the Wheatstone bridge.

5.6 Results

The experiment consisted of 7 series of 10 irradiations using a collimator with a diameter of 70 mm and 5 series of up to 10 irradiations using a 50 mm collimator. In the case of the 50 mm experiments, two series were cut short about halfway through the irradiation cycle.

5.6.1 Mixing effects

Figure 5.13 shows a complete irradiation cycle consisting of 10 discrete irradiations, which is preceded and followed by mixing. During the irradiation, the slope of the temperature increasingly turns into a cooling drift, due to heat diffusing outward radially. At the end of the irradiation, the mixer is turned on and the heat profile is immediately destroyed. Violent spikes are visible throughout the mixing procedure. They are thought to occur because of varying flow velocity over the probe, which changes its heat transfer coefficient to the bulk of the water. This is indicative of turbulence, which implies proper mixing. Following the mixing, the temperature offset of the thermistor probe recovers. The onset of recovery is not perfectly repeatable, but it typically occurs within one minute, which indicates that the flow of water halts quickly. After each recovery, the final temperature is slightly higher compared to the previous mixing. This is almost entirely due to the extra heat from

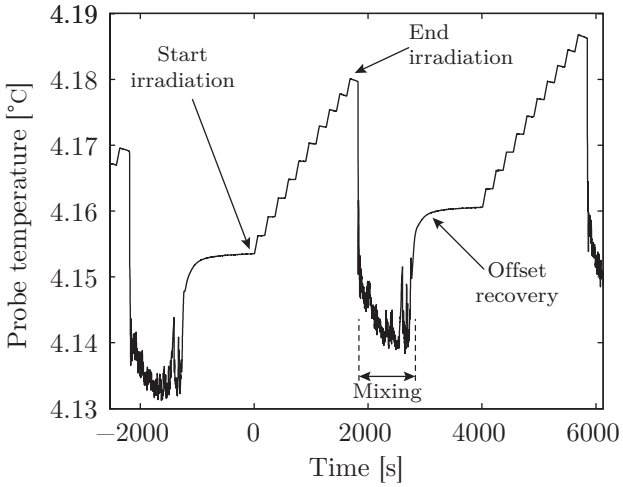

Figure 5.13 – Temperature of the thermistor attached to the DC readout chain. Centered in the figure is a single series of 10 irradiations, which is preceded by mixing as well as followed by mixing. After the end of the mixing cycle the temperature of the probe quickly recovers its offset.

the drive coils. The temperature increase is comparable in magnitude to about one tenth of the nominal temperature increase due to the complete irradiation cycle, which means that almost all of the heat has been removed from the vessel. The mixing technique appears to work as intended, with no obvious signs of instabilities during the recovery period.

5.6.2 Field shape related heat transfer

Figure 5.14 shows a comparison between the measured temperature and the predicted temperature using Comsol, as a function of time. The diameter of the circular collimator openings was 70 mm and 50 mm, respectively. For each collimator, a single series of 10 irradiations is plotted. The calculated curves were obtained from the axi-symmetric radial heat transfer model described in section 5.4.1 and equation 5.32 was used as the input for the simulation. All curves were normalized to unity after the first irradiation. Clearly, the Comsol simulation does a very good job at describing the large scale heat transfer effects. This directly shows that the majority of the heat transfer can be well approximated by radial diffusion.

The heat transfer on long time scales is principally well understood. However, figure 5.14 does not necessarily reveal any fluctuations on fairly small time scales. Heat transfer that occurs on time scales on the order of the repetition time of the irradiation may have an effect on the apparent measured dose, but may not show its presence in an offset at longer time scales. One important example is the

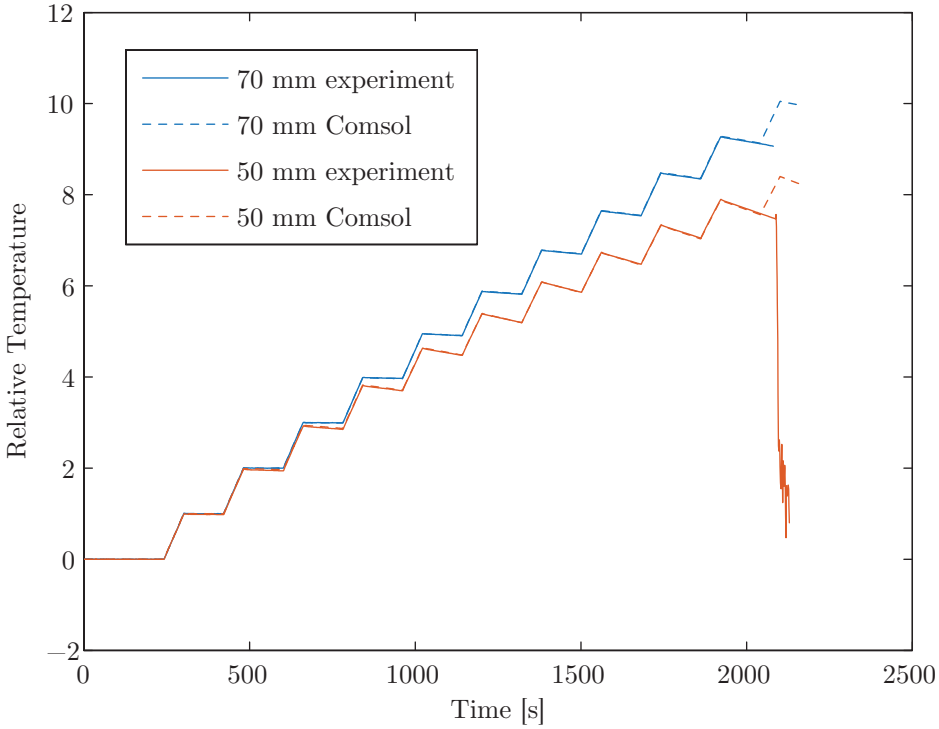

Figure 5.14 – Comparison between experiments and Comsol calculations of the radial heat transfer. Shown are two series of measured data, for the 70 mm and 50 mm collimator. The dashed line shows the Comsol calculations. All of the curves have been normalized to unity after the first irradiation. The 'DC' measurement chain refers to the multimeter resistance measurements while the 'AC' measurement chain refers to the AC Wheatstone bridge system with the lock-in detector. Both were used simultaneously during the measurement on different probes.

excess temperature of the probe. As shown in figure 5.8 in section 5.4.2, the small scale heat transfer phenomenon shows barely any variation between successive irradiations. Other possibilities for small scale heat transfer are averaging effects due to dose inhomogeneities or effects related to the mixing.

The important quantity is however the apparent measured dose, as it results from applying the fitting and extrapolation procedure. By applying the fitting procedure to both the measured and the simulated data the effect of the exact shapes of the curves on the complete procedure can be tested. As shown in figure 5.3, the apparent measured dose will show small fluctuations depending on the number of the irradiation in the sequence.

Figure 5.15 shows a comparison between experiments and the simulation for the 70 mm field. The data is normalized relative to the mean of the full 10 irradiations separately, for each experimental data set and also separately for the Comsol-simulated response. Data from both the AC (lock-in) and DC (multimeter)

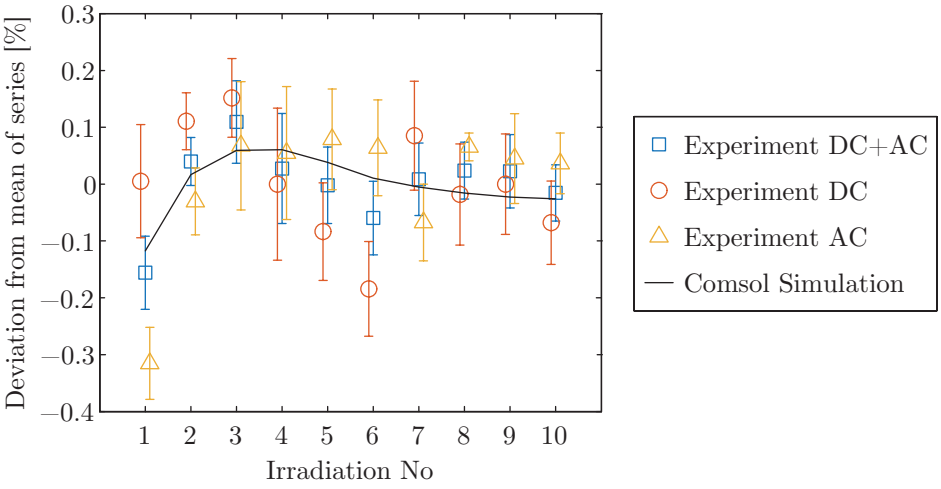

Figure 5.15 – Comparison between experiments and Comsol calculations of the combined effect of radial heat transfer and probe excess temperature. Displayed is data from the experiments with the 70 mm collimator. The data is presented as deviations from the mean dose over the full 10 irradiations in the series. Both measurement chains (DC, AC) and their combined data are plotted with error bars at 68.27 % statistical confidence.

measurement chains is plotted as well as the mean of these data sets. The error bars are derived from the standard deviation of the data. The confidence level is 68.27 % which includes a Student's-t factor as calculated with equation 2.29 in section 2.13.2. In this particular case, the mean value at each irradiation number is derived from samples which are not correlated, because they originated from different irradiation cycles. Therefore no additional factor of $\sqrt{2}$ is applied. It should be pointed out however, that the data for any two adjacent irradiations are still correlated. Figure 5.15 shows the equivalent data for the 50 mm collimator.

In the case of the 70 mm collimator, the signal due to the radial heat transfer is barely visible above the noise. The combined data from both measurement chains is required in order to resolve some of the signal. Except for the first irradiation, most of the differences between the experiments and the simulation is compatible with statistical variations. The mean half-width of the error-bars in the combined data set is 0.06 %.

In the case of the 50 mm collimator, the bump which is expected starting at the second irradiation is also resolved experimentally. Except for the first irradiation, no deviations are observed which can not be attributed to statistical variations. The mean half-width of the error-bars in the combined data set is 0.10 %.

The data set does hint at a problem which is detected in the first irradiation. For both collimators the AC data point for the first irradiation ends up rather low, whereas the data point for the DC measurement chain ends up slightly high. This is likely related to the excess temperature of the probes. As shown in figure 5.8

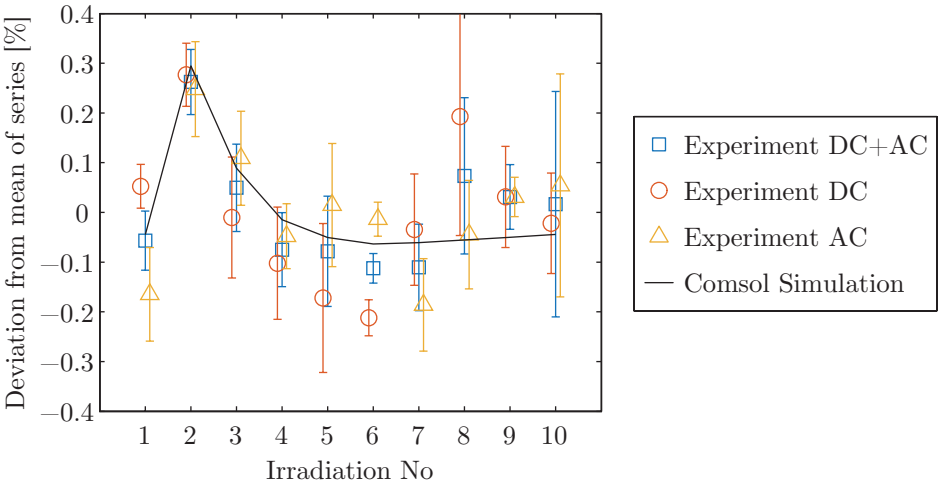

Figure 5.16 – Comparison between experiments and Comsol calculations of the combined effect of radial heat transfer and probe excess temperature. Displayed is data from the experiments with the 50 mm collimator. The data is presented as deviations from the mean dose over the full 10 irradiations in the series. Both measurement chains and their combined data are plotted with error bars at 68.27 % statistical confidence.

the probes are not expected to cause any variations beyond the second irradiation. Any discrepancy in the first irradiation thus hints at issues with the probe excess temperature. The probes that were used in the two measurement chains were not exactly the same. The AC chain used an hand-made version of the probe, which had a diameter that was about 46 % larger than the simulated probe. A Comsol simulation showed that the larger value of the excess temperature in this case explains the discrepancy.

While the plots in figures 5.15 and 5.16 do not show large amplitude swings due to the radial heat transfer, figure 5.14 clearly shows that the slope of the drift curve after an irradiation is significantly different from the slope before an irradiation. Figure 5.17 compares the differences in the slope of the measured data to the Comsol simulations for the two collimators diameters. The data is the combined data set of both the AC and the DC measurement chain. Similarly to the graphs that show the variations in dose, the error bars are statistical error bars at the 68.27 % confidence level, with an included Student's-t factor. Clearly, the measured data is consistent with the calculations.

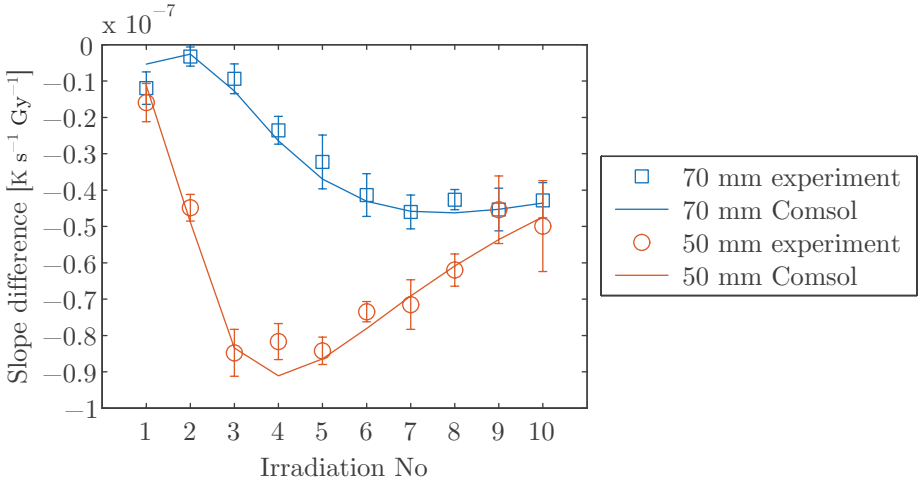

Figure 5.17 – Comparison between experiments and Comsol calculations for the differences in slope that exist before and after each irradiation. The plot shows data for the 70 mm collimator and the 50 mm collimator. The data points are the combined result of both the DC multimeter and the AC lock-in measurement chain.

5.6.3 Temperature probe excess temperature

It is shown in figure 5.8 that the excess temperature of probe causes a very significant measurement error. At the same time it is very difficult to verify the magnitude of the effect, because there is little variation from irradiation to irradiation. For this reason, the shape of the curve after the end of the irradiation must be examined closely. In addition, as described in section 5.4.1.1, the thermal transient also depends on shape of the dose distribution.

Figure 5.18 shows the effect of changing the margin between the end of the irradiation and the start of the fitting interval for the post-drift curve. For decreasing values of t_{PoFM}, the fit starts ever closer to the end of the irradiation, which causes the apparent dose to rise as the linear fit is pushed up the slope. There is a good agreement between the experiment and the Comsol calculation, indicating that the both the magnitude and the curve shape of the excess temperature is accurately predicted.

While figure 5.18 is certainly a good indicator of the quality of the simulations and the level of control in the experiment, it is difficult to assign an uncertainty in terms of dose based on such plots. The plot does not directly reveal the shape of the thermal transients after an irradiation. Generally, when performing a validation experiment, it is desirable to go about the data processing in the same way it is done for regular calorimetric calibration measurements. By keeping the data processing techniques and experimental conditions very similar to the calibration conditions, the validation experiments become meaningful directly in terms of units of absorbed dose. For calorimetric validations, this implies performing the

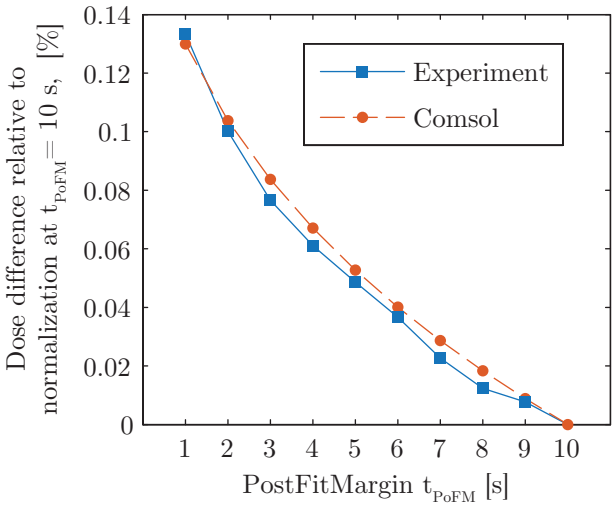

Figure 5.18 – Deviation of the apparent dose for a range of Post-irradiation Fit Margins t_{PoFM}. The data is normalized at $t_{\mathrm{PoFM}} = 10\,\mathrm{s}$. The experimental data is an average over all of the first irradiations belonging to the irradiation cycles in which the 70 mm collimator was used.

linear fitting procedure on the temperature drifts and deriving values of dose, while looking for small variations caused by systematic effects. However, in the case of the temperature probe excess heat, there is little systematic variation in the resulting dose-values, such that the validation of the absolute correction factors must be inferred from the shape of the thermal signals instead.

This requires separating the small transient due to the probe excess temperature from all other signals, including the strong thermal signal of the deposited dose in the water. Unfortunately, the actual shape of the obtained transient depends on the effects of field-shape related heat transfer as well. However, the radial heat transfer data shown in the previous section appears to fit the calculations very well. This opens up the possibility of subtracting the radial heat transfer in order to obtain an experimental excess temperature curve. By taking the fully two dimensional heat transfer calculations for each probe position (section 5.4.1.1, based on simulation data at the left and right probe positions marked in figure 5.4), depth-dose related heat transfer calculations and calculations of the excess temperature signal of each individual probe, the thermal transient of the entire irradiation can be modelled. Comparison of the experimental transient with the calculated transient then gives insight in the consistency of all calculations.

Figure 5.19 shows the result for the DC multimeter measurement chain. In this plot, the data from all of the first irradiations of all series with the 70 mm collimator were averaged. The fitting intervals listed in table 2.1 in section 2.8.2 were used on the experimental data to remove the background drift and to normalize

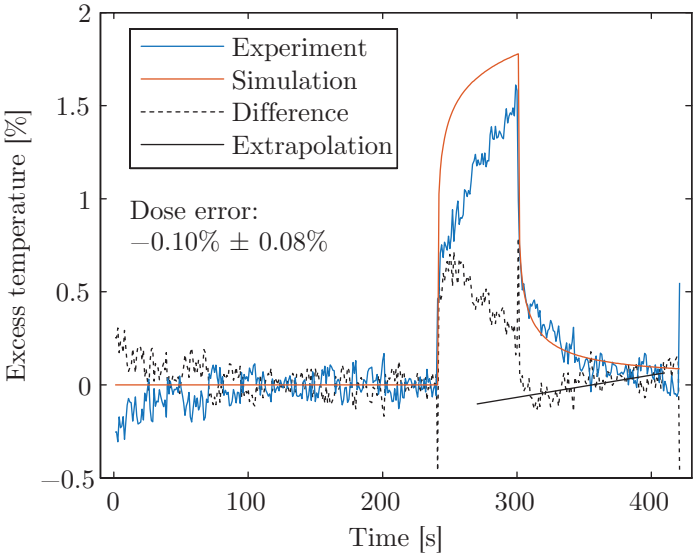

Figure 5.19 – Comparison between the experimental probe excess temperature measured with the DC multimeter and a Comsol calculation. The experimental data is an average over all first irradiations in the series of the 70 mm collimator. The fitting intervals described in section 2.8.2 have been used to remove the background drift and to normalize the simulated curves. After normalizing the full thermal transient (including all modelled effects), the field shape related transients are subtracted to yield the probe excess temperature, which is then compared to the Comsol calculation.

the experimental curve to the Comsol calculations. Subsequently, the simulated dose-distribution-related heat transfer effects (uniquely determined for each probe at its location in the 2D field) are subtracted to yield a experimental curve for the probe excess temperature transient, which is plotted in comparison with the simulated excess temperature transient. Also plotted is the difference between these two curves. This difference-curve is the total discrepancy between the simulated signal and the experimental transient, including all modelled heat transfer effects. The difference-curve is fitted with a linear slope and extrapolated over time to the mid-point of the irradiation, in exactly the same way as it is done for the determination of dose. The resulting dose value reflects the coherence of all the modelled heat transfer effects. It should be noted that the experimental probe transient is not scaled in order to match the simulated probe transient. Instead, the entire simulated signal, which includes the direct deposit of dose in the water, is used for the normalization. This preserves the relation between the amplitude of the probes' excess temperature signal and the nominal temperature increase of the water.

Figure 5.20 shows similar data for the AC Lock-in measurement chain. The procedure that was used to derive the curves is largely the same. The 2D heat transfer data that is specific for the location of the probe that was attached to

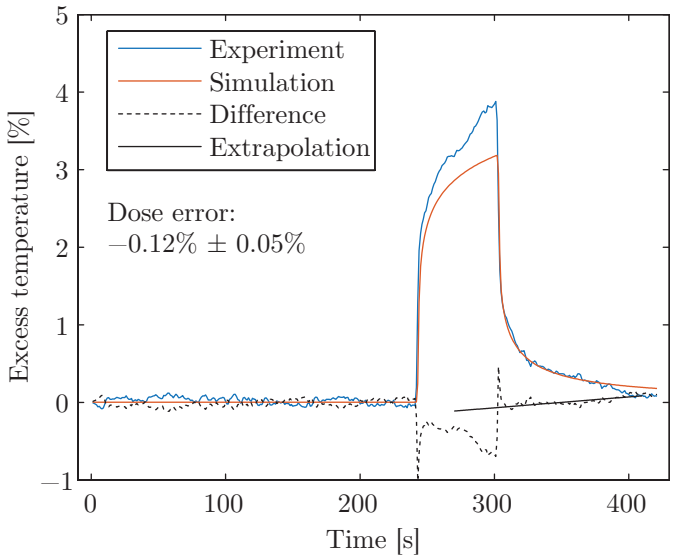

Figure 5.20 – Comparison between the experimental probe excess temperature measured with the AC Lock-in chain and a Comsol calculation. The graph is similar to figure 5.19, except that a unique calculation for the probes' excess temperature was used since the used probe had different dimensions. Additionally, the calculated curves were filtered with the Lock-in step response before further processing.

the AC chain was used. In addition, since the probe has different dimensions, a separate model was constructed for this probe. The result of the Comsol heat transfer calculations was filtered with the step response of the Lock-in detector before normalisation and subtraction.

Clearly, the data in both figure 5.19 and 5.20 show good agreement between the calculations and the experiment. There is a hint of a possible issue with the recovery of the temperature offset due to the self-heating of the probe after mixing, which is visible in figure 5.19 as a decreasing non-linearity in the pre-drift curve. This implies that the mixing procedure is not entirely reproducible, resulting in jitter of the self heat recovery time. The data from the AC Lock-in chain in figure 5.20 does not show any visible curvature in the pre-drift region, which may be explained by the lower excitation current in that measurement chain compared to the DC-chain.

In case of the data from the DC multimeter chain, the dose error is 0.10(8) %, which is not statistically significant. The AC Lock-in chain shows a similar error of 0.12(5) %, which is marginally significant. In principle, this experiment can not distinguish between modelling errors of the probe excess temperature and dose distribution related heat transfer or the effects of mixing. Given the fact that two differently sized probes have been used in the two measurement chains which require unique excess temperature calculations and given the fact that the dose

error is the same in both measurement chains, the more likely explanation for the marginally significant discrepancy in the AC Lock-in chain is a factor that is common to both measurement chains. This indicates that the discrepancy (for as much as it is significant) could have been caused by the modelling uncertainty of the two dimensional heat transfer effects. Thus, it is assumed that the two fitting errors in both chains are correlated and the largest discrepancy of 0.12 % is taken to be a characteristic error of the heat transfer modelling as a whole.

5.7 Estimation of uncertainty due to heat transfer and dose inhomogeneity

Considering the longitudinal heat transfer in the case of plateau irradiations, the uncertainty that is due to the calculated heat transfer corrections is negligible, since the magnitude of the effect itself is negligible.

Considering the radial heat transfer calculations in Comsol, the modelling uncertainty is negligible, because the differences between dose distribution inputs based on measured data and an artificial top-hat distribution are negligible.

The radial heat transfer effects for the 70 mm collimator have been experimentally verified down to a statistical uncertainty of 0.06 % at the 68.27 % confidence level. Within this range, effects related to deviations from the presumed field shape or modelling inaccuracies may still exist. Therefore an uncertainty of 0.06 % is assigned due to the radial heat transfer effects.

Analysis of the transients after the irradiation yields a possible discrepancy of 0.1 % in the combined calculation of the 2D field shape related heat transfer effects and the probe excess temperature modelling. Given the agreement of the discrepancy between two probes of different geometry, the discrepancy is likely due to heat transfer modelling errors related to the 2D field shape. The radial heat transfer modelling has already been included in the 2D field shape related heat transfer calculations. Therefore, a total uncertainty of 0.1 % is assigned to the combined heat transfer calculations.

Other than the mentioned discrepancy, the modelling has shown that the dimension tolerances quoted by the manufacturer of the probe lead to differences of no more than 0.06 %. Therefore an uncertainty due to the probes dimensions of $0.06\,\%/\sqrt{3} = 0.04\,\%$ is assigned.

Adding in quadrature the uncertainty due to heat transfer modelling of 0.12 % and an uncertainty of 0.04 % related to manufacturing tolerances of the probe yields a total standard uncertainty of 0.13 % on the heat transfer corrections as calculated with the models.

The above value is the uncertainty related to the heat transfer. However, due to the field inhomogeneities there is also an uncertainty due to the determination of the field shape as measured with the scintillation imager. Based on the statis-

tical fluctuations in such images, the correction for the difference in dose at the measurement position of the thermistors and the nominal dose at the measurement position carries an uncertainty of 0.09 %.

The combined uncertainty of the heat transfer effects and the position corrections is 0.16 %. The uncertainty on the heat transfer effects dominate this estimate as it contributes about two thirds of the total variance.

5.8 Conclusions

The combined analysis of figures 5.14,5.15,5.16 and 5.17 shows that the observed heat radial transfer is compatible with the calculations in terms of the shapes of the temperature curves, the derived dose and changes in slope. It should be noted that this has been confirmed for two different field sizes, each showing unique heat transfer patterns. These patterns were also approximated by analytical calculations. Slight changes in field shape of the penumbra other than the diameter of the field were shown not to have significant effects. This provides a great level of confidence in the methodology and the implementation of the calculations.

The agreement between measured data and calculations also demonstrates the performance of the mixing technique and the operation of the calorimeter in the environment of the accelerator institute in general. Because of the mixing, the calorimeter can be quickly and reliably brought to a controlled initial state, which is of great importance when performing calorimetry in a beam time limited scenario. While there are many possible disturbances and while some of those disturbances may also find their origin outside the calorimeter in the operation of the beam line, there are no indications of any effect beyond a very small statistical uncertainty of 0.06 %.

Analysis of the transients of the probe excess temperature show fairly good agreement. However, a discrepancy of 0.12 % was found, which may be due to imperfections in either the modelling of the heat transfer of the temperature probe or the heat transfer due to 2D field inhomogeneities. Variations in the dose distribution on the order of a percent have yielded heat transfer corrections on the order of a per mille, showing that field flatness is an issue. Most of the observed discrepancy is attributed to this effect. While it is possible to calculate the necessary heat transfer corrections, the system as a whole loses a degree of robustness. This presents a challenge for any application of calorimetry in scanning beams, since it would require excellent control of the beam in both the spatial and temporal domain.

A total uncertainty of 0.16 % is assigned to the combined effect of heat transfer and position corrections, which is dominated by the effect of field inhomogeneities.

Chapter 6

Summary and outlook

The previous chapters in this thesis highlighted some of the challenges encountered when performing water calorimetry in proton beams. In the scattered proton beam at KVI-CART, the resulting uncertainties are generally not larger than similar uncertainties in ^{60}Co calorimetry. However, usage of a water calorimetry standard in a clinical beam would lead to serious issues regarding the available beam-time in which to do the necessary experiments and would suffer from a general lack-of-control considering the measurement environment. Therefore, the benefit of a possible reduction in ionometric uncertainty by applying calorimetry in a clinical scanned beam should be quantified and weighed against the need for low uncertainties and against the burden of assigning beam-time to calorimetry. At the same time, there is a risk of increased uncertainties due to the calorimetrically more challenging scanning-beam dose delivery.

In this chapter, the experiments are discussed retrospectively. The implications of this work are addressed, as well as the resulting constraints for performing calorimetry that apply, considering the goal to calibrate ionization chambers used in proton therapy. Finally, the various options of setting up a proton dose calibration chain are reviewed.

6.1 Experiments

Before discussing some of the implications of the work described in this thesis, it is appropriate to first summarize the experiments as they are practical examples of some of the challenges involved in performing water calorimetry.

6.1.1 Radiochemistry

The issue of water radiolysis has been examined in chapter 3. In that chapter, it was shown that any practically feasible application of calorimetry in a clinical scanned proton beam requires the use of H_2 saturation of the water to prevent

an uncontrolled chemical heat defect. The water radiolysis model shows that without the use of this technique, calorimetry in a scanned beam would require an unacceptably large pre-irradiation dose. Even when using H_2 saturation, one should be aware that the local chemical state of the water after the pre-irradiation is dependent on the LET of the protons and the local dose rate and is thus dependent on the location within the depth-dose curve. This may create issues if the in-vessel water-mixing technique is used as it can render the pre-irradiation ineffective (it may need to be repeated after each mixing) and these effects have not been examined in this thesis.

For calorimetry in relatively low dose rate scattered beams, the H_2 saturation suffices. The experiments in chapter 3 show that the radiochemistry is under control in the scattered beam at KVI-CART. These experiments are similar to those already performed for ^{60}Co photon calorimetry. Therefore, the value of uncertainty attributed to the chemical heat defect that was obtained for the photon calorimetry is also used for proton calorimetry.

It should be noted that the water radiolysis model does not include certain time-dependent aspects nor any explicit treatment of the effects of organic impurities. Furthermore, the radiolysis yields $g(E)$ (an important set of input variables) have been derived from relatively scarce experimental data. Therefore, rather than applying a correction factor for the chemical heat defect, any water calorimetry calibration (for scattered as well as scanned beams) should be run with sufficient pre-irradiation in order to ensure that the chemical heat defect is reduced to negligible levels. The simulations in chapter 3 suggest that 24 Gy of dose will be sufficient in most cases if H_2 saturation is used, although one should be cautious since the presence of impurities due to an improper cleaning can throw off the results even at low dose rate. Such pre-irradiations should preferably be performed with the in-vessel mixer turned on, to ensure homogeneity within the vessel. Considering the chemical heat defect, the effects of SOBP irradiations in scattered beams have not been examined in this thesis, although it is expected that any non negligible effect will remain limited to the first irradiation in a series, such that it can be detected by comparison to subsequent irradiations.

6.1.2 Neutron dose

The effect of neutron-induced dose on both the calorimeter operation and on ionometry has been examined in chapter 4. This issue is of particular interest, because the neutron-induced dose that is inevitably caused by the proton irradiation is not part of any dosimetry protocol or any patient dose calculations. In principle, the water calorimeter will readily measure neutron dose, since the dose-related temperature increase of the water is independent of the type of radiation, as long as the water radiolysis is under control. However, since the purpose of the calorimeter is to calibrate an ionization chamber, care should be taken to ensure that the delivered calibrations still yield a properly functioning dosimetry system.

As explained in the chapter, the issue is that the ionization chambers have a sensitivity to neutron-induced dose that is different from their sensitivity to proton dose, while this is not the case for the calorimeter. Therefore, if the neutron dose fraction differs between any two proton beams, a calorimetrically determined ionization chamber calibration in one beam will need a correction factor to be applied in order to be applicable in another beam. This limits the possible use of proton beam-lines at physics institutes for calibration purposes, because the neutron dose fraction in such beams is not necessarily the same as in a clinical beam.

As shown by Monte Carlo simulation in chapter 4, the neutron dose fraction in the beam at KVI-CART is mostly due neutrons liberated in the water volume itself. Thus, the scatter system at KVI-CART itself does not contribute any significant neutron dose. The neutron dose fraction depends mostly on the beam diameter, the beam energy, the location of measurement and whether a plateau or SOBP irradiation is performed.

With the exception of performing calorimetric calibrations in a clinical beam directly, a correction factor will always be necessary due to various differences in beam quality. In order to determine the correction factor related to neutron dose, the neutron dose fraction must be calculated via Monte Carlo simulation, both in the calibration beam and in the clinical beam. In addition, the sensitivity of the ionization chamber to neutron dose must be known, either through Monte Carlo simulation or direct measurement. The neutron dose sensitivity of the ionization chamber will contribute the largest neutron-related uncertainty to the total uncertainty budget. Fortunately, the neutron dose fraction is usually not larger than a percent, which limits the effect of this uncertainty. As an example, chapter 4 shows the calculation of the uncertainty due the difference in neutron dose fractions between the KVI-CART beam and a wider beam typically used in clinics. The additional uncertainty need not be very large, but it does depend on the availability of neutron calibrations for the chamber that is used.

The experiments in chapter 4 validate the Monte Carlo simulation for the purpose of calculating neutron dose in water, down to an uncertainty that results from beam current fluctuations during the experiment. This also shows that it is possible to calibrate the ion chambers in terms of the particle spectrum that is associated with the neutron-induced dose fraction. It should be pointed out that the Monte Carlo simulation was validated for dose-to-water only, therefore more work is needed in order to validate the calculation if the intent is to directly calculate the neutron-dose sensitivities.

The lack of neutron-dose accounting in patient dose calculations and dosimetry protocols means that there is a potential issue when relating calorimetric calibrations to patient dose. Beam quality specifications will need to include neutron dose explicitly if ionization chambers are to be calibrated in any beam other than the end-user clinical beam.

The fact that most treatment planning systems do not account for neutron dose means that similar sized or larger errors are being admitted compared to the total uncertainty on calorimetry. While some uncertainty overhead is unavoidable, the dilution of confidence in these cases (even if only dose-to-water is considered) suggests that much of the effort into the quest for sub-percent level uncertainties in calorimetry is questionable. Therefore, clinical dosimetry protocols should include beam quality specifications that are practical for both ends of the dosimetry chain, whether or not calorimetry is performed in the clinic, and which specifically take into account the differences in neutron dose between site-specific beam qualities. More research is required in order to establish the differences in beam qualities between clinical beams and to determine how to best implement calorimetry in the calibration chain. Specific attention is also called for regarding the selection of the types of ionization chambers, since the use of hydrogenous materials in ionization chambers generally makes the dosimetry more robust against changes in neutron dose fraction.

6.1.3 Heat transfer

The effects of heat transfer on the calorimetric measurements have been examined in chapter 5. It was found that the large-scale temperature drift due to heat diffusing outward from the centre of the field can be principally understood from both analytical and numerical calculations. However, even though this mode of heat transfer results in the largest deviations in temperature at long time scales, it does not have a very large effect on the determined dose values.

One emergent issue is the importance of dose field homogeneity. Table 5.1 suggests that if assumption-free calorimetry is to be performed at the 0.1 % accuracy level, the field homogeneity should likewise be on the 0.1 % level within a distance of about 7 mm near the probes. In practice, the required width of the region of flatness is considerably higher, if one considers that two thermistors are used at a small distance from the nominal centre of the measurement system. The inhomogeneity issue is not necessarily only a challenge of volume averaging because the thermal transients that are associated with the thermal diffusion on such inhomogeneities enter directly in the heat transfer calculations. Operationally it is important to create a dose field that is as homogeneous as reasonably achievable. However, in practice, calorimetry in any proton beam can not be assumption-free on the count of the field inhomogeneity related heat transfer.

Therefore, in all cases a spatially resolved heat transfer calculation should be performed that takes measured dose distributions as input. This means that the dose homogeneity should be measured before every calorimetry session, or it has to be shown that it is sufficiently reproducible. Scanning systems are particularly challenging in this aspect, because clinically relevant calibration fields may not have the required flatness nor the required reproducibility. In such cases one will

have to perform heat transfer calculations for each individual pencil beam spot. For SOBP dose distributions, the homogeneity in the depth-direction also becomes important on length scales of about 7 mm.

The modelling of the excess temperature increase of the thermistor probes appears adequate considering the error budget. While there is a statistically significant discrepancy, the current experiment can not differentiate between issues with the modelling or the heat transfer due to field inhomogeneities. In addition, dose rate fluctuations make it hard to interpret the excess temperature response of the probe during the time interval that the beam is on. The statistical uncertainty could potentially be improved, as the current experiment was designed with an emphasis on both long-term and short-term heat transfer effects rather than only the short term probe effects. Experimental validation of probe excess temperature modelling should initially be performed in a scattered beam because of the simpler description of the dose rate as a function of time. In scanning beams, other than the stability of the beam, the nominal dose rate varies as the spots are scanned over the thermistor probe. This will make verification experiments even more challenging.

The addition of a mixing system to the glass vessel has proven useful in performing the heat transfer experiments within limited amounts of beam time. However, if it is to be applied in a clinical beam, one should ensure that the thermistor temperature offset recovery does not yield unacceptably large errors, since clinical doses are typically much smaller than the doses used for the experiments presented here. One other issue that might arise in such cases is that the mixing disturbs the local chemical equilibrium at each point in the vessel, which requires further investigation considering the chemical heat defect.

6.2 A comment on robustness

One of the favourable aspects of ^{60}Co calorimetry as the basis for dose standards is that the system is relatively simple and that it can be used in many places in the world to independently set up a traceable absolute dosimetry system which is tied to the SI derived units of dose. Although calorimetry itself can be considered a rather fragile technique, it has been well researched in combination with ^{60}Co irradiations and has since been replicated successfully around the world. The technique has also been tried in intercomparisons with other calorimetry standards as well as with dose standards other than calorimetry. Thus, the ^{60}Co calibration chain has proven to be quite robust.

For proton dose calibrations, a similar level of robustness is highly desirable. The fact remains that current ^{60}Co standards are all rather similar, while each calorimeter standard is tailored to work with its intended ^{60}Co source. The reproducibility of the dose delivery allows extensive experimental validations to be performed. However, for proton irradiation dosimetry, this is always a challenge, even in scattered beams. The robustness of the dose standard lies in a limited

number of well known input variables and the stability of each variable. This is an inherent issue with calorimetry for proton irradiation systems. For example, the timing of each irradiated pencil beam spot in a clinical scanning system may not always be entirely predictable. In the case of a non clinical scattered beam, the timing can be arbitrarily fixed which reduces the complexity of the required heat transfer calculations because the correction factors can be pre-calculated and subsequently verified in an experiment.

Of course, the measurement model can be made as complex as is desired and it is not necessarily wrong or in error simply because of the complexity. Apart from the inevitable logistics issues, it is usually at least technically possible to measure in any desired beam. However, the complexity does reduce the robustness since it reduces the chance for independent intercomparisons between standards. It also reduces the chances of being able to verify each complex detail of the model in terms of an experiment involving actually measured doses. A desirable trait of a standard is perhaps not only its quoted low numerical uncertainty, but also the extent to which measurements can contribute to confidence in the result.

Thus, the dosimetry system should be set up in such a way that relatively simple measurements dominate throughout the entire dosimetry chain. This involves selecting beam quality specifications that can most likely accommodate the needs of both the primary standards and the clinical use of ionization chambers. If a similar kind of robustness and rigour is desired as is common in the current ^{60}Co photon standards, scanning particle beam calorimetry is only interesting if large amounts of beam time are available. This forces a decision on the perceived need for low uncertainty, weighing both the medical and metrological benefit against the various costs of maintaining a primary standard for a scanned beam. The remainder of this text will briefly consider various options, both long term and short term, mostly from the point of view of the metrological side of the issue.

As a side note, one cannot help but notice the clash between dose-to-water reproducibility and patient-dose reproducibility. Ensuring the reproducibility of both things essentially reduces to reproducing the primary particle fluence (and energy spectrum) in terms of number of protons delivered per unit area at the treatment location. In clinical practice, the dose-to-water is reproduced, rather than the fluence. This involves the calculation of dose by the treatment planning system for both water and the patient, followed by a calibration based on only the dose-to-water reading. Ironically, ensuring that the dose-to-water is reproduced between two clinical systems does not imply that the dose-to-patient in those same two systems is reproduced. It is easy to get carried away in trying to reduce the uncertainty on a water-irradiation by measuring dose while the particle fluence could also be measured directly. Generally one should be reluctant to using primary standards (or ionization chambers for that matter) as tools to correct possible deficiencies in treatment planning systems. The principle of robustness dictates that, if at all possible, correct dose delivery should be possible without dose calibration.

6.3 Measuring the proton Gray

Chapter 2 gives a general description of the calorimeter and the way it is used in proton dosimetry experiments. Considering the various uncertainties that result from the techniques described in that chapter, it is worth repeating that a large subset of the uncertainty contributions in proton irradiations is entirely analogous to corresponding uncertainties in ^{60}Co calorimetry - and the latter have been described extensively[30, 28, 36, 35]. Although the details of various corrections and uncertainties do depend on the characteristics of the proton irradiations as compared to those of the ^{60}Co irradiations, they are not discussed in this thesis, nor is necessarily every aspect of proton calorimetry treated exhaustively. This section compares calorimetry in scattered and scanned beams.

6.3.1 Scattered beam

Operationally, the benefits of a scattered beam are that it is relatively easy to set up, the beam is rather reproducible and the QA is relatively simple. Metrologically, the description of the measurement process is relatively simple with a scattered beam and it is rather analogous to conventional ^{60}Co metrology. Contrary to scanning beams, scattered beams are more easily implemented in a physics institute because they do not require very complicated hardware. Scanned beams will be the dominant clinical proton irradiation technique in the near future. However, if the ultimate goal is to calibrate a scanned-beam dose delivery, there still is some merit in performing calorimetry in a scattered beams.

Even though a scattered beam does not perfectly reproduce the beam quality of a modern clinical scanning-beam facility, the combination of the relatively robust beam delivery with opportunities of performing measurements regularly makes for a rather practical calibration system for proton dose. While in the current implementation at KVI-CART there still are issues with dose inhomogeneity and beam current stability, the estimated uncertainties are only slightly higher than in ^{60}Co calorimetry and the situation regarding these issues can still be improved. It should be pointed out that in the current ^{60}Co-based photon dosimetry system the clinical beam qualities (MV x-rays) are also not the same as the beam quality used for primary calorimetry (^{60}Co).

In this thesis, the calorimetry is performed in the plateau region of the Bragg-curve. Such irradiations would also be easily reproducible in many proton irradiation facilities. This already provides an opportunity to directly test calculated ionization chamber k_Q factors against a water calorimeter. Calibration at lower residual ranges become more difficult calorimetrically due to the curvature of the depth-dose curve, although the positioning uncertainty related to ionometry will also become an issue.

6.3.1.1 Spread out Bragg peak

One of the concerns with a plateau calibration as described above is that the ionization-chamber perturbation factors depend on the location of the measurement in the proton depth-dose curve, because of the change in energy of the protons as they are slowed down in the water volume. Currently, clinical protocols such as TRS398 specify the use of a Spread Out Bragg Peak (SOBP), which involves a mixture of energies corresponding to roughly the last 5 cm of the residual range, rather than measurements in the plateau region.

However, SOBPs can also be delivered using a scattered beam by including a rotating wheel energy modulator in the beam line. The overall match between calculated and predicted effects resulting from heat diffusion with rather narrow beams (chapter 5) suggests that the heat diffusion effects related to the position of the distal edge of the dose distribution can most likely be accounted for. The calculation of the temperature probe excess heat will need to include a stopping power ratio glass/water averaged over the energy range of the SOBP. Except for possible differences in neutron dose and the contributions from collimator scatter, the resulting beam quality will closely resemble the beam that could be delivered by a scanning system.

6.3.2 Scanned beams

While for practical reasons most of the modelling and experiments in this thesis applies to scattered beams, the end-goal is to provide primary metrology in beams that are as similar as possible to those beams that are in use in modern clinical facilities. This means that scanned beams will need to be accommodated in the near future, either by directly using a primary dose standard in a clinical beam or by maintaining the calibration chain across slightly different beam qualities, as it is done for high energy x-rays.

Pencil beam scanning techniques bring about mostly time dependent effects, and since the robustness and repeatability of passive scattering techniques is highly desirable in the context of absolute dose standards, the implementation of scattered-beam calorimetry is recommended before attempting to implement scanning-beam calorimetry. If scanning systems become available outside of a clinic, the possibility arises that much of the validation experiments could be performed without requiring beam time in a clinic.

The use of scanning systems with calorimetry requires a sophisticated level of control over the irradiation. The ‘active nature’ of scanning systems means that there is some inherent variance in the manner in which the dose is delivered with each irradiation. Exactly how this variance is expressed in the dose delivery depends on the implementation of the hardware that is used to perform the irradiation. In principle, each repositioning of the pencil beam and each step in the energy degrading takes a finite amount of time which has to be accounted for when performing heat transfer calculations. Besides fluctuations in the time needed

for such operations, variations in the proton beam current will necessarily cause variations in the time duration of each individual spot and each energy plane. Fixing the timing in such cases will cause dose inhomogeneities which need to be corrected for in both the calorimetry heat transfer calculations and the ionometry volume averaging corrections.

Current photon calorimetry standards rely on ^{60}Co radiation sources which are very stable and reproducible. Robustness being a desirable aspect of primary standards, it is recommended that the scanning systems are configured for stability above anything else, such that the practical operation of the standard can rely on pre-calculated and pre-validated correction factors.

Whether or not the dose delivery is stable enough for such operation, it is clear that the beam monitoring should be rather sophisticated. Even if the dose delivery nominally does not require corrections for the details of each spot, one would still want to have readings of the time-stamp of delivery and duration, the delivered beam charge and the position of each beam spot. This is especially important in the validation phase as one needs to be able to rule out (or confirm) effects of the scanning if any anomalies are detected.

Fortunately, in many cases the 'micro-structure' due to the individual pencil beam spot irradiations will average out over slightly longer time scales[51]. This means that the timing and duration of the energy planes and the full irradiations themselves is more important than the timing and duration of each individual spot. Dose inhomogeneity will be an issue. However, if the inhomogeneities are of statistical nature such that over a large number of irradiations they average out to a flat dose distribution and if at the same time the relative magnitude of the inhomogeneities amounts to less than roughly half of the intrinsic measurement noise of the calorimetry, there will be no significant detriment to the dose calibration.

In water calorimetry, statistical fluctuations due to electronic noise of 2 % to 3 % on a dose of 1 Gy for a single thermistor probe are common. However, clinical doses can be on the order of a few Gy, but possibly larger in some systems. This means that spot-dose variations above about 0.5 % (and sometimes less) should be avoided, otherwise the statistical uncertainty of the result will become adversely affected.

Considering repeatable dose inhomogeneities (such as due to the scanning pattern), the variations should be comparable or lower in magnitude than the remaining systematic uncertainties or the targeted statistical uncertainty. Otherwise, the final uncertainty will once again become adversely affected. Therefore, the flatness of the dose distribution must be evaluated experimentally for each irradiation system - and possibly before each experiment. In principle, repeatable dose inhomogeneities can be corrected for via heat transfer calculations. However, experimental verification of such calculations would require a statistical confidence that is much better than that which would normally be required for a routine water calorimetry measurement. Besides losing a degree of robustness, it would also impose the burden of needing to allocate extensive amounts of beam-time for validation in every irradiation system in which the calorimeter is to be used.

It should be noted that inhomogeneity effects can be partially mitigated by reducing the distance between the energy-planes and the transverse distance between the spots in a plane or by increasing the width of the spots. The increased overlap will generate a more flat dose distribution and will also serve as a local averaging over the multiple dose contributions. Unfortunately, in clinical systems this is often an issue because it may not be possible to change the irradiation parameters.

Performing scanned beam calorimetry in the plateau region is likely simpler to implement and control, because of the reduced complexity of the dose delivery. Single energy planes can be delivered in a very small amount of time, such that the dose delivery becomes quasi-instantaneous on the time scale of the heat transfer that is associated with the beam-width or the depth-dose curve. This should also resolve some of the challenges with beam current stability, because sequences of irradiations can be carried out at a fixed repetition rate.

One option of implementing scanning beam calorimetry is to create a scanning beam outside of the clinic. This would involve a scanning nozzle with fast scanning magnets complete with beam monitoring equipment and a control-system. In addition, it would require a fast switching degrader and energy selection system upstream in the beam line if SOBP irradiations are desired. The beam current stability should be at least as good as can be obtained in any clinical facility, but preferably significantly better since it translates directly into either timing variation or dose inhomogeneity. To facilitate QA and calorimetric and ionometric studies on the effects of the spot scanning, a spatially resolved 2D transmission ionization chamber is required.

Using a non clinical scanning system, the water calorimetry technique can be partially validated outside the clinic. Generally, this means that the non clinical system should display a better degree of control than any clinical system, such that it can simulate the range of properties (beam current variation, dose inhomogeneity, variance in timing) against which the calorimetry is to be shown to be robust. A complicating factor is that traditional scattering systems also require absolute calibrations and there are many variations on the pencil beam scanning technique (such as line-scanning). If validation is required for any random system the beam line would have to be rather versatile.

6.4 In-clinic calorimetry vs. calorimetry at a physics institute

In order to perform water calorimetry and in order to be able to provide a routine calibration service one needs frequent access to a proton beam facility. Since metrology laboratories do not have their own proton accelerators, they need to obtain beam time from either physics institutes or clinics providing experimental access.

A complicating factor is that performing calorimetry requires the use of sensitive measurement equipment in an environment that isn't necessarily well adjusted to such ultra low uncertainty measurements, whether it is in the facilities available to the experimentalist on-site or the amount of time that one has access to the experiment room to set up the equipment or the amount of contiguous time that one has control over the beam. Such practical issues become important quickly when selecting viable options of setting up a calibration service, because the time needed to perform a calorimetry experiment is measured in days, not hours. This section explores the benefits and drawbacks of both in-clinic calorimetry and calorimetry at a physics institute.

6.4.1 Calorimetry at a physics institute

Performing calorimetry at a physics institute has an advantage in that there is usually a good opportunity to gain experimental control. That is, one gets to characterize or even control many aspects of the beam delivery and because of the relative abundance of available beam time there are also possibilities for targeted validation experiments. While the complexities of the beam delivery are still significantly more severe as in ^{60}Co calorimetry (at the least, some amount of quality assurance checks are required before each experiment), the level of control that is granted can make the metrology quite reliable and robust.

In many ways, calorimetry in scattered beams has now been demonstrated and to a large extent validated. Achieving this level of control outside of a physics institute would be very challenging. However, the experiments in this thesis only involve measurements in the plateau region of the proton depth-dose curve. Furthermore, while these measurements would allow ionization chamber calibrations, additional steps are required in transferring the calibration to the clinics.

6.4.1.1 Transfer of calibrations to the clinic

Both plateau- and SOBP irradiations may be used to calibrate ionization chambers through calorimetry in a non clinical beam. Whatever option is chosen, the irradiation conditions in the clinic need to be similar in order for the dosimetry system to work. Both options have benefits and drawbacks.

In the case of plateau irradiations, considering the act of calibration, both the calorimetry and the ionometry operations are simple and quite robust. The downside is that such calibrations do not reveal anything about the variation of the beam quality conversion factors with depth. Thus, clinics implementing dosimetry based on a plateau calibration would still need to implement calculated beam quality conversion factors to measure dose in SOBP irradiations. In fact, this applies for plateau irradiations as well, because the irradiation conditions are never perfectly replicated.

However, since the source of the calibration still is a measurement with protons at a point along the Bragg curve, the traceability to a primary standard is restored. This should result in a lower uncertainty since only the variations of the response as a function of residual range will enter into the uncertainty of conversion factor, rather than the full conversion from ^{60}Co doses to proton doses.

In the case of calibrating the ionization chambers in an SOBP, the beforementioned residual-range dependent correction factors no longer need to be applied in the clinical beam, since the length of the SOBP as used during calibration can be chosen to match the typical length of the clinical SOBPs. While this eliminates much of the uncertainty related to the depth dependency of the beam quality conversion factors, it does introduce an amount of complexity in both the calorimetry calibration and the procedures in the clinic.

Both methods do require corrections between the calibration beam quality and the clinical beam quality. In general, one would prefer to have primary SOBP calibrations, since that is currently the clinical beam of interest. However, one may wonder whether the use of a SOBP calibration as opposed to a plateau calibration provides any additional benefit in terms of dose accuracy in a patient. The idea behind SOBP calibrations is that by measuring the dose near the location where the protons stop, one effectively samples an average proton stopping power as it occurs in the patient, since most of the SOBP in a patient is created by protons of similar energies. However, since the human body does not consist of purely water, there is a loss of correlation between the measured dose in the water phantom and the patient. Ultimately, the dose calibrations (whether in the plateau or SOBP) are proxies for measuring the proton fluence, with the added benefit of calibrating-out physics modelling errors in the dose-to-water calculations. The question to be answered is whether this inclusive benefit of SOBP calibrations outweighs the detriment in uncertainty and robustness caused by the switch to SOBP calibrations.

6.4.2 Calorimetry in a clinic

While calorimetry in a clinic is certainly possible from a technical point of view, there are major issues when it comes to the logistics of operating a primary standard in a clinic. The main issue is the lack of beam time in situations where performing the calorimetry would have to hold back patients in the treatment queue, because this is not an option. In principle, it is possible to perform a meaningful calibration during a weekend when patients are not being treated, however, this requires tight control of the experiment and does not allow for any set backs. The vessel design as shown in this thesis significantly reduces the thermal equilibration time, which would be beneficial in clinical environments. Those facilities that have a dedicated experimental scanning beam line would be able to host a calorimetry experiment during normal clinical operation. However, the control of the beam is still limited to clinical settings and since the measurements would have to be interspersed with patient irradiations, the timing of the beam availability would

be rather unpredictable, requiring one to calculate heat transfer corrections for each unique irradiation. Another issue is that, by definition, the accuracy and reproducibility of dose delivery for irradiation systems that work with the primary standards should be among the best available. Clinical irradiation systems do not necessarily meet those standards (for one thing, field flatnesses on the percent level[127, 128] are common).

More importantly, commissioning and maintaining a standard also means being able to perform experiments rather than just routine calibrations. These measurements are important as they build confidence in the measurement model and they are part of the continuous improvement cycle of the standards. Performing such measurements often requires a more rigorous level of beam control than that which is generally available in the clinic.

An argument for performing calorimetry in the clinic is that the obtained ionization chamber calibrations could be used directly without any incurred beam quality conversion factors. However, the beam quality of each clinic is slightly different, and the beam delivery characteristics also vary from facility to facility (or even between gantries in the same facility). In principle, this requires unique correction factors and commissioning experiments in each facility. While such statements need to be quantified, the metrological benefit of measuring in each clinical beam should also be quantified.

6.4.2.1 Scanned beams

The main rationale for measuring in a clinic is that it is often the only place where a modern, fully operational beam scanning system is available. The challenge is not so much the beam time required to obtain a statistically relevant calibration (it is nevertheless to be considered), but rather the beam time that is needed to perform validation experiments.

Clinical scanned beams will carry all of the challenges associated with scanned beams in general, but with the complexities of the clinical environment - as under no circumstances the patient care must be compromised. Without a dedicated experimental room, the time needed for set-up and tear-down would be prohibitive during a night-time measurement campaign if the patient treatment room needs to be vacated by the next morning. Clinics that have separate experimental beam lines are favoured, especially if the experimental room is accessible during routine clinic operation. Interspersing calorimetry irradiations with patient irradiations is theoretically possible, but this would likely cause an inflation of the total time needed, because the calorimeter operation carries distinct time patterns of its own (irradiation cycle, mixing) while the patient treatment can usually not be synchronized with the calorimetry measurement cycle. Operation during weekends appears the only viable option.

It should be pointed out that performing calorimetry in a (clinical) scanned beam is not by any means physically impossible. Considering the statistical confidence, it is possible to obtain a meaningful calibration over a weekend's worth of beam

time. In practice, the heat transfer effects due to dose inhomogeneities can be corrected through modelling. However, validation experiments such as described in this thesis require the capability to reproduce data points as desired, and the limits of uncertainty on the validation will essentially be determined by the dose variance of individual spots. Generally, one would like to validate calculated corrections which are based on the beam monitor signal from individual spots. This implies measuring at a statistical significance which is a few times better than that which would be required for routine measurements.

6.5 Moving forward

While ionization chambers have yet to be calibrated in the KVI-CART proton beam, the usage of calorimetry as described in this thesis is applicable for such purposes. The best available short-term option is therefore to calibrate ionization chambers in the plateau region, similar to the way the experiments were performed here. This will already provide the sought-after traceability and absolute calibration. In addition, there is a lot to be learned in the form of absolute validation of ionometry models, even if it is only in the plateau. Undoubtedly, actually performing the calibration will reveal epistemic issues that are as of yet unexplored, and provide the necessary experience to move forward.

For the near future, a SOBP calibration in a scattered beam appears feasible. While this possibility has not been examined in this thesis, the SOBP calibrations are not very much different from what already has been shown. The immediate difficulty will be the required redesign of the beam line and its validation (or finding beam time on an existing scattered beam). Calibrating directly in a SOBP will bring the benefit of mimicking the usual clinical beam qualities. Therefore, performing a SOBP calorimetry is recommended as a first step after ionometry calibrations in the plateau, although the extra time and effort should be warranted by the outcome of discussions on the subject of applicable clinical beam qualities for dose calibrations.

Finally, calibrating in scanning beam is, of course, technically possible, but unless a scanning beam is replicated in a non clinical environment, the time available for validation is quite limited. Essentially, this means that one would have to trust the employed computational models almost blindfoldedly. A short term solution would create a scanning beam at a physics institute. Even if the scanning beam is only capable of plateau irradiations, it would still allow for validation experiments to be performed. The clinical environment on the other hand brings about that it is difficult for a metrologist to keep ‘control’. This control, and the related robustness, is essentially what brings about the confidence in existing photon dose standards. Therefore, it is recommended that calorimetry be performed in non clinical (experimental) beams unless a compelling reason is presented why patient dose calibration would require application of calorimetry in a clinic.

Appendix A

Radio chemistry model

Radiolysis modelling and the heat defect calculation depend on a set of reaction equations and associated rate constants which are valid at the operating temperature of the calorimeter, the values for the yields of radicals which drive the reactions during the irradiation and the enthalpy changes associated with the reactions. This appendix provides a description of the radiolysis model which was used in this thesis.

A.1 Generalized radiolysis modelling overview

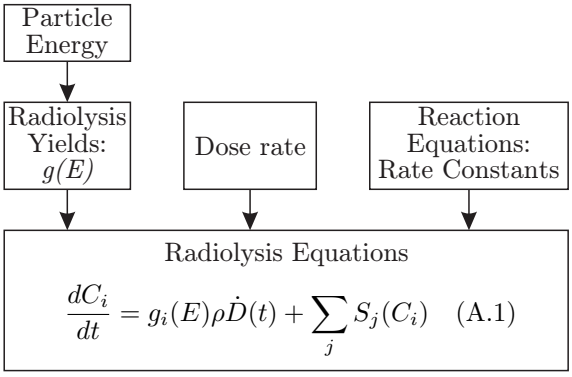

Figure A.1 – Radiolysis model schematic.

The radiolysis model is shown schematically in figure A.1. Equation A.1 describes the time evolution of the concentration C_i of the i^{th} chemical species considered in the model. Equation A.1 is the radiolysis equation, which is applicable under the conditions of homogeneous irradiation and separation of the radiolysis

in direct local effects of the radiation at short time intervals and homogeneous reaction dynamics at longer time intervals. The species included in the model are: e^-(aq), H, H^+, H_2, H_2O_2, O^-, O_2, O_2^-, O_3^-, OH, HO_2, HO_2^- and H_2O. Some of these species are generated directly inside the spurs of the track associated with a passing charged particle, which is modelled by a non-zero source term $g(E)\rho\dot{D}(t)$. This term includes the dose rate $\dot{D}(t)$ and the mass density ρ of the water at the operating temperature of the calorimeter. The differential yields $g(E)$ are listed in section A.5. For H_2O, $g(E)$ is calculated from the mass balance of all the other radiolysis yields. Following the source term is a summation over all possible reactions. The term $S_j(C_i)$ denotes the production rate of species i due to reaction j. The reaction term $S_j(C_i)$ depends on the stoichiometry and order of the reaction:

$$S_j(C_i) = \begin{cases} -k_j C_i & 1^{\text{st}} \text{ order, } C_i \text{ is participant} \\ -k_j C_i C_x & 2^{\text{nd}} \text{ order, } C_i \text{ and } C_x \text{ are participants} \\ -2k_j C_i^2 & 2^{\text{nd}} \text{ order dimerisation, } C_i \text{ is participant} \\ +nk_j \prod C_x & C_i \text{ is product, } C_x \text{ are participants} \\ 0 & \text{neither product nor participant} \end{cases} \tag{A.2}$$

$S_j(C_i) = 0$ if the reaction is not applicable to the species considered. Negative values of the production rate indicate a removal of species. For dimerisations, the factor of two results from the definition of the reaction rate constant, which describes the reaction rate of the whole equation, not just the participant. The factor of n accounts for the yield of more than one product molecule of the same species in a single reaction.

Equation A.1 describes a system of 13 equations based on 50 reactions that has to be solved numerically.

A.2 Model in Comsol

The model described in equation A.1 can be solved using any software package capable of solving coupled differential equations. The calculations in this thesis were performed with the 'general ordinary differential equation' package, which is part of Comsol[121].

Typically, at the start of the calculation, the primary yield values $g_i(E)$ are set as constants and all but three of the initial values of the concentrations C_i are set to zero. The concentration of H_2O is set to the molar concentration of pure water at 4 °C, while the concentration of H_2 and O_2 are set to the values that result from the bubbling mixture or to zero if an inert deaeration gas is used. During the simulation $\dot{D}(t)$ describes the beam cycle of the irradiation. A typical beam cycle consists of irradiation at a constant dose rate for 60 s followed by an idle

time of 120 s. For some high-doserate calculations the duration of the irradiation is shortened to maintain a constant dose per irradiation, while the repetition time of the beam cycle remains 180 s.

A maximum time step of 0.5 s was enforced but the stepping is dynamically reduced to achieve a total estimated committed error of less than $10^{-13}\,\mathrm{mol\,L^{-1}}$ over all species. The resulting calculations typically show conservation of hydrogen and oxygen atoms at a few times $10^{-13}\,\mathrm{mol\,L^{-1}}$. To prevent issues with numerical precision due to the many orders of magnitude difference between the concentration of H_2O and the production in one time step, the radiolysis equation for water was split into a difference variable and an accumulator variable which was factored into the other radiolysis equations where applicable. An additional variable integrates the dose rate from within the time stepping procedure.

The simulation will output the concentration of all chemical species at one second intervals during an entire irradiation sequence. Reliable differences over the time span of one irradiation are obtained by bracketing the irradiations with data points from the calculation that are spaced apart by the repetition cycle, thereby largely avoiding issues related to transients in the chemical response. By multiplying the change in concentrations with the corresponding enthalpies of formation of the species (taking into account the net amount of water converted), the total reaction energy for each irradiation can be calculated. The dose for each irradiation may vary slightly due to the effects of the stepping procedure coupled with very short irradiation pulses. The heat defect for each irradiation is calculated by dividing the reaction energy by the value of dose derived from the integrated dose variable, which compensates for the slight dose variations in the calculation.

A.3 Reaction set and rate constants

Table A.1 lists the set of reaction equations which were used to perform the chemical heat defect calculations. The list was published by Klassen and Ross[73] as their 'Model IIIR' reaction model which had scaled rate constants such that it would work at 4 °C. They took the rate constants (and temperature dependencies) from a publication by Elliot[85]. Except for the explicit indication of surplus water and a fix for a typographical error, the list has been copied verbatim from the paper by Klassen and Ross.

The reactions described here take place in the bulk medium and are driven by the primary radiolysis yields $g_i(E)$. Some reactions produce new chemical species other than the primary species created directly by the beam. Competition by the reactions for the various radiolysis products leads to a system of coupled reaction equations.

The reactions are second order, except in the case of reactions R21, R23, R27, R31, R35 and R46 which are first order. For some reactions (R1, R2, R6, R20, R44 and R48) a surplus of water is indicated in parenthesis. In those cases the reaction rate is determined by only the rate constant k and the concentrations of

the other participants to the reaction. For second order reactions the unit of the rate constant is $\mathrm{L\,mol^{-1}\,s^{-1}}$, while in the case of a first order reaction the unit is $\mathrm{s^{-1}}$.

Table A.1 – Reaction equations for radiolysis at 4 °C as published by Klassen and Ross[73].

Reaction			Rate Constant k
R1: $e^-(aq) + e^-(aq) + (H_2O + H_2O)$	$\longrightarrow$	$H_2 + OH^- + OH^-$	3.48×10^9
R2: $e^-(aq) + H + (H_2O)$	$\longrightarrow$	$H_2 + OH^-$	1.73×10^{10}
R3: $e^-(aq) + OH$	$\longrightarrow$	OH^-	2.38×10^{10}
R4: $e^-(aq) + H_2O_2$	$\longrightarrow$	$OH + OH^-$	8.84×10^9
R5: $e^-(aq) + O_2$	$\longrightarrow$	O_2^-	1.16×10^{10}
R6: $e^-(aq) + O_2^- + (H_2O)$	$\longrightarrow$	$OH^- + HO_2^-$	8.48×10^9
R7: $e^-(aq) + HO_2$	$\longrightarrow$	HO_2^-	8.48×10^9
R8: $H + H$	$\longrightarrow$	H_2	3.44×10^9
R9: $H + OH$	$\longrightarrow$	H_2O	1.21×10^{10}
R10: $H + H_2O_2$	$\longrightarrow$	$OH + H_2O$	3.18×10^7
R11: $H + O_2$	$\longrightarrow$	HO_2	9.58×10^9
R12: $H + HO_2$	$\longrightarrow$	H_2O_2	7.24×10^9
R13: $H + O_2^-$	$\longrightarrow$	HO_2^-	7.24×10^9
R14: $OH + OH$	$\longrightarrow$	H_2O_2	3.76×10^9
R15: $H_2 + OH$	$\longrightarrow$	$H + H_2O$	2.40×10^7
R16: $H_2O_2 + OH$	$\longrightarrow$	$HO_2 + H_2O$	1.79×10^7
R17: $OH + HO_2$	$\longrightarrow$	$O_2 + H_2O$	9.08×10^9
R18: $O_2^- + OH$	$\longrightarrow$	$O_2 + OH^-$	7.89×10^9
R19: $HO_2 + HO_2$	$\longrightarrow$	$H_2O_2 + O_2$	3.72×10^5
R20: $O_2^- + HO_2 + (H_2O)$	$\longrightarrow$	$H_2O_2 + O_2 + OH^-$	5.84×10^7
R21: H_2O	$\longrightarrow$	$H^+ + OH^-$	2.22×10^{-6}
R22: $H^+ + OH^-$	$\longrightarrow$	H_2O	7.23×10^{10}
R23: H_2O_2	$\longrightarrow$	$H^+ + HO_2^-$	1.34×10^{-2}
R24: $H^+ + HO_2^-$	$\longrightarrow$	H_2O_2	3.13×10^{10}
R25: $H_2O_2 + OH^-$	$\longrightarrow$	$HO_2^- + H_2O$	7.56×10^9
R26: $HO_2^- + H_2O$	$\longrightarrow$	$H_2O_2 + OH^-$	5.45×10^5
R27: H	$\longrightarrow$	$e^-(aq) + H^+$	8.83×10^{-1}
R28: $e^-(aq) + H^+$	$\longrightarrow$	H	1.88×10^{10}
R29: $e^-(aq) + H_2O$	$\longrightarrow$	$H + OH^-$	5.08×10^0
R30: $H + OH^-$	$\longrightarrow$	$e^-(aq) + H_2O$	7.77×10^6
R31: OH	$\longrightarrow$	$H^+ + O^-$	1.34×10^{-2}
R32: $H^+ + O^-$	$\longrightarrow$	OH	3.13×10^{10}
R33: $OH + OH^-$	$\longrightarrow$	$O^- + H_2O$	7.56×10^9
R34: $O^- + H_2O$	$\longrightarrow$	$OH + OH^-$	5.45×10^5
R35: HO_2	$\longrightarrow$	$H^+ + O_2^-$	4.21×10^5
R36: $H^+ + O_2^-$	$\longrightarrow$	HO_2	3.13×10^{10}

Table A.1 – Continued

Reaction			Rate Constant k
R37: $OH^- + HO_2$	$\longrightarrow$	$O_2^- + H_2O$	7.91×10^9
R38: $O_2^- + H_2O$	$\longrightarrow$	$OH^- + HO_2$	1.94×10^{-2}
R39: $H_2 + O^-$	$\longrightarrow$	$H + OH^-$	7.95×10^7
R40: $H_2O_2 + O^-$	$\longrightarrow$	$O_2^- + H_2O$	3.44×10^8
R41: $OH + HO_2^-$	$\longrightarrow$	$OH^- + HO_2$	5.17×10^9
R42: $O^- + OH$	$\longrightarrow$	HO_2^-	6.02×10^9
R43: $e^-(aq) + HO_2^-$	$\longrightarrow$	$O^- + OH^-$	2.19×10^9
R44: $e^-(aq) + O^- + (H_2O)$	$\longrightarrow$	$OH^- + OH^-$	1.82×10^{10}
R45: $O^- + O_2$	$\longrightarrow$	O_3^-	2.63×10^9
R46: O_3^-	$\longrightarrow$	$O^- + O_2$	6.70×10^2
R47: $O^- + HO_2^-$	$\longrightarrow$	$O_2^- + OH^-$	2.84×10^8
R48: $O^- + O_2^- + (H_2O)$	$\longrightarrow$	$O_2 + OH^- + OH^-$	4.26×10^8
R49: $H_2O_2 + HO_2$	$\longrightarrow$	$O_2 + OH + H_2O$	2.90×10^{-1}
R50: $H_2O_2 + O_2^-$	$\longrightarrow$	$O_2 + OH + OH^-$	9.30×10^{-2}

A.4 Radiolysis yields (G-values)

A.4.1 LET dependence

The radiolysis yields are based on tabulated energy and temperature dependencies obtained from a review paper by Elliot and Bartels[77]. They list the radiolysis yields as a function of track averaged LET, which is thought to characterize the yields independent of particle type.

It should be pointed out that the LET is perhaps not the only important variable determining the radiolysis yields. For their evaluation of the yields Elliot and Bartels did not consider the effects of multiple ionisation, which introduces sharp changes in yields at high LET depending on the particle type. However, simulations[129, 130] suggest that this only becomes important above a LET of $10\,\mathrm{keV\,\mu m^{-1}}$. Additionally, it has been suggested that a more two-dimensional picture of dose deposition is more appropriate since the energy of the delta electrons defines the radius within which dose is deposited[131, 132]. Simulations[133] indicate that also these effects become important only above a LET of about $10\,\mathrm{keV\,\mu m^{-1}}$. Moreover, in the LET range of clinical interest for protons (mostly below $10\,\mathrm{keV\,\mu m^{-1}}$) there are few experimental data points available. Since the shape of the characterisation polynomials in the work of Elliot and Bartels is mostly determined by data points at a LET higher than $10\,\mathrm{keV\,\mu m^{-1}}$ and sometimes using datasets from experiments with particles other than protons, the increase of molecular versus radical yield with LET at clinically relevant LET ranges for protons might be underestimated.

An consistent set of radiolysis yields based on carefully reviewed experimental data such as published by Elliot and Bartels is highly valuable because it is the only direct link between simulations and reality. In view of the desire to base primary standards on experimental data rather than on simulations, using the data published by Elliot and Bartels is probably the best option. The characterisation polynomials listed in table A.2 are copied verbatim from the publication by Elliot and Bartels. The listed yields were mentioned to be valid at 'room temperature', which is assumed to be 25 °C.

Species	Polynomial
$G(e^-(aq))$	$2.429 - 0.647L - 0.311L^2 + 2.726\times10^{-2}\,L^3 + 2.241\times10^{-2}\,L^4$
$G(H_2)$	$0.435 + 9.401\times10^{-2}\,L + 9.962\times10^{-2}\,L^2 - 5.794\times10^{-3}\,L^3$
$G(H)$	$0.583 + 3.924\times10^{-3}\,L + 1.959\times10^{-2}\,L^2 - 3.773\times10^{-3}\,L^3 - 2.351\times10^{-2}\,L^4$
$G(OH)$	$2.605 - 0.608L - 0.440L^2 + 0.123L^3$
$G(H_2O_2)$	$0.675 + 0.135L - 1.221\times10^{-2}\,L^2$
$G(HO_2)$	$2.415\times10^{-2} + 7.237\times10^{-3}\,L - 2.246\times10^{-3}\,L^2 - 6.382\times10^{-3}\,L^3 + 4.778\times10^{-3}\,L^4$

Table A.2 – Polynomial characterisations of radiolysis yields due to recoil protons depending on the track averaged LET of the protons[77] at a water temperature of 25 °C. The resulting values have units of #species/100 eV. SI units can be obtained by multiplying the polynomials with $\frac{1}{100\cdot[1.6\times10^{-19}\,\mathrm{J\,eV^{-1}}]\cdot N_A} = 1.036\times10^{-7}\,\mathrm{mol\,J^{-1}\,\#^{-1}}$. Note that $L = \mathrm{Log}_{10}\left(\langle\mathrm{LET}\rangle\right)$.

In table A.2 L is defined in terms of the track average LET:

$$L = \mathrm{Log}_{10}\left(\langle\mathrm{LET}\rangle\right) = \mathrm{Log}_{10}\left(\frac{1}{E_0}\int_0^{E_0} -\frac{dE}{dx}dE\right) \tag{A.3}$$

The track average LET as defined above is not the same as the average stopping power (energy divided by the proton range). In fact, for medium energy protons the track average LET is about 2.4 times the average stopping power.

A.4.2 Temperature dependence

The radiolysis yields depend on the water temperature. The primary interest of radiolysis studies at higher LET has been its application to nuclear reactors. As a result radiolysis is usually studied at higher temperatures. Table A.3 lists fits of the temperature dependencies of the radiolysis yields in the range of 25 °C to 180 °C[77]. Assuming linear behaviour, Elliot and Bartels extrapolated the temperature dependence to reactor operation temperatures (up to 350 °C). In this work the temperature dependence is also assumed to be valid down to the calorimeter operating temperature (4 °C).

Species	Temperature Dependence $\frac{dG}{dT}$ [#/(100 eV °C^{-1})]
$e^-(aq)$	$1.92 \times 10^{-3} - 2.56 \times 10^{-5} \cdot \langle LET \rangle$
H_2	$7.59 \times 10^{-4} + 1.32 \times 10^{-6} \cdot \langle LET \rangle$
H	$6.70 \times 10^{-4} - 1.08 \times 10^{-5} \cdot \langle LET \rangle$
OH	$7.34 \times 10^{-3} - 3.37 \times 10^{-5} \cdot \langle LET \rangle$
H_2O_2	-1.62×10^{-3}
HO_2	0

Table A.3 – Temperature dependence of the radiolysis yields (G-Values)[77], which in turn depend on the track average LET (using units of eV nm^{-1} in this equation))

A.4.3 Yields of H^+, OH^- and H

An important aspect of radiolysis modelling is achieving charge balance and material balance, which is essential when calculating the heat defect because the reaction heat is directly calculated from changes in chemical concentrations. Besides this immediate effect on the accuracy of the calculated heat defect, any lack of material or charge balance would provide a continuous supply of a specific chemical species. This causes the operating points of the dynamic equilibria associated with those chemical species to deviate in the radiolysis calculation, which may radically change the overall behaviour of the chemical system as a whole.

The specified radiolysis yields in table A.2 and their temperature dependences listed in table A.3 do not necessarily result in material balance because experimentally, the yields have been determined independently. Material balance is achieved by defining the yield of one radiolysis product in terms of the yields of the other products. Following Elliots' suggestion[77] the yield of the hydrogen atom is determined from the material balance equation:

$$G(H) = G(OH) + 2\,G(H_2O_2) + 3\,G(HO_2) - G(e^-(aq)) - 2\,G(H_2) \tag{A.4}$$

The equation can be understood by setting up material balances for the H-atom and O-atom which include H_2O followed by eliminating H_2O from these equations. According to Elliot, using the material balance equation above to calculate G(H) as opposed to using the polynomial from table A.2 results in differences of no more than [0.13 #/100 eV], from which he claims that the G-values are self-consistent within experimental uncertainty. In many studies yields of H^+ and OH^- are not included in the model as primary yields. However, through the mechanism of equation 3.3 and equation 3.4 an amount of OH radicals is produced that is not associated with the production of H radicals, but with hydration of an electron. This requires subtracting the yield $G(e^-(aq))$ from G(OH) in the above equation. In principle, the yields of H^+ and OH^- are of minor importance as these species are the water autoionization products and they are quickly absorbed in the re-association reaction R22 from table A.1, which prevents these species

from appearing above the baseline concentration of $1 \times 10^{-7}\,\mathrm{mol\,L^{-1}}$. Assuming a value of $G(H^+)$=3 #/(100 eV) (which is just about the highest possible value that occurs in any system), the required dose rate resulting in an increase of reaction R22 by 10 % would be $23\,\mathrm{Gy\,s^{-1}}$. Clinical proton irradiation systems have similar or lower dose rates which means that the yields of H^+ and OH^- can be neglected. However, there are systems which can reach higher instantaneous dose rates. For completeness sake, the radiolysis yields of H^+ and OH^- are included in the radiolysis model. Following Klassen and Ross[24], the value for $G(OH^-)$ at low $\langle LET \rangle$ is obtained from a publication by Anderson[79]:

$$G(OH^-) = 0.43\,\#/(100\,\mathrm{eV}) \tag{A.5}$$

At higher $\langle LET \rangle$ the yield $G(OH^-)$ is estimated from charge balance considerations by attributing half of the decrease of $G(e^-(aq))$ at higher $\langle LET \rangle$ to an increase of $G(OH^-)$:

$$G(OH^-, \langle LET \rangle) = 0.43 + \tfrac{1}{2}\left(G(e^-(aq), 0.2\,\mathrm{eV\,nm^{-1}}) - G(e^-(aq), \langle LET \rangle)\right) \tag{A.6}$$

Values for $G(H^+)$ have also been published by Anderson[79]. However, for the purpose of radiolysis modelling charge must be conserved. Following Klassen and Ross[24] the value of $G(H^+)$ is defined to be:

$$G(H^+, \langle LET \rangle) = G(e^-(aq), \langle LET \rangle) + G(OH^-, \langle LET \rangle) \tag{A.7}$$

Thus the values of both $G(H^+)$ and $G(OH^-)$ are assumed to depend only on changes in $G(e^-(aq))$, a separate value for $G(OH^-)$ is only specified at low LET and the observed decrease in $G(e^-(aq))$ at higher LET is split symmetrically between changes in $G(H^+)$ and $G(OH^-)$.

A.4.4 Values of the radiolysis yields depending on track averaged LET

Table A.4 lists the radiolysis yields for a number of different of values of $\langle LET \rangle$ calculated with the data from sections A.4.1, A.4.2 and A.4.3.

The value of $\langle LET \rangle = 0.2\,\mathrm{eV\,nm^{-1}}$ corresponds to ^{60}Co irradiation. The values listed under $2\,\mathrm{eV\,nm^{-1}}$ correspond to a proton with a range of 21 cm while the value for $10\,\mathrm{eV\,nm^{-1}}$ represents the effects of a proton with a range of 5 mm.

Species	Track Averaged LET [eV nm^{-1}]		
	0.2 (^{60}Co)	2	10
G(e^-(aq))	2.69	2.17	1.49
G(H_2)	0.40	0.46	0.61
G(H)	0.41	0.73	0.58
G(OH)	2.62	2.23	1.53
G(H_2O_2)	0.61	0.75	0.83
G(HO_2)	0.02	0.03	0.03
G(H^+)	3.14	2.88	2.54
G(OH^-)	0.46	0.71	1.05
Radiolysis yields [#/100 eV]			

Table A.4 – Radiolysis yields calculated at 4 °C using the procedure described in sections A.4.1, A.4.2 and A.4.3.

A.4.5 Differential radiolysis yields (g-values)

Radiolysis yields are typically measured by fully stopping a beam with a known LET spectrum in water which contains a scavenger for the radiolysis product of interest after which standard chemical analytical techniques are used to measure the concentration. As such, the reported G-values reflect the dose-weighted (LET weighted) average of the radiolysis yields along the track. Data from direct measurements of differential g-values is not readily available.

However, if the integral G-values are known at a sufficient number of points in the applicable LET-range, these values also become meaningful in the differential sense, because the differential g-values can be folded out. While usage of such techniques for absolute quantitative purposes is questionable, it still serves a purpose in providing a qualitative method of studying radiolysis modelling at any point along the Bragg-curve.

The method employed here relies on folding out the nearly power-law behaviour of the stopping power curve from the polynomials listed in table A.2. To good approximation, the range of a proton is described by the following power law relation[134, 135]:

$$R = \alpha E^{p_0} \tag{A.8}$$

In the above equation, the range R has units of [cm] and the proton energy E has units of [MeV]. Fitting this equation to range versus energy tables calculated with PSTAR[111] in the range of 1×10^{-3} MeV to 200 MeV gives the following fitting parameters:

$$\alpha = 0.00231 \tag{A.9}$$

$$p_0 = 1.761 \tag{A.10}$$

Assuming that the stopping power equals the LET, the track average LET can be written as:

$$\langle \text{LET} \rangle = \frac{\int_0^{E_0} S(E)dE}{E_0} = \frac{\int_0^{E_0} -\frac{dE}{dx}dE}{E_0} \tag{A.11}$$

It should be pointed out that the track averaged LET is not a spatial average. It is an average over the energy deposited by the particle and not over the traversed distance. The integral radiolysis yields $G(E_0)$ as listed in table A.2 cover all of the yield due to a particle with primary energy E_0. The differential yield $g(E)$ is defined such that the total number of molecules produced is:

$$N(E_0) = \int_0^{E_0} g(E)dE \tag{A.12}$$

The integral yield $G(E_0)$ is:

$$G(E_0) = \frac{N(E_0)}{E_0} = \frac{\int_0^{E_0} g(E)dE}{E_0} \tag{A.13}$$

Then the differential yield is:

$$g(E) = g(E_0) = \frac{d\left(E_0 G(E_0)\right)}{dE_0} = G(E_0) + \frac{dG(E_0)}{dE_0}E_0 \tag{A.14}$$

The above equation is universally valid, but care should be taken about the units of $g(E)$. It could be $[\#/100\,\text{eV}]$ or $[\text{mol}\,\text{J}^{-1}]$ depending on how the integral yield $G(E)$ is specified. Differentials yields can now be obtained by differentiation of the integral yields. The integral yield is given by the characterisation polynomials as listed in table A.2 with an added temperature correction:

$$G(E) = \Delta T \frac{dG}{dT} + a_0 + \sum_{i=1}^{i=N} a_i L(E)^i \tag{A.15}$$

The term $\Delta T \frac{dG}{dT}$ is the temperature correction from section A.4.2, which adds in the behaviour at a temperature difference ΔT from room temperature. Differentiating the integral yield:

$$\frac{dG(E_0)}{dE_0} = c\Delta T \frac{d\langle \text{LET} \rangle}{dE_0} + \sum_{i=1}^{i=N} a_i \frac{d}{dE_0} L(E_0)^i \tag{A.16}$$

In the above equation, c is the factor from the temperature dependence (with its sign) that multiplies the track average LET from table A.4 and the a_i factors are the polynomial coefficients from table A.2.

The dependence on energy, which is strongly correlated to the proton stopping power, still needs to be factored in. Assuming that equation A.8 provides a good estimate for the range, the stopping power is:

$$\frac{dE}{dx} = -\frac{dE}{dR} = -\frac{E^{-(p-1)}}{\alpha p} \tag{A.17}$$

Using the previously mentioned values for α and p the resulting value has a unit of [MeV cm^{-1}]. Plugging the above equation into equation A.11(defining the track average LET), the track averaged LET can be approximated as:

$$\langle \text{LET} \rangle = -\frac{E^{-(p-1)}}{p(p-2)\alpha} \tag{A.18}$$

It should be pointed out that the estimate of stopping power according to equation A.17 is only applicable to intermediate energy ranges. Both the stopping power estimate and the estimate of track averaged LET break down below a few MeV. Figure A.2 shows the difference between the approximation of the stopping power and the NIST PSTAR calculation. Below a few MeV the deviation is very large due to the Bragg peak which equation A.8 cannot accommodate. The stopping power and the track average LET of equation A.18 become meaningful beyond ranges of a centimetre or so, because the fraction of energy expended in the Bragg peak region is small. The approximation for the track averaged LET in equation

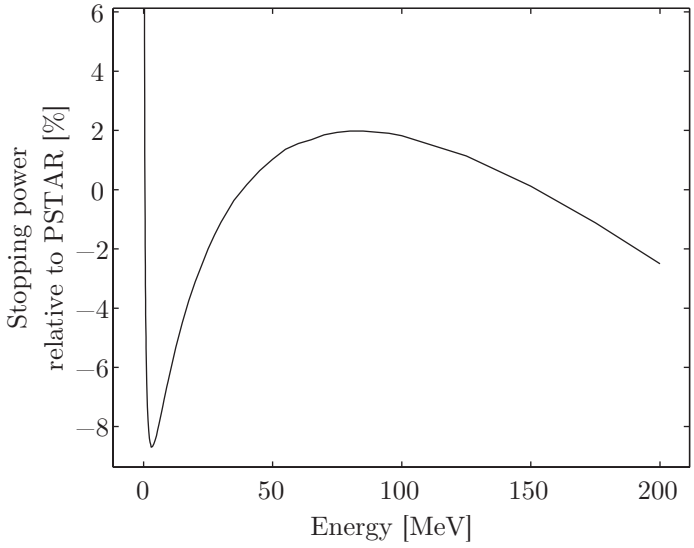

Figure A.2 – Difference between the stopping power as calculated with equation A.17 and the result from PSTAR.

A.18 is plugged into equation A.3:

$$L = \mathrm{Log}_{10}\left(\langle \mathrm{LET} \rangle\right) = \mathrm{Log}_{10}\left(-\frac{E^{-(p-1)}}{p(p-2)\alpha}\right) \tag{A.19}$$

Differentiating L and $\langle \mathrm{LET} \rangle$:

$$\frac{dL(E)}{dE} = \frac{-(p-1)}{ln(10)\cdot E} \tag{A.20}$$

$$\frac{d\langle \mathrm{LET} \rangle}{dE} = (p-1)\frac{E^{-(p)}}{p(p-2)\alpha} \tag{A.21}$$

The approximation for the track averaged LET in equation A.18 can now be used to calculate the differentials in equation A.16:

$$\frac{dG(E)}{dE} = c\Delta T \frac{d\langle \mathrm{LET} \rangle}{dE_0} + \sum_{i=1}^{i=N} a_i \frac{d}{dE} L(E)^i \tag{A.22}$$

$$= c\Delta T \frac{d\langle \mathrm{LET} \rangle}{dE_0} + \sum_{i=1}^{i=N} i \cdot a_i L(E)^{i-1} \cdot \frac{dL(E)}{dE} \tag{A.23}$$

$$\frac{dG(E)}{dE} = c\Delta T \frac{(p-1)E^{-(p)}}{p(p-2)\alpha} + \sum_{i=1}^{i=N} i \cdot a_i \mathrm{Log}_{10}^{i-1}\left(-\frac{E^{-(p-1)}}{p(p-2)\alpha}\right) \cdot \frac{-(p-1)}{ln(10)\cdot E} \tag{A.24}$$

Finally, combining equation A.24 and A.14:

$$g(E) = G(E) + c\Delta T \frac{(p-1)E^{-(p-1)}}{p(p-2)\alpha} + \sum_{i=1}^{i=N} i \cdot a_i \mathrm{Log}_{10}^{i-1}\left(-\frac{E^{-(p-1)}}{p(p-2)\alpha}\right) \cdot \frac{-(p-1)}{ln(10)} \tag{A.25}$$

$$g(E) = G(\langle \mathrm{LET} \rangle) - (p-1)\left(c\Delta T \langle \mathrm{LET} \rangle + \sum_{i=1}^{i=N} \frac{i \cdot a_i}{ln(10)} \cdot \mathrm{Log}_{10}^{i-1}\left(\langle \mathrm{LET} \rangle\right)\right) \tag{A.26}$$

The above equation calculates the differential yield at intermediate proton energies, based on a polynomial characterisation of the logarithmic dependence of the integral yield on the track averaged LET. This formulation is an approximation that is generally consistent with the definition of the integral yield of equation A.13. Mass conservation is obtained naturally as was the case with the integral yields by the use of charge and mass balances. The exact definition shown in equation A.14 could be used to calculate differential yields directly. This requires numerical calculation of the stopping power curve and track averaged LET as well as numerical differentiation of the results. In that case also the Bragg peak could be folded out, but such use of the characterisation polynomials is not warranted due to the sparsity of the original measurement data and the various experimental difficulties of measuring at high LET.

A.5 Differential yield values

Using equation A.26 in section A.4.5 the differential (local) radiolysis yields can be estimated. Figure A.3 and table A.5 list the differential yields at a water temperature of 4 °C for various proton energies. The energies of 160 MeV, 78 MeV and 22 MeV correspond to proton ranges of 17.6 cm, 5.0 cm and 5.0 mm respectively. The energy of 160 MeV could be considered a low-LET 'plateau dose', while the energies of 78 MeV and 22 MeV roughly bracket the energies at the centre of a SOBP.

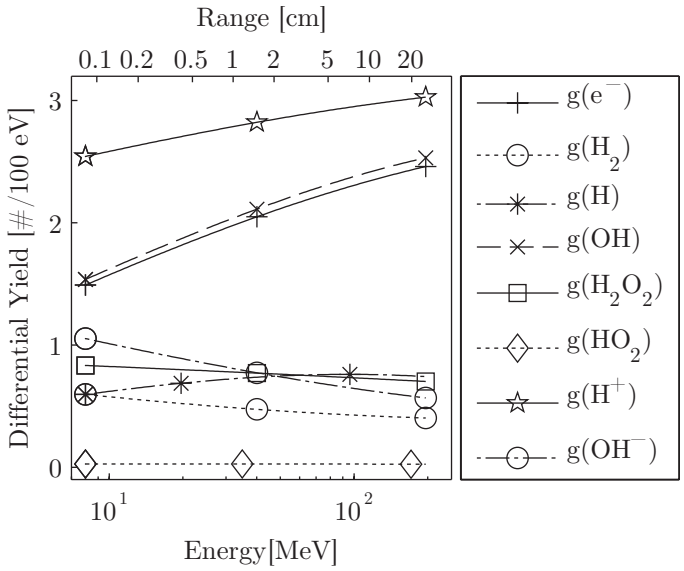

Figure A.3 – Differential radiolysis yields calculated at 4 °C using equation A.26. The listed protons ranges were calculated with PSTAR[111].

Comparing table A.5 with table A.4 shows that irradiation at high proton energies should give a similar response as ^{60}Co irradiation. The magnitude of the differences between protons and ^{60}Co for the low-LET portion of the table is similar to the differences between table A.4 and actual measurements at ^{60}Co beam qualities[77]. The differences are comparable to the residuals from the polynomial fits which were used to create table A.4 and the differential yields can not be expected to be known with better accuracy. In the energy range of 160 MeV down to 22 MeV the yields g(e^-(aq)) , g(H_2) and g(OH) change by a little over 24 %. Especially the g(OH) yield actually varies significantly in the last 5 cm of the proton range. Given the importance of this radical in establishing chemical equilibrium under radiolysis, calorimetry in a SOBP requires careful control of the radio chemistry.

Species	Proton Energy [MeV]		
	160	78	22
$g(e^-(aq))$	2.42	2.24	1.85
$g(H_2)$	0.41	0.44	0.51
$g(H)$	0.75	0.76	0.70
$g(OH)$	2.49	2.31	1.91
$g(H_2O_2)$	0.71	0.74	0.79
$g(HO_2)$	0.02	0.03	0.03
$g(H^+)$	3.01	2.92	2.72
$g(OH^-)$	0.59	0.68	0.87
Differential radiolysis yields [#/100 eV]			

Table A.5 – Differential radiolysis yields calculated at 4 °C using equation A.26.

A.6 Enthalpies of formation for radiolytic species

The net heat defect of radiolysis is determined by the outcome of the chemical reactions (listed in table A.1), driven by the spur production according to the g-values (listed in section A.4). In principle, each individual reaction in table A.1 contributes with a certain heat-of-reaction (either exothermal or endothermal). At long time scales however (seconds after the beam is turned off), only the stable radiolysis products survive. It suffices to know the standard enthalpy of formation for each of the long lived species. Thus, over any time interval (one irradiation) the total heat of radiolysis per unit volume may be calculated as:

$$E_R = -\sum_i \Delta C_i H_{f,i} \tag{A.27}$$

In the above equation, E_R is the generated heat due to radiolysis, ΔC_i is the change in concentration of the i'th species considered and $H_{f,i}$ is the enthalpy of formation of the i'th species. Water is one of these species and its change in concentration is accounted for. In the above equation E_R has units of $\mathrm{J\,L^{-1}}$ which is equivalent to dose:

$$D_R = -\frac{1}{\rho}\sum_i \Delta C_i H_{f,i} \tag{A.28}$$

The dose-equivalent-heat due to radiolysis D_R can be used to calculate the magnitude of the heat defect. The required enthalpies of formation were obtained from an article by Klassen and Ross[49] and are listed in table A.6. The listed enthalpies are not the standard enthalpies of formation however, because the data in table A.6 includes the enthalpy of solution, assuming that the radiolysis products dissolve in pure water.

Species	H_f kJ mol^{-1}
H_2O	−285.83
H^+	0.0
OH^-	−229.99
H_2O_2	−191.17
O_2	−11.7
O_2^-	−24.7
H_2	−4.2

Table A.6 – Enthalpies of formation[49, 136, 137] for aqueous radiolysis products.

Bibliography

[1] Robert R. Wilson. Radiological use of fast protons. *Radiology*, 47(5):487–491, 1946. Cited on page 9.

[2] Martin Jermann. Particle therapy statistics in 2014. *International Journal of Particle Therapy*, 2(1):50–54, 2015. Cited on page 9.

[3] PTCOG. Particle therapy center statistics. `http://www.ptcog.ch/index.php/facilities-in-operation` — `http://www.ptcog.ch/index.php/facilities-under-construction` — `http://www.ptcog.ch/index.php/facilities-in-planning-stage`, April 2016. Cited on page 9.

[4] Mark W. McDonald and Markus M. Fitzek. Proton therapy. *Current Problems in Cancer*, 34(4):257 – 296, 2010. Proton Therapy. Cited on page 9.

[5] Harald Paganetti. *Proton therapy physics*. CRC Press, December 2011. Cited on page 9.

[6] ICRU. Prescribing, recording, and reporting proton-beam therapy. *Journal of the ICRU*, 7(2):NP, 2007. Cited on pages 10, 16, 23, 53, and 120.

[7] B.J. Mijnheer, J.J. Battermann, and A. Wambersie. What degree of accuracy is required and can be achieved in photon and neutron therapy? *Radiotherapy and Oncology*, 8(3):237 – 252, 1987. Cited on page 10.

[8] A. Brahme. Dosimetric precision requirements in radiation therapy. *Acta Radiologica: Oncology*, 23(5):379–391, 1984. Cited on page 10.

[9] David Thwaites. Accuracy required and achievable in radiotherapy dosimetry: have modern technology and techniques changed our views? *Journal of Physics: Conference Series*, 444(1):012006, 2013. Cited on page 10.

[10] Protonenbestraling. Signalement. Technical report, Gezondheidsraad, 2009. Cited on page 11.

[11] G. Ligtenberg, P.C. Staal, and S. Kleijnen. Rapport protonentherapie. Technical report, College Voor Zorgverzekeringen, March 2009. Cited on page 11.

[12] Indicaties voor protonentherapie - deel 1. Technical report, College Voor Zorgverzekeringen, March 2010. Cited on page 11.

[13] G. Ligtenberg and P.C. Staal. Indicaties voor protonentherapie - deel 2 - model-based indicaties. Technical report, College Voor Zorgverzekeringen, August 2011. Cited on page 11.

[14] P Andreo, D T Burns, K Hohlfeld, M S Huq, T Kanai, F Laitano, V G Smyth, and S Vynckier. Absorbed dose determination in external beam radiotherapy: An international code of practice for dosimetry based on standards of absorbed dose to water. IAEA Technical Report Series 398, IAEA, Vienna, June 2006. Version 12. Cited on pages 11, 12, 13, 14, 16, 20, 21, 53, 59, 119, 120, 123, and 125.

[15] A.H.L. Aalbers, M-T. Hoornaert, A. Minken, H. Palmans, M.W.H. Pieksma, L.A. de Prez, N. Reynaert, S. Vynckier, and F.W. Wittkämper. Code of practice for the absorbed dose determination in high energy photon and electron beams. Technical Report 18, NEDERLANDSE COMMISSIE VOOR STRALINGSDOSIMETRIE, Delft, The Netherlands, August 2012. Revised edition, August 2012. Cited on pages 11 and 13.

[16] Joao Seco and Frank Verhaegen, editors. *Monte Carlo techniques in radiation therapy*. Taylor & Francis, 2013. Cited on page 12.

[17] Dan T.L. Jones. The w-value in air for proton therapy beams. *Radiation Physics and Chemistry*, 75(5):541 – 550, 2006. Cited on page 14.

[18] Carles Gomà, Bénédicte Hofstetter-Boillat, Sairos Safai, and Sándor Vörös. Experimental validation of beam quality correction factors for proton beams. *Physics in Medicine and Biology*, 60(8):3207, 2015. Cited on page 14.

[19] Carles Gomà, Pedro Andreo, and Josep Sempau. Monte Carlo calculation of beam quality correction factors in proton beams using detailed simulation of ionization chambers. *Physics in Medicine and Biology*, 61(6):2389, 2016. Cited on page 14.

[20] Hugo Palmans, Russell Thomas, Mary Simon, Simon Duane, Andrzej Kacperek, Alan DuSautoy, and Frank Verhaegen. A small-body portable graphite calorimeter for dosimetry in low-energy clinical proton beams. *Physics in Medicine and Biology*, 49(16):3737, 2004. Cited on pages 16 and 22.

[21] Frank Herbert Attix. *Introduction to radiological physics and radiation dosimetry*. Wiley-VCH Verlag GmbH, 2007. Cited on page 19.

[22] ICRU. Fundamental quantities and units for ionizing radiation. *ICRU Reports*, 60, 1998. Cited on page 19.

[23] Steve R. Domen. A sealed water calorimeter for measuring absorbed dose. *Journal of Research of the National Institute of Standards and Technology*, 99(2):121–141, March–April 1994. Cited on pages 21, 25, 35, 36, and 59.

[24] C K Ross and N V Klassen. Water calorimetry for radiation dosimetry. *Physics in Medicine and Biology*, 41(1):1, 1996. Cited on pages 21, 25, 26, 59, 137, and 200.

[25] Steve R. Domen. Absorbed dose water calorimeter. *Med Phys*, 7(2):157–159, 1980. Cited on pages 21 and 25.

[26] Nathan S. Osborne, Harold F. Stimson, and Defoe C. Ginnings. Measurements of heat capacity and heat of vaporization of water in the range 0° to 100°C. *Journal of Research of the National Bureau of Standards*, 23(2):197 – 260, August 1939. Cited on pages 21 and 41.

[27] IAPWS. Revised release on the IAPWS formulation 1995 for the thermodynamic properties of ordinary water substance for general and scientific use, June 2014. Cited on pages 21 and 41.

[28] Achim Krauss. The PTB water calorimeter for the absolute determination of absorbed dose to water in 60Co radiation. *Metrologia*, 43(3):259, 2006. Cited on pages 21, 23, 25, 29, 64, 65, 90, 93, 98, 99, 148, 155, 162, 164, and 185.

[29] Joakim Medin. Implementation of water calorimetry in a 180 MeV scanned pulsed proton beam including an experimental determination of k_Q for a Farmer chamber. *Physics in Medicine and Biology*, 55(12):3287, 2010. Cited on page 21.

[30] L.A. de Prez. De NMi standaard voor geabsorbeerde dosis in water in hoogenergetische fotonenstraling. private communication VSL, NMi-rapport nr. VSL-ESL-IO-2007/02, March 2008. Cited on pages 21, 23, 35, 36, 41, 93, and 185.

[31] H. Palmans, R. Thomas, M. Simon, S. Duane, A. Kacperek, J. Seco, R. Nutbrown, D. Shipley, A. DuSautoy, and F. Verhaegen. Feasibility of graphite calorimetry in a modulated low-energy clinical proton beam. In *Workshop on Recent Advances in Absorbed Dose Standards*, 2003. Cited on page 22.

[32] L.M. Petrie. *Characterisation of a graphite calorimeter in scanned proton beams*. PhD thesis, University of Surrey, July 2016. Cited on page 22.

[33] A. Krauss. Experimental verification of calculated radiation-induced heat conduction effects in the water absorbed dose calorimeter. *Thermochimica Acta*, 382(1-2):99 – 107, 2002. Cited on pages 22, 25, 29, 33, 137, 146, 147, 148, 155, 156, 160, 162, and 163.

[34] Christian P Karger, Oliver Jäkel, Hugo Palmans, and Tatsuaki Kanai. Dosimetry for ion beam radiotherapy. *Physics in Medicine and Biology*, 55(21):R193, 2010. Cited on pages 23 and 25.

[35] Steve R. Domen. An absorbed dose water calorimeter: Theory, design, and performance. *JOURNAL OF RESEARCH of the National Bureau of Standards*, 87(3):211–235, May–June 1982. Cited on pages 23, 25, 136, 137, and 185.

[36] J Medin, C K Ross, G Stucki, N V Klassen, and J P Seuntjens. Commissioning of an NRC-type sealed water calorimeter at METAS using 60Co γ-rays. *Physics in Medicine and Biology*, 49(17):4073, 2004. Cited on pages 23 and 185.

[37] H. Palmans, J. Seuntjens, F. Verhaegen, J.-M. Denis, S. Vynckier, and H. Thierens. Water calorimetry and ionization chamber dosimetry in an 85-MeV clinical proton beam. *Medical Physics*, 23:643–650, May 1996. Cited on page 24.

[38] A Sarfehnia, B Clasie, E Chung, H M Lu, J Flanz, E Cascio, M Engelsman, H Paganetti, and J Seuntjens. Direct absorbed dose to water determination based on water calorimetry in scanning proton beam delivery. *Medical Physics*, 37(7):3541–3550, 2010. Cited on pages 24, 148, 162, and 163.

[39] Joakim Medin, Carl K Ross, Norman V Klassen, Hugo Palmans, Erik Grusell, and Jan-Erik Grindborg. Experimental determination of beam quality factors, k_Q, for two types of Farmer chamber in a 10 MV photon and a 175 MeV proton beam. *Physics in Medicine and Biology*, 51(6):1503, 2006. Cited on page 24.

[40] Steve R. Domen. Absorbed dose water calorimeter, 1982. Cited on pages 25 and 136.

[41] R. J. Schulz, C. S. Wuu, and M. S. Weinhous. The direct determination of dose-to-water using a water calorimeter. *Medical Physics*, 14:790–796, September 1987. Cited on pages 25 and 28.

[42] Solange Gagnebin, Damian Twerenbold, Christian Bula, Christian Hilbes, David Meer, Eros Pedroni, and Silvan Zenklusen. Absolute dosimetry of scanned protons with a water calorimeter. Technical report, Center for Proton Radiation Therapy, PSI, 2006. Cited on page 26.

[43] Solange Gagnebin, Damian Twerenbold, Eros Pedroni, David Meer, Silvan Zenklusen, and Christian Bula. Experimental determination of the absorbed dose to water in a scanned proton beam using a water calorimeter and an ionization chamber. *Nuclear Instruments and Methods in Physics Research Section B: Beam Interactions with Materials and Atoms*, 268(5):524 – 528, 2010. Cited on page 26.

[44] Solange Gagnebin. *Experimental determination of absorbed dose to water in a scanned proton beam using a water calorimeter and an ionization chamber*. PhD thesis, SWISS FEDERAL INSTITUTE OF TECHNOLOGY ZURICH, 2010. Cited on page 26.

[45] L A de Prez and J A de Pooter. The new NMi orthovolt x-rays absorbed dose to water primary standard based on water calorimetry. *Physics in Medicine and Biology*, 53(13):3531, 2008. Cited on page 27.

[46] C. K. Ross, N. V. Klassen, and G. D. Smith. The effect of various dissolved gases on the heat defect of water. *Medical Physics*, 11:653–658, September 1984. Cited on pages 31, 59, 60, 64, 71, 79, 80, and 94.

[47] METAS. Nettoyage et remplissage du récipient en verre. Document No 155.1 A 03, August 2011. Cited on page 32.

[48] A. Krauss. private communication Achim Krauss, PTB, December 2014. Cited on page 33.

[49] Norman V. Klassen and Carl K. Ross. Absorbed dose calorimetry using various aqueous solutions. *International Journal of Radiation Applications and Instrumentation. Part C. Radiation Physics and Chemistry*, 38(1):95 – 104, 1991. Cited on pages 33, 60, 79, 80, 90, 206, and 207.

[50] METAS. Gazage du récipient en verre. Document No 155.1 A 04, June 2007. Cited on page 33.

[51] M Sassowsky and E Pedroni. On the feasibility of water calorimetry with scanned proton radiation. *Physics in Medicine and Biology*, 50(22):5381, 2005. Cited on pages 33, 75, 83, 85, 87, 89, 148, 162, and 187.

[52] Billy W. Mangum, G T. Furukawa, Kenneth G. Kreider, Christopher W. Meyer, Dean C. Ripple, Gregory F. Strouse, Weston L. Tew, Robert D. Saunders, Bettye C. Johnson, Howard W. Yoon, Michael R. Moldover, and Charles E. Gibson. The Kelvin and temperature measurements. *Journal of Research of the National Institute of Standards and Technology*, 106(1):105–149, January–February 2001. Cited on page 35.

[53] John S. Steinhart and Stanley R. Hart. Calibration curves for thermistors. *Deep Sea Research and Oceanographic Abstracts*, 15(4):497 – 503, 1968. Cited on page 36.

[54] E.R. van der Graaf, R.W. Ostendorf, M.-J. van Goethem, H.H. Kiewiet, M.A. Hofstee, and S. Brandenburg. AGORFIRM, the AGOR Facility for IRradiations of Materials. In *Radiation and Its Effects on Components and Systems (RADECS), 2009 European Conference on*, pages 451–454, Sept 2009. Cited on pages 41 and 43.

[55] S. Brandenburg, R. Ostendorf, M. Hofstee, H. Kiewiet, and H. Beijers. The irradiation facility at the AGOR cyclotron. *Nuclear Instruments and Methods in Physics Research B*, 261:82–85, aug 2007. Cited on page 43.

[56] E.R. van der Graaf. MCNPX simulations for the Multi User Facility beam line of the AGOR cyclotron, June 2008. Cited on pages 43 and 116.

[57] P. van Luijk. *Dose-volume effects in rat spinal cord irradiated with protons*. PhD thesis, University of Groningen, nov 2003. Cited on pages 43, 45, 47, 51, and 117.

[58] E Grusell, A Montelius, A Brahme, G Rikner, and K Russell. A general solution to charged particle beam flattening using an optimized dual-scattering-foil technique, with application to proton therapy beams. *Physics in Medicine and Biology*, 39(12):2201, 1994. Cited on page 44.

[59] S. N. Boon. *Dosimetry and quality control of scanning proton beams*. PhD thesis, University of Groningen, 1998. Cited on page 47.

[60] Virgil L. Highland. Some practical remarks on multiple scattering. *Nuclear Instruments and Methods*, 129(2):497 – 499, 1975. See also Erratum Nucl. Instr. and Meth. 129 (1975) 497-499. Cited on page 51.

[61] JCGM/WG 1. Evaluation of measurement data - guide to the expression of uncertainty in measurement. JCGM 100:2008, Joint Committee for Guides in Metrology, 2008. Cited on pages 56, 58, and 112.

[62] Frederick James. *Statistical methods in experimental physics*. World Scientific Publishing, 2006. Cited on page 57.

[63] Wayne H. Holtzman. The unbiased estimate of the population variance and standard deviation. *The American Journal of Psychology*, 63(4):pp. 615–617, 1950. Cited on page 57.

[64] Charles D. Jonah. A short history of the radiation chemistry of water. *Radiation Research*, 144(2):pp. 141–147, 1995. Cited on pages 59 and 61.

[65] Gregory Choppin, Jan-Olov Liljenzin, and Jan Rydberg. *Radiochemistry and nuclear chemistry*. Butterworth-Heinemann, Woburn, third edition edition, 2002. Cited on pages 59, 61, and 65.

[66] M. Roos and K. Hohlfeld. A measurement of the heat defect of water caused by high energy electrons. *Thermochimica Acta*, 119(1):95 – 101, 1987. Cited on pages 59 and 60.

[67] H.J. Brede, O. Hecker, and R. Hollnagel. Measurement of the heat defect in water and A-150 plastic for high-energy protons, deuterons, and alpha-particles. *Radiation Protection Dosimetry*, 70(1-4):505–508, 1997. Cited on pages 60, 83, and 93.

[68] U. Giesen, H. J. Brede, and K.-D. Greif. Dosimetry with a transportable water calorimeter in neutron, proton and heavy-ion radiation fields. *Radiation Protection Dosimetry*, 126(1-4):600–603, 2007. Cited on pages 60, 83, and 93.

[69] H J Brede, K-D Greif, O Hecker, P Heeg, J Heese, D T L Jones, H Kluge, and D Schardt. Absorbed dose to water determination with ionization chamber dosimetry and calorimetry in restricted neutron, photon, proton and heavy-ion radiation fields. *Physics in Medicine and Biology*, 51(15):3667, 2006. Cited on pages 60, 83, 93, and 106.

[70] B.G. Ershov and A.V. Gordeev. A model for radiolysis of water and aqueous solutions of H_2, H_2O_2 and O_2. *Radiation Physics and Chemistry*, 77(8):928 – 935, 2008. Cited on pages 60 and 71.

[71] A.W. Boyd, M.B. Carver, and R.S. Dixon. Computed and experimental product concentrations in the radiolysis of water. *Radiation Physics and Chemistry (1977)*, 15(2-3):177 – 185, 1980. Cited on page 60.

[72] NV Klassen and CK Ross. Water calorimetry: The heat defect. *JOURNAL OF RESEARCH OF THE NATIONAL INSTITUTE OF STANDARDS AND TECHNOLOGY*, 102(1):63–74, JAN-FEB 1997. Cited on page 60.

[73] NV Klassen and CK Ross. Water calorimetry: A correction to the heat defect calculations. *JOURNAL OF RESEARCH OF THE NATIONAL INSTITUTE OF STANDARDS AND TECHNOLOGY*, 107(2):171–178, MARCH-APRIL 2002. Cited on pages 60, 63, 64, 65, 70, 195, and 196.

[74] M Roos, B Grosswendt, and K Hohlfeld. An experimental method for determining the heat defect of water using total absorption of high-energy electrons. *Metrologia*, 29(1):59, 1992. Cited on page 60.

[75] A. Mozumder. *Fundamentals of radiation chemistry*. Academic Press, 1999. Cited on pages 61 and 62.

[76] D.R. McCracken, K.T. Tsang, and P.J. Laughton. Aspects of the physics and chemistry of waterradiolysis by fast neutrons and fast electrons in nuclear reactors. Report aecl-11895, Atomic Energy of Canada Ltd., Chalk River, Ontario, 1998. Cited on pages 61, 62, and 63.

[77] A.J. Elliot and D.M. Bartels. The reaction set, rate constants and g-values for the simulation of the radiolysis of light water over the range 20 to 350C based on information available in 2008. Report aecl-153-127160-450-001, Atomic Energy of Canada Ltd., Chalk River, Ontario, 2009. Cited on pages 62, 63, 64, 67, 87, 197, 198, 199, and 205.

[78] James F. Wishart and B. S. M. Rao. *Recent trends in radiation chemistry*. World Scientific Publishing Co. Pte. Ltd., 2010. Cited on page 62.

[79] Robert F. Anderson, Borivoj Vojnovic, and Barry D. Michael. The radiation-chemical yields of H_3O^+ and OH^- as determined by nanosecond conductimetric measurements. *Radiation Physics and Chemistry (1977)*, 26(3):301 – 303, 1985. Cited on pages 62 and 200.

[80] J.W. Fletcher. Radiation chemistry of water at low dose rates - emphasis on the energy balance: A computer study. Report AECL-7834, Atomic Energy of Canada Ltd., Chalk River, Ontario, 1982. Cited on pages 64 and 68.

[81] A. Krauss and H.-M. Kramer. The heat defect in the PTB water calorimeter: A discussion on uncertainty. In *Workshop on Recent Advances in Absorbed Dose Standards*, 2003. Cited on pages 65, 90, 97, and 98.

[82] A. O. Allen. *The radiation chemistry of water and aqueous solutions*. D. Van Nostrand Company, Inc.,, 1961. Cited on pages 65, 67, 68, 71, 79, 84, and 90.

[83] Edwin J. Hart, William R. McDonell, and Sheffield Gordon. The decomposition of light and heavy water boric acid solutions by nuclear reactor radiations. In *Proceedings of the international conference on peaceful uses of atomic energy*, volume 7, pages 593–598, New York, 1956. United Nations, United Nations. Cited on pages 67, 84, and 87.

[84] A. O. Allen, C. J. Hochanadel, J. A. Ghormley, and T. W. Davis. Decomposition of water and aqueous solutions under mixed fast neutron and gamma-radiation. *The Journal of Physical Chemistry*, 56(5):575–586, 1952. Cited on page 68.

[85] A.J. Elliot. Rate constants and g-values for the simulation of the radiolysis of light water over the range 0-300C. Report aecl-11073 cog-94-167, Atomic Energy of Canada Ltd., Chalk River, Ontario, October 1994. Cited on pages 70 and 195.

[86] David R. Lide. *CRC handbook of chemistry and physics*. CRC Press/Taylor and Francis, Boca Raton, FL, 2009. Cited on pages 79, 89, and 95.

[87] H. J. Brede, O. Hecker, and R. Hollnagel. An absorbed dose to water calorimeter for collimated radiation fields. *Nuclear Instruments and Methods in Physics Research Section A: Accelerators, Spectrometers, Detectors and Associated Equipment*, 455(3):721 – 732, 2000. Cited on pages 83 and 106.

[88] B. Pastina, J. Isabey, and B. Hickel. The influence of water chemistry on the radiolysis of the primary coolant water in pressurized water reactors. *Journal of Nuclear Materials*, 264(3):309 – 318, 1999. Cited on pages 83 and 87.

[89] Barbara Pastina and Jay A. LaVerne. Effect of molecular hydrogen on hydrogen peroxide in water radiolysis. *The Journal of Physical Chemistry A*, 105(40):9316–9322, 2001. Cited on pages 84 and 87.

[90] D.M. Bartels, M. Anderson, P. Wilson, T. Allen, and K. Sridharan. Supercritical water radiolysis chemistry - supercritical water corrosion. Generation iv nuclear energy systems technical documents, Idaho National Laboratory, 2006. Cited on page 87.

[91] Hilbert Christensen. Fundamental aspects of water coolant radiolysis. Ski report 2006:16, Swedish Nuclear Power Inspectorate SKI, 2006. Cited on page 87.

[92] V. Onoufriev. High temperature on-line monitoring of water chemistry and corrosion control in water cooled power reactors. Iaea-tecdoc-1303, International Atomic Energy Agency, 2002. Cited on page 87.

[93] Eric Edwards. *Determination of pure neutron radiolysis yields for use in chemical modeling of supercritical water*. PhD thesis, UNIVERSITY OF WISCONSIN-MADISON, 2007. Cited on page 87.

[94] George V. Buxton, Clive L. Greenstock, W. Phillip Helman, and Alberta B. Ross. Critical review of rate constants for reactions of hydrated electrons, hydrogen atoms and hydroxyl radicals in aqueous solution. *Journal of Physical and Chemical Reference Data*, 17(2):513, 1988. Cited on page 90.

[95] Jan Seuntjens and Hugo Palmans. Correction factors and performance of a 4 degrees celsius sealed water calorimeter. *Physics in Medicine and Biology*, 44(3):627, 1999. Cited on page 93.

[96] A Krauss and M Roos. Heat conduction, convection and radiolysis of the H_2/O_2 system in the water absorbed dose calorimeter. *Thermochimica Acta*, 310(1-2):53 – 60, 1998. Cited on pages 94, 95, 96, and 98.

[97] Christina Zacharatou Jarlskog and Harald Paganetti. Risk of developing second cancer from neutron dose in proton therapy as function of field characteristics, organ, and patient age. *International Journal of Radiation Oncology*Biology*Physics*, 72(1):228 – 235, 2008. Cited on page 104.

[98] David J. Brenner and Eric J. Hall. Secondary neutrons in clinical proton radiotherapy: A charged issue. *Radiotherapy and Oncology*, 86(2):165 – 170, 2008. Cited on page 104.

[99] Zdenek Morávek and Ludwig Bogner. Analysis of the physical interactions of therapeutic proton beams in water with the use of Geant4 Monte Carlo calculations. *Zeitschrift für Medizinische Physik*, 19(3):174 – 181, 2009. Cited on page 104.

[100] M. F. Moyers, E. R. Benton, A. Ghebremedhin, and G. Coutrakon. Leakage and scatter radiation from a double scattering based proton beamline. *Medical Physics*, 35(1):128–144, 2008. Cited on pages 104 and 106.

[101] K. Tesch. A simple estimation of the lateral shielding for proton accelerators in the energy range 50 to 1000 MeV. *Radiation Protection Dosimetry*, 11(3):165–172, 1985. Cited on page 104.

[102] J. Donald Cossairt. *Radiation physics for personnel and environmental protection*. Fermi National Accelerator Laboratory, revision 14 edition, 2016. FERMILAB REPORT TM-1834. Cited on page 104.

[103] G Galloway, J R Greening, and J R Williams. A water calorimeter for neutron dosimetry. *Physics in Medicine and Biology*, 31(4):397, 1986. Cited on page 106.

[104] S. Agostinelli, J. Allison, K. Amako, J. Apostolakis, H. Araujo, P. Arce, M. Asai, D. Axen, S. Banerjee, G. Barrand, F. Behner, L. Bellagamba, J. Boudreau, L. Broglia, A. Brunengo, H. Burkhardt, S. Chauvie, J. Chuma, R. Chytracek, G. Cooperman, G. Cosmo, P. Degtyarenko, A. Dell'Acqua, G. Depaola, D. Dietrich, R. Enami, A. Feliciello, C. Ferguson, H. Fesefeldt, G. Folger, F. Foppiano, A. Forti, S. Garelli, S. Giani, R. Giannitrapani, D. Gibin, J.J. Gómez Cadenas, I. González, G. Gracia Abril, G. Greeniaus, W. Greiner, V. Grichine, A. Grossheim, S. Guatelli, P. Gumplinger, R. Hamatsu, K. Hashimoto, H. Hasui, A. Heikkinen, A. Howard, V. Ivanchenko, A. Johnson, F.W. Jones, J. Kallenbach, N. Kanaya, M. Kawabata, Y. Kawabata, M. Kawaguti, S. Kelner, P. Kent, A. Kimura, T. Kodama, R. Kokoulin, M. Kossov, H. Kurashige, E. Lamanna, T. Lampén, V. Lara, V. Lefebure, F. Lei, M. Liendl, W. Lockman, F. Longo, S. Magni, M. Maire, E. Medernach, K. Minamimoto, P. Mora de Freitas, Y. Morita, K. Murakami, M. Nagamatu, R. Nartallo, P. Nieminen, T. Nishimura, K. Ohtsubo, M. Okamura, S. O'Neale, Y. Oohata, K. Paech, J. Perl, A. Pfeiffer, M.G. Pia, F. Ranjard, A. Rybin, S. Sadilov, E. Di Salvo, G. Santin, T. Sasaki, N. Savvas, Y. Sawada, S. Scherer, S. Sei, V. Sirotenko, D. Smith, N. Starkov, H. Stoecker, J. Sulkimo, M. Takahata, S. Tanaka, E. Tcherniaev, E. Safai Tehrani, M. Tropeano, P. Truscott, H. Uno, L. Urban, P. Urban, M. Verderi, A. Walkden, W. Wander, H. Weber, J.P. Wellisch, T. Wenaus, D.C. Williams, D. Wright, T. Yamada, H. Yoshida, and D. Zschiesche. Geant4 - a simulation toolkit. *Nuclear Instruments and Methods in Physics Research Section A: Accelerators, Spectrometers, Detectors and Associated Equipment*, 506(3):250 – 303, 2003. Cited on page 116.

[105] J. Allison, K. Amako, J. Apostolakis, H. Araujo, P.A. Dubois, M. Asai, G. Barrand, R. Capra, S. Chauvie, R. Chytracek, G.A.P. Cirrone, G. Cooperman, G. Cosmo, G. Cuttone, G.G. Daquino, M. Donszelmann, M. Dressel, G. Folger, F. Foppiano, J. Generowicz, V. Grichine, S. Guatelli, P. Gumplinger, A. Heikkinen, I. Hrivnacova, A. Howard, S. Incerti, V. Ivanchenko, T. Johnson, F. Jones, T. Koi, R. Kokoulin, M. Kossov, H. Kurashige, V. Lara, S. Larsson, F. Lei, O. Link, F. Longo, M. Maire, A. Mantero, B. Mascialino, I. McLaren, P.M. Lorenzo, K. Minamimoto, K. Murakami, P. Nieminen, L. Pandola, S. Parlati, L. Peralta, J. Perl, A. Pfeiffer, M.G. Pia, A. Ribon, P. Rodrigues, G. Russo, S. Sadilov, G. Santin, T. Sasaki, D. Smith, N. Starkov, S. Tanaka, E. Tcherniaev, B. Tome, A. Trindade, P. Truscott, L. Urban, M. Verderi, A. Walkden, J.P. Wellisch, D.C. Williams, D. Wright, and H. Yoshida. Geant4 developments and applications. *Nuclear Science, IEEE Transactions on*, 53(1):270–278, Feb 2006. Cited on page 116.

[106] John Apostolakis. The Geant4 simulation toolkit and applications. In Yves Lemoigne and Alessandra Caner, editors, *Molecular Imaging: Computer Reconstruction and Practice*, NATO Science for Peace and Security Series B: Physics and Biophysics, pages 73–92. Springer Netherlands, 2008. 10.1007/978-1-4020-8752-3_5. Cited on page 118.

[107] Physics parameters for proton therapy applications. Technical report, OpenGATE Collaboration. Cited on page 118.

[108] Mauro Testa, Chul Hee Min, Joost M Verburg, Jan Schümann, Hsiao-Ming Lu, and Harald Paganetti. Range verification of passively scattered proton beams based on prompt gamma time patterns. *Physics in Medicine and Biology*, 59(15):4181, 2014. Cited on page 118.

[109] M. Testa, J. Schümann, H.-M. Lu, J. Shin, B. Faddegon, J. Perl, and H. Paganetti. Experimental validation of the TOPAS Monte Carlo system for passive scattering proton therapy. *Medical Physics*, 40(12):–, 2013. Cited on page 118.

[110] *Geant4 physics reference manual - geant4.10.0*. Cited on page 118.

[111] M.J. Berger, J.S. Coursey, M.A. Zucker, and J. Chang. ESTAR, PSTAR, and ASTAR: Computer programs for calculating stopping-power and range tables for electrons, protons, and helium ions (version 1.2.3). http://physics.nist.gov/Star, January 2012. National Institute of Standards and Technology. Cited on pages 119, 156, 201, and 205.

[112] Hugo Bouchard, Jan Seuntjens, and Hugo Palmans. On charged particle equilibrium violation in external photon fields. *Medical Physics*, 39(3):1473–1480, 2012. Cited on page 120.

[113] Peter Wootton. Protocol for neutron beam dosimetry. AAPM Report 7, American Association of Physicists in Medicine, 1980. Task Group No. 18, Fast Neutron Beam Dosimetry Phsics, Radiation Therapy Committee. Cited on pages 124 and 125.

[114] Elin Brunckhorst. *Experimental investigations of the neutron contamination in high-energy photon fields at medical linear accelerators*. PhD thesis, Universität Hamburg, Von-Melle-Park 3, 20146 Hamburg, 2009. Cited on page 124.

[115] J Becker, E Brunckhorst, A Roca, F Stecher-Rasmussen, R Moss, R Böttger, and R Schmidt. Set-up and calibration of a triple ionization chamber system for dosimetry in mixed neutron/photon fields. *Physics in Medicine and Biology*, 52(13):3715, 2007. Cited on page 124.

[116] V. S. Vladimirov. *Equations of mathematical physics*. Marcel Dekker, 1971. Cited on page 137.

[117] Frank W. Olver, Daniel W. Lozier, Ronald F. Boisvert, and Charles W. Clark. *NIST handbook of mathematical functions*. Cambridge University Press, New York, NY, USA, 1st edition, 2010. Cited on page 143.

[118] J.M. Smith, E. Stammers, and L.P.B.M. Janssen. *Fysische transport verschijnselen 1*. Rijksuniversiteit Groningen, May 2004. Cited on page 146.

[119] Arman Sarfehnia and Jan Seuntjens. Development of a water calorimetry-based standard for absorbed dose to water in HDR ^{192}Ir brachytherapy. *Medical Physics*, 37(4):1914–1923, 2010. Cited on pages 148 and 162.

[120] Leon de Prez, Jacco de Pooter, Bartel Jansen, and Tony Aalbers. A water calorimeter for on-site absorbed dose to water calibrations in 60-Co and MV-photon beams including MRI incorporated treatment equipment. *Physics in Medicine and Biology*, 61(13):5051, 2016. Cited on page 148.

[121] COMSOL Multiphysics 4.2.0.150. Cited on pages 148 and 194.

[122] Henkel Technologies. *LOCTITE 603 technical data sheet*, May 2004. Cited on page 156.

[123] Dymax. Safety data sheet #401, June 2013. Cited on page 156.

[124] A. Krauss and M. Roos. Heat transport by material-dependent heating during absorption of radiation in the water absorbed dose calorimeter. *Thermochimica Acta*, 337(1-2):45 – 49, 1999. Cited on page 162.

[125] A. Krauss, M. Bambynek, and H.-J. Selbach. Towards the general application of water calorimetry as absorbed dose standard for radiotherapy dosimetry. In *Absorbed Dose and Air Kerma Primary Standards Workshop*, 2007. Cited on page 162.

[126] A. Krauss. Heat conduction effects during the calorimetric determination of absorbed dose to water in radiotherapy beams. *Thermochimica Acta*, 445(2):126 – 132, 2006. A selection of papers presented at the 16th Ulm-Freiberger Calorimetry Conference. Cited on page 162.

[127] Bijan Arjomandy, Narayan Sahoo, Xiaoning Ding, and Michael Gillin. Use of a two-dimensional ionization chamber array for proton therapy beam quality assurance. *Medical Physics*, 35(9):3889–3894, 2008. Cited on page 191.

[128] Benjamin Clasie, Nicolas Depauw, Maurice Fransen, Carles Gomà, Hamid Reza Panahandeh, Joao Seco, Jacob B Flanz, and Hanne M Kooy. Golden beam data for proton pencil-beam scanning. *Physics in Medicine and Biology*, 57(5):1147, 2012. Cited on page 191.

[129] Jintana Meesungnoen and Jean-Paul Jay-Gerin. High-LET radiolysis of liquid water with $^{1}H^{+}$, $^{4}He^{2+}$, $^{12}C^{6+}$, and $^{20}Ne^{9+}$ ions: Effects of multiple ionization. *The Journal of Physical Chemistry A*, 109(29):6406–6419, 2005. PMID: 16833985. Cited on page 197.

[130] Benoit Gervais, Michaël Beuve, G.H. Olivera, M.E. Galassi, and R.D. Rivarola. Production of HO_2 and O_2 by multiple ionization in water radiolysis by swift carbon ions. *Chemical Physics Letters*, 410(4-6):330–334, July 2005. Cited on page 197.

[131] Robert Katz. RBE, LET and z/β^{α}. *Health Physics*, 18:175, 1970. Cited on page 197.

[132] Robert Katz and E.J. Kobetich. Particle tracks in emulsion. *Physical Review*, 186:344–351, October 1969. Cited on page 197.

[133] Maximilian Kreipl, Werner Friedland, and Herwig Paretzke. Time- and space-resolved Monte Carlo study of water radiolysis for photon, electron and ion irradiation. *Radiation and Environmental Biophysics*, 48:11–20, 2009. 10.1007/s00411-008-0194-8. Cited on page 197.

[134] Thomas Bortfeld and Wolfgang Schlegel. An analytical approximation of depth - dose distributions for therapeutic proton beams. *Physics in Medicine and Biology*, 41(8):1331, 1996. Cited on page 201.

[135] David Jette and Weimin Chen. Creating a spread-out Bragg peak in proton beams. *Physics in Medicine and Biology*, 56(11):N131, 2011. Cited on page 201.

[136] Donald D. Wagman, William H. Evans, Vivian B. Parker, Richard H. Schumm, Iva Halow, Sylvia M. Bailey, Kenneth L. Churney, and Ralph L. Nuttall. The NBS tables of chemical thermodynamic properties - Selected values for

inorganic and C1 and C2 organic substances in SI units. *Journal of Physical and Chemical Reference Data*, 11, 1982. Supplement No. 2. Cited on page 207.

[137] Sidney W. Benson and Prakash S. Nangia. Electron affinity of HO_2 and HO_x radicals. *Journal of the American Chemical Society*, 102(8):2843–2844, 1980. Cited on page 207.

Glossary and acronyms

AGOR	Accelerateur Groningen-ORsay. Cyclotron delivering 190 MeV protons at KVI-CART.
AGOR-FIRM	AGOR Facility for Irradiations of Materials.
BIM	Beam Intensity Monitor. Thin-walled parallel plate transmission ionization chamber.
Beam-quality	The phase space of all ionizing radiation in a measurement geometry. A full description of beam quality includes the types of particles, their energies or spectra and their directions *at the location of the measurement*.
Bragg-peak	Peak in the spatial dose distribution caused by the increase of the LET towards the end of a charged particle track.
Comsol	Comsol Multiphysics. Commercial numerical physics simulation software.
Farmer-chamber	A specific design of ionization chamber.
FPGA	Field Programmable Gate Array. Used at AGORFIRM to control beam delivery based on BIM signals.
FWHM	Full Width Half Maximum. The width of a peaked distribution measured at half peak amplitude.
Geant4	A specific Monte Carlo toolkit for the simulation of the passage of particles through matter.
GUM	Guide to the expression of Uncertainty in Measurement, published by BIPM.
G-value	Generation value, number of molecules of a certain chemical species created in water per 100 eV of deposited energy.
HPC	High Purity Cell, also called 'vessel'. Glass vessel to contain ultra pure water.
IAEA	International Atomic Energy Agency.
ICRU	International Commission on Radiation Units and Measurements.
IMRT	Intensity-Modulated Radiation Therapy.
ITS90	International Temperature Scale of 1990, a set of calibration points defining an absolute temperature scale.

k_{Q_x,Q_0}	Beam quality conversion factor for obtaining the calibration value of an ionization chamber in a beam quality Q_x based on an existing calibration in beam quality Q_0 (^{60}Co).
KVI-CART	KVI Center for Advanced Radiation Technology.
LANEX	Scintillator sheet material, used to image the beam and transverse dose distributions.
hd	(Chemical) Heat Defect. Relative amount of energy lost to chemical reactions.
LET	Linear Energy Transfer. Amount of energy transferred to the medium by an energetic charged particle per unit path length.
Matlab	Commercial mathematics and data processing software.
METAS	Eidgenössisches Institut für Metrologie METAS.
MU	Monitor Unit. Measure of delivered proton flux or dose based on BIM signals.
NCS	Nederlandse Commissie voor Stralingsdosimetrie.
NCS18	Report number 18 by the NCS. Dosimetry protocol for photon and electron beam qualities.
NTC	Negative Temperature Coefficient (resistive thermometer).
NTP	Network Time Protocol. Protocol allowing synchronisation and clock-rate calibration between computer devices on a network.
PBS	Pencil Beam Scanning dose delivery. Technique of creating an approximately flat dose distribution by using fast magnets to move a narrow pencil beam over a target area, effectively 'painting' a wide and flat dose distribution with a narrow beam.
PID	Proportional-Integral-Derivative.
PMMA	Poly Methyl Methacrylate. Transparent plastic used to construct water phantoms and ionization chambers.
PSI	Paul Scherrer Institute.
PTB	Physikalisch-Technische Bundesanstalt.
PTC	Positive Temperature Coefficient (resistive thermometer).
PT100	Platinum PTC temperature sensor, nominally 100 Ω at 0 °C.
Scattered-beam	Technique of widening a narrow pencil beam obtained from an accelerator by placing a sheet of scattering material in the beam path, with the aim of covering a larger area with an approximately flat dose distribution.
SOBP	Spread Out Bragg Peak. Technique of irradiating multiple times with small steps in particle energy such that the Bragg-peak is shifted in position each time. In summation, the overlapping Bragg-peaks create an approximately spatially flat dose distribution.
TRS398	IAEA Topic Report Series, number 398. Dosimetry protocol for various beam qualities as published by the IAEA.
VSL	Van Swinden Laboratory, Dutch Metrology Institute.

Samenvatting

Protonentherapie

Protonentherapie is een geavanceerde behandeling voor kanker die in de komende tijd breder beschikbaar zal worden. Deze behandeling bestaat uit het van buitenaf bestralen van het aangetaste weefsel met hoogenergetische geladen deeltjes. Het verschil met op dit moment reeds veelvuldig gebruikte Röntgen bestralingen is gelegen in het patroon van de stralingsdosis in het lichaamsweefsel.

De door hoogenergetische deeltjes afgegeven energie heeft een dodelijke werking op zowel kankerweefsel als gezond lichaamsweefsel. Deze werking hangt samen met de dosering van deze energie, de zogeheten 'stralingsdosis'. Belangrijk voor het begrijpen van verschillen tussen de bestralingstechnieken is dat de hoogte van de stralingsdosis niet over het hele lichaam gelijk hoeft te zijn. Een arts zal proberen de bestraling zo in te richten dat de stralingsdosis het hoogste is in het kankerweefsel en zo laag mogelijk in het gezonde weefsel daarbuiten. Dit draagt ertoe bij dat in veel gevallen ernstige schade aan het gezonde weefsel (en daarbij horende complicaties) voorkomen kan worden. Enige mate van schade (of enige kans op complicaties) is echter altijd aanwezig. De unieke eigenschappen van de in protonentherapie gebruikte energetische deeltjes stellen ons in staat om de stralingsdosis in gevoelige gezonde weefsels verder te beperken, zodat de kans op ernstige complicaties nog meer afneemt.

De huidige Röntgen behandelingen bestaan uit het bestralen met hoogenergetische fotonen (x-rays). De nieuwe protonentherapie maakt gebruik van protonen, dat wil zeggen: de positief geladen atoomkernen uit waterstofgas. Deze protonen onderscheiden zich van fotonen voornamelijk door de ruimtelijke verdeling van de energiedepositie (stralingsdosis) over het lichaamsweefsel. In het geval van fotonen zal de stralingsdosis exponentieel afnemen als functie van de indringdiepte in het lichaam. In het geval van protonen neemt de stralingsdosis juist toe met de indringdiepte. Bijzonder aan protonen is dat dit niet oneindig door gaat. Er ontstaat een piek in de stralingsdosis die echter snel weer afneemt zodat de stralingsdosis in dieper gelegen weefsels vrijwel nul is. Dit effect maakt dat in voorkomende gevallen ook kankerweefsel bestraald kan worden dat dichtbij kwetsbare organen ligt.

Dosimetrie

De schade aan zowel het gezonde weefsel als het kanker-weefsel is gerelateerd aan de stralingsdosis. Deze dosis wordt uitgedrukt in de fysische eenheid $\mathrm{Gy} = \mathrm{J\,kg^{-1}}$. Klinische studies geven aan dat voor een betrouwbare behandeling de onzekerheid in toegediende stralingsdosis aan het kankerweefsel (en het mee-bestraalde gezonde weefsel) kleiner moet zijn dan 3 % (1 SD) van de gewenste dosis. Deze nauwkeurigheid kan alleen behaald worden als de verschillende onzekerheden die bijdragen aan deze 3 % veel kleiner zijn dan het totaal.

Eén van de onzekerheden bij dosisbepaling is de kalibratie van de bestralingsapparatuur. Gewoonlijk wordt in een ziekenhuis de stralingsdosis afgeregeld door deze te meten in een bak met water (het water volume staat dan model voor een patiënt). Het meetinstrument dat hierbij gebruikt wordt is een ionisatiekamer. Dit meetinstrument stelt de stralingsdosis vast door de elektrische lading te meten van luchtmoleculen die door de hoog energetische deeltjes zijn geïoniseerd. Om de vereiste nauwkeurigheid in de behandeling te kunnen halen moet dit meetinstrument de dosis in de waterbak vaststellen met een onzekerheid van 1 % (1 SD) of minder. Dit vereist dat de gebruikte ionisatiekamer zelf ook gekalibreerd is.

In het geval van de reeds in gebruik zijnde fotonen-bestralingen bieden de nationale meetstandaard-laboratoria* een dienst aan om de ionisatiekamer te kalibreren door deze te vergelijken met een primaire meetstandaard voor stralingsdosis in water. Deze meetstandaard moet in staat zijn om stralingsdosis vast te stellen met een onzekerheid die significant onder de 1 % (1 SD) ligt. Voor de bestaande fotonenbestralingen is de meetstandaard vaak een zogeheten 'watercalorimeter', echter voor protonenbestralingen zijn nog geen meetstandaarden in gebruik†.

Watercalorimetrie

Om de vereiste nauwkeurigheid in de kalibratie van stralingsdosis te kunnen halen maken veel standaard laboratoria gebruik van zogeheten watercalorimeters. Dit zijn meetstandaarden die op een zeer nauwkeurige manier de dosis in water kunnen meten. Het werkingsprincipe is, zoals de naam aangeeft, het meten van een temperatuurstijging van een volume water ten gevolge van de geabsorbeerde energie (dosis) tijdens een bestraling.

Figuur 1 geeft de meetmethode schematisch weer. Net als in de kliniek wordt een bak water bestraald met hoog energetische deeltjes (protonen dan wel fotonen). Als gevolg van de bestraling zal het water opwarmen op de plek waar de stralingsbundel zijn energie afgeeft. Omdat water geen goede warmtegeleider is zal de warmte

* Een Nationaal Meet Instituut (NMI) beheert de standaard maten en gewichten, zoals de standaard meter (m) en de standaard kilogram (kg), maar ook een standaard voor stralingsdosis (Gy). In Nederland is dat het Van Swinden Laboratorium in Delft.

† Tot het moment dat er een meetstandaard beschikbaar zal zijn moet de kalibratiewaarde van ionisatiekamers voor protonen middels een berekening afgeleid worden van de reeds bestaande kalibraties voor fotonen. Voor het doen van deze correctie zijn protocollen beschikbaar. Dit brengt ook een onzekerheid van iets minder dan 2 % met zich mee.

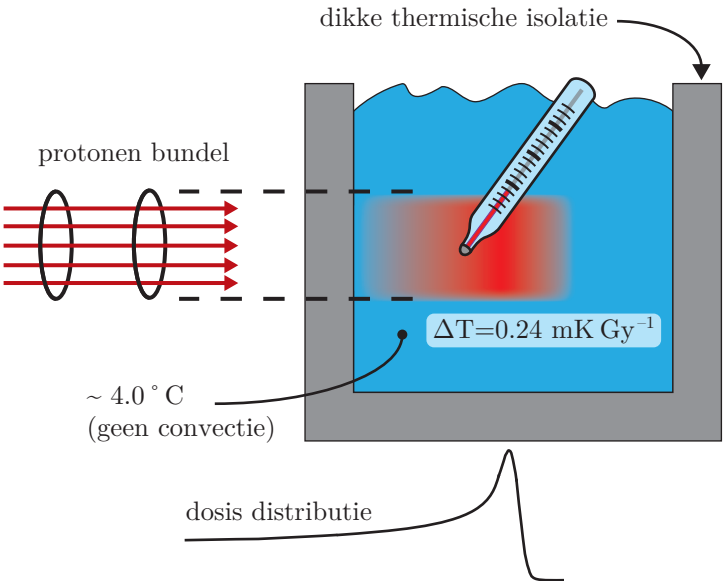

Figuur 1 – Schematische weergave van het watercalorimetrie meetprincipe.

nog enige tijd aanwezig blijven, ook nadat de bestraling beëindigd is. Om te voorkomen dat de warmte wegstroomt door beweging van het water moet het water gekoeld worden tot een temperatuur van 4 °C. Omdat bij deze temperatuur de thermische uitzettingscoëfficiënt van water nul is zal er geen convectie plaatsvinden. De temperatuur van het water voor, tijdens en na de bestraling wordt gemeten door een zeer gevoelige thermometer.

De dosis wordt (op kleine correcties na) als volgt vastgesteld:

$$D_w = C \cdot \Delta T \tag{1}$$

Dat wil zeggen, de stralingsdosis die is afgegeven aan het water volume (eenheid Gy = J kg^{-1}) kan worden bepaald door de warmtecapaciteit van het water C (eenheid J kg^{-1} K^{-1}) te vermenigvuldigen met de gemeten temperatuurstijging van het water ΔT (eenheid K). Voor een klinisch relevante hoeveelheid dosis van 1 Gy bedraagt deze temperatuur stijging slechts 0.24 mK, dat wil zeggen, één vierde deel van een duizendste van een graad. Dit verklaart ook waarom het water volume erg goed geïsoleerd moet zijn, omdat zonder deze isolatie de temperatuurschommelingen van buitenaf invloed zullen hebben op de meting.

Protonen watercalorimetrie

Hoewel meetsystemen zoals weergegeven in figuur 1 voor fotonenbestralingen (x-rays) al vele jaren in gebruik zijn, ontbreekt het nog aan stabiele meetstandaarden voor protonen. Hoewel het meetprincipe niet wezenlijk verschilt bij het meten van fotonenbestralingen of protonenbestralingen, zijn er op detail-niveau toch zaken die uitgezocht, gevalideerd of anderszins aangepakt moeten worden.

Een puur praktisch probleem is dat er een plaats moet zijn waar met een protonenbestraling gemeten kan worden. De benodigde techniek voor het uitvoeren van een bestraling is dermate complex en duur dat in de praktijk alleen ziekenhuizen zelf of natuurkundige onderzoeksinstituten het kunnen aanbieden. Dit is in tegenstelling tot meetstandaarden voor fotonen, waarbij een metrologie instituut in veel gevallen zelf een ^{60}Co stralingsbron beschikbaar kan hebben. Vanwege het gebrek aan eigen proton-bestralingsfaciliteiten zullen metingen met de primaire dosisstandaard altijd buiten het metrologie instituut moeten plaatsvinden en zal zorgvuldig met de beschikbare meettijd moeten worden omgesprongen. Problematisch voor calorimetrie is dat het signaal niveau (d.w.z. ΔT) zodanig laag is dat zeer veel metingen nodig zijn om een statistisch nauwkeurig resultaat te verkrijgen. Voordat een meetstandaard in bedrijf genomen kan worden moet deze ook onderworpen worden aan validatiemetingen. Dit zijn metingen die het onderliggende meetmodel en de bijbehorende aannames testen, zodat er vertrouwen ontstaat in de werking van de standaard.

Centraal in de water calorimetrie staan een aantal factoren die voor zowel de fotonen- als protonencalorimetrie het meeste bijdragen aan de meetonzekerheid. In dit proefschrift worden de effecten onderzocht van chemische reacties in het water ten gevolge van de inwerking van de stralingsdosis, de effecten van neutronenstralingsdosis en de gevolgen van het langzame weglekken van warmte uit het meetpunt door warmtegeleiding in het water.

Waterradiolyse

De achterliggende veronderstelling in water calorimetrie is dat alle energie die door de ioniserende deeltjes wordt afgegeven zal leiden tot een temperatuurstijging van het water. Echter, de energie die door de ioniserende straling word afgegeven kan ook aangewend worden om het water op te breken, zodat verscheidene andere chemische verbindingen ontstaan:

$$\mathrm{H_2O} \xrightarrow{\text{Bestraling}} \mathrm{H_2} + \mathrm{H_2O_2} + \mathrm{O_2} \tag{2}$$

De energie die nodig is om het water op te breken (de reactie-enthalpie) zal niet bijdragen aan de temperatuurstijging van het water, waardoor er een meetfout ontstaat wanneer de dosis volgens vergelijking 1 word vastgesteld. Dit zogenaamde warmte-defect ('heat defect') moet verdisconteerd worden in de berekening van

de stralingsdosis. Dit heeft tot gevolg dat er een meetonzekerheid moet worden toegekend aan de dosis ten gevolge van de energie die samenhangt met chemische reacties in het water.

Echter, de ontstane chemische verbindingen zullen ten dele onderling reageren zodat er opnieuw water ontstaat. Bij deze reacties komt de ingebrachte energie weer als warmte vrij. Het blijkt dat er in de praktijk een evenwicht ontstaat tussen de ontbinding van water in reactieproducten enerzijds en de tegengestelde reactie waarbij de reactie producten onderling reageren tot water anderzijds:

$$H_2O \xrightleftharpoons{\text{Bestraling}} \begin{cases} H_2 \\ O_2 \\ H_2O_2 \end{cases} \tag{3}$$

Het bovenstaande evenwicht stelt zich tijdens de bestralingen in. Zodra het evenwicht bereikt is zal telkens evenveel water worden teruggewonnen uit de reactie producten als de hoeveelheid die wordt verloren bij het maken van deze chemische verbindingen. Daardoor zal er geen sprake meer zijn van een meetfout, dat wil zeggen, bij een bereikt evenwicht is het warmte-defect gelijk aan nul.

De praktische werkbaarheid van water calorimetrie is afhankelijk van het betrouwbaar bereiken van dit evenwicht in een redelijke hoeveelheid tijd. Voor protonendosimetrie is dit punt van relatief groot belang, omdat de beschikbare hoeveelheid meettijd doorgaans beperkt is vanwege de drukke bezetting van de bestralingsfaciliteiten. Het achterliggende reactie schema voor de versimpelde weergave in vergelijking 3 is complex. De ligging van het evenwicht (en de benodigde tijd om het te bereiken) is afhankelijk van het dosis-tempo van de bestraling, maar ook van het type ioniserende deeltje, de energie van de deeltjes en de aanwezigheid van eventuele verontreinigingen in het water. Hierdoor is er een verschil te verwachten tussen calorimetrie voor fotonenbestralingen en protonenbestralingen. In het geval van ^{60}Co fotonenbestralingen is de betrouwbaarheid van deze processen afdoende vastgesteld - echter voor protonenbestralingen ontbreekt het nog aan modellen en de bijbehorende validatie experimenten.

Hoofdstuk 3 in dit proefschrift geeft een beschrijving van de waterradiolyse, toegespitst op protonen watercalorimetrie. Het hoofdstuk levert schattingen van de effecten van de radiolyse op een calorimetrische meting, waarbij gebruik gemaakt wordt van modellen die voor protonencalorimetrie aangepast zijn, op basis van bestaande modellen voor ^{60}Co fotonencalorimetrie. Een beschrijving van het model voor de radiolyse is te vinden in appendix A.

Een centrale conclusie is dat het bereiken van evenwicht in positieve zin beïnvloed kan worden door het toevoegen van een redelijke hoeveelheid H_2-gas aan het water. Dit is noodzakelijk voor een betrouwbare meting met protonen bestralingen, met name als die worden uitgevoerd in een moderne klinische bestralingsfaciliteit, vanwege het uitzonderlijk hoge instantane dosistempo dat onder die omstandigheden gehaald wordt.

Hoofdstuk 3 bevat ook een beschrijving van een experiment dat is uitgevoerd op KVI-CART, waaruit blijkt dat het chemisch evenwicht betrouwbaar bereikt kan worden. Daardoor is het mogelijk om de maat van onzekerheid ten gevolge van deze reacties te reduceren tot dezelfde waarde die in gebruik is voor fotonencalorimetrie.

Neutronendosis

Eén van de aspecten van zowel de dosimetrie als klinische dosis bepaling die tot nog toe weinig aandacht heeft gekregen is de bijdrage van neutronen (ongeladen kerndeeltjes) aan de totale dosis. Neutronen ontstaan bij protonenbestralingen door botsingen tussen de protonen en atoomkernen. Dit gebeurt in vrijwel elk materiaal dat wordt bestraald en ook in het lichaam van een patiënt of in de calorimeter. De vrijgekomen neutronen zijn zelf ook een oorzaak van stralingsdosis doordat ze hun energie kunnen overdragen aan atoomkernen of doordat ze betrokken zijn bij kernreacties. Om deze reden is de behandelruimte in een ziekenhuis goed afgeschermd met dikke muren.

De neutronen dosis heeft echter ook gevolgen voor de dosismetingen in het ziekenhuis en de plek van de primaire meetstandaard (de water calorimeter) in de meetketen. Een aanlokkelijke optie is namelijk om de bestralingen die nodig zijn voor een calorimetrische metingen en de daarop volgende ionisatiekamer-kalibraties uit te voeren in een natuurkundig onderzoeksinstituut, zoals bijvoorbeeld KVI-CART. Daardoor hoeft niet een klinische behandelfaciliteit bezet gehouden te worden voor het doen van kalibratie metingen. Echter, er zijn altijd kleine verschillen tussen de bestralingen op instituten als KVI-CART en in een ziekenhuis, waardoor de ionisatiekamer kalibraties die verkregen zijn niet zonder meer te gebruiken zijn in het ziekenhuis.

Eén van die verschillen is dat op KVI-CART op dit moment het bestraalde gebied van de water calorimeter afgebakend word met een zogeheten collimator. De collimator is in feite een dik stuk metaal dat de protonen tegenhoud met een gat op de plek waar de bestraling gewenst is. Een moderne behandelfaciliteit in een ziekenhuis zal de vorm van de tumoren afbakenen door een dunne en goed gerichte proton straal heen en weer te bewegen zodat uiteindelijk het gehele te bestralen gebied bedekt is (de zogenaamde 'Pencil Beam Scanning' techniek). In vergelijking met een ziekenhuis zal er op KVI-CART een extra neutronen-productie zijn in het materiaal van de collimator die de protonen onderschept. Een ander verschil tussen KVI-CART en een ziekenhuis heeft te maken met de neutronen productie in het water volume zelf. Omdat de breedte van het te bestralen gebied zeer klein is in vergelijking met de dracht van de neutronen zal het relatieve aandeel van de neutronen-dosis op de totale dosis afhangen van de breedte van het bestraalde gebied. Om een kalibratie die uitgevoerd is buiten het ziekenhuis van toepassing te laten zijn in het ziekenhuis is een kleine correctie nodig die te maken heeft met dit verschil in neutrondosis.

Hoofdstuk 4 beschrijft een experiment waarbij de neutronendosis direct gemeten wordt met de water calorimeter. Door het gat in de collimator volledig te sluiten zal alleen de bijdrage van de neutronendosis ten gevolge van neutronen die in het collimator materiaal geproduceerd worden overblijven. Uit deze meting kan direct de relatieve bijdrage van de collimator-neutronen bepaald worden. Een ander experiment bestaat uit het volledig afremmen van de protonen in een bak met water waarbij de calorimeter achter deze bak geplaatst wordt. Doordat de protonen hun volledige energie al buiten de calorimeter hebben afgegeven meet de calorimeter in deze situatie alleen de dosisbijdrage van neutronen die in water geproduceerd worden. Op eenzelfde manier kan de gevoeligheid van een ionisatiekamer voor neutronendosis bepaald worden.

Door deze metingen te gebruiken om modellen voor neutronendosis te valideren kunnen de modellen gebruikt worden om te bepalen hoe groot de correcties moeten zijn zodat de kalibraties ook buiten een ziekenhuis uitgevoerd kunnen worden. Deze correctie kan uitgevoerd worden ten koste van slechts een kleine onzekerheidscomponent. Een centrale conclusie is dat dergelijke correcties altijd uitgevoerd moeten worden, tenzij de calorimeter direct in het ziekenhuis zelf is gebruikt.

Warmteoverdracht

Watercalorimetrie volgens vergelijking 1 is een meettechniek die afhankelijk is van het meten van een zekere temperatuurstijging ΔT ten gevolge van de geabsorbeerde dosis tijdens een bestraling. Echter, de tijdschaal van een calorimetrische meting is van zodanige lengte dat de warmtegeleiding in het water een rol speelt.

Het bestraalde gebied in het water volume zal warmer worden dan het water buiten dit gebied. Gedurende de meting mag de warmte uit het bestraalde gebied niet weglekken. De bestraling zelf neemt echter enige tijd in beslag (typisch ongeveer één minuut). Daarnaast is vanwege meetruis per individuele bestraling nog extra tijd nodig om een goede gemiddelde waarde voor de temperatuurstijging ΔT te verkrijgen. Gedurende de meettijd zal door warmtegeleiding in het water het temperatuurverschil ΔT weer langzaam wegzakken zodat een meetfout ontstaat. Wanneer verschillende metingen achter elkaar gedaan worden moet rekening gehouden worden met het feit dat de waarde van ΔT ook kan veranderen ten gevolge van warmte overdracht die samenhangt met voorgaande bestralingen.

Een ander effect heeft te maken met het feit dat de temperatuur sensor zelf ook opwarmt vanwege de bestraling. Echter, omdat de warmtecapaciteit van het materiaal (glas) waaruit de sensor is gemaakt veel lager is dan de warmtecapaciteit van het water zal de temperatuur van de sensor tijdens de bestraling sneller toe nemen dan de temperatuur van het water. Omdat de calorimeter de temperatuurstijging van alleen het water moet meten ontstaat een meetfout. Gelukkig kan tijdens de bestraling zelf al een groot gedeelte van deze boventallige temperatuurstijging wegvloeien naar het omliggende water. Echter, een klein deel zal ook op langere tijdschaal aanwezig blijven waardoor een correctie noodzakelijk is.

Hoofdstuk 5 van dit proefschrift beschrijft modellen voor zowel het wegvloeien van de warmte uit het bestraalde gebied als modellen voor de opwarming van de temperatuur sensor. Voor beide effecten zijn numerieke modellen opgesteld door gebruik te maken van de eindige-elementen methode om de warmte-diffusie vergelijking op te lossen. Voor het eerste effect is ook een analytische benadering gemaakt die goede overeenkomst vertoond met de numerieke berekeningen.

Om de modellen experimenteel te kunnen valideren met voldoende statistische nauwkeurigheid moet de begintoestand van de calorimeter betrouwbaar gereproduceerd kunnen worden. Dat wil zeggen, aan het begin van elke meting mogen er geen temperatuur gradiënten meer aanwezig zijn. Daarom moet aan het begin van elke meting het water opgemengd worden zodat de temperatuur in de waterbak homogeen is. Echter, om efficiënt gebruik te kunnen maken van de beschikbare meettijd moet ook het water in de meetcel van het systeem opgemengd worden. Dit zorgt ervoor dat na een serie metingen de ingebrachte warmte snel weggevoerd kan worden. Omdat de stroming van het water over de temperatuursensor ook aanleiding kan geven tot een meetfout, moest eerst het gedrag van het systeem zelf gekarakteriseerd worden.

Uit de metingen en berekeningen blijkt dat de warmteoverdracht effecten goed begrepen zijn, hoewel er buiten de statistische onzekerheid nog steeds een kleine discrepantie aanwezig is. De waargenomen afwijkingen worden gebruikt als basis voor een onzekerheidsschatting. Eén van de uitdagingen voor protonen-watercalorimetrie is het voorkomen van grote dosisgradiënten ten gevolge van dosisinhomogeniteiten nabij de temperatuur sensoren. Hoewel het mogelijk is om ook hier voor numerieke modellen op te stellen maakt dit wel dat de warmteoverdracht ten gevolge van de samenhangende temperatuurgradiënten lastig onder controle te krijgen is. Desalniettemin is de warmteoverdracht-gerelateerde onzekerheid voor protonencalorimetrie in de KVI-CART protonen bundel slechts marginaal groter dan de gerelateerde onzekerheid in het geval van fotonencalorimetrie.

Toekomst

De in dit proefschrift beschreven modellen en experimenten laten zien dat het uitvoeren van watercalorimetrie in een gescatterde protonen bundel zoals die op KVI-CART zonder meer mogelijk is. Er zijn nog verbeteringen te behalen op het gebied van dosis homogeniteit en de stabiliteit van het dosistempo. Toch zijn de gerelateerde waarden van de onzekerheidsschattingen niet bijzonder veel hoger dan al voor fotonencalorimetrie het geval is. Daarmee staat nu de weg open voor het daadwerkelijk uitvoeren van een ionisatiekamer kalibratie.

Tegelijk komt ook naar voren dat naast het hebben van een goed meetmodel een algehele mate van experimentele controle noodzakelijk is. In principe kunnen allerlei detaileffecten en experimentele varianties in het uitvoeren van de bestraling worden voorzien van een meetmodel met een bijbehorende nauwkeurigheidsschatting. Echter, het vertrouwen in een standaard wordt niet alleen bepaald door de numerieke waarde van de geschatte totale nauwkeurigheid, maar ook door

de ingewikkeldheid of juist eenvoud en daarmee robuustheid van de praktische implementatie. Daarom moeten er naast het kiezen van randvoorwaarden die leiden tot een robuust systeem bij voorkeur ook experimenten plaatsvinden die deze robuustheid kunnen onderschrijven.

Voor Pencil Beam Scanning (PBS) systemen is er in het algemeen een uitdaging op het gebied van bovengenoemde controle, de vrijheid randvoorwaarden te kiezen en de mogelijkheid om relevante experimenten uit te voeren. Vooralsnog zijn klinisch bestralingsfaciliteiten ook alleen in klinieken te vinden. Daarmee zou een klinische bestralingsfaciliteit in feite onderdeel worden van de meetstandaard. Hoewel een klinische faciliteit per definitie de representatiefste bestralingen kan bieden zijn er wel beperkingen in de manier waarop de bestraling uitgevoerd kan worden en vooral ook in de hoeveelheid meettijd die beschikbaar is.

Dat laatste maakt dat het uitvoerig valideren van het meetmodel (dat vanwege een verminderde controle ook complex is) in een kliniek een grote uitdaging zal zijn. Een alternatieve optie is het uitvoeren van klinisch relevante bestralingen buiten de kliniek. Dit betekent dat in een natuurkundig instituut zoals het KVI-CART een bestralingsfaciliteit neergezet moet worden die representatief is voor een klinische situatie. In de praktijk betekent dit het opstellen van een Pencil Beam Scanning systeem. Dit maakt het mogelijk voldoende goed-gecontroleerde meettijd in te zetten voor de benodigde validaties van het meetmodel. Eventueel kan er daarna ook in de kliniek zelf gemeten worden, maar ook directe kalibraties van ionisatie kamers zijn dan mogelijk zonder dat er kostbare meettijd gevonden hoeft worden in een kliniek.

In het algemeen zullen er altijd kleine numerieke correcties nodig zijn op de gemeten kalibraties wanneer in de kliniek gebruik gemaakt word van buiten de kliniek gekalibreerde ionisatiekamers, zelfs als een PBS systeem ingezet wordt. Dit is nu ook het geval voor reguliere fotonen bestralingen omdat de gebruikte bestralingstechniek in de kliniek verschilt van de technieken die in de nationale meetinstituten beschikbaar zijn. Dit werpt ook de vraag op wat de noodzaak en het nut is van een primaire standaard die specifiek gevalideerd is voor scanning systemen. Het antwoord op die vraag zal onder andere afhangen van de vereiste nauwkeurigheid van een protonen stralings dosis (die nu nog wordt geschat op basis van klinische resultaten met fotonen bestralingen) en van de verhouding tussen de toename van de onzekerheid van watercalorimetrie voor de complexere scanning systemen ten opzichte van scatter systemen enerzijds en de afname van de onzekerheid in de ionisatiekamer kalibratie (die het gevolg is van vertaalslagen tussen scatter systemen en scanning systemen) anderzijds.

Dankwoord

Dan nu, een dankwoord...

Zo'n boekje is natuurlijk niet compleet *zonder*. Het is 't bijzonderste hoofdstuk in elk proefschrift — een sectie zonder nummer, maar toch met vermelding in de inhoudsopgave — een sectie waarvan de goedkeuring vooraf door de promotores niet noodzakelijk nog voldoende of zelfs maar gewenst is. En dus ook meteen het moeilijkste hoofdstuk, want, behalve voor de feitelijke behulpzaamheid die door jullie is geboden in het kader van het onderzoek wil ik ook mijn dankbaarheid uitspreken voor de personen die jullie voor mij wilden zijn.

En dat brengt mij meteen bij mijn promotores. Beste Sytze, ik denk dat je een klassieke Doktorvater bent. Dank daarvoor. Ik ken je als een betrokken persoon met een soepel lopend kompas. Daardoor was je altijd toegankelijk voor een persoonlijk palaver — ook als het niet werkinhoudelijk was — wat maakte dat deze promovendus tussen enige zandbanken door heeft kunnen laveren. Zonder jouw fysisch-inhoudelijke commentaar en schier eindeloos geduld was het alles niet gelukt. Marco, 't was wonderbaarlijk zoals het allemaal nog gelopen is en ik was blij te horen dat je nog steeds mijn promotor wilde zijn. Heren, beiden veel dank dat jullie je door de vele versies van mijn schrijfsels heen hebben willen werken.

Dear members of the assessment committee mr. Paans, mr. Verhaegen, mr. Lomax, thank you very much for your interest in my work and for your commitment in reading my thesis.

Beste Jacco de Pooter en Leon de Prez bij VSL, veel dank voor jullie inzet over de afgelopen jaren. Het vroeg enige choreografie om de door jullie uitgeleende apparatuur op het juiste moment in Groningen beschikbaar te hebben, maar het is altijd nog gelukt. Verder wil ik jullie (en VSL in het algemeen) bedanken voor de vele inhoudelijke discussies die we hebben gehad over elk aspect van de meetketen en de analyse van de meetgegevens. Mede dankzij jullie inbreng en suggesties hebben we sommige effecten tot ver achter de komma kunnen karakteriseren.

Mr. Krauss at PTB, thank you for extensive discussions on water radiolysis, glassware design and heat transfer modelling and for getting me up to speed on the various challenges in water calorimetry.

Mr. Damian Twerenbold and mr. Sándor Vörös at METAS, thank you very much for lending me the calorimeter and much of the electronics and instructing me on how to use it. Your advice on glassware cleaning techniques and thermistor probe design and various practicalities turned out to be very useful.

Aan de leden van het AGOR cyclotron bedrijf, operateurs, technici en wetenschappers, veel dank voor jullie aandeel in het welslagen van de experimenten. Ik kan mij een keer herinneren dat er bij nacht en ontij een aantal van jullie op het KVI verschenen om mijn experiment weer op de rails te helpen. Jullie beheerste maar toch ook flexibele werkmethodiek is essentieel bij dit soort precisie experimenten. Veel dank ook voor het bieden van oplossingen voor allerlei andere niet bundel-gerelateerde technische zaken die bij deze experimenten speelden.

Medewerkers van de mechanische werkplaats, ik waardeer het zeer dat jullie altijd nog mijn last-minute ingediende opdrachten bijtijds af hebben gekregen en dat jullie met mij mee werkten doordat jullie de moeite namen om uit te vinden wat ik *eigenlijk* bedoelde in plaats van wat ik zei.

Maarten Vervoort, ik was erg blij met een glasblazer zo dicht bij huis. Ik had misschien wat onmogelijke technische wensen, maar jij had zeer ruim de tijd genomen om een manier te vinden om het allemaal te laten werken. En die keren dat je noodreparaties uitvoerde omdat anders mijn bundeltijd in gevaar zou komen ben ik ook niet vergeten. Dank.

Emiel, Nafiseh, Tom, Faruk, Ola, Reint, thank you very much for being wonderful colleagues. Your participation by taking (night)shifts to keep the experiments going or helping me with some important calculations is much appreciated. Mariet, dank je wel voor de incidentele bemoedigende wandelgangen/koffieautomaatgesprekken. Emiel, bedankt dat je bij het schrijven van dit alles mee wilde lezen.

Dear 'lunch people', over the many years there have been too many of you to list each of your names here individually. Therefore i would just like to say, thank you, for that moment each day, filled with humor and relaxation and for the occasional movie, dinner, barbecue, bowling-night and even a pain(t)ball fight. I've also enjoyed the many witty conversations covering the broadest variety of subjects.

Beste Marc-Jan, ik denk niet dat er één experiment is waar jij niet aan hebt bijgedragen. Veel dank voor de vele inzet, vaak tot diep in de nacht. Jij fungeerde een beetje als de go-to-guy voor allerlei uitdagingen — en dan bedoel ik niet perse alleen fysisch inhoudelijke zaken. Altijd was je beschikbaar voor raad en jouw 'birds-eye view' was af en toe onmisbaar.

Beste Oksana, ik weet niet of er in de taal zoiets bestaat als een 'Doktormutter', maar volgens mij komt jou die eer toe. Bedankt dat je mij een beetje wegwijs wilde maken. En eerlijk gezegd, zonder jouw inzet ... ik zou niet weten waar we dan hadden gestaan. Bedankt voor al jouw inzichtvolle commentaar en advies. De

vele uren bundeltijd die we er op hebben zitten waren ook best gezellig. En die hebben ook goede ideeën opgeleverd*. En het moet gezegd worden: de bundel*taart* (behorende bij de bundel*tijd*, na voorafgaand bundel*taartoverleg*) ging er ook best in.

Harry, zonder jouw hulp zouden veel experimenten nog niet eens door de deur naar binnen kunnen rijden (in mijn geval letterlijk). Vlak voorafgaand aan elk experiment was er veel voorbereiding nodig (wat naar mijn smaak dan soms zelfs nog overnieuw moest) en daarin was jij een bijzonder behulpzame collega. Hetzelfde geld voor het inregelen van de bundel en de vele technische vraagstukken die ik op je bord gegooid heb. En nog vele andere dingen. Mede dankzij jouw humoristische, maar toch ook rustige en professionele benadering hebben deze experimenten doorgang kunnen vinden.

Beste Marcel, bedankt dat je wilde paranimfiëren. Kenmerkend voor jou is dat je altijd uitnodigend bent en anderen op hun gemak weet te stellen. Dat blijkt ook wel uit de sociale spil-functie die je elke dag om 12:02:59 vervult. Dank.

Beste Joanne, bedankt dat jij voor meer dan 6 jaar mijn kantoorgenoot wilde zijn. Terwijl ik dit schrijf zit je je net door het — naar verwachting — laatste commentaar op jouw proefschrift heen te werken. Bij het ter perse gaan van dit boekje zou het klaar moeten zijn. Alvast gefeliciteerd! ☺ Datgene wat je voor mij betekend hebt laat zich helaas wat moeilijk in woorden vangen. Maar ik wil hier toch even mijn bewondering uitspreken, voor jouw frisse optimisme en jouw aanstekelijke vrolijkheid. En, wat mij betreft kan jij in vele opzichten anderen tot voorbeeld zijn†. Maar belangrijk voor mij was dat je al die positieve dingen ook meenam naar het werk. Bedankt voor die keren van gedeelde vrolijkheid, als dingen mee zaten. Soms zat het me flink tegen, maar dan was je er ook gewoon. De afgelopen paar maanden is me duidelijk geworden hoe bijzonder dat eigenlijk is - en dat waardeer‡ ik sterk. En dus, Joanne, ik ga je straks missen.

...jullie allemaal trouwens.

Aan mijn ouders,
bedankt, voor alles.

* Bijvoorbeeld hoofdstuk 5, roertechniek. Ik had jouw idee in het begin afgeschoten, maar toch in het achterhoofd gehouden totdat ik een manier zag om het *wel* voor elkaar te krijgen. Maar goed ook, want zonder dat was het experiment niet uitvoerbaar geweest.

† En, ... - ach, je weet wel ☺

‡ 'kon minder' heet dat hier.

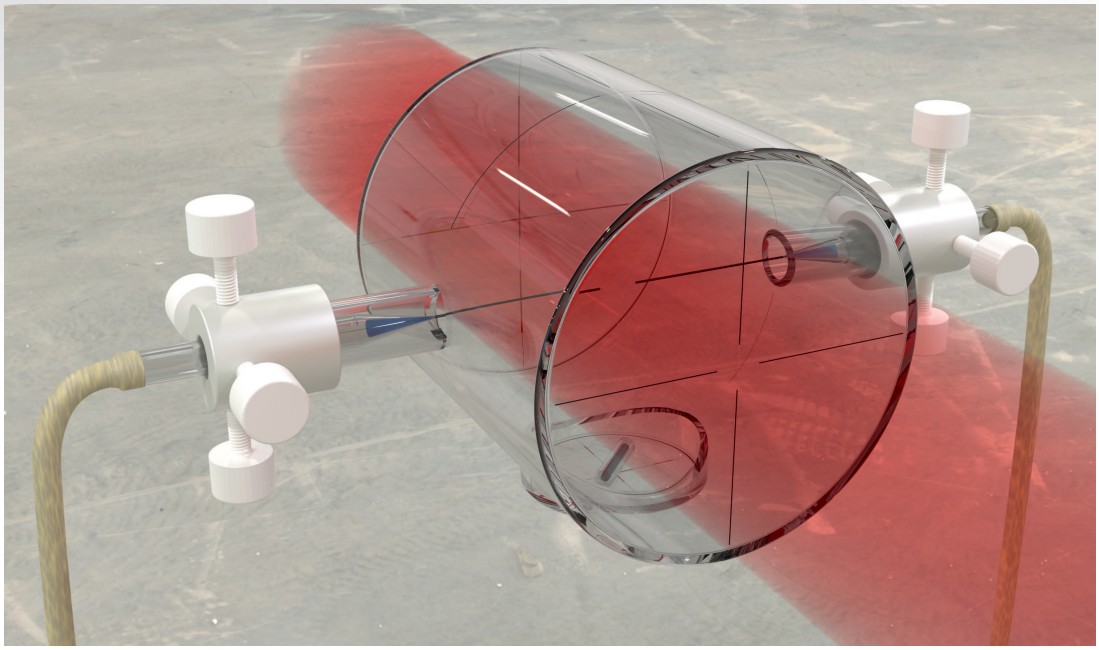

ISBN 978-90-367-9853-2